

## **Distribution Agreement**

In presenting this thesis or dissertation as a partial fulfillment of the requirements for an advanced degree from Emory University, I hereby grant to Emory University and its agents the non-exclusive license to archive, make accessible, and display my thesis or dissertation in whole or in part in all forms of media, now or hereafter known, including display on the world wide web. I understand that I may select some access restrictions as part of the online submission of this thesis or dissertation. I retain all ownership rights to the copyright of the thesis or dissertation. I also retain the right to use in future works (such as articles or books) all or part of this thesis or dissertation.

Signature:

---

Rolando F. Rengifo

---

Date

**From Amyloid to Copper Arrays:**

**The design of a functional Metalloamyloid Nanostructure (MAN)**

By

Rolando F. Rengifo  
Doctor of Philosophy

Chemistry

---

David G. Lynn, Ph.D.  
Advisor

---

Vincent Conticello, Ph.D.  
Committee Member

---

Khalid Salaita, Ph.D.  
Committee Member

Accepted:

---

Lisa A. Tedesco, Ph.D.  
Dean of the James T. Laney School of Graduate Studies

---

Date

**From Amyloid to Copper Arrays:  
The design of a functional Metalloamyloid Nanostructure (MAN)**

By

Rolando F. Rengifo  
B.S. Duke University, 2011

Advisor: David G. Lynn, Ph.D.

An abstract of  
A dissertation submitted to the Faculty of the James T. Laney School of Graduate Studies  
of Emory University  
in partial fulfillment of the requirements for the degree of Doctor of Philosophy in  
Chemistry  
2017

## Abstract

### From Amyloid to Copper Arrays: The design of a functional Metalloamyloid Nanostructure (MAN)

By Rolando F. Rengifo

Amyloidogenic diseases are characterized by abnormal collections of self-assembling peptides that form beautifully organized peptide arrays. Amyloid- $\beta$  ( $A\beta$ ), a hallmark protein in Alzheimer's Disease (AD), forms aggregates that have been linked with AD etiology, though their role in disease onset and progression has been poorly correlated. Recent efforts have brought  $A\beta$  to the forefront of AD research once again, however, as the intermediate stages of assembly have been identified as neurotoxic pathologies. In this work, we outline the first example of a fully characterized oligomeric particle – a marker in the working hypothesis of AD progression – formed from an extension of the  $A\beta$  nucleating core,  $A\beta(13-21)K16A$  (K16A). Motivated by the functional capacity ascribed to such small self-assembling units, and having characterized the well-organized supramolecular fibers that evolve from these oligomeric intermediates, we sought to modify their assembly pathway and tailor their function by incorporating redox active metal ions. In the presence of  $Cu^{2+}$ , K16A fibers transform to form nanoribbons with a rich blue color. The K16A- $Cu^{2+}$  metalloamyloid nanostructure (MAN) displays characteristics parallel to cupredoxins. We demonstrate, however, that  $Cu^{2+}$  is incorporated at a density ratio between 0.6 and 0.8 ( $Cu^{2+}$ /peptide), insulated within a peptide bilayer in two distinct coordination environments regularly arrayed throughout the MAN. Indeed, these structures are composed of cupredoxin arrays with a redox potential of +670 mV vs. RHE. Furthermore, this MAN displays quasi-reversible redox behavior, and it can undergo substrate level reduction with no effect on its overall morphology over a period of at least 16 hrs. The level of stability, order, and homogeneity achieved in the design of this material coupled with the degree of  $Cu^{2+}$  incorporation insulated in a peptide bilayer and directing the rearrangement of the peptide arrays, makes the K16A- $Cu^{2+}$  MAN a functional material unlike any other. Such a material paves the way for the rational design of new materials that will increase the complexity of MANs to demonstrate electron transport over controlled distances, electron storage in high density and redox chemistry within the self-assembling core.

**From Amyloid to Copper Arrays:  
The design of a functional Metalloamyloid Nanostructure (MAN)**

By

Rolando F. Rengifo  
B.S. Duke University, 2011

Advisor: David G. Lynn, Ph.D.

A dissertation submitted to the Faculty of the  
James T. Laney School of Graduate Studies of Emory University  
in partial fulfillment of the requirements for the degree of Doctor of Philosophy in  
Chemistry  
2017

## **Acknowledgements**

First and foremost, I would like to thank my research advisor, Dr. David G. Lynn, for his overwhelming support in research, professional development, and community engagement. Without his support, I would not have been able to develop into the academic professional I am today. His open mindedness and commitment to understanding the effects of globalization in research and education have translated to some revolutionizing ideas in the Emory academic curriculum and science education in the Atlanta community at large. I have been fortunate to share in these experiences.

I also thank the Robert P. Apkarian Electron Microscopy Core team of Emory University – Dr. Elizabeth R. Wright, Hong Yi, Jeannette V. Taylor and Arthur McCanna for TEM training and help with data collection. Thanks to the Emory X-ray Center for powder diffraction training and data collection with specific gratitude to Dr. John Bacsa. Thanks to the Emory NMR center for all solid-state NMR analysis with special thanks to Dr. Anil Mehta for all training, invaluable discussions, Chinese coin demos and his dedication to student academic development and professionalism. Thanks to Dr. Kurt Warncke and Dr. Umar Twahir for their invaluable support in EPR and ESEEM experiments that helped define the critical elements of this work. Thanks to Joshua Brockman for his collaboration and support with fluorescence anisotropy experiments. Thanks to Steve Krebs and Claire Scott for their support getting all chemicals and equipment needed – without your help this work would not have been possible.

Finally, thanks to my committee members, Dr. Khalid Salaita and Dr. Vincent Conticello, for their support and discussion in the past years, your commitment to academic excellence helped shape this work. Thanks to all labmates (past and current)

and friends who supported me throughout my research career. Special thanks to the most important people in my life, my parents, Rosa Baltodano de Rengifo and Dr. Hector Rengifo, brother, David Rengifo, and girlfriend, Dr. Ellen Litkowski – without your consistent words of support I would not have succeeded in any of my academic endeavors.

Gracias por su apoyo, los quiero mucho y les dedico este trabajo.

## Table of Contents

Chapter 1 : Amyloid Applications in Nanobiotechnology .....	1
Introduction .....	1
Toward Conducting and Energy-Storing Amyloids.....	4
Designing an Amyloid Antenna .....	4
Breaking Amyloid Assembly Symmetry.....	9
Metalloamyloid Nanostructures .....	12
Rational Design of Small-Molecule Incorporating Amyloid Nanostructures .....	19
Conclusion.....	20
Chapter 2 : Dynamics of Amyloid Granules in the Oligomer Cascade Hypothesis .....	23
Introduction .....	23
Results and Discussion.....	25
Oligomeric Particles and Supramolecular Fibers of H-H <sup>13</sup> HQALVFFA <sup>21</sup> -NH <sub>2</sub> (K16A).....	25
Defining the Structure of K16A Oligomeric Particles .....	28
Conclusion.....	37
Materials and Methods .....	39
Chapter 3 : Designing Metalloamyloid Nanostructures (MANs) .....	52



Introduction .....	52
Results and Discussion.....	55
Peptide Design.....	55
Templating K16A and Ac-K16A assembly with metals .....	66
Cu <sup>2+</sup> and Zn <sup>2+</sup> influence on Ac-K16A and K16A assembly and morphology .....	73
Solid-state NMR analysis of Ac-K16A and K16A assemblies in the presence of Zn <sup>2+</sup> .....	87
Structure and stability of Ac-K16A-Cu <sup>2+</sup> and K16A-Cu <sup>2+</sup> MANs.....	99
Reversibility of Cu <sup>2+</sup> /Cu <sup>+</sup> cycle in Ac-K16A-Cu <sup>2+</sup> and K16A-Cu <sup>2+</sup> MANs.....	112
Conclusion.....	120
Materials and Methods .....	123
Chapter 4 : Metalloamyloid Nanostructure (MAN) as a Blue Copper Protein Mimic ...	132
Introduction .....	132
Results and Discussion.....	134
A ratiometric study of Cu <sup>2+</sup> incorporation by optical spectroscopy and ITC.....	134
EPR analysis of K16A-Cu <sup>2+</sup> nanostructures.....	148
Cu <sup>2+</sup> is isolated in the K16A peptide bilayer, not at the nanoribbon surface .....	150
Assessing K16A-Cu <sup>2+</sup> reactivity .....	171
Conclusion.....	183
Materials and Methods .....	194

Chapter 5 What next?.....	201
Non-canonical amino-acids serve as e <sup>-</sup> acceptors in the presence of Cu <sup>2+</sup> . .....	202
Peptide driven polyoxometalate (POM) self-assembly.....	204
Expanding the complexity of self-assembling nanostructures by rational design. ....	206
Conclusion.....	212
References.....	213

## List of Figures

### Chapter 1

Figure 1.1 – Models of a chlorosome and an amyloid nanotube. ....	3
Figure 1.2 – Representation of three key elements in the design of bionanomaterials. ....	3
Figure 1.3 – Congo Red binding on the surface grooves of the peptide a nanotube. ....	6
Figure 1.4 – Modeling energy transfer on the peptide nanotube surface.....	8
Figure 1.5 – Building charge asymmetry across a nanotube surface.....	9
Figure 1.6 – TEM images of A $\beta$ (10-21) and A $\beta$ (13-21)K16A in the absence and presence of Zn <sup>2+</sup> .....	15
Figure 1.7 – TEM images of Ac-H14A and K16A in the absence and presence of Cu <sup>2+</sup> . 17	
Figure 1.8 – Model of Ac-H14A fibers decorated with Cu <sup>2+</sup> along a single face of the assembly.....	18
Figure 2.1 – TEM micrographs of K16A fibers and particles. ....	26
Figure 2.2 – Width measurements of K16A particles.....	26
Figure 2.3 – CD and FT-IR of K16A over-time. ....	28
Figure 2.4 – Fluorescence anisotropy images of K16A fibers with different light polarizers.....	29
Figure 2.5 – Fluorescence anisotropy analysis of K16A particles.....	30
Figure 2.6 – TEM micrograph of fiber pellet with supernatant added after lyophilization. ....	33
Figure 2.7 – Solid-state NMR analysis of K16A particles and fibers. ....	34
Figure 2.8 – CP-MAS NMR spectra of K16A with and without supernatant. ....	35

Figure 2.9 – Cartoon representation of the evolution of order in the assembly of K16A over time. ....	38
Figure 3.1 –Representation of top-down and bottom-up approaches to development of nanomaterials. ....	53
Figure 3.2 – Ac-H14A in the presence and absence of $\text{Cu}^{2+}$ . ....	57
Figure 3.3 – Ac-K16A and K16A assemblies in MES (pH: 5.6) and HEPES buffer (pH: 7.4). ....	58
Figure 3.4 – CD spectra of Ac-K16A and K16A fibers. ....	62
Figure 3.5 – TEM micrographs of K16A assembled at different temperatures.....	63
Figure 3.6 – TEM micrographs and width measurements of K16A and Ac-K16A fibers. ....	64
Figure 3.7 – Solid-state NMR analysis of Ac-K16A fibers. ....	65
Figure 3.8 – TEM summary of metal-survey results with alkaline earth metals, transition metals, post-transition metals, and lanthanoids. ....	69
Figure 3.9 – TEM analyses of K16A/metal co-assemblies as a function of temperature. ....	72
Figure 3.10 – UV-Vis of aquo- $\text{Cu}^{2+}$ and in the presence of K16A- $\text{Cu}^{2+}$ and Ac-K16A- $\text{Cu}^{2+}$ . ....	73
Figure 3.11 – CD spectra of K16A and Ac-K16A in the presence of $\text{Cu}^{2+}$ and $\text{Zn}^{2+}$ .....	75
Figure 3.12 – CD spectra of mature K16A and Ac-K16A assemblies in the presence of $\text{Cu}^{2+}$ and $\text{Zn}^{2+}$ . ....	76
Figure 3.13 – TEM micrographs of Ac-K16A assembly over the time in the presence and absence of $\text{Cu}^{2+}$ and $\text{Zn}^{2+}$ . ....	80
Figure 3.14 – TEM micrographs of K16A assembly.....	82

Figure 3.15 – Width histograms of Ac-K16A and K16A in the presence and absence of Cu <sup>2+</sup> and Zn <sup>2+</sup> .....	86
Figure 3.16 – Solid-state NMR analysis of Ac-K16A-Zn <sup>2+</sup> nanostructures. ....	89
Figure 3.17– Solid-state NMR analysis of K16A-Zn <sup>2+</sup> nanostructures. ....	92
Figure 3.18 – Diversity of peptide arrangements identified by solid-state NMR in the [1- <sup>13</sup> C]Ala16, [ <sup>15</sup> N]Phe19 K16A-Zn <sup>2+</sup> assemblies. ....	93
Figure 3.19 – Fits to <sup>13</sup> C{ <sup>15</sup> N} REDOR data for K16A-Zn <sup>2+</sup> antiparallel in-register population. ....	94
Figure 3.20 – TEM and AFM images of K16A-Zn <sup>2+</sup> assemblies.....	97
Figure 3.21 – Morphological effects of Zn <sup>2+</sup> addition to preassembled K16A fibers. ....	98
Figure 3.22 – Morphological effects of Cu <sup>2+</sup> addition to preassembled K16A fibers....	103
Figure 3.23 – TEM micrographs and FT-IR of K16A and Ac-K16A in the absence and presence of Cu <sup>2+</sup> .....	105
Figure 3.24 – CP-MAS NMR spectra of Ac-K16A and K16A in the presence of Cu <sup>2+</sup> . 106	
Figure 3.25 – <sup>13</sup> C{ <sup>15</sup> N} REDOR dephasing curves for Ac-K16A-Cu <sup>2+</sup> and K16A-Cu <sup>2+</sup> ribbons.....	107
Figure 3.26 – AFM of Ac-K16A-Cu <sup>2+</sup> ribbons. ....	108
Figure 3.27– AFM of K16A-Cu <sup>2+</sup> ribbons.: ....	108
Figure 3.28 – Melting curves for Ac-K16A-Cu <sup>2+</sup> , K16A-Cu <sup>2+</sup> and Ac-H14A-Cu <sup>2+</sup> .....	111
Figure 3.29 – Cyclic voltammograms of K16A-Cu <sup>2+</sup> and Ac-K16A-Cu <sup>2+</sup> over different scan rates. ....	114
Figure 3.30 – Randles-Sevcik plots for K16A-Cu <sup>2+</sup> and Ac-K16A-Cu <sup>2+</sup> ribbons.....	116

Figure 3.31 – Preorganization electron transfer mechanism (POET). (Reprinted from (Balland et al., 2010) with permission of PNAS publication) .....	117
Figure 3.32 – Plots of $\log  i_p $ vs $\log (v)$ to assess dependence of K16A-Cu <sup>2+</sup> and Ac-K16A-Cu <sup>2+</sup> assemblies on diffusion or adsorption to the glassy carbon electrode. ....	119
Figure 4.1 – CD of K16A-Cu <sup>2+</sup> over 20 days at different Cu <sup>2+</sup> ratios. ....	135
Figure 4.2 – Absorbance values for basis-set used in UV-Vis fits. ....	138
Figure 4.3 – Summary of basis-set fitting results comparing Cu <sup>2+</sup> coordinate species over a range of CuCl <sub>2</sub> concentrations at a constant peptide ratio. ....	139
Figure 4.4 – UV-Vis fits using basis-set absorbance values.....	144
Figure 4.5 – ITC of Cu <sup>2+</sup> titration of Aβ(13-21)K16A in MES buffer.....	147
Figure 4.6 – CW-EPR spectra of the K16A- Cu <sup>2+</sup> complex for different Cu <sup>2+</sup> :peptide ratios.....	149
Figure 4.7 – Surface characterization of K16A-Cu <sup>2+</sup> nanoribbons.....	152
Figure 4.8 – Cartoon representation and TEM micrograph of nanotubes formed by E22L. ....	156
Figure 4.9 – TEM micrographs of K16H,E22L assembly in different solvents.....	157
Figure 4.10 – CD spectra of E22L and K16H,E22L nanotubes. ....	158
Figure 4.11 – <sup>13</sup> C{ <sup>15</sup> N} REDOR fit of K16H,E22L nanotubes. ....	159
Figure 4.12 – Surface characterization of E22L and K16H,E22L nanotubes. ....	161
Figure 4.13 – TEM micrographs of K16H,E22L nanotubes in the presence and absence of CuCl <sub>2</sub> .....	161
Figure 4.14 – UV-Vis spectrum for K16H,E22L nanotubes in the presence of CuCl <sub>2</sub> . .	162
Figure 4.15 – Assembly of K16HH,E22L in different solvent systems. ....	164

Figure 4.16 – CD spectra of K16HH,E22L assemblies in different solvent systems. ....	166
Figure 4.17 – TEM micrographs of K16HH,E22L in the presence of CuCl <sub>2</sub> .....	168
Figure 4.18 – FTIR and UV-Vis of K16HH,E22L nanotubes. ....	169
Figure 4.19 – Cartoon representation of the K16A peptide bilayer and the insulated copper, away from the ribbon surface.....	170
Figure 4.20 – Concentration effects on electrochemical signal for K16A-Cu <sup>2+</sup> nanostructures. ....	172
Figure 4.21 – Voltammograms and Randles-Sevcik plots of K16A-Cu <sup>2+</sup> ribbons at different scan rates. ....	174
Figure 4.22 – Plots of log  i <sub>p</sub>   vs. log (v). ....	178
Figure 4.23 – Ascorbate reduced K16A-Cu <sup>2+</sup> MAN. ....	182
Figure 4.24 – Width measurements of E22L, K16H,E22L, and K16HH,E22L nanotubes. ....	187
Figure 4.25 – AFM micrographs of K16H,E22L and K16HH,E22L nanotubes.....	192
Figure 4.26 – Complete structural model of the K16A-Cu <sup>2+</sup> MAN. ....	193
Figure 5.1 – Structural representation of genetically engineered pyTyr amino-acid in GFP. ....	203
Figure 5.2 – Synthesis of pyTyr.....	203
Figure 5.3 – Mn-Anderson type POM functionalized for peptide synthesis. ....	205
Figure 5.4 – Representation of Sn functionalization of a POM for peptide incorporation. ....	206
Figure 5.5 – Benzylamine driven assembly of nanotubes. ....	207

Figure 5.6 – TEM micrographs of hydroquinone and quinone driven assembly of peptide nanotubes. ....	209
Figure 5.7 – Width distribution of rationally designed nanotubes.....	210
Figure 5.8 - Quinone arrangement in peptide nanotubes.....	211



## Chapter 1 : Amyloid Applications in Nanobiotechnology

**Text adapted from:** Rengifo, R. F., Li, N. X. A., Sementilli, A., & Lynn, D. (2017).

Amyloid Scaffolds as Alternative Chlorosomes. *Organic & Biomolecular Chemistry*.

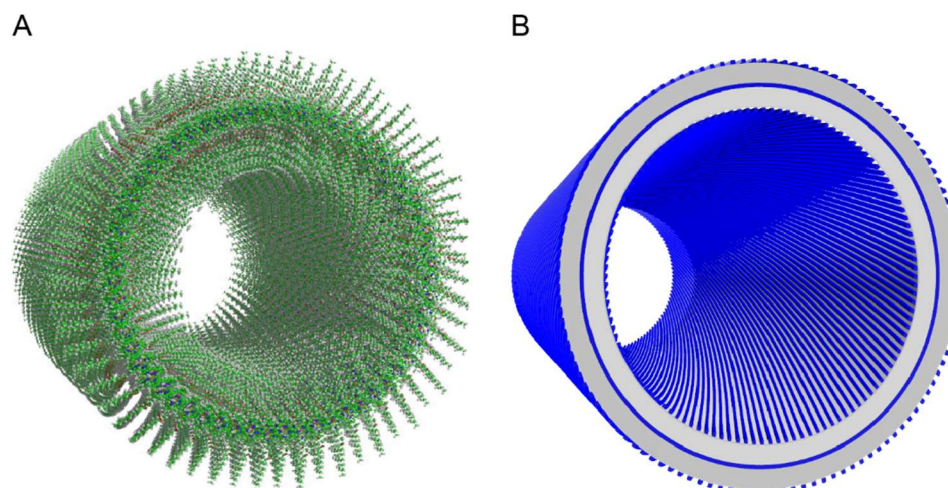
DOI:10.1039/C7OB01170A

### Introduction

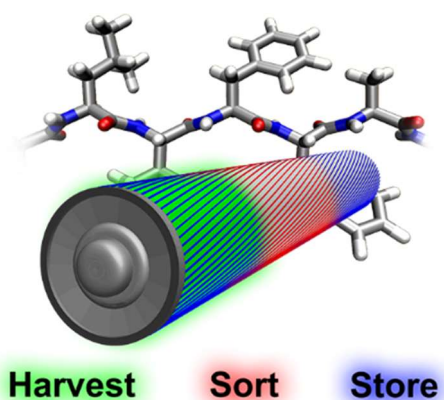
Biochemical ingenuity is beautifully displayed in photosynthesis. Solar energy is captured within complex pigments housed in intricate protein networks where the remarkable light-harvesting efficiency is attributed to the precise arrangement of these chromophores and electron transfer sites (Govindjee, Kern, Messinger, & Whitmarsh, 2001). Designing and constructing such mesoscale arrays presents a significant challenge, particularly when considering organizing such arrays for high-energy photoredox processes (Kim, Lee, Lee, & Park, 2012).

As shown in the structural model of **Figure 1.1A**, the chlorosomes of green sulfur bacteria present a relatively simple model of a system which has evolved a remarkable level of chromophore organization. Containing over 250,000 chlorophyll and carotenoid pigments packed into multilamellar nanotubes (Ansari-Oghol-Beig et al., 2013; M de Groot, 2010), this repeating architecture underlies a remarkably efficient light-harvesting capability, powering green sulfur bacteria in the very low-light conditions found one hundred meters below sea level (Manske, Glaeser, Kuypers, & Overmann, 2005; Oostergetel, van Amerongen, & Boekema, 2010). Over the years, we have characterized long range order within cross- $\beta$  amyloids ranging from nanotubes (Anthony, Berland,

Mehta, Lynn, & Seth Childers, 2014a; Ian W. Hamley, 2014; S. Li et al., 2016; Pachahara & Nagaraj, 2015; Scanlon & Aggeli, 2008; Valery, Artzner, & Paternostre, 2011) ribbons,(Castelletto, Hamley, Hule, & Pochan, 2009; W. Seth Childers, Anthony, Mehta, Berland, & Lynn, 2012; Guo et al., 2013), sheets (Dai et al., 2015; T. Jiang et al., 2014; Xie, Luo, & Wei, 2013), and fiber (W. Seth Childers et al., 2012; Ivanova, Sievers, Sawaya, Wall, & Eisenberg, 2009; Jayawarna & Ulijn, 2012; Y. Liang, Pingali, et al., 2008; Paparcone, Sanchez, & Buehler, 2010; Paramonov, Jun, & Hartgerink, 2006) architectures. Using these structures as organizing scaffolds, we have demonstrated the construction of chlorosome-like arrays (**Figure 1.1B**). The potential to template chromophore arrays on a protein scaffold that can sustainably self-propagate in living cells might extend the functions of extant biology. In this introductory chapter, we develop a comprehensive overview on the advancement of self-assembling and self-healing bionanomaterials designed as the separate components of a photosynthetic cell. Our group specifically exploits amyloid peptides as scaffolds that have been demonstrated to be capable of (1) organizing light-harvesting chromophores, (2) breaking peptide bilayer symmetry for directional energy and electron transfer, (3) incorporating redox active metal ions at high density, and (4) accommodating redox active small molecules within the supramolecular architecture. Combining each capability sets the stage for developing materials capable of directional net electron transfer and energy storage on a cell-compatible scaffold (**Figure 1.2**).



**Figure 1.1 – Models of a chlorosome and an amyloid nanotube.** Schematic models of (A) bacteriochlorophyll pigments (green) organized as a nanotube in a chlorosome and (B) an engineered nanotube consisting of peptides self-assembled in a cross- $\beta$  array. Peptide amphiphiles (e.g. Ac-KLVFFAL-NH<sub>2</sub>), unlike simple amphiphiles, form ordered arrays by pairing solubilizing groups (K, blue) with amyloidogenic domains (LVFFAL, gray). (Figure 1A reprinted from (Ansari-Oghol-Beig et al., 2013), with the permission of AIP Publishing)



**Figure 1.2 – Representation of three key elements in the design of bionanomaterials.** Cartoon representation of the different elements the Lynn lab has collectively discovered

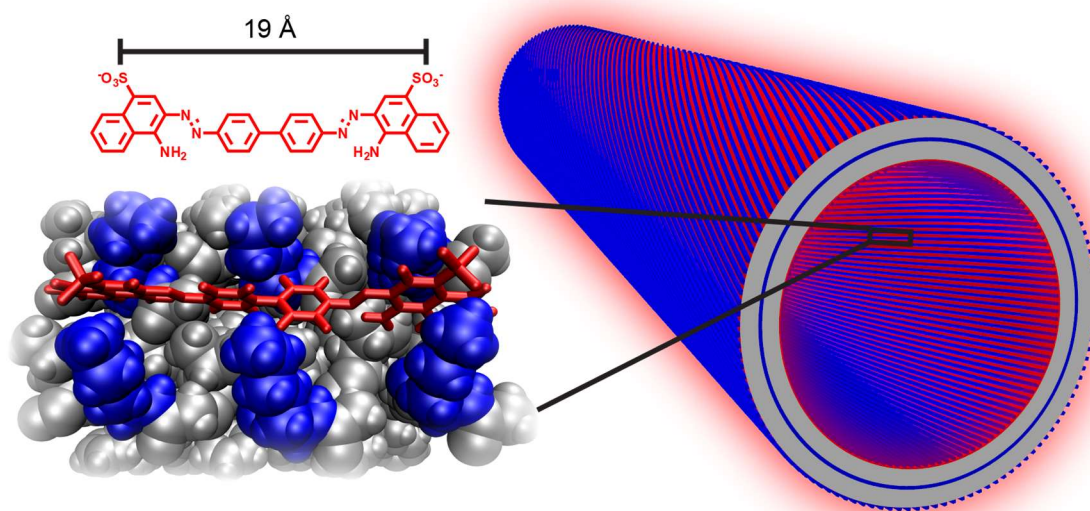
towards the design of nanomaterials, from a small peptide sequence derived from amyloid- $\beta$ , in the advancement of the emerging field of nanobiotechnology. (Reproduced from (Rengifo, Li, Sementilli, & Lynn, 2017) with permission from the Royal Society of Chemistry)

## **Toward Conducting and Energy-Storing Amyloids**

### **Designing an Amyloid Antenna**

The folding pathway for the nucleating core of the A $\beta$  peptide of Alzheimer's disease (AD), L<sup>17</sup>VFFA<sup>21</sup>, may be the most widely studied amyloid, both empirically and through simulation (Anthony, Berland, et al., 2014a; Anthony, Mehta, Lynn, & Berland, 2014; Balbach et al., 2000; Brovchenko, Burri, Krukau, & Oleinikova, 2009; Cheon, Chang, & Hall, 2011; Debeljuh, Barrow, & Byrne, 2011; Elgersma et al., 2009; Gehman, Separovic, Lu, & Mehta, 2007; Irback & Mitternacht, 2008; Klimov, Straub, &

Thirumalai, 2004; Klimov & Thirumalai, 2003; Krone et al., 2008; G. Li & Pomès, 2013; H. Li, Luo, Derreumaux, & Wei, 2011; Lin et al., 2014; Ma & Nussinov, 2002; Martinez, Malolepsza, Rivera, Lu, & Straub, 2014; Pan, Liu, Zhang, Yu, & Dong, 2012; Petty & Decatur, 2005; Santini, Mousseau, & Derreumaux, 2004; Shanmugam & Polavarapu, 2011; Smith et al., 2015). Indeed, many congeners of A $\beta$  peptide have been studied under a variety of solvents, pH and temperature conditions. Notably, when constructed as Ac-KLVFFAE-NH<sub>2</sub> and incubated under acid conditions in 40% CH<sub>3</sub>CN, the nucleating core can self-associate to form nanotubes from antiparallel  $\beta$ -sheets with strands shifted out-of-register by the N-terminal residue. This organization creates grooves that run the length of the internal and external surfaces that define the hollow nanotube assembly (**Figure 1.1B**). The predicted dimensions of these grooves are large enough to bind aromatic ligands (**Figure 1.3**) (W. Seth Childers, Mehta, Lu, & Lynn, 2009). Specifically, the nanotube grooves have been shown to organize Congo Red (CR) molecules end-to-end and side-by-side, spacing the chromophores in tracks one nanometer apart along the length of the inside and outside of the hollow nanotube. This density and chromophore organization approaches that seen in the chlorosome models, but benefits from organization on a peptide scaffold that can be further tailored by design.



**Figure 1.3 – Congo Red binding on the surface grooves of the peptide a nanotube.**

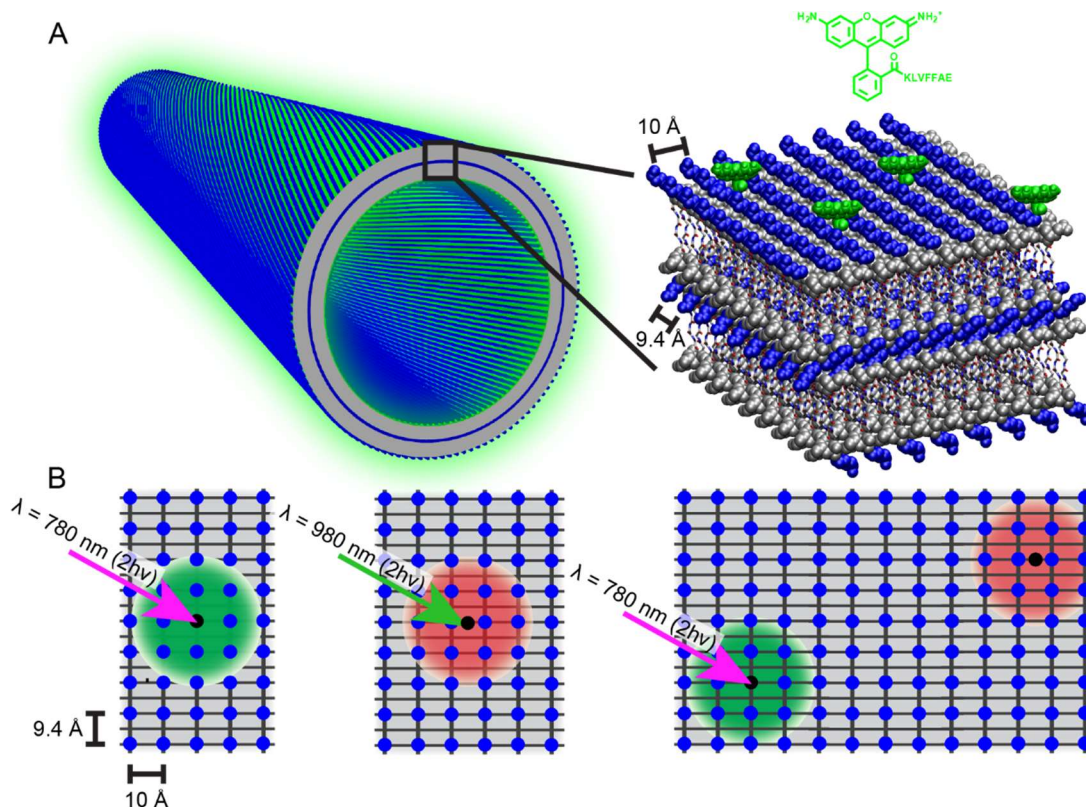
Surface insert highlights the organization of Congo Red in the hydrophobic grooves of the nanotube surface. A single Congo Red (CR) molecule extends 19 Å. Nanotube cartoon highlights the high density of CR incorporation on the nanotube surface.

The assembly characteristics of this peptide were further extended via covalent attachment of chromophores in the peptide-pigment chimera Rho110-KLVFFAE-NH<sub>2</sub>. With rhodamine 110 (Rho110) grafted to the N-terminus, the chimera assembles as pigmented twisted fibers (Y. Liang, Guo, et al., 2008). When co-assembled with Ac-KLVFFAE-NH<sub>2</sub> in a 1:250 molar ratio, nanotubes form as shown in the cartoon in **Figure 1.4**. These nanotubes are morphologically indistinguishable from the Ac-KLVFFAE-NH<sub>2</sub> assemblies by TEM and WAXS, with the fluorophore randomly distributed along the nanotube surfaces (Ni, Childers, Hardcastle, Mehta, & Lynn, 2012). The same homogeneous morphology persists when the Rho110-KLVFFAE-NH<sub>2</sub> ratio is increased to 1:75, but the fluorescence lifetime of the Rho 110 becomes very heterogeneous.

Multiple discrete regions of Rho110-KLVFFAE-NH<sub>2</sub> fluorescence lifetimes exist in well-defined regions along the long axis of a single nanotube as visualized by fluorescence-lifetime imaging microscopy (FLIM). These domains of fluorescence lifetimes are consistent with subtle structural variations that propagate as the nanotubes grow, likely the result of differences in side chain packing. Variations within single nanotubes suggest that the packing differences can mutate, and that change can continue to propagate. This observation opens the distinct possibility of controlling the architecture laterally along the growing nanotube and using these dynamic differences to control energy and electron transfer efficiencies within defined regions of the peptide nanotubes (Anthony, Berland, et al., 2014a; Anthony, Mehta, et al., 2014).

Like CR, the negatively charged Alexa 555 (A555) binds the positively charged Ac-KLVFFAE-NH<sub>2</sub> nanotube surface, and when bound to the Rho110-KLVFFAE-NH<sub>2</sub>-seeded nanotubes, Förster resonance energy transfer (FRET) was demonstrated, paralleling the energy transfer achieved with chlorosomes. When introduced at a 4:1 Rho110-KLVFFAE-NH<sub>2</sub>:A555 molar ratio, this system achieves 11% FRET efficiency (Y. Liang, Guo, et al., 2008). Other chromophore organizing assemblies driven by electrostatic interactions have also been reported. Using the biologically relevant molecule tetra(p-hydroxyphenyl) porphyrin (THPP) it has been shown that porphyrin-peptide co-assemblies can be effectively constructed. In these structures, long-range order is achieved via the self-orienting assembly pathway of THPP which is driven in solution phase by electrostatics of the positively charged dipeptides (KK<sup>3+</sup>), generating fibrillar structures, and other weak peptide-peptide and peptide-chromophore interactions (K. Liu, Kang, Ma, Mohwald, & Yan, 2016; K. Liu et al., 2015). Indeed, this material serves as a

powerful light-harvesting antennae and applications as nanomaterials for hydrogen evolution have been proposed and reviewed elsewhere (K. Liu, Abass, Zou, & Yan, 2017; K. Liu, Xing, et al., 2016; Zou, Liu, Abbas, & Yan, 2016). In our work, we explore the plasticity of self-assembling peptides and seek to develop an unparalleled understanding of the assembly pathways of various amyloid templates for the formation of homogeneous antennae with controlled chromophore alignment analogous to the chlorosome. Results so far support our attempts to extend the chlorosome model for the development of new bionanomaterials capable of physicochemical energy transfer; future applications of the porphyrin-peptide antennae to generate hybrid photochemical scaffolds should not go unexplored.



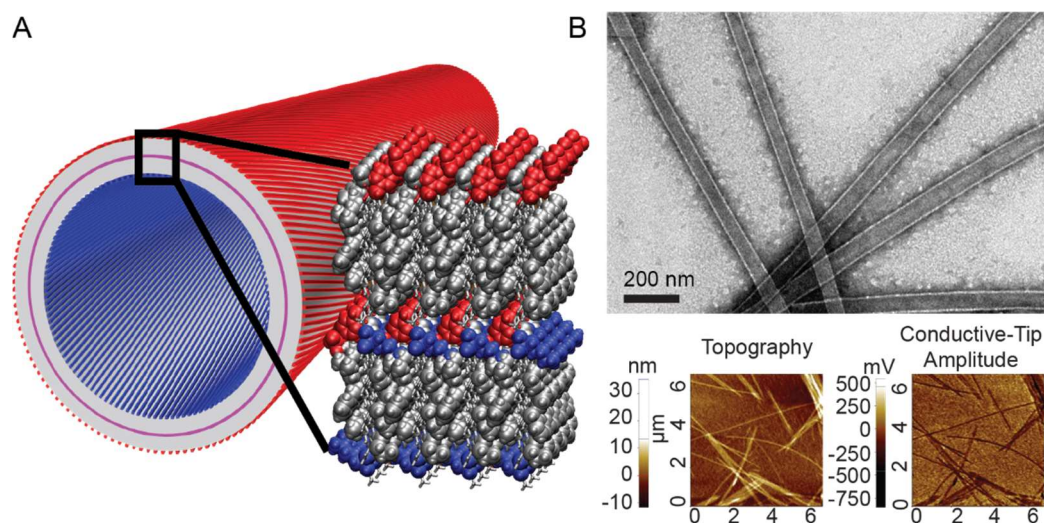
**Figure 1.4 – Modeling energy transfer on the peptide nanotube surface. (A)**

Derivatizing Rho110 to the N-terminus of the A $\beta$  nucleating core (KLVFFAE-NH<sub>2</sub>),



photofunctionalizes the ensuing nanotube. Assembly forces anchor Rho110 along the peptide array with dose-dependent density. (B) Covalently anchored Rho110 (left) and electrostatically bound A555 (middle) display antennae capabilities when both fluorophores are present on the nanotube surface (right). Unlike solution-state Rho110 and A555, Ac-KLVFFAE-NH<sub>2</sub> successfully prompts energy transfer between Rho110-KLVFFAE-NH<sub>2</sub> and A555 across an average 10 nm donor-acceptor distance with 11% FRET efficiency. (Figure 3 adapted from (W. S. Childers, Ni, Mehta, & Lynn, 2009) with permission of Elsevier)

### Breaking Amyloid Assembly Symmetry



**Figure 1.5 – Building charge asymmetry across a nanotube surface.** (A) Positively charged Ac-KLVFFAL-NH<sub>2</sub> and negatively charged Ac-pYLVFFAL-NH<sub>2</sub> co-assemble into asymmetric peptide membranes. (B) This dual peptide system forms nanotubes of monodisperse width (TEM) and height (AFM) with a preferred positioning of the

negatively charged pY to the outer nanotube leaflet (EFM). (Figure 4B adapted with permission from (S. Li et al., 2016). Copyright 2016 American Chemical Society)

Biological phospholipids assemble into membranes that are symmetric across the bilayer but asymmetric across each individual leaflet. In contrast, amphiphilic peptides assemble with antiparallel strand arrangements that give symmetric cross- $\beta$  leaflets. The resulting bilayer of leaflets containing antiparallel  $\beta$ -sheets packs protonated lysines within the bilayer interface (W. Seth Childers, Mehta, Ni, Taylor, & Lynn, 2010). Sequestering these charges from the aqueous environment represents the major energetic constraint on assembly (Y. Liang, Pingali, et al., 2008), but the more hydrophobic Ac-KLVFFAL-NH<sub>2</sub> peptide forms these bilayer membranes when the interface is sufficiently passivated. When trifluoroacetic acid (TFA) is used as the counterion to assemble the bilayer, this bilayer interface has been probed with <sup>19</sup>F-NMR to define the stoichiometric association of TFA with each interfacial amine (W. Seth Childers et al., 2010; S. Li et al., 2016).

To explore the extent of this leaflet electrochemical constraint, the phosphorylated Ac-pYLVFFAL-NH<sub>2</sub> was constructed and shown to assemble as bilayer nanotubes with triethylammonium (TEA) as the counterion. This phosphorylated peptide then forms homogeneous negative charged nanotubes, greatly extending the general approach to assemble more complex scaffolds (S. Li et al., 2014). More importantly, the co-assembly of these two complementarily charged peptides, Ac-KLVFFAL-NH<sub>2</sub> and Ac-pYLVFFAL-NH<sub>2</sub>, at equimolar concentrations form nanotube bilayers with cross-passivating leaflets (**Figure 1.5A**) (S. Li et al., 2016). In principle, there are two limiting ways of structurally achieving the cross-passivated leaflet interface. The first would be

laminating two homogeneous leaflets, one containing only Ac-KLVFFAL-NH<sub>2</sub> and the other containing only Ac-pYLVFFAL-NH<sub>2</sub>. The second would be a complete interdigitation of the lysine (K) and phosphotyrosine (pY) peptides in both leaflets. Remarkably, electrochemical force microscopy established that all the assembled nanotubes maintain a homogeneous negative surface charge, and solid-state NMR analyses demonstrated that both limiting assemblies are equally represented in the nanotube assemblies. Most strikingly, these limiting structures exist as distinct blocks within individual nanotubes, appearing by TEM as block co-polymer nanotubes. As with the fluorescent lifetime blocks mentioned in the discussion of “amyloid antennae” above, the block size appears to be acquired during propagation with its length defined by the assembly mutation rate.

This evidence shows that molecular-level mutations arise and propagate along an assembly; it further opens new levels of longitudinal variation and greatly extends the structural diversity and functionality of these scaffolds. Mechanistic evidence for conformational mutation during fiber and nanotube propagation has been achieved by mapping the existence of a two-step pathway for the assembly of mature amyloid (W. Seth Childers et al., 2012; Dong, Apkarian, & Lynn, 2005). The data using a simple peptide argues that assembly involves an initial phase transition to a particle form where nucleation of the fibrous form occurs. While initial growth occurs in the particle, when the growing end emerges into the solution phase, the initial strand arrangement is not stable during propagation leading the assembly to mutate. As a result, the structural mutation is autocatalytically amplified at the expense of the initial particle phase assembly (C. Liang et al., 2014). This mechanistic understanding suggests that tuning

these conformational mutations can provide new and powerful approaches for selecting specific nanotubes domains that localize specific chemistry to defined regions of a supramolecular assembly. In **Chapter 2**, we expand on previous data collected on the intermediate particle phase of assembly and introduce the first example of fully characterized A $\beta$  particle intermediates.

Nowhere is such control and understanding of spatial reactivity more important than in buffering reactive photoredox chemistries along hollow nanotubes. For example, Ac-KLVFFAL-NH<sub>2</sub> and Ac-pYLVFFAL-NH<sub>2</sub> co-assemble nanotubes that have already been differentially decorated on their internal and external surfaces with complementary positive and negatively charged fluorophores (S. Li et al., 2016). To our knowledge, these nanotubes are the first to extend the concept of expanding membrane-like assembly to create innate electrochemical gradients. The extent to which this inherent membrane asymmetry at the inner and outer surfaces can be architecturally controlled along the nanotube would significantly extend the function of these chlorosome mimics. If each surface can be decorated in defined regions with redox active chromophores, incorporating differential functional potential within defined domains, we could achieve directed energy and electron transfer. In so doing, an entire functional photoredox network would be built on a self-propagating scaffold. Now, we describe the design of materials toward storing the acquired energy.

### **Metalloamyloid Nanostructures**

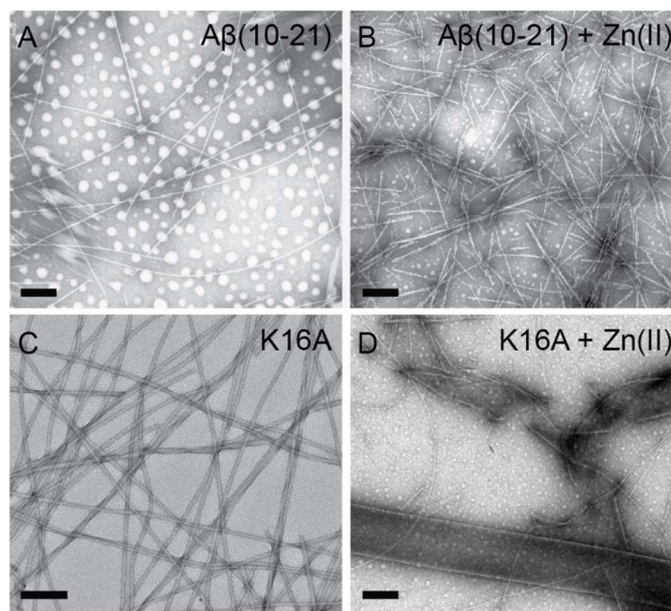
One-third to one-half of all proteins depend on inorganic cofactors for their function; capturing these cofactors on amyloid scaffolds may broaden their functions in disease (Allsop, Mayes, Moore, Masad, & Tabner, 2008; Dong et al., 2007; Hung et al.,

2009; Hureau & Faller, 2009; D. L. Jiang et al., 2013; Jomova, Vondrakova, Lawson, & Valko, 2010; B. Liu et al., 2011; Roberts, Ryan, Bush, Masters, & Duce, 2012) and in health (Mariusz Mital et al., 2016; Roberts et al., 2012). The controlled incorporation of metal ions at a high density in functional material design has blossomed over the past twenty years (Gangu, Maddila, Mukkamala, & Jonnalagadda, 2016). Specifically, metal organic frameworks (MOFs) are functional nonporous materials that incorporate metal ions ranging from transition metals to lanthanides housed within organic frameworks. The structural versatility afforded to MOFs by the diversity of its building blocks has allowed for new applications in gas/vapor sorption, separation, drug delivery, and heterogeneous catalysis (Sabale et al., 2016). In 1966, Gramaccioli expanded the frontiers in MOF design, being the first to use biomolecules as the organic linkers to a material he termed bioMOFs. Since their inception, several such structures have been developed (Rojas, Devic, & Horcajada, 2017); however, one limitation in the design of these metal-organic materials is that growth along a specific selected dimension remains a challenge. While new strategies are emerging (Lee, Kwak, & Choe, 2017), amyloids and the energetic code embedded in the cross- $\beta$  structure allows for the introduction of new materials whose growth can now be controlled along a single dimension in assemblies we term metalloamyloid nanostructures.

Divalent metal ions, particularly  $Zn^{2+}$  and  $Cu^{2+}$ , are known to be regulated by the A $\beta$ -derived amyloid precursor protein (Adlard & Bush, 2006; Barnham et al., 2003; Baumkötter et al., 2014; Hesse, Beher, Masters, & Multhaup, 1994), and these same metals have been shown to induce the nucleation of supramolecular assemblies (Dong et al., 2007; Morgan et al., 2002). For example, as shown in **Figure 1.6A**, the peptide

YEVHHQKLVFFA-NH<sub>2</sub> (A $\beta$ (10-21)) assembles to form a mixture of fibers and particles. In the presence of Zn<sup>2+</sup>, the peptide assembles more homogeneously (**Figure 1.6B**). Even though the metal and peptide are introduced in equimolar amounts, the resulting fibrils contain  $\leq 0.03$  molar equivalents of the metal – no more than 3% of the total metal present. At such a low degree of incorporation, we hypothesize that the Zn<sup>2+</sup>-peptide complexes only template fiber growth. We reasoned that higher Zn<sup>2+</sup> incorporation may be inhibited as the likely metal binding peptide HH-dyad lies at the middle of the sequence, restricting Zn<sup>2+</sup> accessibility. In an effort to increase metal ion access to the HH-dyad, the peptide was truncated to begin with the N-terminal HH-dyad (Dong, Shokes, Scott, & Lynn, 2006). Shortening the peptide also removed two amino acid side chains which could compete with the HH-dyad for metal binding, tyrosine (Y) and glutamic acid (E).

To completely isolate the HH-dyad, lysine (K) is replaced with alanine (A) to give HHQALVFFA-NH<sub>2</sub>, (K16A). This peptide assembles as fibers (**Figure 1.6C**), and in the presence of equimolar Zn<sup>2+</sup>, K16A assembles as fibers, helical ribbons, and nanotubes (**Figure 1.6D**). These assemblies contain 60 – 80% of the added Zn<sup>2+</sup>, in stark contrast with the longer peptide (**Figure 1.6B**). The high degree of Zn<sup>2+</sup> incorporation opened possibilities in creating new kinds of nanoscale materials incorporating high metal concentrations with extended redox functions.



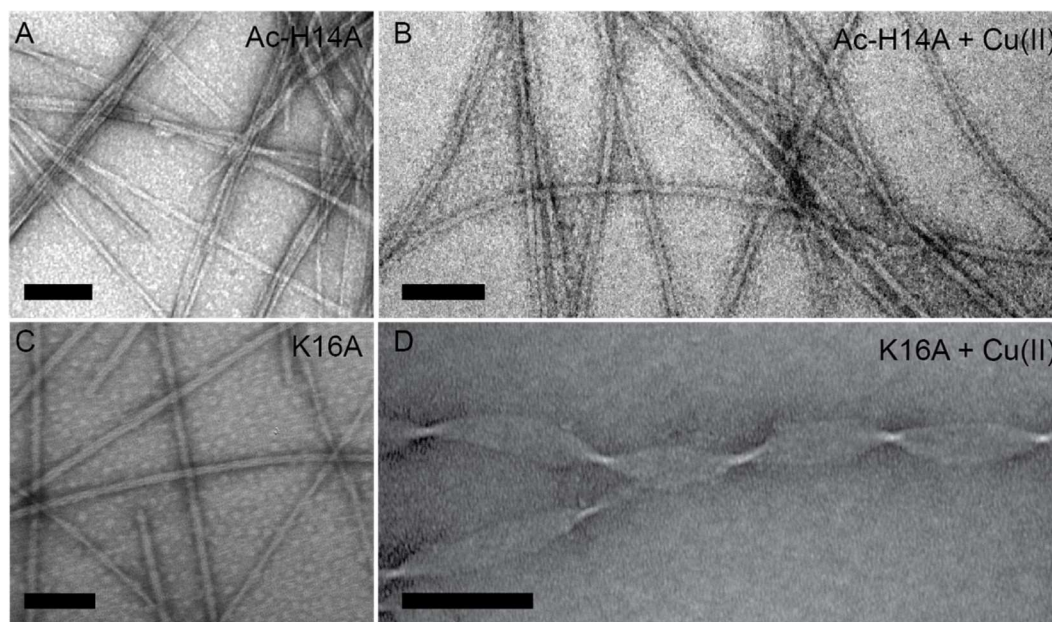
**Figure 1.6 – TEM images of A $\beta$ (10-21) and A $\beta$ (13-21)K16A in the absence and presence of Zn<sup>2+</sup>.** Electron micrograph of fibrils formed by A $\beta$ (10-21), YE VHHQKLVFFA-NH<sub>2</sub> (A), A $\beta$ (10-21) + 1 mM ZnCl<sub>2</sub> (B), A $\beta$ (13-21), HHQALVFFA-NH<sub>2</sub> (K16A) (C) and K16A + 1mM ZnCl<sub>2</sub> (D). Peptides assembled in 25mM MES, pH: 5.6. Two-week incubation. Scale bar = 200 nm. (Figure 5A and B adapted with permission from (Morgan et al., 2002). Copyright 2002 American Chemical Society)

While both K16A and a congener, Ac-HAQKLVFFA-NH<sub>2</sub> (H14A),<sup>54</sup> form homogeneous fibers in metal-free environments (**Figure 1.7A and C**), Cu<sup>2+</sup> inhibited K16A peptide assembly but improved the rate of H14A assembly without affecting its morphology (**Figure 1.7B**). Binding of Cu<sup>2+</sup> was confirmed by a clear spectroscopic blue-shift in the  $\lambda_{\text{max}}$  of Cu<sup>2+</sup>, apparent for both Cu<sup>2+</sup>-peptide mixtures. Furthermore, electron paramagnetic resonance (EPR) confirmed metal coordination for H14A fibers. Electron spin echo envelope modulation (ESEEM) spectroscopy provided evidence that Cu<sup>2+</sup> ions are arrayed continuously along the long-axis of the micron-long H14A fibers,

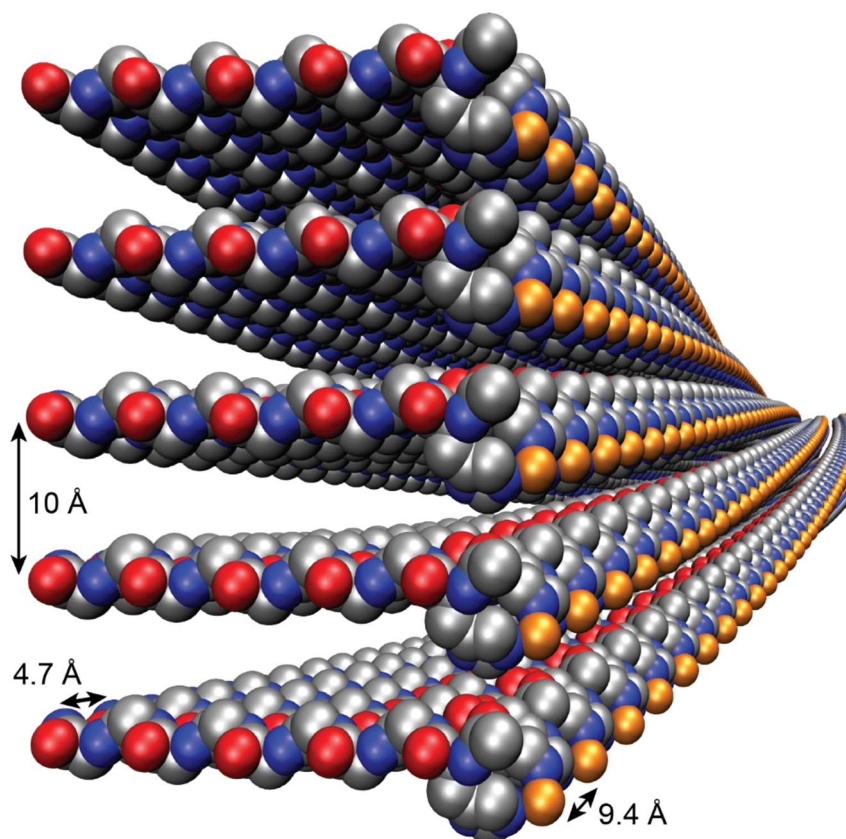
positioning the  $\text{Cu}^{2+}$  ions 9.4 Å apart on the fiber surface (**Figure 1.8**) (Hernández-Guzmán et al., 2013). The high density of  $\text{Cu}^{2+}$  ions incorporated in single tracks is unprecedented, appearing remarkably similar to the proximal binding of CR along the laminate groove of amyloid. Recently, a reexamination of the K16A- $\text{Cu}^{2+}$  assembly conditions found that with longer assembly times a unique morphology emerges (**Figure 1.7D**). K16A- $\text{Cu}^{2+}$  complexes form ribbons that isolate  $\text{Cu}^{2+}$  ions within the peptide bilayer leaflet interface, much like TFA in the nanotubes formed by Ac-KLVFFAL-NH<sub>2</sub> described in the previous section on “breaking amyloid assembly symmetry” of this introductory chapter. Using the His residues as binding sites,  $\text{Cu}^{2+}$  passivates the leaflet interface and stabilizes the bilayer.

Computational models for this organization bury the  $\text{Cu}^{2+}$  ions within extended rows of metal ions spaced closely enough to function as unique redox catalysts and as bionanomaterials capable of electron storage and transfer (Rengifo et. al, under review). In **Chapter 3** and **Chapter 4**, we explore the design, selection, and characterization of this and other metalloamyloid arrays, highlighting its reactivity by studying the redox potential of the material. Incorporating such design with  $\text{Cu}^{2+}$  with the amyloid-chromophore of the porphyrin antennae might greatly extend the function of the chlorosome-like assemblies to self-propagating photoredox organelles, extending the options for new light harvesting functions.





**Figure 1.7 – TEM images of Ac-H14A and K16A in the absence and presence of  $\text{Cu}^{2+}$ .** (A and B) TEM images show that H14A does not undergo a morphological transition when co-assembled with  $\text{CuCl}_2$ . (C and D) TEM images highlight the morphological transition K16A undergoes when  $\text{Cu}^{2+}$  is co-assembled with peptide monomers from  $t = 0$  in the supramolecular assembly timeline, from the moment the peptide monomers are introduced in the assembly environment. Scale bar = 100 nm. (Reproduced from (Rengifo et al., 2017) with permission from the Royal Society of Chemistry)



**Figure 1.8 – Model of Ac-H14A fibers decorated with Cu<sup>2+</sup> along a single face of the assembly.** Representation of the molecular structure model for the Cu<sup>2+</sup>-H14A fibers. Only the peptide backbone and Cu<sup>2+</sup> ions (gold) are displayed. Distances correspond to the hydrogen-bonded, intra-sheet peptide spacing (4.7 Å), intra-sheet spacing of Cu<sup>2+</sup> sites (9.4 Å), and β-sheet lamination distance (10 Å). Backbone color code: Oxygen red, carbon grey, nitrogen blue. Hydrogen atoms are omitted for clarity. (Figure 7 reprinted from (Hernández-Guzmán et al., 2013) with permission of John Wiley and Sons)

## **Rational Design of Small-Molecule Incorporating Amyloid Nanostructures**

While chromophores can be used to decorate the surface of an amyloid scaffold or as a functional core surrounded by a self-assembling peptide shell, we have been interested in exploiting the self-assembly code of amyloid to engineer functional nanostructures with increased complexity. The design of charge asymmetry across a nanotube surface and the development of metalloamyloid nanostructures are examples where we have achieved increased complexity with functional potential. One of the most exciting challenges in my research came when we decided to test just how well we understood the self-assembly propensity of A $\beta$  congeners. To test this, we turned to a model system we have studied extensively in the lab because of its homogeneous morphology and functional lysine rich surface, the E22L nanotubes. In **Chapter 5** of this dissertation, we briefly discuss the design of a small molecule binding dock and binding pocket to introduce a small molecule within the amyloid architecture. By design, without the small molecule, assembly propensity of the previously amyloidogenic model peptide, E22L, is broken. However, morphology is fully recovered when the small molecule is reintroduced – a molecule that has the characteristics necessary to fit the engineered molecular pocket. We hypothesize and propose a model for the way the small molecule may fit inside the engineered pocket. Given the necessity of the small molecule to initiate self-assembly, we propose that the small molecules are organized along the length of the supramolecular assembly. Characterization of these structures has been challenging, but proposed methods for developing a clear structural picture of these materials is discussed.

## Conclusion

The elegant arrangement of pigments in chlorosomes underlies the remarkable light-harvesting ability of these self-assembling structures. Similar ordered density has been achieved on cross- $\beta$  scaffolds, and the amyloid assemblies have revealed opportunities that greatly extend the functions of these efficient antennae. This research motivated me to design bionanomaterials with potential applications in electron transfer and storage, building blocks that together could work as an amyloid constructed photochemical cell. During my Ph.D., I have been inspired by discoveries that have extended our understanding of the energetic landscape of assembly, teaching us how to design a light harvesting antenna on an amyloid scaffold and create peptide bilayer asymmetry – opening a distinct opportunity for directed energy and electron transport. In **Chapter 2** and **Chapter 3** of this dissertation, I discuss important structural insights on the assembly landscape of amyloidogenic peptides, in **Chapter 3** and **Chapter 4** I describe the design, selection, characterization and reactivity of a new family of bionanomaterials, metalloamyloid nanostructures (MANs). In **Chapter 5** I discuss the rational design of a small molecule encapsulating amyloid, highlighting a degree of assembly control not yet seen or reported in the literature. While these puzzle pieces have not yet been combined, we have introduced and comprehensively characterized the elements needed to guide the functional extension of cross- $\beta$  assemblies towards a functional photochemical bionanomaterial, while gaining greater insight into the amyloidogenic assembly pathway, and showcasing our understanding of the assembly code of peptides.

Nature's biochemical ingenuity provides valuable insight into new materials design, however, the most immediate and potentially impactful lessons taken from this research may be what we continue to discover about the energetic landscape that selects for specific assemblies within cellular matrices. Prions are critical in health and disease, but how the powerful information content of these self-propagating structures leads to cellular malfunction remains poorly defined after many decades of study. Strains, defined here as conformationally distinct propagating assemblies, are selected by their ability to spread deleterious information from cell to cell in disease and health. In AD, as well as in many other neurodegenerative diseases, this seeming infection manifests as a progressive spread of information. Therapeutic approaches to limiting the initiation and spread of disease causing assemblies may depend on an understanding of nucleation and spread of these robust cross- $\beta$  assemblies. The insights provided by the characterization of particle intermediates in **Chapter 2**, and the design of the bionanostructures described in **Chapter 3, Chapter 4** and **Chapter 5**, should continue to reveal critical insights for intervention in disease progression and provide new beneficial self-organizing assemblies for creating alternative functions new to extant biology.

## **Chapter 2 : Dynamics of Amyloid Granules in the Oligomer Cascade Hypothesis**

**In Preparation:** Rolando F. Rengifo, Joshua M. Brockman, Anthony Sementilli, Chen Liang, Noel X. Li, Anil K. Mehta\*, Khalid Salaita\*, David G. Lynn\*

### **Introduction**

Late-onset Alzheimer's Disease (AD) is the most prevalent form of dementia in the United States. It is characterized by memory loss, behavioral abnormalities and mood shifts (Cummings, 2004; Fraser et al., 1994; Holtzman, Morris, & Goate, 2011; Kabir & Safar, 2014; Minter, Taylor, & Crack, 2015; Nelson et al., 2012; O'Brien & Wong, 2011). Over the years, our understanding of AD has grown but efforts to treat and eradicate the disease have not yet come to fruition. It has been shown that the brain of individuals with AD exhibits extensive neuronal cell loss and the formation of protein plaques has been correlated with the disease state *post mortem*. In these protein plaques, amyloid- $\beta$  ( $A\beta$ ) is the major protein component and has thus gained much attention by scientists trying to understand the neurodegenerative pathway of AD (Fraser et al., 1994; Holtzman et al., 2011; Knauer, Soreghan, Burdick, Kosmoski, & Glabe, 1992; Walker, Rosen, & Levine, 2008). Composed of 38-42 amino acids,  $A\beta$  forms oligomers which self-assemble into paracrystalline supramolecular assemblies (Bagriantsev, Kushnirov, & Liebman, 2006; Walsh et al., 1999; Walsh, Lomakin, Benedek, Condron, & Teplow, 1997). The degree to which this peptide self-assembles can be influenced by environmental factors and the different stages of assembly, from monomers to oligomers to paracrystalline fibers, have been studied in relation to disease development using full-length  $A\beta$  and  $A\beta$  truncations

that produce analogous fibrillar nanostructures (Ahmed et al., 2010; Anthony, Berland, Mehta, Lynn, & Seth Childers, 2014b; W. Seth Childers et al., 2012; Gilead & Gazit, 2005; A. K. Mehta et al., 2013). In spite of intense research efforts, structural information on oligomeric molten particles – intermediates that precede fiber formation – is limited. Though assembly intermediates have been proposed and thought to be associated with disease onset, they have not yet been experimentally defined. Interestingly, over the last fifteen years it has been observed that A $\beta$  oligomers play a central role in AD pathogenesis (Sengupta, Nilson, & Kaye, 2016). Thus, a clear paradigm shift has developed that emphasizes the key role of A $\beta$  oligomers in disease causation, the hypothesis known as the oligomer cascade hypothesis (Kitazawa, Medeiros, & LaFerla, 2012).

The oligomer cascade hypothesis (Catalano et al., 2006; Karran, Mercken, & Strooper, 2011; Klein, Krafft, & Finch, 2001) assigns amyloid- $\beta$  (A $\beta$ ) oligomers a critical role in disease spread (Jucker & Walker, 2015; Soto, 2011). Recently bolstered by clinical trials (Sengupta et al., 2016; Sevigny et al., 2016), A $\beta$  has been shown to elevate and maintain neurodegenerative disease through prion-like infections. However, the structures of these dynamic self-assembling intermediates and the nature of their contribution to amyloid assembly remain poorly defined. Model systems have supported two-step nucleation (Auer, Ricchiuto, & Kashchiev, 2012; Peng et al., 2015; Vorontsova, Maes, & Vekilov, 2015) of amyloid within these intermediate oligomers en route to the formation of paracrystalline fibers (Chen et al., 2017; Hsieh, Liang, Mehta, Lynn, & Grover; C. Liang et al., 2014). We hypothesize that dynamic nuclei form early in the intermediate oligomers and characterize the early transitions using an extension of the

nucleating core of the A $\beta$  peptide, H-H<sup>13</sup>HQALVFFA<sup>21</sup>-NH<sub>2</sub> (K16A). These dynamic intermediate assemblies reveal the context dependence of amyloid assembly seeding and help explain the persistence of analog-like functional information propagation in neurodegenerative diseases.

In this chapter, we demonstrate that the particles that precede the formation of paracrystalline fibers have inherent order. We show that order arises from the molten particles in a specific peptide conformation and matures into fibers with a different peptide arrangement. This is the first example, to our knowledge, of such a detailed structural description of this intermediate stage of assembly and it sets the stage for the design and characterization of more complex nanostructures, topics to be discussed in greater detail in the following chapters of this dissertation.

## **Results and Discussion**

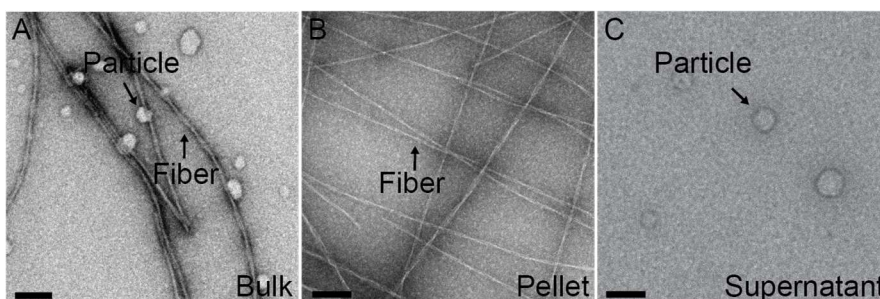
### **Oligomeric Particles and Supramolecular Fibers of H-H<sup>13</sup>HQALVFFA<sup>21</sup>-NH<sub>2</sub> (K16A)**

Evidence has been presented that congeners of the A $\beta$  nucleating core assemble through intermediate oligomeric states (W. Seth Childers et al., 2012; Y. Liang, Lynn, & Berland, 2010). With K16A, the difference in density of these intermediates and mature fibers is sufficiently large to enable separation via centrifugation at 6792 x g for 90 min at 4°C. Transmission electron microscopy (TEM) images of immature assemblies highlight a mixture of both fibers and spherical oligomers during assembly (**Figure 2.1A**).

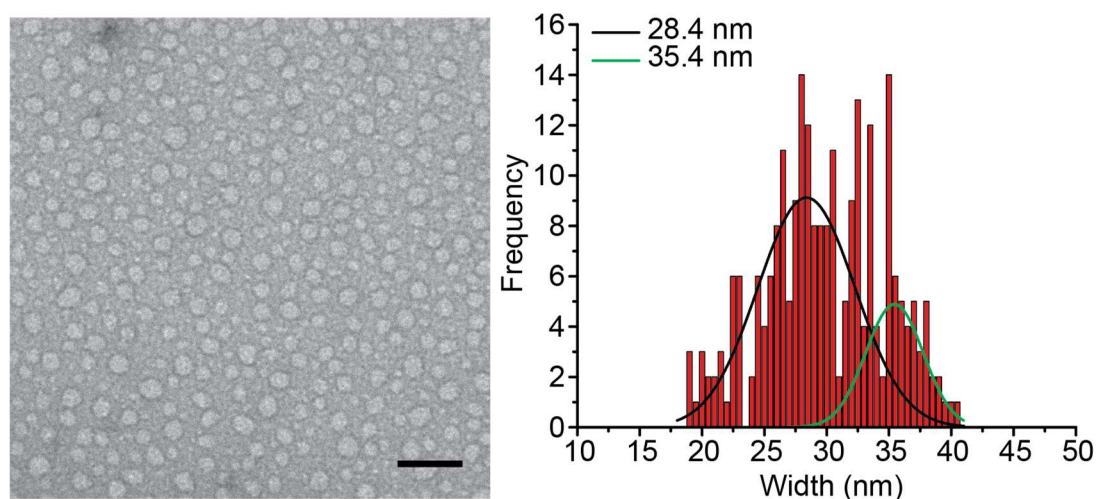
Centrifugation enriches the fibers in the pellet (**Figure 2.1B**) and the oligomers in the supernatant (**Figure 2.1C**). Both fibers and particles are stable to drying on TEM grids, and these show the fibers to be homogeneous with characteristic long persistence lengths



while the spherical particles have smaller widths (**Figure 2.2**) than those obtained with shorter A $\beta$  congeners (W. Seth Childers et al., 2012).

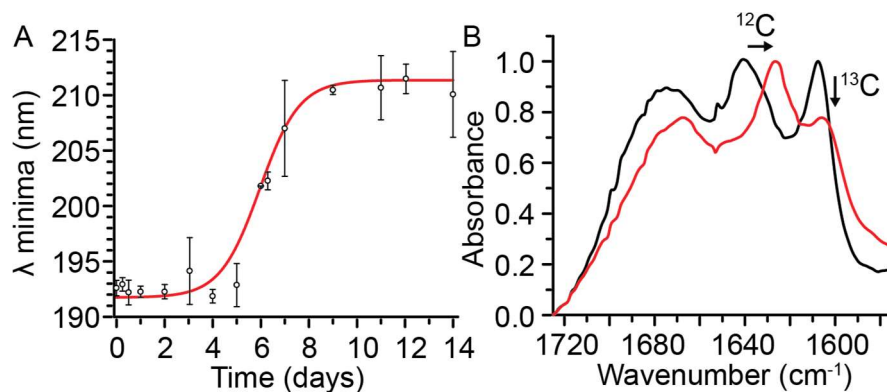


**Figure 2.1 – TEM micrographs of K16A fibers and particles.** (A) TEM image of HHQALVFFA-NH<sub>2</sub> (K16A) peptides after a week-and-a-half of assembly in 25 mM MES at pH: 5, at 25°C show predominantly fibers and particles. After centrifugation, (B) TEM of pellet shows fibers are separated from the particles and (C) TEM of supernatant shows that only particles remain. Scale bar = 100 nm.



**Figure 2.2 – Width measurements of K16A particles.** Particle widths distributed across two major populations with Gaussian fits centered at  $28.4 \pm 1.5$  nm and  $35.4 \pm 1.4$  nm with a width distribution of  $7.8 \pm 2.4$  nm and  $4.6 \pm 2.4$  nm, respectively. Scale bar = 100 nm.

Upon dissolution of K16A peptides in 25 mM MES buffer at pH 5.6 incubated at 25°C, oligomers appear within five minutes with fibers emerging at longer times, consistent with other peptides (Anthony, Berland, et al., 2014b; W. Seth Childers et al., 2012; Dong et al., 2005). The negative ellipticity transition monitored by circular dichroism (CD) shows  $\beta$ -sheet structural maturation as the particles transition to fibers, which takes about nine days at a 1 mM K16A peptide concentration (**Figure 2.3A**). Evidence for amyloid assemblies in the oligomers (W. Seth Childers et al., 2012) is first supported by a more sensitive isotope-enriched FT-IR analyses. We hypothesized that, because the peptide particle environment is distinct from the peptide fiber environment, peptides in the fiber may have a different arrangement than peptides in the particles. Indeed, it has been demonstrated that a structural rearrangement of peptides in a self-assembling peptide could be followed by FT-IR using isotope enriched peptides (C. Liang et al., 2014). When  $[1-^{13}\text{C}]\text{Phe}_{20}$  K16A,  $\text{H-H}^{13}\text{HQALVF}[1-^{13}\text{C}]\text{FA}^{21}\text{-NH}_2$ , peptides are suspended under these same conditions, the dominant amide-I IR bands at zero time appear at  $1640\text{ cm}^{-1}$  and  $1608\text{ cm}^{-1}$ , diagnostic of  $^{12}\text{C}$  and  $^{13}\text{C}$  stretching transitions in  $\beta$ -sheets. After four weeks of assembly, the  $^{12}\text{C}$  transition has red-shifted to  $1629\text{ cm}^{-1}$  and the  $^{13}\text{C}$  band red-shifted slightly with an accompanying reduction in intensity (**Figure 2.3B**), consistent with a more condensed structure with extended normal mode delocalization (Brauner, Dugan, & Mendelsohn, 2000). In addition to more condensed assemblies, these changes are also consistent with a change in  $\beta$ -sheet peptide orientation from antiparallel to parallel  $\beta$ -sheet peptide strands (Brauner et al., 2000; C. Liang et al., 2014; Smith et al., 2015).

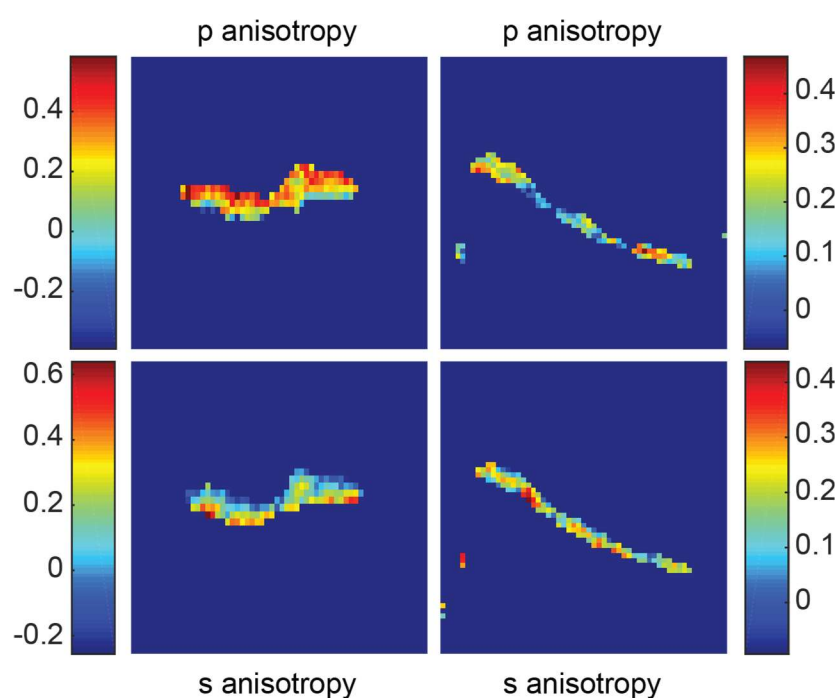


**Figure 2.3 – CD and FT-IR of K16A over-time.** (A) 1 mM K16A peptide assembly over 14 days monitored by the CD negative ellipticity  $\lambda$  value. Maturation transition ends on day 9, where particles transform to the dominant fiber morphology. (B) FT-IR spectra for enriched K16A ( $\text{H-H}^{13}\text{C}\text{HQALVF}[1\text{-}^{13}\text{C}]\text{FA}^{21}\text{-NH}_2$ ) at  $t=0$  hrs (black) and after 4 weeks of assembly (red) at  $25^\circ\text{C}$ . The  $^{12}\text{C}$  amide-I band observed at  $1640\text{ cm}^{-1}$  (black) shifts to  $1629\text{ cm}^{-1}$  in mature fibers (red) with a small red-shift and a strong change in relative intensity for the  $^{13}\text{C}$  amide-I band over time.

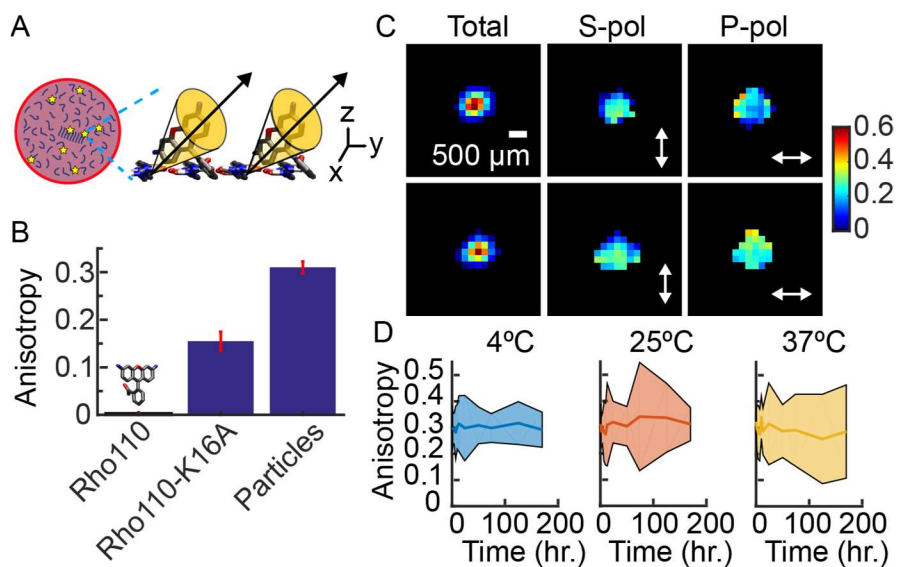
### Defining the Structure of K16A Oligomeric Particles

To further confirm ordering within individual oligomers, rhodamine-110 (Rho110) has been coupled to the N-terminus of K16A, giving Rho110-K16A as an optical probe of assembly (**Figure 2.5**) (Anthony, Berland, et al., 2014b; Anthony, Mehta, et al., 2014; Y. Liang et al., 2010). Fluorescence anisotropy of Rho110 in solution ( $0.003 \pm 0.001$ ), unassembled Rho110-K16A peptide ( $0.1548 \pm 0.02$ ) and oligomers containing 4% Rho110-K16A ( $0.31 \pm 0.1$ ) increases with the size and phase of the assembly (**Figure 2.5B**). In contrast to the unassembled Rho110-K16A monomer in solution, the anisotropy of some oligomers varies as a function of the polarization of the excitation, suggesting that oligomers possess intrinsic order which, interestingly, appears

to be independent of temperature (**Figure 2.5C, D**). This anisotropy develops immediately and does not change over the course of at least a week, consistent with order that remains until the oligomer/fiber transition is complete (**Figure 2.4**) (Chen et al., 2017; W. Seth Childers et al., 2012; C. Liang et al., 2014). This data gives us confidence that order emerges early in oligomeric particles. To unequivocally define the peptide-peptide organization of particles we turn to solid-state NMR.



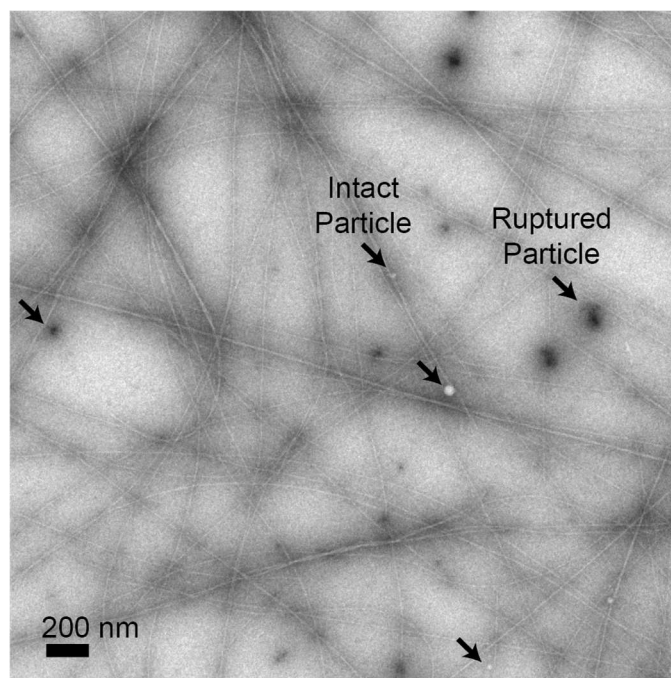
**Figure 2.4 – Fluorescence anisotropy images of K16A fibers with different light polarizers.** Varying the orientation of the excitation illumination causes shifts in individual fiber anisotropy, demonstrating individual fibers have an ordered phase.



**Figure 2.5 – Fluorescence anisotropy analysis of K16A particles.** (A) Particles were assembled from a mixture of K16A (96%) and Rho110-K16A (4%). Ordered phases within the particle are likely to confine Rho110 orientation (yellow cone). (B) The fluorescence anisotropy of Rho110 ( $0.003 \pm 0.001$ ) is much smaller than that of Rho110-K16A peptide ( $0.1548 \pm 0.02$ ,  $n = 3$  experiments, 30 measurements) and Rho110-K16A peptide found within self-assembled particles ( $0.31 \pm 0.1$ ,  $n = 3$  experiments, 669 particles). (C) Varying the orientation of the excitation illumination (white arrow) causes shifts in individual particle anisotropy, suggesting that individual particles may have an ordered phase. (D) Particle anisotropy is invariant with respect to temperature and time herein reported, suggesting that inherent particle order exists immediately upon particle formation and persists as sample matures (mean  $\pm$  standard deviation,  $n = 3$  experiments, with 30 particles per time-point).

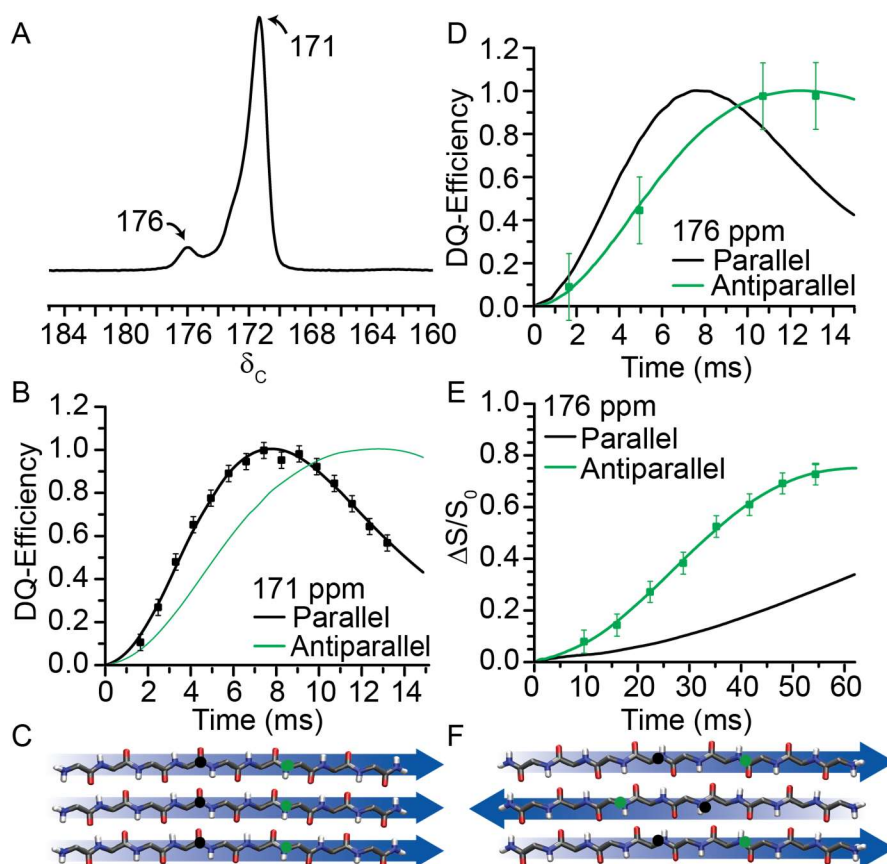
Solid-state NMR is a useful tool for defining the arrangement of molecules in a crystalline or paracrystalline assembly phase (Antzutkin, Leapman, Balbach, & Tycko, 2002; Burkoth et al., 2000; Habenstein, Loquet, Giller, Becker, & Lange, 2013; I. W. Hamley, 2007; C. Liang et al., 2014; P. Liu et al., 2008; Schneider et al., 2011; Wallace & Shen, 2010). The solid-state NMR experiment can directly interrogate peptide arrangement by measuring the distance between selectively enriched isotope positions in a peptide sequence by measuring their dipolar coupling. In preparing the experiment, the first challenge came with getting the sample ready, as efforts to stabilize oligomeric particles during lyophilization gave mixed results. However, adding a fraction of the supernatant to the pelleted fibers helped stabilize and maintain the structural integrity of the oligomers and removed unassembled peptide (**Figure 2.6**). These preparations give reasonable NMR line shapes (**Figure 2.7A**), and motivated analysis of the antiparallel to parallel peptide transition suggested in the IR experiments. K16A peptide, enriched at Ala16 and Phe19 to give HHQ[1-<sup>13</sup>C]A<sup>16</sup>LV[<sup>15</sup>N]F<sup>19</sup>FA-NH<sub>2</sub>, is incubated under standard conditions for six weeks, pelleted at 4°C, and mixed with ~15 mL of the supernatant prior to lyophilization. The CP-MAS NMR spectrum shows two carbonyl resonances (**Figure 2.7A**), the dominant one at 171 ppm consistent with β-sheet secondary structure and a minor resonance at 176 ppm, similar to what is expected if the residue is in an α-helix (Wishart, Sykes, & Richards, 1991). The pelleted sample with no supernatant added does not contain the 176 ppm resonance (**Figure 2.8**), assigning this resonance to the oligomers. The 5 ppm chemical shift difference indicates a distinct chemical environments, and indeed when evaluated by <sup>13</sup>C – <sup>13</sup>C homonuclear recoupling via a Double-Quantum Filtered Dipolar Recoupling with A Windowless Sequence (DQF-

DRAWS) NMR pulse sequence (Benzinger et al., 2000; C. Liang et al., 2014; P. Liu et al., 2008; J. R. Long et al., 1998; M. A. Mehta, Eddy, McNeill, Mills, & Long, 2008), gave a DQF-DRAWS buildup (**Figure 2.7D**) fit to distances in extended antiparallel in-register  $\beta$ -sheets (**Figure 2.7F**). The 171 ppm resonance fits to a distance of 4.6 Å (**Figure 2.7B**) uniquely constraining the peptide to be in homogeneous extended arrays of parallel in-register peptide  $\beta$ -strands (**Figure 2.7C**), consistent with the fiber IR analyses. Although consistent with the IR analyses of the oligomers (**Figure 2.3B – red**) the discrepancy between the observed chemical shift (176 ppm) and that expected for a  $\beta$ -strand was further evaluated via heteronuclear  $^{13}\text{C}$ - $^{15}\text{N}$  dipolar recoupling  $^{13}\text{C}\{^{15}\text{N}\}$  Rotational-Echo Double-Resonance ( $^{13}\text{C}\{^{15}\text{N}\}$  REDOR) NMR experiments (Terry Gullion, 1998; T. Gullion & J. Schaefer, 1989) (**Figure 2.7E**). These data fit to a  $^{13}\text{C}$  coupled to two  $^{15}\text{N}$ 's from adjacent H-bonded strands (**Figure 2.7F**), with  $^{13}\text{C}$ - $^{15}\text{N}$  distances of 4.32 Å and 5.3 Å with an angle between the two  $^{13}\text{C}$ - $^{15}\text{N}$  internuclear vectors of  $155^\circ$ . These measurements fit the 176 ppm resonance uniquely to an antiparallel in-register peptide arrangement (**Figure 2.7F**) in the K16A oligomers. The non- $\beta$ -strand chemical shift may arise from slight conformational differences due to the environment of the oligomer or the dynamic nature of the nucleus.

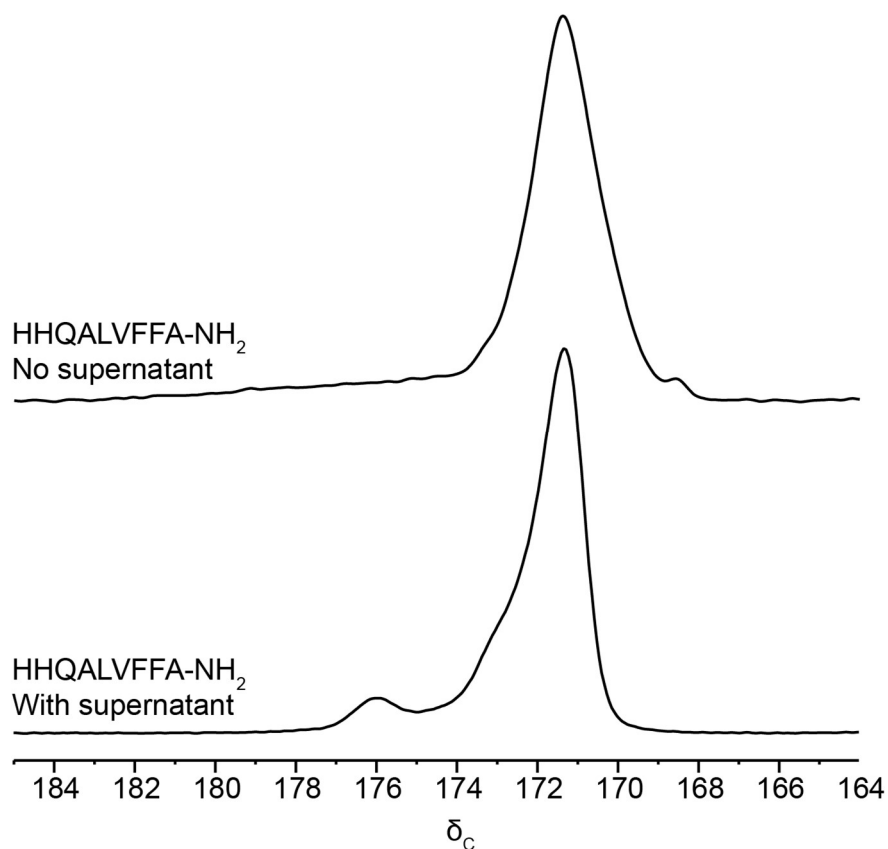


**Figure 2.6 – TEM micrograph of fiber pellet with supernatant added after lyophilization.** Particles and fibers are evident on the TEM micrograph. A population of ruptured particles is present.





**Figure 2.7 – Solid-state NMR analysis of K16A particles and fibers.** Isotope enriched K16A peptide (HHQ[1- $^{13}\text{C}$ ]ALV[ $^{15}\text{N}$ ]FFA-NH $_2$ ) in 25 mM MES buffer, pH: 5.6 incubated at 25°C. (A) CP-MAS NMR spectrum of a lyophilized mixture of K16A particles and fibers with carbonyl resonances at 176 and 171 ppm. (B) Normalized DQF-DRAWS experimental data for the resonance with a chemical shift at 171 ppm (black squares) fits the parallel prediction curve (solid black line) confirming that the K16A fibers have a (C) parallel  $\beta$ -strand orientation. (D) Normalized DQF-DRAWS data (green squares) fits antiparallel in-register simulation (solid green line) for the 176 ppm resonance. (E)  $^{13}\text{C}\{^{15}\text{N}\}$  REDOR confirms peptide arrangement (green squares) as (F) antiparallel in-register (solid green line).



**Figure 2.8 – CP-MAS NMR spectra of K16A with and without supernatant.** Isotope enriched K16A peptide (HHQ[1-<sup>13</sup>C]ALV[<sup>15</sup>N]FFA-NH<sub>2</sub>) in 25 mM MES buffer, pH: 5.6 incubated at 25°C. CP-MAS NMR spectra of a lyophilized fibers (no supernatant, top) with carbonyl resonance at 171 ppm and the mixture of K16A particles and fibers (bottom) with carbonyl resonances at 176 and 171 ppm.

Like molten globules in protein folding (Baldwin & Rose, 2013; Ohgushi & Wada, 1983), the intermediate particle phases accessed in amyloid assembly constitutes a thermodynamic state that is clearly different from either mature or denatured states. This state achieves native-like secondary structure as well as higher order tertiary and quaternary structure of lower density than obtained in the fully formed amyloid. The particle phase environment is buffered from environmental modulators, including H<sub>2</sub>O content, pH, counter ions and other substances impacting amyloid assembly (Hsieh et al.). For the K16A peptide, the antiparallel in-register  $\beta$ -strand peptide orientation originates in the oligomer phase and transitions to the parallel in-register  $\beta$ -strand orientation as the fibers mature. Previous experiments argue (Anthony, Mehta, et al., 2014; Chen et al., 2017), consistent with these results, that only a single nucleus forms in the oligomers, and that these nuclei template growth in solution and conformational mutation during propagation to enable transition to the more stable amyloid (Hsieh et al.; S. Li et al., 2016; C. Liang et al., 2014; Smith et al., 2015).

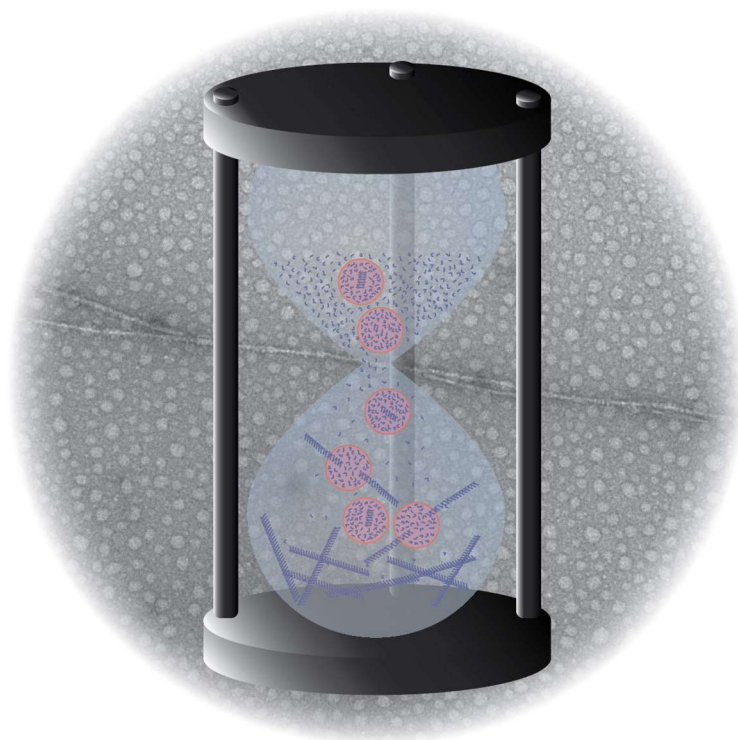
## Conclusion

In this chapter, to better understand what aspects of the oligomeric structures are directly related to disease, we set out to define the structural differences between A $\beta$  oligomeric peptide particles and fibrils *in vitro*. Using a truncation of the A $\beta$  peptide that self-assembles into structurally and morphologically identical supramolecular fibrils similar to full-length A $\beta$ , K16A, we have unequivocally identified the structural order that exists within the oligomeric particles, which maintain a unique peptide organization. Particles transition, over time, as supramolecular fibers begin to emerge (**Figure 2.9**). While a morphological transition is readily observed by TEM and has been alluded to for similar peptides (W. Seth Childers et al., 2012; C. Liang et al., 2014), we demonstrate that the specific structural transition is from antiparallel peptides in the oligomeric particles to parallel peptides in the fiber assembly. This is the first example, to our knowledge, of such structural resolution of the particle phase of assembly of the amyloidogenic A $\beta$  peptide.

Such a dynamic pathway for amyloid assembly, chameleon-like in the peptide's ability to adapt to different environments, supports the two-step nucleation mechanism as a critical attribute to neurodegenerative disease etiology. The ability of these peptides to move from cell to cell, through intercellular spaces and across cell membranes, to spread infection throughout the human brain over decades, now has physical support in this defined oligomer cascade. Amyloid's ability to adapt, nucleate, and template homologous proteins in different physical environments also provides an ever-regenerating cast of infectious amyloid assemblies for propagation that in addition to late-onset Alzheimer's Disease, the most prevalent form of human dementia (Holtzman et al., 2011), may well

explain the propagation of many other amyloid diseases. Moreover, this dynamically adaptable process can now be applied to other analog assembly pathways for the construction of more complex mesoscale functional assemblies.

In **Chapter 3**, we exploit the kinetically preferred peptide arrangement discovered by the investigation of these oligomeric particles to make metalamyloid nanostructures. In turn, further insight into the structural landscape of self-assembling peptides is revealed. The discovery sheds light into the mutation mechanism discussed in this chapter for the structural transition between oligomeric particles and fibers.



**Figure 2.9 – Cartoon representation of the evolution of order in the assembly of K16A over time.** Particles form upon monomer dissolution in solvent with a degree of inherent order. Over time, a mutation occurs that autocatalyzes the formation of supramolecular fibrils with a unique peptide arrangement distinct from that seen in the oligomeric particles.

## Materials and Methods

### Synthesis and purification of H-HHQALVFFA-NH<sub>2</sub>

Peptide was synthesized on a CEM Corporation microwave peptide synthesizer (Matthews, NC, USA) using standard Fmoc chemistry. The solid support for peptide synthesis was Fmoc Rink-amide polystyrene resin (AnaSpec, Inc., usually with substitution 0.4-0.6meq/g) and HBTU/NMM as the coupling reagents. Each amino acid was coupled for 30 minutes, with a 330 second microwave step, unless otherwise specified. Histidine amino acids were double coupled at 50 degrees Celsius. No capping step with acetylation was performed. After cleavage and deprotection by 95% trifluoroacetic acid (TFA) with scavengers (thioanisole/EDT/anisole, 5%/3%/2%, respectively) the crude peptides were isolated by ether extraction repeated 3-4 times and dried under vacuum. H-HHQALVFFA-NH<sub>2</sub> has a free N-terminus, while the C-terminus is carboxyamided.

Peptide was purified using the Jasco Analytical Instruments HPLC (Easton, MD, USA) with an Atlantis dC 18 preparative HPLC column by Waters (Milford, MA, USA). Peptide eluted at 20mL/min, at room temperature, with a linear gradient from H<sub>2</sub>O/CH<sub>3</sub>CN. The elution gradient method moved from 15% H<sub>2</sub>O/85% CH<sub>3</sub>CN to 45% H<sub>2</sub>O/55% CH<sub>3</sub>CN each solvent with 0.1% TFA. Single percentage point increased over 1min, the gradient ran for 30min. Purity of product was confirmed by MALDI-TOF mass spectral analysis using a Applied Biosystem 4700 Proteomics analyzer using a 355 nm ND:Yag laser operating at 200Hz (Foster City, CA, USA). A  $\alpha$ -cyano-4-hydroxycinnamic acid (CHCA) matrix was used for MALDI-TOF experiments (H-HHQALVFFA-NH<sub>2</sub>, 1068.228 (M+H<sup>+</sup>)). The peptide fractions were manually collected,

CH<sub>3</sub>CN was removed by rotary evaporation, leftover water/peptide mixture was frozen at -80°C and lyophilized by FreeZone Plus 12 Liter Cascade, Labconco, freeze dryer system (Kansas City, MO, USA). Lyophilized peptides were stored at room temperature inside a vacuum desiccator until needed.

### **FMOC protection of isotope enriched amino-acids**

FMOC protection of isotope enriched amino-acids (purchased from Cambridge Isotope Laboratories, Inc., Andover, MA, USA) for peptide synthesis was done following standard methods (Gawande & Branco, 2011; Samuel-Landtiser, Zachariah, Williams, Edison, & Long, 2001). Briefly, 2.25 mmol of isotopically labeled amino acid in minimal volume of 10% (w/v) Na<sub>2</sub>CO<sub>3</sub> was added dropwise to a solution of 2.5 mmol FMOC-O-succinimide in 5 mL of dioxane. The reaction was continuously stirred for 24 hours at room temperature, and reaction completion was monitored by TLC using 10:1 toluene:acetic acid as an eluting solvent (ninhydrin staining was used to monitor amino acid that was not FMOC protected). If reaction was incomplete an additional 0.88 mmol of FMOC-O-succinimide in 2 mL dioxane was added and allowed to react for an additional 24 hours at room temperature.

After completion, the reaction mixture was diluted with 30 mL of DI water and washed 3 times with 20mL of diethyl ether each time. The water layer, containing FMOC labeled amino acids, was titrated to pH 2 using HCl while stirring and cooling. FMOC labeled amino acid was extracted 3 times using ethyl acetate. The ethyl acetate washes were collected and washed twice with 100 mL of 1N HCl, then once with 100 mL of DI water. Anhydrous MgSO<sub>4</sub> was added to dry the ethyl acetate layers for 60 minutes.

Filtered ethyl acetate solutions were concentrated using a rotary evaporator and dried in a desiccator overnight.

### **Rhodamine 110 conjugation to H-HHQUALVFFA-NH<sub>2</sub>**

Peptides were prepared using standard Fmoc peptide synthesis protocols with a Liberty CEM peptide synthesizer as described above. Once synthesized, the peptide-bound resin was pre-swelled in minimal anhydrous DMF (1-2 mL) 30 min prior to fluorophore conjugation. In a separate vial, 75% dye content rhodamine 110 (147 mg, 0.3 mmol) was mixed with O-(7-Azabenzotriazole-1-yl)-N,N,N,N'-tetramethyluronium hexafluorophosphate (HATU, 114 mg, 0.3 mmol) in 1 mL anhydrous DMF for 10 min at room temperature. The activated rhodamine 110 solution was transferring to the swollen resin and stirred for 20 min. Diisopropylethylamine (140  $\mu$ l, 0.8 mmol) was added to the reaction mixture via pipette and stirred for 16 hr in the dark and under N<sub>2</sub>. Rhodamine 110-conjugated resin was isolated by vacuum filtration and washed with 2 x 200 mL DMSO/DMF (1:1), 2 x 200 mL DMF, and 2 x 200 mL DCM. The peptide was cleaved from the resin using Reagent R (TFA/thioanisole/ethanedithiol/anisole, 90:5:3:2) and precipitated in ice-cold diethyl ether. RP-HPLC was used for peptide purification in 0.1 % TFA-buffered water/acetonitrile gradient.

### **Circular dichroism Spectroscopy (CD)**

CD spectra were recorded using the Jasco-810 CD spectropolarimeter. All measurements were done at room temperature. Spectra between 260 nm and 180 nm were collected with a 0.1mm path length cell, with a step size of 0.2 nm and a speed of 50 nm/s. Three spectra were recorded for each sample and averaged automatically. Data was



plotted and fit using Origin 9.0 to a Boltzmann fit algorithm. Samples were incubated in 25 mM MES, pH 5.6 at 25°C for the specified time points.

### **Attenuated Total Reflectance Fourier Transform Infrared Spectroscopy (AT-FTIR)**

FT-IR spectra were recorded using a Jasco FT-IR 4100 (Easton, MD, USA). For sample at prepared at  $t = 0$  hrs. in 25 mM MES, pH 5.6 at 25°C: Aliquots (10 $\mu$ L) of peptide solution were dried as thin films on a Pike GaldiATR (Madison, WI, USA) ATR diamond crystal immediately after dissolution of the peptide. For stabilized sample: Mature sample prepared as described above but incubated for 4 weeks was first pelleted by centrifugation at 4°C for 90 min at 9000 rpm (6792 x g calculated with a Horizontal Drum rotor (T-60-11)) using an Eppendorf centrifuge 5804 R (Mississauga, Ontario, CAN) to remove any unassembled peptide monomers. Supernatant was completely removed and placed in a -80°C freezer over night before sample was lyophilized to yield dry powder. TEM confirmed the presence of only intact fibers after lyophilization. The lyophilized powder was pushed onto the diamond crystal. FT-IR spectra were acquired at room temperature, averaging 450 scans with 2  $\text{cm}^{-1}$  resolution, using a MCT detector, 5 mm aperture and a scanning speed of 4mm/sec. Spectra were processed with zero-filling and a cosine apodization function. IE-IR spectra were normalized to the peak height of the  $^{12}\text{C}$  band. The data for  $t=0$  was processed by built-in water elimination function in FT-IR software.

### **Transmission Electron Microscopy (TEM)**

Peptide assemblies were diluted ten times their original volume to a final concentration of 0.05mM, 0.1mM or 0.2mM respectively. About 10 $\mu$ L of the diluted solution was placed on a CF200-Cu Carbon Film 200 Mesh Copper grid purchased from

Fisher Scientific (Electron Microscopy Sciences is the provider, Hatfield, PA) held on a set of forceps above the surface. Peptide assemblies were allowed to settle on the grid surface for at least one minute. Excess solution was wicked away using filter paper. Immediately following, 10 $\mu$ L of a 1.5% methylamine tungstate or 1.2% uranyl acetate staining solution was placed on the same grid for about three minutes. Excess staining solution was wicked away. All grids were stored under vacuum in a desiccator before TEM analysis to remove any excess liquid on the grid surface. Electron micrographs were obtained using a Hitachi HT-7700 Transmission Electron Microscope (TEM) operating at 80 kV at the Robert P. Apkarian Integrated Electron Microscopy Core, part of the Emory Integrated Core Facilities.

### **Fluorescence Anisotropy Imaging**

Imaging was accomplished on an inverted Nikon Eclipse Ti microscope, run by Nikon Elements software. The microscope was equipped with a 1.49 NA CFI Apo x 100 objective, and a TIRF laser launch with an 80 mW 488 nm laser (Andor). Focus was maintained in time-lapse images via a Nikon perfect focus system. A Chroma quad cube (ET-405/488/561/640 nm Laser Quad Band) was used for imaging. An Andor TuCam system mounted with a wire grid polarizer (Moxtek, Andor: TR-EMFS-F03) was used to split the fluorescence by polarization to two Andor iXon Ultra 897 electron multiplying charge coupled devices. To flip the polarization of the laser light, a half wave plate (Thorlabs) mounted on a slider could be inserted at 45° into the light path.

Images were collected with the laser operating at 25% power in epifluorescence mode with an exposure time of 100 ms. To correct for the polarization bias of the microscope, a correcting G-factor was determined by measuring the anisotropy of

fluorescein in solution. The microscope's accuracy was determined by measuring the anisotropy of rose bengal in solution ( $r = 0.28$ ). Additionally, because we used a high numerical aperture objective for these experiments, we corrected for polarization scrambling due to the objective as previously described (Axelrod, 1979).

### **Excitation Resolved Fluorescence Imaging**

Fluorescence azimuth experiments were conducted on a Nikon Eclipse Ti, run by Nikon elements software, with a Chroma quad cube. A 150 mW OBIS 488 nm laser was used to illuminate the sample. The polarization of the laser was rotated via a 400-800 nm SM1-threaded mounted 1 inch achromatic half wave plate (Thorlabs). The half wave plate was rotated via a motorized precision rotation stage (Thorlabs) and a k-cube brushed DC servo motor controller (Thorlabs). Total fluorescence images were taken on a Hamamatsu ORCA-Flash4.0 v2 Digital cMOS. Images were collected at 100x magnification with a 1.49 NA CFI Apochromat TIRF series oil-immersion objective (Nikon).

### **Excitation Resolved Fluorescence Image Processing**

We performed all image processing in MATLAB (Mathworks). The codes is available upon request. The bioformats toolbox enabled direct transfer of Nikon elements image files (.nd2) into the MATLAB environment.

### **Correcting for Microscope Polarization Bias and Laser Illumination Profile**

To correct for the microscope's inherent polarization bias and for the uneven illumination of the laser, we took polarization images of an autofluorescent plastic slide (Chroma). The autofluorescence of the Chroma slide is not ordered, thus any changes in intensity as a function of polarization must be due to the bias introduced by the

microscope. We normalized polarization images to the maximum intensity, producing a set of normalized images. Intensity changes reflect the illumination profile of the laser and the polarization bias of the microscope. We normalized particle images to this set of normalized illumination correction images, correcting both for the uneven illumination profile of the laser and for the polarization bias of the microscope.

### **Background Subtraction and Signal to Noise Ratio (SNR)**

The user-defined rectangular ROI provided us with the local background intensity. We defined a “frame” of pixels consisting of all pixels within 3 pixels of the edge of the ROI. The local background intensity was taken as the mean greyscale value within this frame while the noise was defined as the standard deviation of the greyscale values within the frame. We subtracted the local background from all particle signal intensities before further processing.

### **Photobleach Correction**

To correct for the loss of fluorescence intensity due to photobleaching, we employed a modified version of DeMay’s et al.’s method (DeMay, Noda, Gladfelter, & Oldenbourg, 2011). Briefly, we defined a bleaching exponent as:

$$\text{Bleach Exp} = \ln \left( \frac{I_{0^\circ}}{I_{180^\circ}} \right) / 4$$

Where  $I_{0^\circ}$  is the image corresponding to  $\Phi_{\text{excitation}}=0^\circ$  and  $I_{180^\circ}$  is the image and corresponding to  $\Phi_{\text{excitation}}=180^\circ$ . To correct for bleaching, we applied the following formula:

$$I_n^{\text{Bleach Corrected}} = I_n * \exp(\text{Bleach Exp} * n)$$

## Determining Particle Order

The azimuth gives the ensemble average fluorophore orientation within a pixel.

Azimuth is calculated as:

$$\text{azimuth} = \frac{1}{2} \arctan \left( \frac{I_{45^\circ} - I_{135^\circ}}{I_{0^\circ} - I_{90^\circ}} \right)$$

## Solid-state NMR

NMR spectra were collected with a Bruker (Billerica, MA) Avance 600 spectrometer using a Bruker 4 mm HCN BioSolids magic-angle spinning (MAS) probe. MAS frequency was actively controlled at  $\pm 2$  Hz with cooling and spinning air exit temperature maintained below  $-1$  °C to ensure MAS and RF heating did not denature the samples.  $^{13}\text{C}$  (150.8 MHz) CP-MAS spectra before and after DQF-DRAWS and  $^{13}\text{C}\{^{15}\text{N}\}$ REDOR experiments confirmed that the samples did not change during the experiment. The NMR sample (~40 mg) is packed into a 4 mm solid-state NMR rotor and centered using boron nitride spacers.

To prepare H-HHQ[1- $^{13}\text{C}$ ]ALV[ $^{15}\text{N}$ ]FFA-NH<sub>2</sub> for solid-state NMR, the sample was first pelleted by centrifugation at 4°C for 90 min at 9000 rpm (6792 x g calculated with a Horizontal Drum rotor (T-60-11)) using a Eppendorf centrifuge 5804 R (Mississauga, Ontario, CAN) to remove any unassembled peptide. Supernatant was removed and both pellet and supernatant were frozen and lyophilized to yield dry powder. TEM confirmed the presence of only intact fibers and particles after lyophilization.

$^{13}\text{C}$  DQF-DRAWS Solid-state NMR:  $^{13}\text{C}$  Double-Quantum Filtered Dipolar Recoupling with A Windowless Sequence (DQF-DRAWS) NMR was used to measure the dipolar coupling between two  $^{13}\text{C}$  isotopes. While magic -angle spinning (MAS)

averages the homonuclear dipolar coupling of the sample to zero, application of the DRAWS pulses reintroduces the  $^{13}\text{C}$ - $^{13}\text{C}$  dipolar coupling. This coupling results in  $^{13}\text{C}$  signal decay, also known as dephasing, as the  $^{13}\text{C}$  signal single quantum magnetization is converted into unobservable double-quantum (DQ) magnetization. The dephasing rate and magnitude is directly proportional to the strength of the  $^{13}\text{C}$ - $^{13}\text{C}$  dipolar coupling which is directly related to  $1/r^3$ , where 'r' is the distance between the  $^{13}\text{C}$  nuclei. Therefore, at the end of the DRAWS evolution time, only signal from spins that have no dipolar coupling is observed.

DQF-DRAWS experiments (Bower et al., 1999; Gregory, Mehta, Shiels, & Drobny, 1997) were implemented with the addition of spin-temperature alternation of the initial  $^1\text{H}$  (600.3 MHz)  $1.9\mu\text{s}$   $\pi/2$  pulse to the pulse sequence and phase cycling previously described (M. A. Mehta et al., 2008).  $^1\text{H}$  cross-polarization RF fields were ramped from 50 to 70 kHz and the  $^{13}\text{C}$  (150.8 MHz) cross-polarization RF field was kept constant at 50kHz. SPINAL-64 (Fung, Khitritin, & Ermolaev, 2000)  $^1\text{H}$  decoupling at 128 kHz was used during both dipolar evolution and acquisition. For DRAWS recoupling, a 41.23 kHz  $^{13}\text{C}$  RF field, measured by fitting a  $^{13}\text{C}$  nutation curve to a sine function with a decaying exponential, was used. The rotor period ( $206.2\mu\text{s}$   $\square$   $\square_r = 4.85$  kHz) was set to 8.5 times the  $^{13}\text{C}$   $\square$  pulse length.  $T_2\text{DQ}$  was measured in separate experiments by placing a composite  $\square 90x-90y-90x$  DQ coherence refocusing pulse between the two DRAWS evolution periods (Gregory et al., 1998) which were fixed at  $40\text{-Tr}$ , resulting in maximum DQ coherence excitation efficiency.

Data points are the ratio of the sum of center- and sideband-integrated peak intensities for each evolution time to the  $^{13}\text{C}$  CP-MAS intensities. Error bars were

calculated using the noise of each spectrum as the maximum peak height deviation. DQF-DRAWS curves were calculated using SIMPSON (Bak, Rasmussen, & Nielsen, 2000), where an array of  $^{13}\text{C}$  spins were approximated with a three spin “infinite-loop” model (Gregory et al., 1998) and chemical shift tensor components  $\sigma_{11}=74.1\text{ppm}$ ,  $\sigma_{22}=6.0\text{ppm}$  and  $\sigma_{33}=-80.1\text{ppm}$ , which were measured from the  $^{13}\text{C}$  CP-MAS spectra. The infinite loop model consists of three spins with identical dipolar couplings but with the orientation of the CSA to dipolar tensors are identical between spins 1-2 and spins 3-1. The effects of DQ-relaxation were approximated by multiplying the calculated SQ intensity with a decaying exponential (Gregory et al., 1998) of the form:

$$e^{-\frac{t}{2 * T_2 DQ}}$$

DRAWS curves were calculated from 3Å to 7Å and used to find a best fit to the experimental data points of the H-HHQ[1- $^{13}\text{C}$ ]ALV[ $^{15}\text{N}$ ]FFA-NH<sub>2</sub> resonance with a chemical shift at 171 ppm and 176 ppm, assigned to fibers and particles respectively, by minimizing the residual:

$$\chi = \sqrt{\frac{\sum_{i=1}^n w_i (x_i - x_{\text{calc}})^2}{n}}$$

, where  $x_i$  and  $w_i$  are the experimental data and error respectively.

REDOR Solid-state NMR: Rotational-Echo DOuble-Resonance (REDOR) (Terry Gullion & Jacob Schaefer, 1989; T. Gullion & J. Schaefer, 1989; Saitô & Ando, 1989) spectra were collected on a Avance 600 spectrometer with an HCN biosolids probe. The pulse sequence for  $^{13}\text{C}\{^{15}\text{N}\}$  REDOR consists of two parts, an S sequence that contains both  $^{13}\text{C}$  (150.928 MHz) and  $^{15}\text{N}$  (60.818 MHz) rotor synchronized  $\pi$ -pulses, and the S<sub>0</sub> sequence which is identical but does not contain any  $^{15}\text{N}$  dephasing pulses. xy8-REDOR

with half of the  $\pi$ -pulses on the observed spin  $^{13}\text{C}$  channel and the other half on the dephasing spin (Christensen & Schaefer, 1993)  $^{15}\text{N}$  channel is used to maximize the observed  $^{13}\text{C}$   $T_2$ . Radio frequency (RF) excitation of the dephasing  $^{15}\text{N}$  spins interferes with the averaging of the  $^{13}\text{C}$ - $^{15}\text{N}$  dipolar coupling due to magic-angle spinning and is observed in the REDOR S spectrum, where the signal decays according to both  $T_2$  (spin-spin relaxation) and the heteronuclear  $^{13}\text{C}$ - $^{15}\text{N}$  dipolar coupling. Maximum dephasing occurs when the spacing between the  $\pi$ -pulses is equal to  $\frac{1}{2}$  of the rotor-cycle. The sequence without any  $^{15}\text{N}$  dephasing  $\pi$ -pulses gives the REDOR full-echo or  $S_0$  spectra, where the magnetization decays according to only  $T_2$ . The difference between the REDOR S and  $S_0$  signal ( $\Delta S$ ) is directly proportional to the dipolar coupling, hence the distance between the two spins.

To compensate for pulse imperfections, xy8 phase cycling (T. Gullion, Baker, & Conradi, 1990) of  $^{13}\text{C}\{^{15}\text{N}\}$  REDOR 4 and 8  $\mu\text{s}$  rotor-synchronized  $^{13}\text{C}$  and  $^{15}\text{N}$   $\pi$ -pulses, respectively, and EXORCYCLE phase cycling<sup>19,20</sup> of the final  $^{13}\text{C}$  Hahn-echo refocusing pulse is applied with 128 kHz Spinal64 (Fung et al., 2000)  $^1\text{H}$  (600.133 MHz) decoupling. To minimize the effects of RF inhomogeneity<sup>20,22</sup>,  $^{13}\text{C}$   $\pi$ -pulse power level is arrayed in the REDOR  $S_0$  pulse sequence at a REDOR evolution time of 54.4 ms (corresponding to  $\sim 544.4$  s  $^{13}\text{C}$   $\pi$  pulses) and choosing the power level that corresponded to maximum signal intensity (Ni et al., 2012). Similarly,  $^{15}\text{N}$   $\pi$ -pulses are optimized by arraying the  $^{15}\text{N}$  power level using the REDOR S experiment at REDOR evolution times corresponding to a  $\Delta S/S_0$  between 0.3 and 0.5 (Ni et al., 2012). REDOR data points are the integrated sum of center- and sideband peaks. Error bars are calculated using the noise of each spectrum as the maximum peak height deviation. To normalize for the



decay due to  $T_2$  (spin-spin relaxation), individual REDOR curves are plotted as  $\Delta S/S_0$ . The steepness attributed to the slope of the REDOR dephasing curves is directly related to the  $^{13}\text{C}$ - $^{15}\text{N}$  dipolar coupling, hence the distance between the spins. When more than one  $^{15}\text{N}$  is present, the resulting  $^{13}\text{C}\{^{15}\text{N}\}$  REDOR curve depends on both the  $^{13}\text{C}$ - $^{15}\text{N}$  distances as well as the relative orientations of the  $^{13}\text{C}$ - $^{15}\text{N}$  internuclear vectors (Goetz & Schaefer, 1997; Jarvie, Went, & Mueller, 1996).

By plotting REDOR as  $\Delta S/S_0$ , the plateau (max dephasing) is directly related to the number of spins that are coupled. For example, if only half of the observe spins (in this case  $^{13}\text{C}$ ) are coupled to a dephasing spin (in this case  $^{15}\text{N}$ ), the REDOR curve will achieve half the value observed when all the spins are coupled. In dephasing the carbonyl carbon of H-HHQ[1- $^{13}\text{C}$ ]ALV[ $^{15}\text{N}$ ]FFA-NH<sub>2</sub> for the resonance with a chemical shift at 176 ppm, assigned to the particles, the distance of the H-bonded  $^{15}\text{N}$  from the adjacent carbonyl was fit to 4.8 Å ( $r_1$ ) and the distances to the two non-H-bonded  $^{15}\text{N}$ 's were fit to 6.9 Å ( $r_2$ ) and 8.7 Å ( $r_3$ ). The angle between the three  $^{13}\text{C}$ - $^{15}\text{N}$  internuclear vectors was fit to 108.5°, consistent with dephasing of H-HHQ[1- $^{13}\text{C}$ ]ALV[ $^{15}\text{N}$ ]FFA-NH<sub>2</sub> self-assemblies. The experimental data was fit to a 4-spin system (one  $^{13}\text{C}$  and three  $^{15}\text{N}$ 's) with two of the  $^{15}\text{N}$  's constrained to distance between 9.2 Å and 9.6 Å (Goetz & Schaefer, 1997).

### **Fibril and Particle Formation**

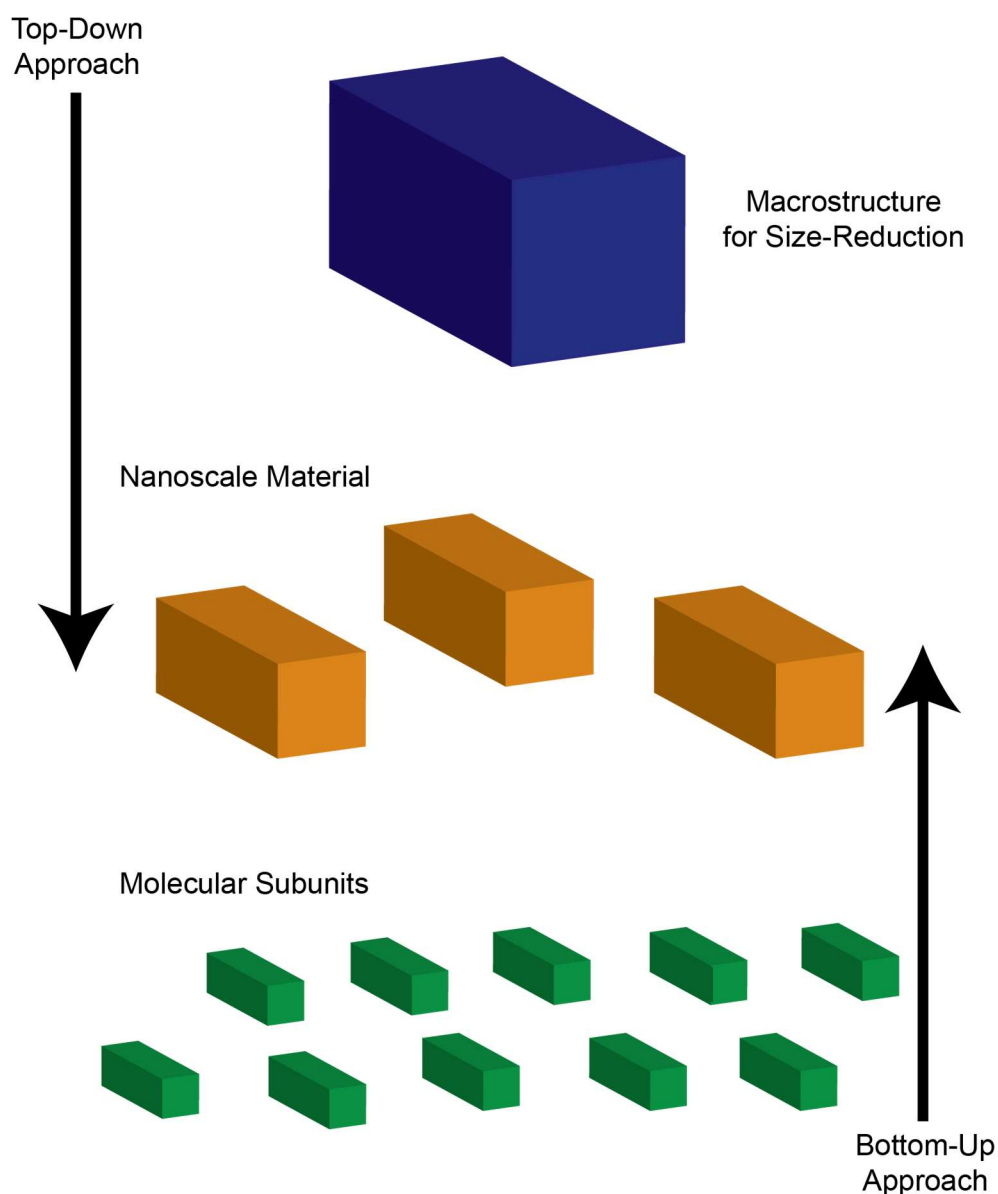
H-HHQALVFFA-CONH<sub>2</sub> (K16A) was dissolved and allowed to mature in 25mM MES buffer, pH 5.6. Fibers and particles were prepared by first adding half the desired volume of water. Following water addition and a 2-5 sec. vortex period, 50 mM MES buffer at pH 5.6 was added to the desired final volume, this was followed by a brief 1-2

sec. vortex period. For any future dilutions of peptide sample to overall concentration, a stock solution of 25 mM MES buffer at pH 5.6 was used. Peptide concentration ranged from 0.5 mM, 1 mM and 2 mM. At all concentrations, homogeneous fibril formation was evident after 2 to 3 weeks. Time needed to reach full maturation was shortened with increasing temperature, 4°C, 25°C and 37°C. At 25°C a homogeneous collection of particles was evident within the first 24 hrs. with the emergence of fibers following this timepoint. Particles were maintained for a longer time at 4°C and only for a period of about 12 hrs. at 37°C at all concentrations tested.

## Chapter 3 : Designing Metalloamyloid Nanostructures (MANs)

### Introduction

The development of functional nanostructures has posed an interesting challenge in the advancement of nanotechnology. There are two accepted practices in the manufacturing of nanoscale materials, 1) a top-down approach and 2) a bottom-up approach (Iqbal, Preece, & Mendes, 2012). In the top-down approach a macrostructure is broken down into smaller components until a nanoscale structure is achieved. One of the major challenges with this approach is that the nanostructures produced are seldom homogeneous in dimension and oftentimes full of imperfections. The differences from unit to unit can mean a defective structural lattice which can influence the overall function and efficiency of the designed material. On the other hand, the bottom-up approach can produce homogeneous structures regulated by programmable constraints on the monomeric units that self-associate to make the nanostructure. In this approach, the individual building blocks come together, via chemical forces, to form clusters that mature into well-defined nanoscale materials (**Figure 3.1**). These clusters are not perfect, as the properties that drive the assembly of the monomeric subunits used to build different nanoscale material are not always fully defined. Efforts to understand the programmability of such monomeric subunits is a current challenge in bottom-up nanometal design.



**Figure 3.1 –Representation of top-down and bottom-up approaches to development of nanomaterials.**

Over the past 20 years, important strides have been made in the design of self-assembling frameworks with applications in nanotechnology. Research has boomed in the study of metal-organic frameworks (MOFs) (Bonneyoy, Legrand, Quadrelli, Canivet, & Farrusseng, 2015; Dias & Petit, 2016; Gangu et al., 2016; Horcajada et al., 2012; Lee

et al., 2017; McGuire & Forgan, 2015; Silva, Corma, & Garcia, 2010; H. Wang, Zhu, Zou, & Xu, 2017; Zhou, Long, & Yaghi, 2012), an area of research that emerged from the study of inorganic frameworks (IFs) abundant in nature (Weitkamp, 2000). Unlike IFs, also known as aluminosilicates, MOFs can incorporate a large library of organic linkers and metal ions to enhance MOFs functional diversity (Manton et al., 2008; Rojas et al., 2017). The variability of the organic and inorganic building elements of MOFs have made them “superior materials for applications in gas/vapor sorption, separation, drug delivery and heterogeneous catalysis” (Sabale et al., 2016). The versatility that has been achieved in designing different MOFs with distinct functional applications shows clear benefits of hybridizing organic and inorganic components into materials. Taking this concept of hybridization as inspiration, we turned to biology which has perfected the design and manufacturing of nanoscale machines that facilitate and sustain life.

From mineral rocks to the ribosome, nature’s machines are the most exquisite representation of evolutionary success. Introducing biologically optimized building blocks into nanomaterial design could dramatically improve manufacturing efficiency, costs, and the diversity of applications. Manton and co-workers introduced the first metal-peptide frameworks (MPFs) and coined the term (Manton et al., 2008). Built on the inherent chirality of peptides, researchers suggested these MPFs would be good candidates for gas adsorption and storage as well as purification and/or chiral separation. With the goal of developing bioinspired nanomaterials capable of serving as electron conduits, we have designed and developed amyloid nanostructures similar in principle to the building elements used in MPFs, but with some important distinctions. First, unlike IFs, MOFs and MPFs, amyloid nanostructures are paracrystalline. Paracrystallinity

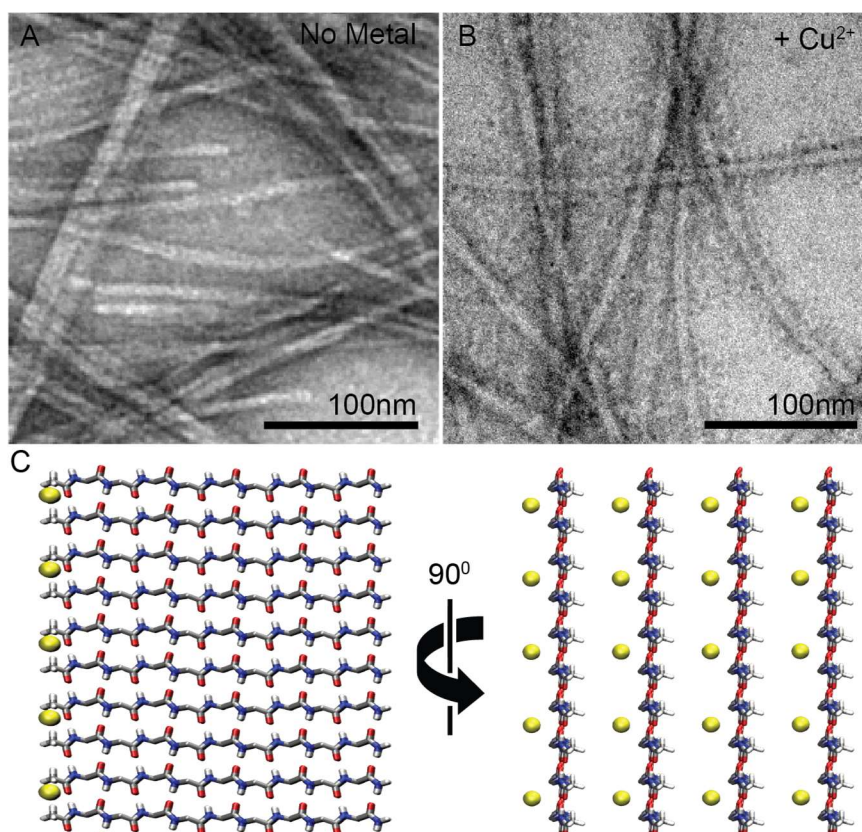
affords repeating structural arrays that maintain structural malleability for incorporation in a variety of precisely positioned functional elements. Second, control of lateral growth yields long, ordered supramolecular morphologies. Third, our peptides are nine natural amino acids long whereas all MPFs thus far reported use dipeptides or tripeptides (Rojas et al., 2017). The level of complexity with structural control allows these bio-inspired nanostructures to break new ground by exploiting our growing understanding of the peptide self-assembly codes. Finally, our material is composed only of naturally occurring amino acids, lowering design costs to manufacturing these materials and opening the possibility of synthetic enzymes for electron storage and transport functioning within cells. Given these opportunities, it would be limiting to classify the designed amyloid nanostructures as simply MPFs, and from here on we will refer to the bio-inspired structures as metalloamyloid nanostructures (MANs). With our increasing understanding of self-assembly as a programmable property of matter, this chapter focuses on describing the design and characterization of MANs, carrying one nanostructure forward to demonstrate its potential as a redox catalyst.

## Results and Discussion

### Peptide Design

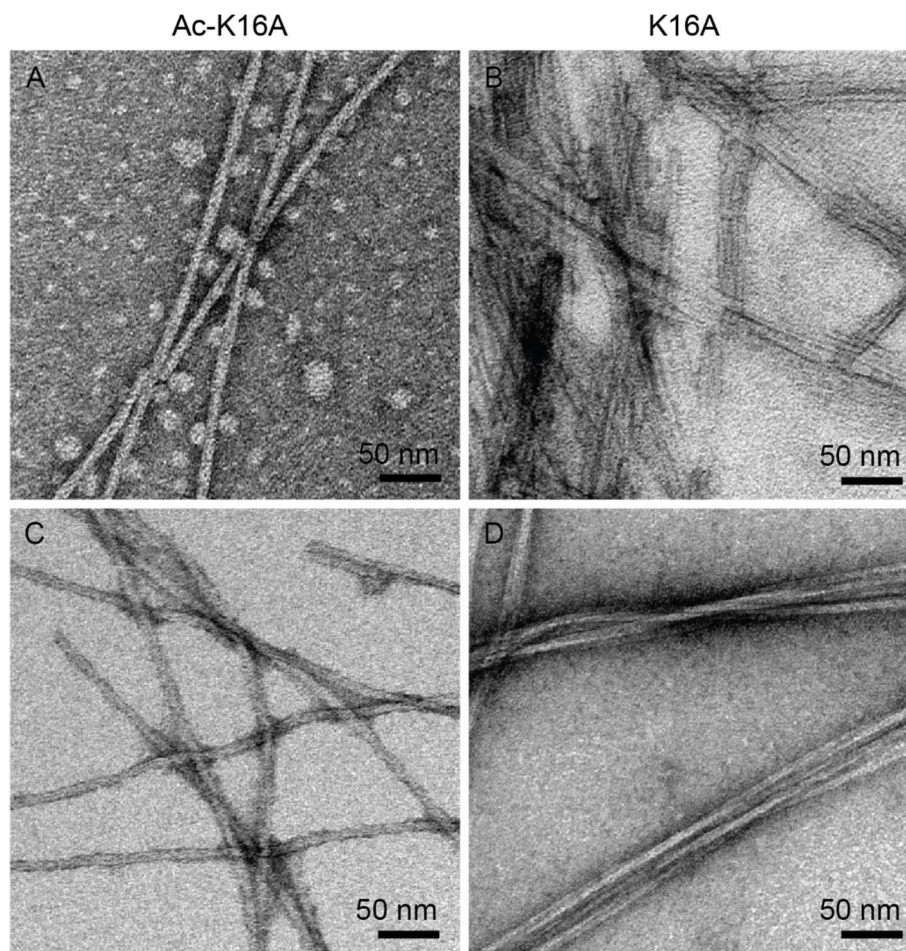
As discussed in **Chapter 1**, Dong and co-workers showed that a congener of a nine-residue peptide section of A $\beta$ , A $\beta$ (13-21)H14A (Ac-H<sup>13</sup>AQKLVFFA<sup>21</sup>-NH<sub>2</sub>), abbreviated Ac-H14A where the N-terminus is acyl capped and the C-terminus is amide capped, forms fibrous supramolecular assemblies with parallel peptide arrangement in the absence and presence of Cu<sup>2+</sup> ions (**Figure 3.2**) (Dong et al., 2007). Initial studies demonstrated that the Cu<sup>2+</sup> ions in the co-assembled Ac-H14A-Cu<sup>2+</sup> fibers are arranged

on the histidine rich surface of the fiber in a regular repeating pattern where the  $\text{Cu}^{2+}$  ions are separated by 1 nm (**Figure 3.2C**) (Hernández-Guzmán et al., 2013). To expand on this model and increase the density of  $\text{M}^{n+}$  ions that can be incorporated, we reintroduced His14 as an additional ligand. This peptide,  $\text{A}\beta(13-21)$  H-H<sup>13</sup>HQKLVFFA<sup>21</sup>, does not assemble into homogeneous structures, but substituting the hydrophilic lysine (K<sup>16</sup>) with alanine (A) resulted in H-H<sup>13</sup>HQALVFFA<sup>21</sup>-NH<sub>2</sub> or K16A and its acetylated congener Ac-K16A. When assembled in HEPES buffer (**Figure 3.3A, B**), pH: 7.4 and MES buffer (**Figure 3.3C, D**), pH: 5.6, both peptides assemble as fibrous structures, but the homogeneity of the samples in MES buffer are more obvious after an incubation period of two weeks. Furthermore, HEPES has been shown to interact with metals and to compromise  $\text{M}^{n+}$  reactivity (Hegetschweiler & Saltman, 1986; Sokolowska, Pawlas, & Bal, 2010). Thus, all supramolecular assemblies with Ac-K16A and K16A discussed in this chapter were incubated in 25 mM MES buffer, pH: 5.6.



**Figure 3.2 – Ac-H14A in the presence and absence of  $\text{Cu}^{2+}$ .** Ac-HAQKLVFFA-NH<sub>2</sub> peptide (Ac-H14A) assembled in 25 mM HEPES buffer, pH: 7.4 on its own (A) and in the presence of  $\text{Cu}^{2+}$  (B). Peptide forms fibers on its own with similar characteristics as the fibers that form in the presence of  $\text{Cu}^{2+}$ . (C) Cartoon representation of the single face arrangement of  $\text{Cu}^{2+}$  along the hydrogen bonding peptides (left) and between laminates (right) of the fiber assembly, this was described as the metal-vacancy model of assembly where the coordinating metal ions are separated by 1 nm in all directions along a single face of the fiber (Dong et al., 2007; Hernández-Guzmán et al., 2013).



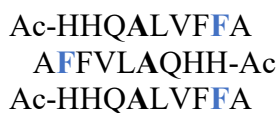


**Figure 3.3 – Ac-K16A and K16A assemblies in MES (pH: 5.6) and HEPES buffer (pH: 7.4).** (A) Ac-K16A fibers assembled in 25 mM HEPES buffered at pH: 7.4 and (C) 25 mM MES buffered at pH: 5.6. (B) K16A fibers assembled in 25mM HEPES buffered at pH: 7.4 and (D) 25 mM MES buffered at pH: 5.6. Fiber assemblies bundle less in MES buffer and appear to laminate more robustly as larger, more well-defined fibers.

The structures of these assemblies were defined to be  $\beta$ -sheet rich by circular dichroism (CD) with negative ellipticity minima at 214 nm and 216 nm for Ac-K16A and K16A respectively (**Figure 3.4**). The homogeneity of the assemblies formed by K16A and Ac-K16A is demonstrated across different temperatures by TEM. **Figure 3.5** highlights the structural heterogeneity observed for K16A after a two week incubation at 4°C, containing both particles and fibers. The same heterogeneity is observed for Ac-K16A (data not shown). The K16A particles seen in the TEM micrographs appear similar to the particles discussed in **Chapter 2**, whose structure was resolved by solid-state NMR and whose order was optically interrogated by fluorescence anisotropy and spectroscopically by isotope edited FT-IR. These particles persist at low temperatures within the timeline considered but the heterogeneity of the sample is morphologically resolved at 25°C and 37°C after a period of two weeks. A similar behavior is observed for Ac-K16A. **Figure 3.6** shows a micrograph and the frequency of the fiber width measurements across many different TEM grids and batches. The widths measured for K16A (**Figure 3.6A**) fit to a single distribution with a center at  $14.61 \pm 0.10$  nm and a width distribution of  $3.89 \pm 0.20$  nm (**Figure 3.6B**). The widths measured for Ac-K16A (**Figure 3.6C**) fit to a single distribution with a center at  $11.40 \pm 0.10$  nm and a width distribution of  $2.78 \pm 0.20$  nm (**Figure 3.6D**). The width differences may reflect the degree of lamination of each fiber with K16A containing about ~15 laminates per fiber and Ac-K16A containing ~11 laminates per fiber, on average. The difference in lamination suggests a higher assembly propensity of K16A or a difference in the degree of structural heterogeneity within the Ac-K16A assembly that is not resolved by TEM

and CD. To assess the degree of structural heterogeneity within the Ac-K16A fibers we turn to solid-state NMR.

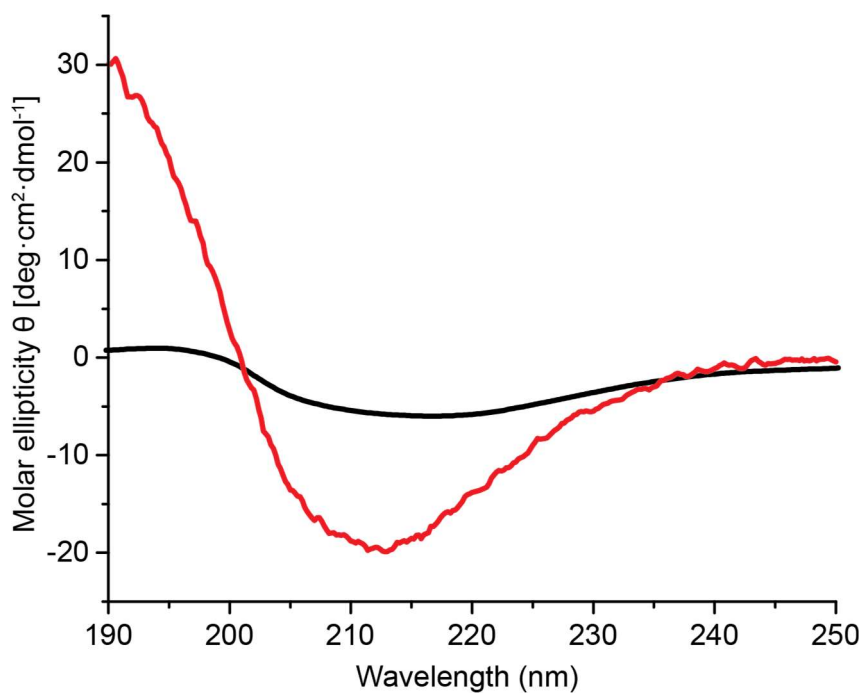
Ac-K16A, enriched at the Ala16 and Phe20 positions to give Ac-HHQ[1-<sup>13</sup>C]ALVF[<sup>15</sup>N]FA-NH<sub>2</sub>, was incubated under standard conditions for eight weeks and centrifuged at 4°C to remove supernatant with unassembled monomer. The resulting pellet was frozen in a -80°C freezer overnight and lyophilized before sample packing for solid-state NMR experiments. The CP-MAS NMR spectrum shows a single carbonyl resonance with a chemical shift at 173 ppm (**Figure 3.7A**). The peptide arrangement of Ac-K16A fibers was interrogated using heteronuclear <sup>13</sup>C-<sup>15</sup>N dipolar recoupling <sup>13</sup>C{<sup>15</sup>N} Rotational-Echo Double-Resonance (<sup>13</sup>C{<sup>15</sup>N} REDOR) NMR experiments (Terry Gullion, 1998; T. Gullion & J. Schaefer, 1989) (**Figure 3.7B**). Data collected fits to a 3-spin system composed of a <sup>13</sup>C coupled to two <sup>15</sup>N's from adjacent H-bonded strands, with <sup>13</sup>C-<sup>15</sup>N distances of 7.9Å and 8.9Å with an angle between the two <sup>13</sup>C-<sup>15</sup>N internuclear vectors of 68°. These measurements fit the 173 ppm resonance uniquely to an antiparallel in-register peptide arrangement:



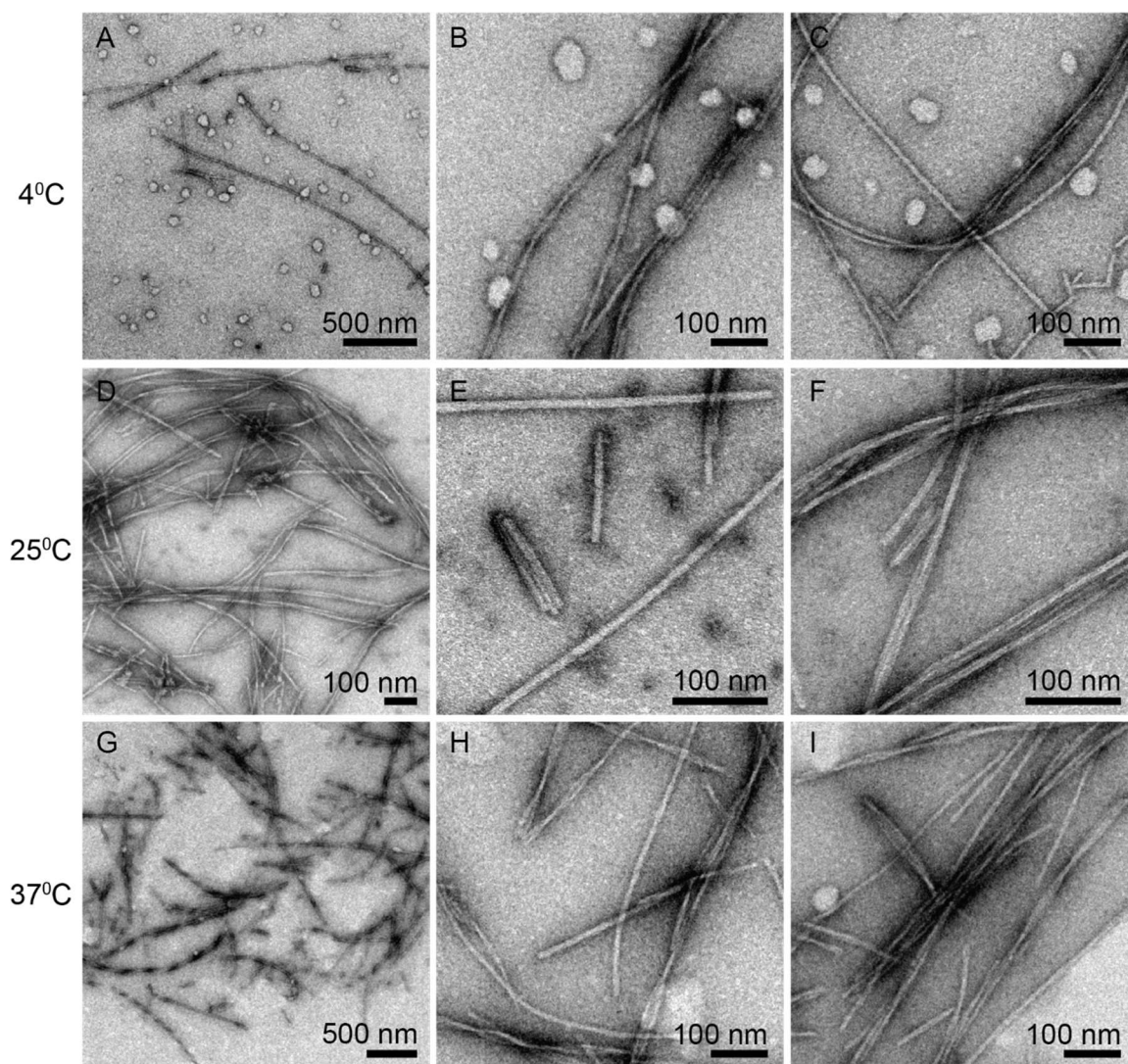
To fully fit the data, five populations (two major and three minor) with the same peptide arrangement had to be considered— as these samples diphase at the same rate across the single CP-MAS NMR spectrum (**Figure 3.7**). The heterogeneity in the structure may arise due to polymorphism of the peptide laminates, which supports our initial hypothesis that heterogeneity affects the degree of lamination measured for Ac-K16A fibers when compared to K16A fibers. Indeed, this level of heterogeneity is not observed for K16A

fibers where the peptides have a parallel, in-register arrangement (for a structural analysis for K16A fibers please refer to **Chapter 2**, pg. 28). However, as previously shown Ac-K16A can form fibers and helical ribbons, two morphologies that develop with the same underlying architecture.

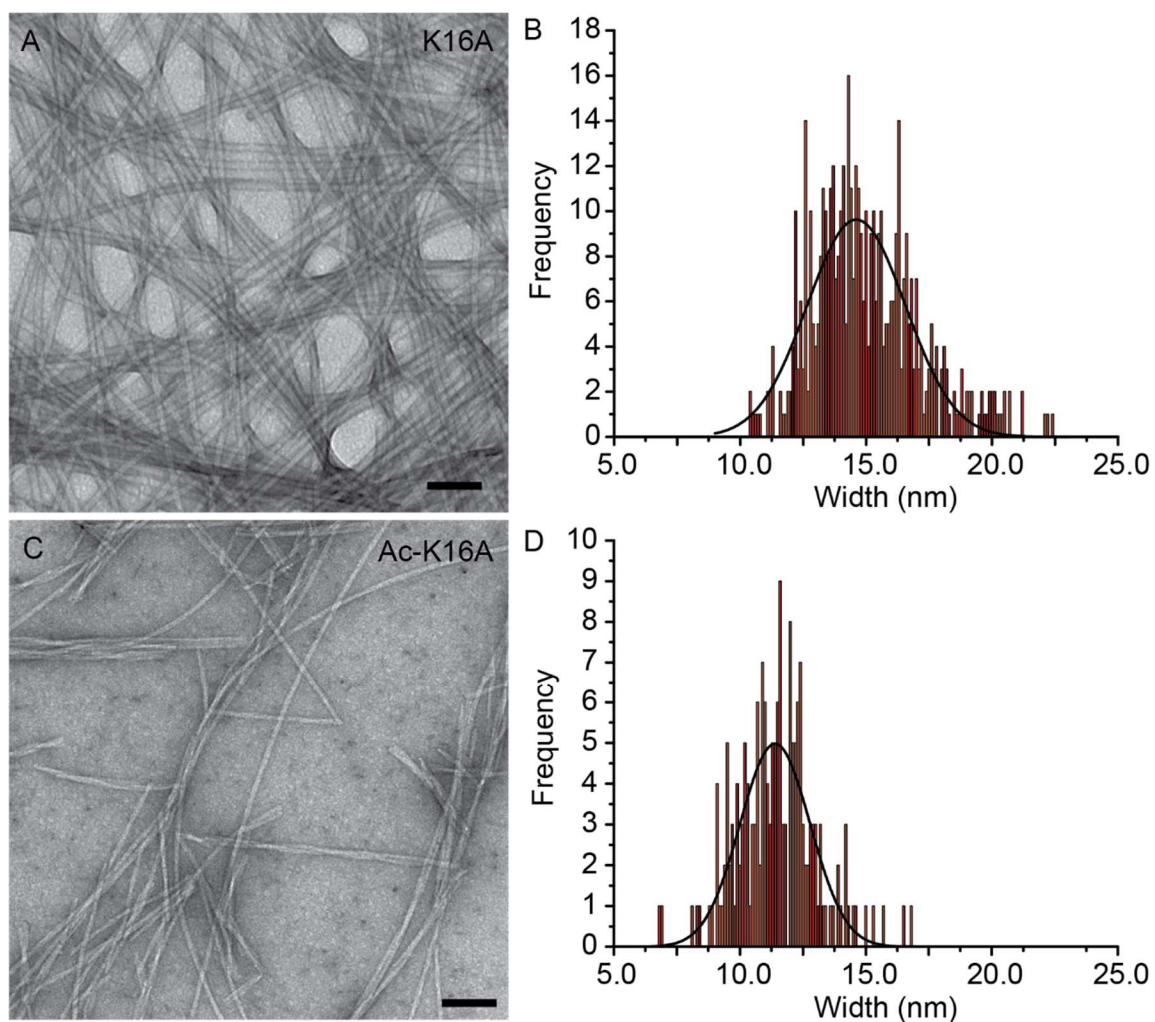
Interestingly, in the antiparallel, in-register Ac-K16A peptide arrangement, the sidechain of His14 is fully buried from the solvent environment and inaccessible to bind  $M^{n+}$ , a feature shared with K16A fibers. Unique to the Ac-K16A antiparallel fibers however, the His13 sidechains are separated by  $\sim 1$  nm in distance across the laminate and along a single  $\beta$ -sheet. Such an arrangement makes it difficult for this assembly to serve as a strong candidate for  $M^{n+}$  binding on a single preassembled fiber surface. Given this limitation, for all  $M^{n+}$  survey studies to be discussed, K16A and Ac-K16A were co-assembled with the  $M^{n+}$  of interest, to allow for  $M^{n+}$  driven rearrangement of peptides if necessary for their incorporation.



**Figure 3.4 – CD spectra of Ac-K16A and K16A fibers.** Cyclic dichroism spectra of 2mM Ac-K16A (red) and 0.5 mM K16A (black) fibers. Intensity difference by a factor of four reflects concentration difference. Negative ellipticity minima is 214 nm for Ac-K16A fibers and 216 for K16A fibers, characteristic absorbance for  $\beta$ -sheet assemblies. The 4-fold difference in intensity is attributed to the 4-fold difference in peptide concentration.

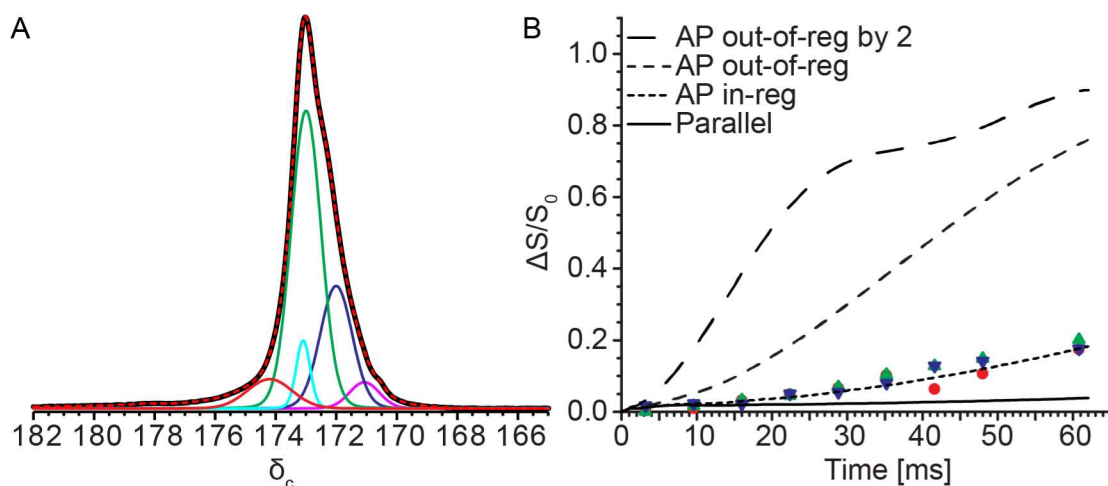


**Figure 3.5 – TEM micrographs of K16A assembled at different temperatures.** TEM micrographs taken after 2 weeks of assembly. At 4°C (A, B, and C), particles and fibers are both seen in the TEM grid. At 25°C (D, E, and F) flat and twisted fibers dominate the grid, though some small aggregates persist in the background. At 37°C (G, H, and I) twisted and flat fibers are the major species on the TEM grid. Smaller aggregates are not as prevalent though some particles are seen, this suggests that particles and small aggregates may coexist with the fully assembled fibers even sample is fully matured.



**Figure 3.6 – TEM micrographs and width measurements of K16A and Ac-K16A**

**fibers.** (A) TEM micrograph of H-HHQALVFFA-NH<sub>2</sub> (K16A) fibers, assembled in 25 mM MES buffer, pH: 5.6. (B) Fiber size distribution follows a normal distribution centered at  $14.61 \pm 0.10$  nm with a width distribution of  $3.89 \pm 0.20$  nm. (C). TEM micrograph of Ac-HHQALVFFA-NH<sub>2</sub> (Ac-K16A) fibers, also assembled in 25 mM MES buffer, pH: 5.6. (D) Fiber size distribution follows a normal distribution centered at  $11.40 \pm 0.10$  nm with a width distribution of  $2.78 \pm 0.20$  nm.



**Figure 3.7 – Solid-state NMR analysis of Ac-K16A fibers.** (A) CP-MAS NMR spectrum for Ac-K16A fibers (black). Deconvolution needed to fit the experimental spectrum: population at 174.2 ppm (red) makes up 7.3% of the sample, population at 173.1 ppm (cyan) makes up 5.4% of sample, population at 173.0 ppm (green) makes up 50.4% of the sample, population at 172.0 ppm (blue) makes up 20.1% of sample, population 171.1 ppm (magenta) makes up 4.4% of sample. Dashed red line represents the sum of all contributions and the best fit. (B) Dashed lines show predicted  $^{13}\text{C}\{^{15}\text{N}\}$  REDOR dephasing line shapes, given the isotope enrichment model for each of the different peptide arrangements described (parallel, antiparallel and antiparallel with registry shifts). Data fits the ideal antiparallel and in-register peptide arrangement.

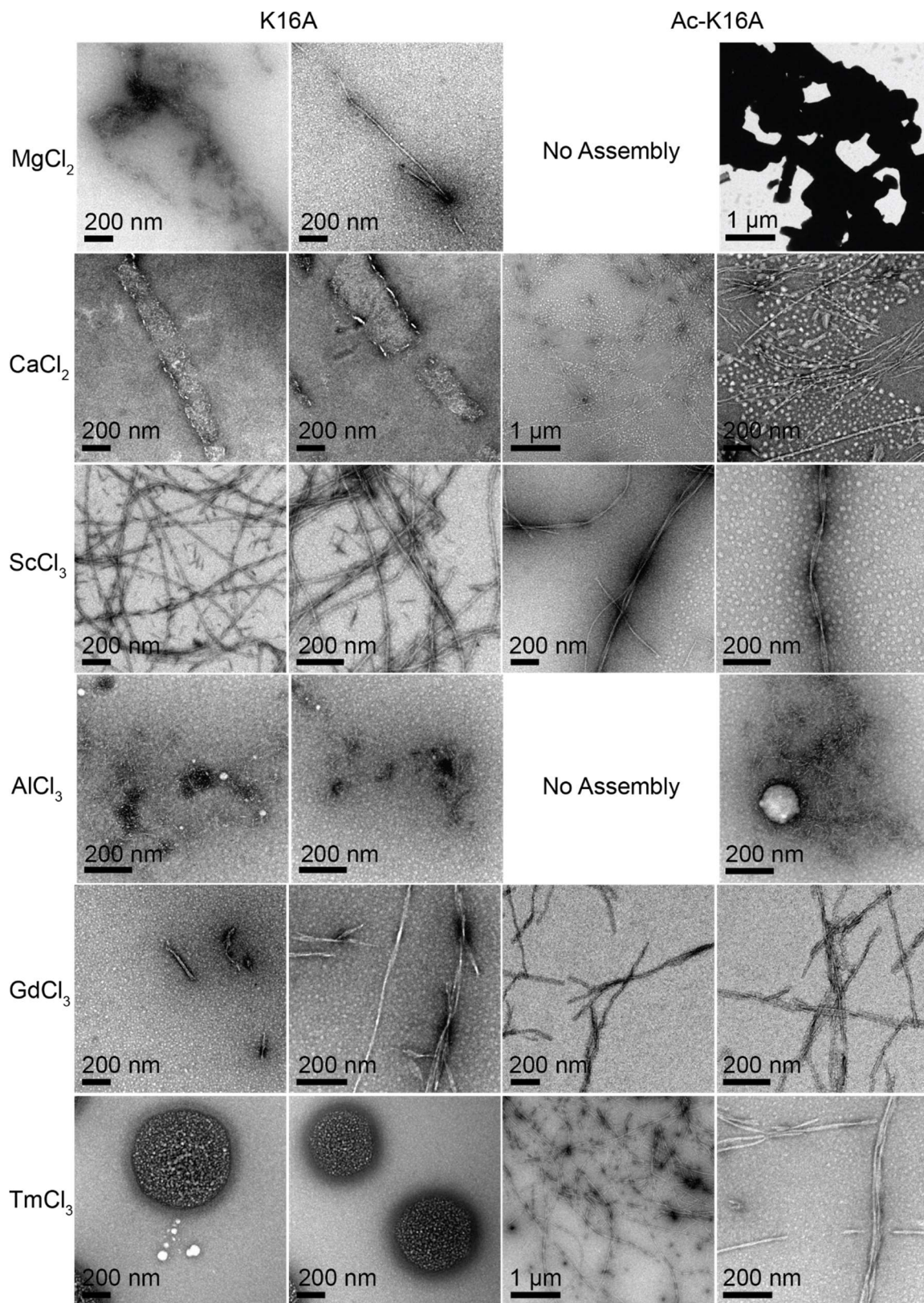


### Templating K16A and Ac-K16A assembly with metals

Three key features were surveyed for metal co-assembly: 1) do metal ions facilitate self-assembly, 2) are the structures homogenous, and 3) is there a temperature dependence to achieve final assembly. These studies are informed by previous functional nanostructures (Gorbitz, 2013; Kasotakis et al., 2009; Mitraki & Kasotakis, 2013) as well as the desirable features of other amyloids (Hernández-Guzmán et al., 2013; S. Li et al., 2016; Lu et al., 2007; Lu, Jacob, Thiyagarajan, Conticello, & Lynn, 2003; Torok et al., 2002; J. X. Wang et al., 2013). The metal ions investigated ranged in atomic radius, accessible coordination geometries, ionization energy, electronegativity, metallic and nonmetallic character and electron affinity. We reasoned that by surveying a range of alkaline earth metals, transition metals, post-transition metals, and lanthanides, we would be able to extend the range of functional nanomaterials and **Figure 3.8** summarizes the results obtained in the initial survey. Alkaline earth metals, magnesium ( $Mg^{2+}$ ) and calcium ( $Ca^{2+}$ ), gave heterogeneous mixtures of amorphous aggregates, particles, fibers and crystal deposits for both K16A and Ac-K16A. This result is surprising as divalent salts typically promote peptide assembly (Hong, Pritzker, Legge, & Chen, 2005; Lu et al., 2007; Otsuka, Maeda, & Hotta, 2014; Ozbas, Kretsinger, Rajagopal, Schneider, & Pochan, 2004). A single metal binding histidine appears to limit peptide templating likely due to a low binding affinity of these side-chains as previously noted (Arvanitis, Vafiadaki, Sanoudou, & Kranias, 2011; Sinz, Jin, & Zschornig, 2003). The metal does disrupt the peptide's ability to assemble as homogenous structures and the addition of strongly coordinated metals, for example scandium ( $Sc^{3+}$ ), results in the most robust assemblies of the survey. These structures are morphologically similar to the fibers

formed by K16A without metal, and for Ac-K16A, a less robust and heterogeneous collection of peptide assemblies emerged ranging from fibers to ribbons and particles.

As shown in **Figure 3.8**, co-assembly with post-transition metal aluminum ( $\text{Al}^{3+}$ ) gives amorphous aggregates and particles with both K16A and Ac-K16A. Lanthanoids gadolinium ( $\text{Gd}^{3+}$ ) and thulium ( $\text{Tm}^{3+}$ ) also give mixed results. In the presence of  $\text{Gd}^{3+}$ , both K16A and Ac-K16A form fibers morphologically similar with and without the lanthanoids, consistent with no direct interaction. In the presence of  $\text{Tm}^{3+}$ , K16A forms very large particles and Ac-K16A forms fibers similar to the structures formed by the peptide alone. The toxicity of lanthanoids and other rare earth metals (including  $\text{Sc}^{3+}$ ) is well documented (Tichy & MRucki, 2013), so even though these metals are useful in car catalytic converters, magnets, rechargeable batteries and fertilizers, their cost and their link to cellular oxidative stress upon prolonged exposure make them poor candidates for cell-compatible nanomaterial (Hatch, 2012; Pagano, Guida, Tommasi, & Oral, 2015; "Preparation of Nanostructures," 2007).



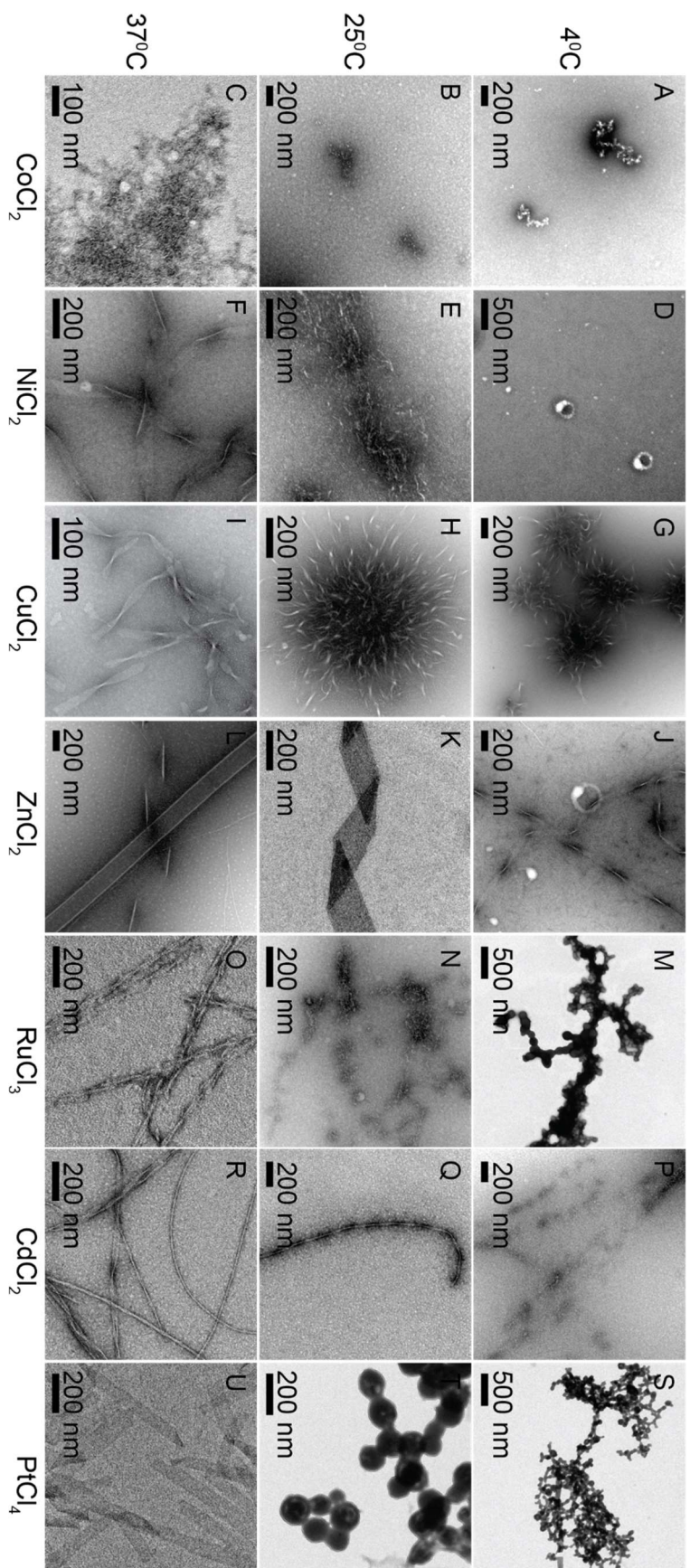
**Figure 3.8 – TEM summary of metal-survey results with alkaline earth metals, transition metals, post-transition metals, and lanthanoids.** Heterogeneous assemblies form for each of the metal co-assemblies with K16A and Ac-K16A ranging from fibers, ribbons, particles, sheets, and amorphous aggregates. The most regular structures are seen with  $\text{ScCl}_3$ ,  $\text{GdCl}_3$ , and  $\text{TmCl}_3$ .

In selecting transition metal ions to survey we considered their relative abundance, their current applications in the development of functional nanoscale materials, and again, selected a range varying in atomic radius, accessible coordination geometries, ionization energy, electronegativity, and electron affinity. We focused these studies on K16A and used the results to direct development of Ac-K16A assembly conditions. As shown in the TEMs of **Figure 3.9**, assembly of these peptides is notably sensitive to temperature. K16A forms amorphous aggregates across all temperatures in the presence of cobalt ( $\text{Co}^{2+}$ ) (**Figure 3.9A-C**). When exposed to nickel ( $\text{Ni}^{2+}$ ) (**Figure 3.9D-F**), amorphous aggregates are observed at 4°C and 25°C, while regular twisted ribbons dominate assembly at 37°.  $\text{Cu}^{2+}$  co-assemblies (**Figure 3.9G-I**) formed regular twisted ribbons at all temperatures, although the bundling of these assemblies is temperature sensitive. The unique urchin-like ribbons observed at 4°C and 25°C will be discussed in the next section. In the presence of  $\text{Zn}^{2+}$  (**Figure 3.9J-L**) heterogeneous assemblies of fibers, twisted ribbons, helical ribbons and nanotubes are observed. It is evident that with higher temperatures the degree of lamination and thus, the helical character of the assembly, is increased. This lamination is consistent with previous reports of K16A morphology in the presence of  $\text{Zn}^{2+}$ .(Dong, Shokes, et al., 2006) Later in

this chapter we characterize the structure and discuss how this heterogeneity provides important insight to the mechanism of peptide assembly as a whole.

Assemblies with ruthenium ( $\text{Ru}^{3+}$ ) (**Figure 3.9M-O**), a popular but expensive transition metal used in the development of water splitting catalysts (Sheldon & Arends, 2006; Soltau et al., 2015; Yi, Kwon, & Lee, 2009), form collections of particles at 4°C, amorphous aggregates at 25°C, and regular twisted fibers at 37°C. This temperature dependence on assembly is similar to what was observed with  $\text{Ni}^{2+}$ , though the assemblies appear less robust at 37°C. Cadmium ( $\text{Cd}^{2+}$ ) and platinum ( $\text{Pt}^{4+}$ ) also facilitated the formation of a range of structures (i.e., amorphous aggregates, twisted ribbons, fibers and sheets) across the different temperatures (**Figure 3.9P-U**).

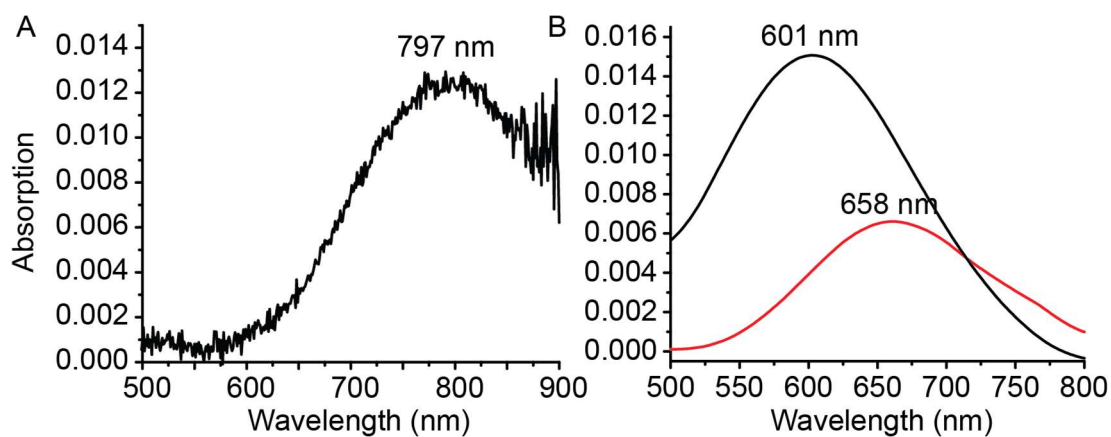
Given the selection criteria defined at the beginning of this section, we concluded that  $\text{Cu}^{2+}$ ,  $\text{Ni}^{2+}$ ,  $\text{Ru}^{3+}$ , and  $\text{Zn}^{2+}$  are good candidates for the development and characterization of MANs. While  $\text{Ni}^{2+}$  and  $\text{Ru}^{3+}$  co-assemblies result in interesting structures at 37°C, the temperature heterogeneity may be hard to control initially, but could offer future selection criteria. The relative abundance and cheap costs of  $\text{Cu}^{2+}$  and  $\text{Zn}^{2+}$ , the offer of both redox capability and known structural arrays within proteins, as well as their biological relevance for the development of the cell-compatible nanostructures, focused our initial efforts on these metals.



**Figure 3.9 – TEM analyses of K16A/metal co-assemblies as a function of temperature.** 0.5 mM K16A assembled for 2 weeks at 4°C, 25°C, and 37°C in the presence of Co<sup>2+</sup> (A,B and C), Ni<sup>2+</sup> (D,E and F), Cu<sup>2+</sup> (G,H and I), Zn<sup>2+</sup> (J,K and L), Ru<sup>3+</sup> (M,N and O), Cd<sup>2+</sup> (P,Q and R) and Pt<sup>4+</sup> (S,T and U). While most conditions derived a structure, it is apparent that the most robust structures, at all temperatures, arise from assemblies formed in the presence of Zn<sup>2+</sup> and Cu<sup>2+</sup>. However, sample heterogeneity in size and morphology arises at early temperatures and timepoints for assemblies in the presence of Zn<sup>2+</sup> and persists at higher temperatures. This heterogeneity is not observed for ribbons assembled in the presence of Cu<sup>2+</sup> across temperatures. Refer to Materials and Methods for TEM preparation details.

### **Cu<sup>2+</sup> and Zn<sup>2+</sup> influence on Ac-K16A and K16A assembly and morphology**

After defining Cu<sup>2+</sup> and Zn<sup>2+</sup> as the focus for initial development of MANs with K16A, Ac-K16A has been investigated. When incubated with Cu<sup>2+</sup> and Zn<sup>2+</sup> in 25mM MES buffer, pH: 5.6, Ac-K16A also assembles readily, forming highly regular structures, analogous to those formed with K16A. UV-Vis spectra confirm the incorporation of Cu<sup>2+</sup> in the assemblies by the blue shifted  $\lambda_{\max}$  values for both Ac-K16A -Cu<sup>2+</sup> and K16A-Cu<sup>2+</sup> assemblies relative to the aquo-Cu<sup>2+</sup> species in MES (**Figure 3.10**). This blue shift arises from the d-d transition of Cu<sup>2+</sup> that depends on the ligands. More electronegative ligands coordinating the Cu<sup>2+</sup> sphere give a more intense blue shift arises (Sigel & Martin, 1982), and this effect is exploited further in **Chapter 4**.

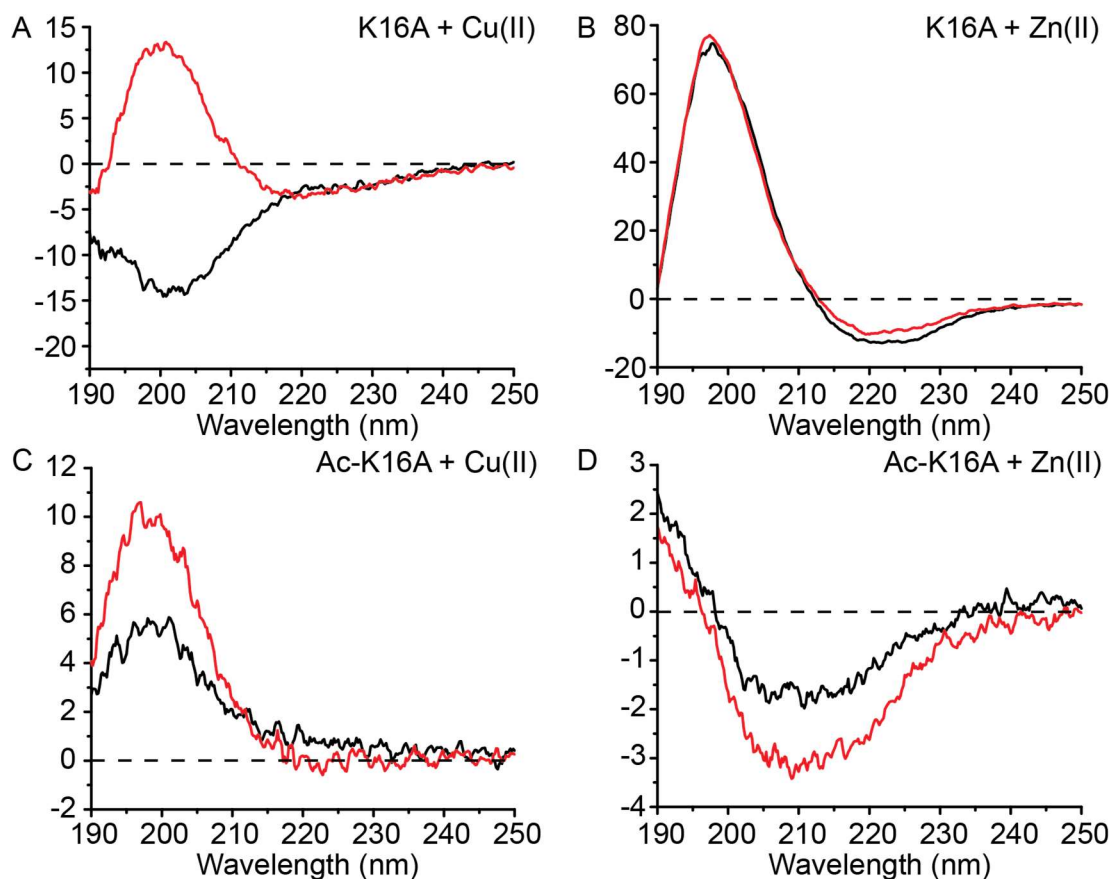


**Figure 3.10 – UV-Vis of aquo-Cu<sup>2+</sup> and in the presence of K16A-Cu<sup>2+</sup> and Ac-K16A-Cu<sup>2+</sup>.** (A) UV-Vis spectra of 1 mM CuCl<sub>2</sub> in 25 mM MES, pH: 5.6 shows a  $\lambda_{\max}$  = 797 nm. (B) UV-Vis spectra of Ac-K16A-Cu<sup>2+</sup> (red) with a  $\lambda_{\max}$  value at 658 nm and K16A-Cu<sup>2+</sup> (black) with a  $\lambda_{\max}$  at 601 nm.



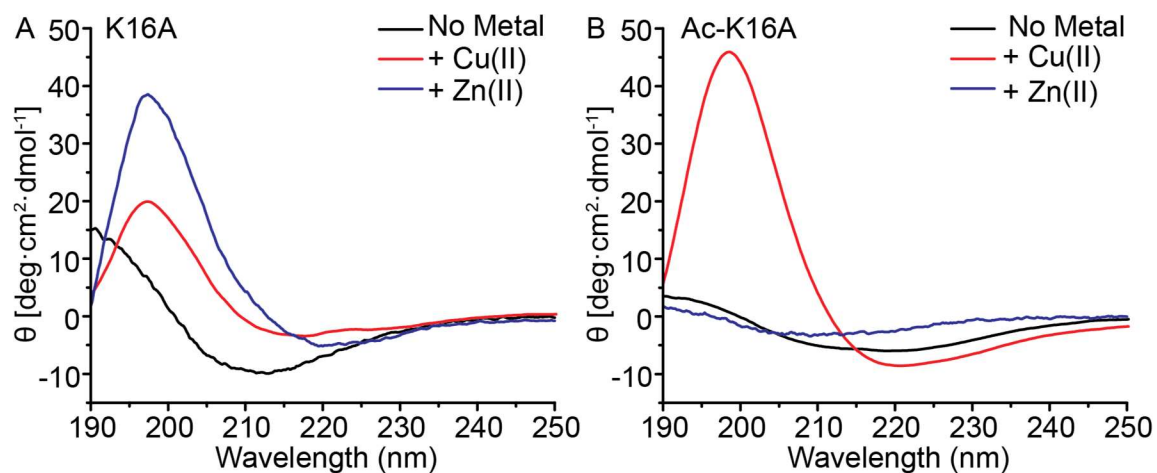
**Figure 3.11** summarizes the results obtained with CD signature at 25°C and 37°C for both Ac-K16A and K16A assemblies with Cu<sup>2+</sup> and Zn<sup>2+</sup>. After four weeks, K16A + Zn<sup>2+</sup> displays the highest degree of assembled peptide at both temperatures (**Figure 3.11B**) and Ac-K16A-Zn<sup>2+</sup> assembly signatures are much weaker, suggesting that the N-terminus plays a more direct role in Zn<sup>2+</sup> coordination. No assignable peptide signature was apparent in the Cu<sup>2+</sup> co-assemblies at this time point, but after eight weeks (**Figure 3.12**), the Cu<sup>2+</sup> assemblies show the most intense b-sheet signatures. While these assemblies form slowly, this result suggests that the Cu<sup>2+</sup> assemblies may be viable for developing functional MAN assemblies.

**Figure 3.13A, D and G** contain low magnification TEM micrographs of Ac-K16A assemblies after one week of assembly. At higher magnification (**B, E, and H**) and after one month (**C, F, and I**), both fibers and helical ribbons grow with and without metal (**Figure 3.13A-C**). In the presence of Cu<sup>2+</sup>, a robust collection of urchin-like aggregates with radiating twisted ribbons (**Figure 3.13D-F**), while fibers remain the dominant species in the presence of Zn<sup>2+</sup> (**Figure 3.13G-I**). The morphology of the assemblies with these metals are distinct and the bundling may be stabilized by inter-fiber Zn<sup>2+</sup> coordination.



**Figure 3.11 – CD spectra of K16A and Ac-K16A in the presence of  $\text{Cu}^{2+}$  and  $\text{Zn}^{2+}$ .**

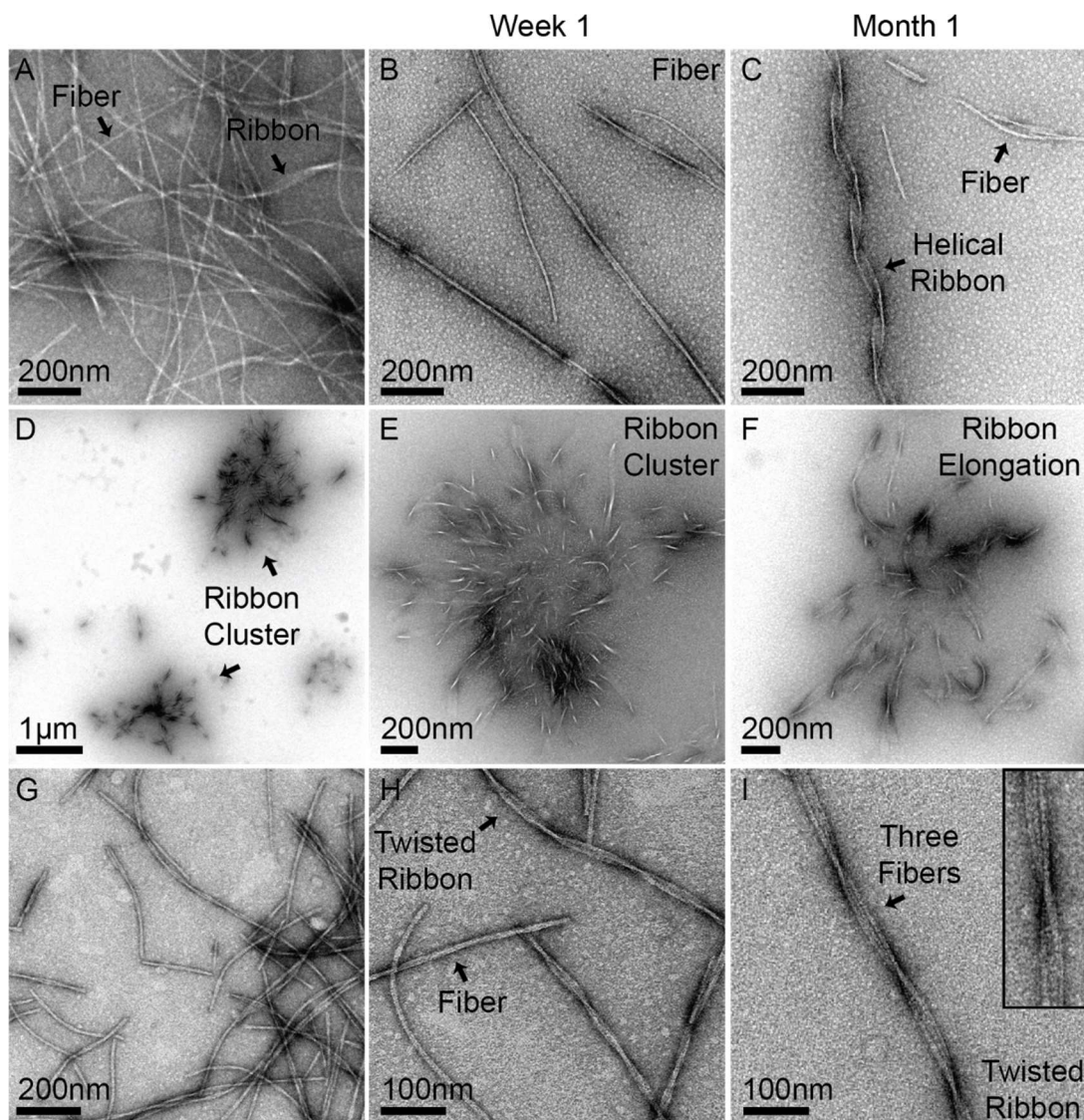
Circular dichroism spectra collected at 25°C (black) and 37°C (red) for K16A and Ac-K16A assemblies with  $\text{Cu}^{2+}$  (A and D),  $\text{Zn}^{2+}$  (B and E), respectively after 28 days of assembly.



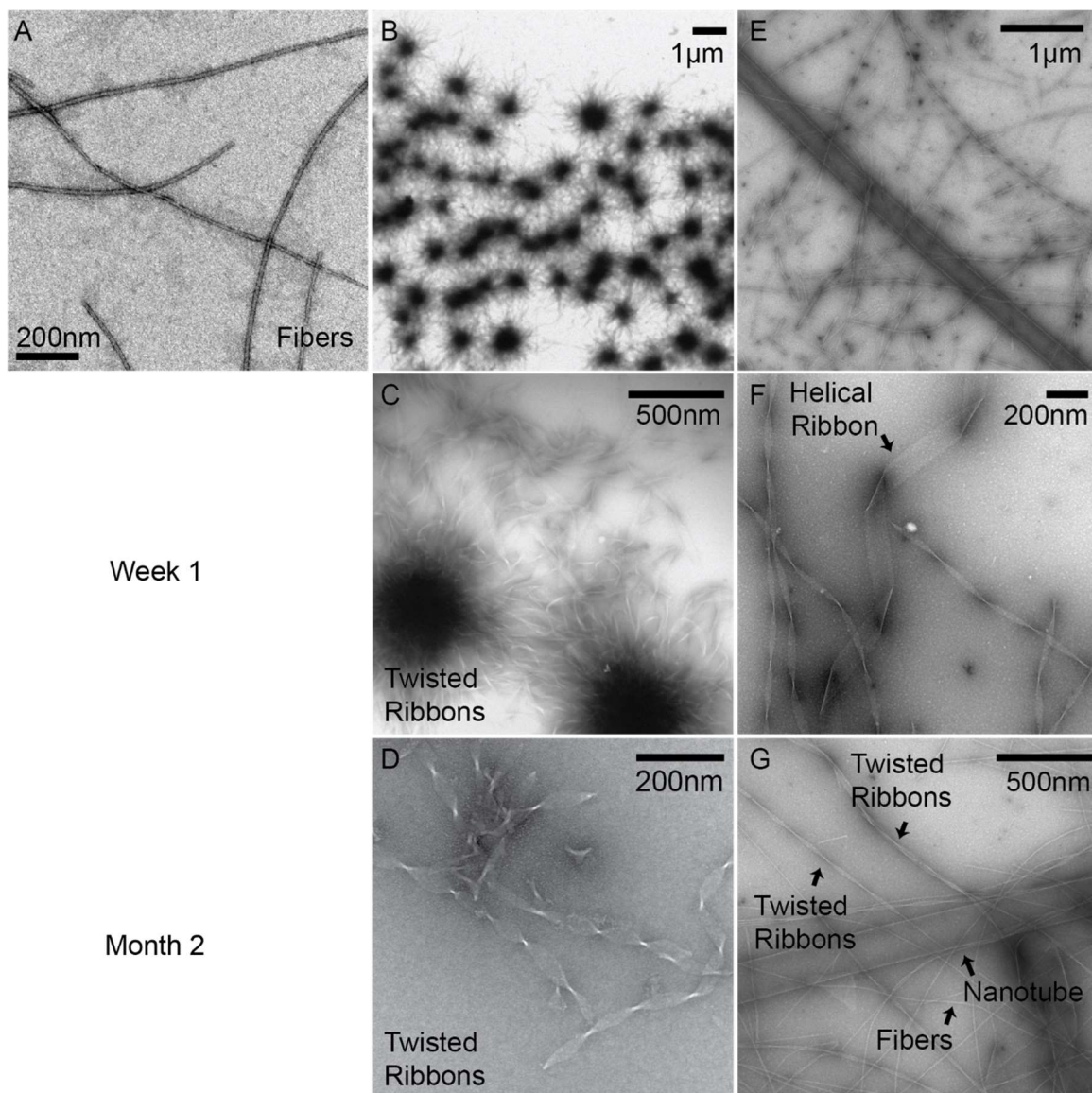
**Figure 3.12 – CD spectra of mature K16A and Ac-K16A assemblies in the presence of Cu<sup>2+</sup> and Zn<sup>2+</sup>.** Circular dichroism of mature ( $\geq 8$  weeks) (A) 1 mM K16A and (B) 1 mM Ac-K16A assemblies in the presence of equimolar amounts of Cu<sup>2+</sup> and Zn<sup>2+</sup>, incubated at 25°C in 25 mM MES, pH: 5.6. The 210 to 220 nm region of the CD spectra of assemblies with no metal (black), Cu<sup>2+</sup> (red) and Zn<sup>2+</sup> (blue) highlight the relative abundance and  $\beta$ -sheet character of the assembly.

In contrast to Ac-K16A assemblies, the K16A assemblies show an even more dramatic morphological transformation in the presence of  $\text{Cu}^{2+}$  and  $\text{Zn}^{2+}$ . **Figure 3.14** shows TEM micrographs of K16A incubated with  $\text{Cu}^{2+}$  (**B-D**) and  $\text{Zn}^{2+}$  (**E-G**), over the course of one week and two months. The morphological heterogeneity was first observed with K16A- $\text{Zn}^{2+}$  assemblies at three different temperatures. Strikingly, the final degree of heterogeneity maintained for  $\text{Zn}^{2+}$  assemblies, contain a mixture of fibers, twisted ribbons of varying sizes, and nanotubes (**Figure 3.14G**), while  $\text{Cu}^{2+}$  assemblies contain a single population of ribbons (**Figure 3.14D**). One possibility for this heterogeneity is that homogeneity seen for K16A- $\text{Cu}^{2+}$  ribbons arises from the broad coordination environment accessible to  $\text{Cu}^{2+}$  compared to  $\text{Zn}^{2+}$  (**Table 3.1**). Since  $\text{Zn}^{2+}$  typically adopts only a tetrahedral or distorted tetrahedral geometry, the accessible His- $\text{Zn}^{2+}$  interactions are limited. Counter intuitively, because  $\text{M}^{n+}$ -ligand interactions are typically stronger than chemical forces that drive peptide self-assembly,  $\text{Zn}^{2+}$  could help template an otherwise unstable kinetically formed structure. Thus, K16A- $\text{Zn}^{2+}$  assemblies may ‘trap’ a kinetic product and, in so doing, facilitate the study of structural mutations that are accessible in the peptide’s assembly ‘landscape’. Furthermore, the heterogeneity can be further explained by the lower binding affinity toward biological ligands when compared to  $\text{Cu}^{2+}$ . Thus,  $\text{Zn}^{2+}$  coordinating assemblies may not be able to autocatalyze a single coordination environment, facilitating the formation of various heterogeneous structures. In contrast,  $\text{Cu}^{2+}$  can access a wider range of coordination geometries with accessible ligands (i.e., square planar, compressed tetrahedral, elongated square pyramidal, elongated octahedral) and it has a higher binding affinity toward biological ligands when compared to  $\text{Zn}^{2+}$ , following the Irving-Williams series (Foster, Osman, &

Robinson, 2014; Masuoka & Saltman, 1994). Thus, once a template for growth is formed, it is more difficult for a mutation to propagate outside the defined framework. The mutation argument on which this hypothesis is based was introduced in **Chapter 2**, where a kinetic template is proposed to undergo a mutation as it elongates outside the particle environment which autocatalytically propagates, eventually promoting the rearrangement of the kinetic template. In contrast, while  $\text{Zn}^{2+}$  can also stabilize the kinetic assembly template that may form, it is unable to prevent mutations leading to a mixture of MANs.



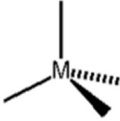

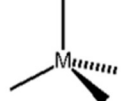


**Figure 3.13 – TEM micrographs of Ac-K16A assembly over the time in the presence and absence of  $\text{Cu}^{2+}$  and  $\text{Zn}^{2+}$ .** TEM micrographs of Ac-K16A assemblies (A, B and C) in the presence of  $\text{CuCl}_2$  (D, E and F) and  $\text{ZnCl}_2$  (G, H and I). After one week of assembly fibers dominate the metal free conditions (B), ribbon clusters dominate the assemblies in the presence of  $\text{Cu}^{2+}$  (E) and a mixture of fibers and ribbons are formed with  $\text{Zn}^{2+}$  (H). After one month of assembly, helical ribbons are observed under metal free conditions, though fibers still dominate the assembly (C), ribbons persist and elongate in the presence of  $\text{Cu}^{2+}$  (F) and individual fibers as well as bundled fibers are observed in the presence of  $\text{Zn}^{2+}$ . Bundled fibers, 3 shown here, collect and resemble the twisted ribbon morphologies (I).





**Figure 3.14 – TEM micrographs of K16A assembly.** (A) Assembly of K16A. (B, C and D) K16A assembly in the presence of  $\text{CuCl}_2$ . (E, F and G) K16A assembly in the presence of  $\text{ZnCl}_2$ . (C) After one week, urchin-like growth of ribbons are observed in the presence of  $\text{Cu}^{2+}$ , while a mixture of fibers and ribbons of different dimensions exists in the presence of  $\text{Zn}^{2+}$  (F). After two months, ribbons persist and elongate in the presence of  $\text{Cu}^{2+}$  (D), with fibers, ribbons and nanotubes evident in the presence of  $\text{Zn}^{2+}$  (G). Fiber morphology does not change for the metal-free assembly.

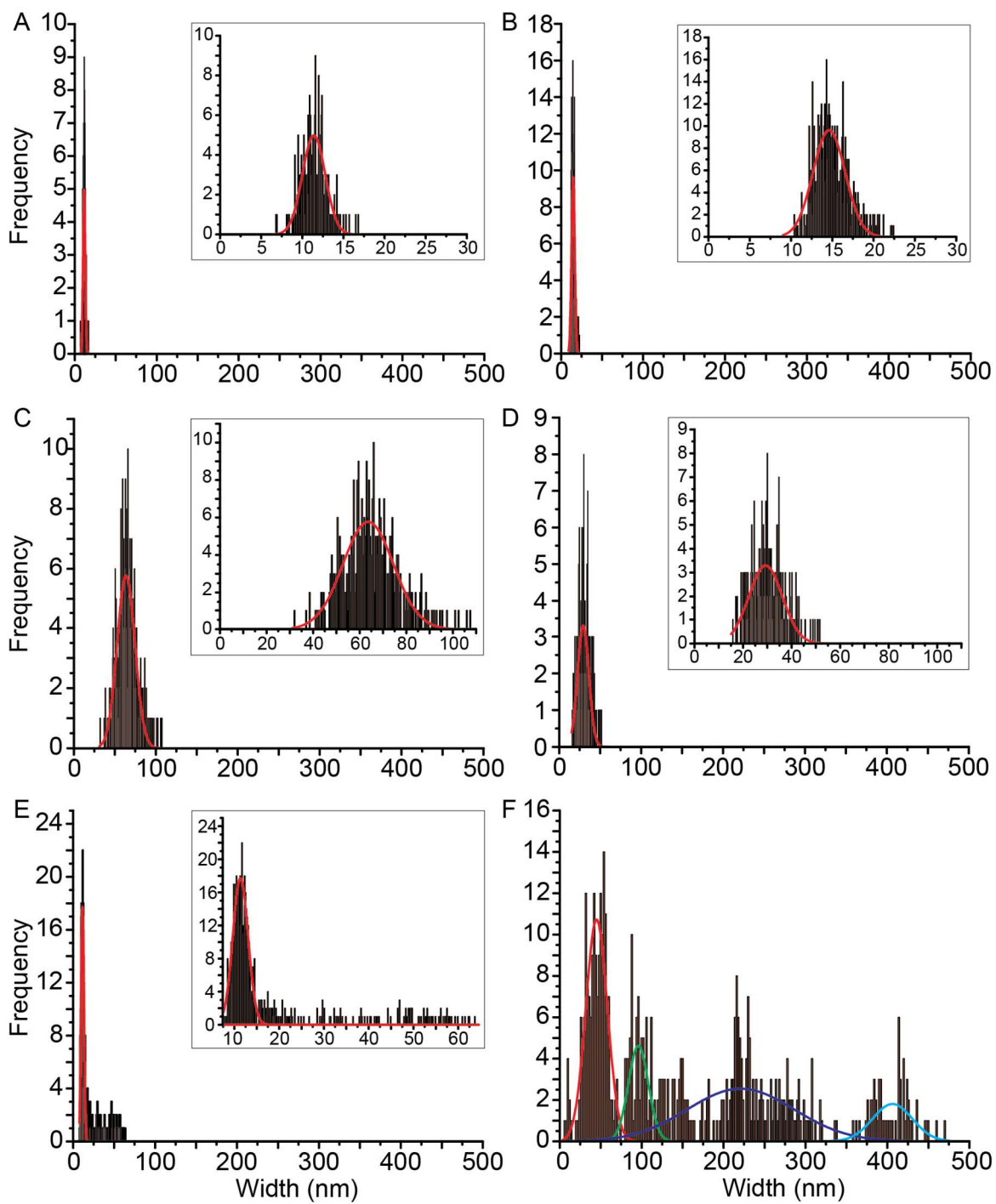
**Table 3.1: Accessible ligand geometry of  $\text{Zn}^{2+}$  and  $\text{Cu}^{2+}$  in proteins**

	Ligand Composition	Geometry
<b>Zn (II)</b>	Class I: HEXXHXXGXXH Class II: HXH.....H Class III: Combination of H and C Class IV: Two separated H, an acidic unibidentate and $1\text{H}_2\text{O}$ Class V: predominantly acidic ligands	Tetrahedral or distorted tetrahedral 
<b>Cu (II)</b>	Type I (Blue copper): $\text{CX}_m\text{HX}_n\text{M}$ , $m, n=2-4$ . monomeric copper with very distorted coordination  Type II: "normal" monomeric CuII is an essentially square planar (equatorial) environment with additional, very weak, tetragonal (axial) interactions  Type III: a pair of copper(I) ions attached to the protein through histidine residues.	 Square planar  Compressed tetrahedral  Elongated square pyramidal  Elongated Octahedral

The heterogeneities of the supramolecular morphologies can be more clearly represented by a study of the width distribution of species across TEM micrographs. **Figure 3.15** presents the widths measured from each individual micrograph for each of the different Ac-K16A and K16A assemblies. The histograms highlight a normal distribution of species for the fibers formed by the lone peptide and the ribbons templated by  $\text{Cu}^{2+}$  for both peptides. The difference in widths is evidence of an increased degree of  $\beta$ -sheet lamination facilitated by  $\text{Cu}^{2+}$ . Ac-K16A- $\text{Cu}^{2+}$  ribbons have a normal width distribution centered around  $63.6 \pm 0.6$  nm, roughly representing 60  $\beta$ -sheets, with a width that expands  $21.8 \pm 1.1$  nm (**Figure 3.15C**). In contrast, K16A- $\text{Cu}^{2+}$  ribbons have a normal width distribution centered around  $29.3 \pm 0.4$  nm, roughly representing 30  $\beta$ -sheets, with a width that expands  $13.8 \pm 0.8$  nm (**Figure 3.15D**). The increased lamination of the Ac-K16A peptide is an improvement from the lone peptide fibers (**Figure 3.15A and B**), demonstrating a more homogeneous sample compared to the lone peptide.

Ac-K16A- $\text{Zn}^{2+}$  fibers have a normal width distribution centered around  $11.5 \pm 0.1$  nm, expanding  $3.4 \pm 0.1$ . The width distribution here is a bit deceiving, however, as measurements were recorded up to 50 nm beyond the Gaussian center. However, not enough measurements were accumulated due to a low number of assemblies within this range (**Figure 3.15E**). The minor populations that exist above 15 nm are likely the result of the fiber bundling seen in the micrographs discussed above (**Figure 3.13G, H, and I**). K16A- $\text{Zn}^{2+}$  distribution of assemblies displays the largest range and assembles the largest number of  $\beta$ -sheet laminates across the different morphologies of fibers, ribbons, and tubes shown in their respective TEM micrograph (**Figure 3.14E, F, and G**). The

populations fit to four normal width distributions:  $45.0 \pm 0.9$  nm (fibers) expanding  $26.2 \pm 1.8$  nm;  $96.0 \pm 2.0$  nm (ribbons) expanding  $24.4 \pm 4.3$  nm;  $220.9 \pm 9.0$  nm (ribbons/tubes) expanding  $130.5 \pm 20.3$ ;  $406.2 \pm 6.8$  nm (tubes) expanding  $48.6 \pm 13.8$  nm (**Figure 3.15F**). The range of structures herein described encouraged us to pursue a more in depth structural analysis of the  $\text{Zn}^{2+}$  assemblies in the presence of Ac-K16A and K16A. Though not likely to serve as candidate structures for functional material development, we were motivated by the prospect of gaining more insight into the assembly pathway that was outlined in **Chapter 2**. If a subset of these structures are products of kinetic traps, we can make a more direct statement about the mutational model described for the particle  $\rightarrow$  fiber phase transition.



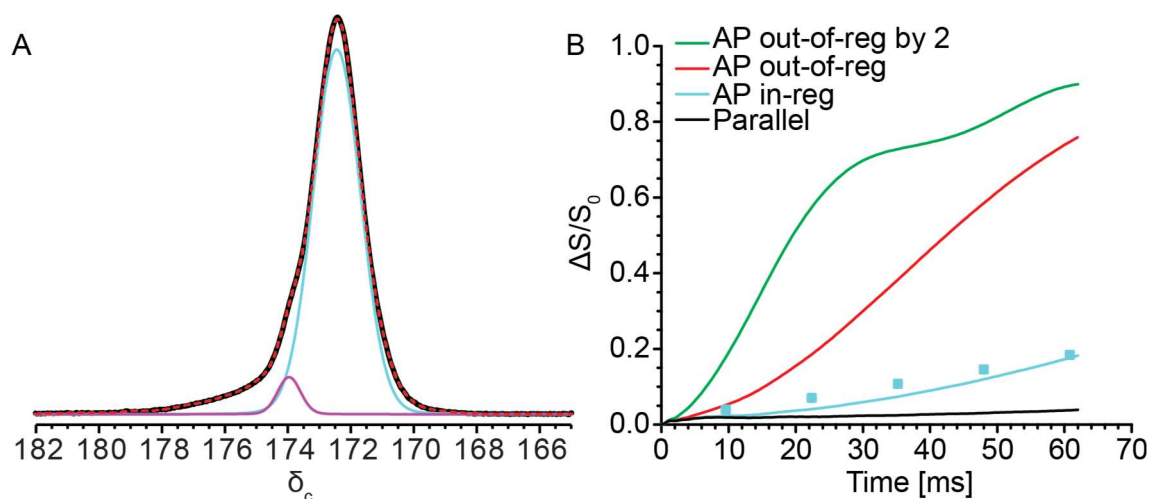
**Figure 3.15 – Width histograms of Ac-K16A and K16A in the presence and absence of Cu<sup>2+</sup> and Zn<sup>2+</sup>.** Width measurements of Ac-K16A (A, C, and E) and K16A (B, D, and F) fibers and ribbons assemblies in the presence and absence of metal ions. For these measurements, ‘center’ describes the best Gaussian fit and is the first reported value. The range of the Gaussian fit expands the x-axis and is the second reported value. (A) Ac-K16A fibers, no metal added, have a normal width distribution centered around  $11.4 \pm 0.1$  nm, expanding  $2.8 \pm 0.2$  nm. (B) K16A fibers, no metal added, have a homogeneous width distribution centered around  $14.6 \pm 0.1$  nm, expanding  $3.9 \pm 0.2$  nm. (C) Ac-K16A + CuCl<sub>2</sub> ribbons have a normal width distribution centered around,  $63.6 \pm 0.6$  nm, expanding  $21.8 \pm 1.1$  nm. (D) K16A + CuCl<sub>2</sub> ribbons have a normal width distribution centered around  $29.3 \pm 0.4$  nm, expanding  $13.8 \pm 0.8$  nm. (E) Ac-K16A + ZnCl<sub>2</sub> fibers have a normal width distribution centered around  $11.5 \pm 0.1$  nm, expanding  $3.4 \pm 0.1$  nm. Minor populations above 15 nm were not fit because not enough assemblies in this range were measured. (F) K16A + ZnCl<sub>2</sub> fibers, ribbons and tubes have a normal width distribution around four major populations:  $45.0 \pm 0.9$  nm (fibers) expanding  $26.2 \pm 1.8$  nm;  $96.0 \pm 2.0$  nm (ribbons) expanding  $24.4 \pm 4.3$  nm;  $220.9 \pm 9.0$  nm (ribbons/tubes) expanding  $130.5 \pm 20.3$ ;  $406.2 \pm 6.8$  nm (tubes) expanding  $48.6 \pm 13.8$  nm.

### Solid-state NMR analysis of Ac-K16A and K16A assemblies in the presence of Zn<sup>2+</sup>

To gain a more complete picture of the peptide arrangement distribution across samples with heterogeneous morphologies, namely Ac-K16A-Zn<sup>2+</sup> and K16A-Zn<sup>2+</sup>, we prepared them for solid-state NMR experiments. Peptides were synthesized with enrichments [1-<sup>13</sup>C]Ala16 and [<sup>15</sup>N]Phe20 to give Ac-HHQ[1-<sup>13</sup>C]ALVF[<sup>15</sup>N]FA-NH<sub>2</sub> and H-HHQ[1-<sup>13</sup>C]ALVF[<sup>15</sup>N]FA-NH<sub>2</sub>. As shown in the previous section (**Figure 3.13H and I**), Ac-K16A-Zn<sup>2+</sup> assembled into fibers and twisted ribbons composed of three bundled fibers. Measurements across many TEM micrographs resolved one major population, defined by fiber width, and several minor populations that were unresolvable as measurements were not sufficient to obtain a reliable distribution (**Figure 3.15E**). The size diversity, however, could be explained by the presence of the twisted ribbons composed of multiple mature fibers, as previously discussed. Regardless, the possibility of a heterogeneous distribution of peptide arrangements could not be discarded without experimental data. We previously observed morphological diversity for the Ac-K16A peptide alone, discussed in the “Peptide Design” section of this chapter, where Ac-K16A forms fibers and helical ribbons at long times of assembly. These morphological heterogeneities were structurally justified after solid-state NMR analysis of the sample, where we identified two major and one minor populations (populations we hypothesized arise from polymorphism across laminates) that shared the same peptide arrangement, antiparallel and in-register, as determined by a <sup>13</sup>C-<sup>15</sup>N dipolar recoupling <sup>13</sup>C{<sup>15</sup>N} Rotational-Echo Double-Resonance (<sup>13</sup>C{<sup>15</sup>N} REDOR) NMR experiment (Terry Gullion, 1998; T. Gullion & J. Schaefer, 1989). Given the peptide arrangement, we defined the conditions of M<sup>n+</sup> addition, before fiber formation, as histidine sidechain

accessibility would otherwise be limited to the  $M^{n+}$ . Given the morphologies captured by TEM for Ac-K16A- $Zn^{2+}$  assemblies, we hypothesized that  $Zn^{2+}$  incorporation may occur between fibers or across laminates (possibly selecting for a single morphology), assuming the same peptide arrangement as that seen for Ac-K16A fibers which positions the  $\beta$ -strands about 1 nm apart along H-bonding peptides.

The CP-MAS NMR spectrum of Ac-K16A- $Zn^{2+}$  gives a single carbonyl resonance with a chemical shift at 172.2 ppm (**Figure 3.16A**) that fits to a single population. Sample preparation is described in the ‘Materials and Methods’ at the end of this chapter. Distances of the  $^{15}N$  from the adjacent carbonyls were fit to 7.9 Å ( $r_1$ ) and 8.9 Å ( $r_2$ ) with an angle between the two  $^{13}C$ - $^{15}N$  internuclear vectors of 68.0°. These distances correspond to the same peptide arrangement seen for Ac-K16A fibers, antiparallel and in-register (**Figure 3.16B**). The data is encouraging, demonstrating that  $Zn^{2+}$  can facilitate the homogenous propagation of a single morphology – no helical ribbons were observed in the Ac-K16A- $Zn^{2+}$  sample, and the twisted fibers that are evident by TEM over longer time periods of incubation are composed of fibers of a single width and a homogeneous structure. Thus, we hypothesize that for the Ac-K16A- $Zn^{2+}$  assemblies, minimal but important contributions occur early in fiber formation which limits the lamination of the fiber from developing into helical ribbons. However, at longer times, the propagation of the twisted ribbons composed of three fibers likely incorporate increasing amounts of  $Zn^{2+}$  between fibers, where the terminal histidine sidechains from adjacent fibers can combine to sequester  $Zn^{2+}$ . Initial studies by mass spectroscopy suggest a low percent incorporation of  $Zn^{2+}$ , in agreement with our hypothesis, but this result is not yet conclusive.



**Figure 3.16 – Solid-state NMR analysis of Ac-K16A-Zn<sup>2+</sup> nanostructures.** A) CP-MAS NMR spectrum for Ac-K16A-Zn<sup>2+</sup> assemblies (black). Deconvolution needed to fit the experimental spectrum: population at 174.0 ppm (magenta) makes up 3.8% of the sample, population at 172.5 ppm (turquoise) makes up 78.1% of sample. Dashed red line represents the sum of all contributions and the best fit of the spectrum. (B) Solid lines show predicted <sup>13</sup>C{<sup>15</sup>N} REDOR dephasing line shapes, given the isotope enrichment model, for each of the different peptide arrangements described (parallel (black), antiparallel in-register (turquoise) and antiparallel with registry shifts of one (red) or two amino-acids (green)). Data show fits to the ideal anti-parallel, in-register peptide arrangement.

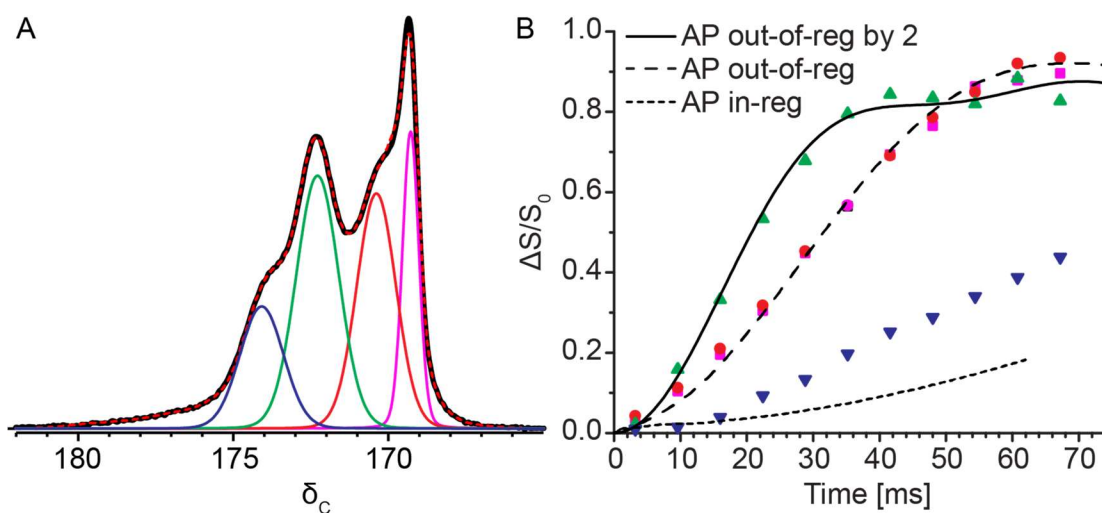


K16A forms homogeneous fibers on its own. However, unlike what was seen for Ac-K16A and Ac-K16A-Zn<sup>2+</sup> assemblies, a more diverse range of morphologies (i.e., fibers, twisted ribbons, helical ribbons and nanotubes) is evident by TEM when K16A is co-assembled with Zn<sup>2+</sup>, **Figure 3.14E, F, and G**. Furthermore, measurements of the width distributions attributed to each morphology suggests the possibility of a unique peptide arrangement for each morphology (**Figure 3.15F**). While this is not the first study of K16A-Zn<sup>2+</sup> assemblies ((Dong, Lu, Lakdawala, Mehta, & Lynn, 2006; Dong, Shokes, et al., 2006), we present the first structural description of each of the different morphologies identified. We also present an interpretation of the data that sheds light to the peptide assembly landscape accessible to K16A, initially discussed in **Chapter 2**.

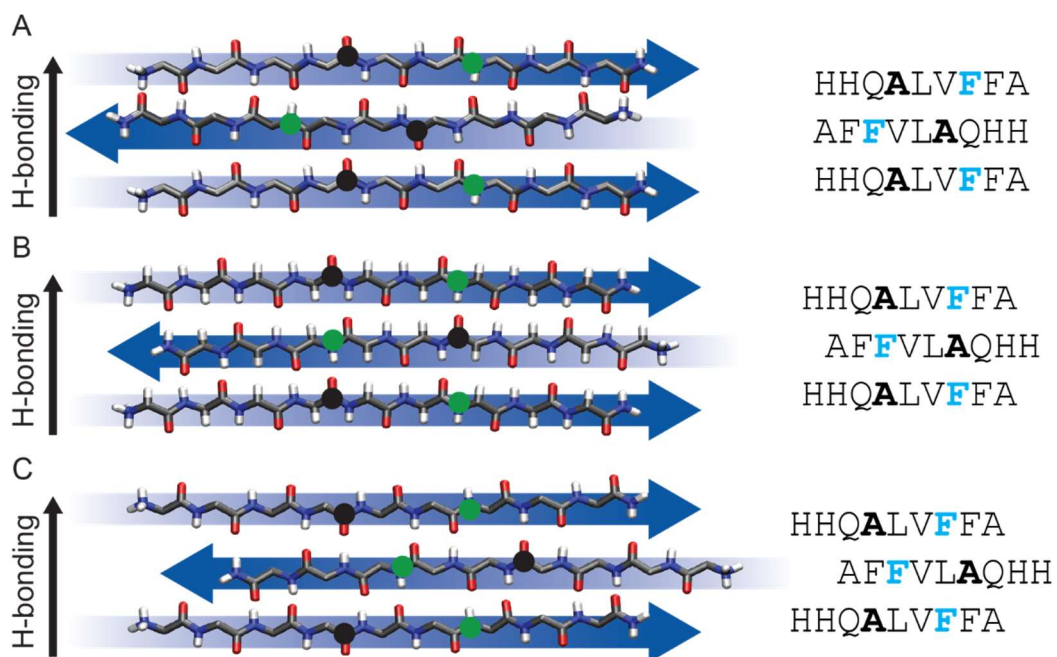
The CP-MAS NMR spectrum of K16A-Zn<sup>2+</sup> gives a broad spectrum associated with various carbonyl resonances (**Figure 3.17A**). From the CP-MAS NMR spectrum two distinct carbonyl resonances are evident, one at 169.3 ppm with a shoulder at 170.0 ppm, and one at 172.3 ppm with a shoulder at 173.9 ppm. To fit the data, four major populations are identified with resonances at 169.3 ppm (13%), 170.4 ppm (25%), 172.3 ppm (30%), and 174.1 ppm (15%) (**Figure 3.17A**). The deconvolution of populations provides insight into the diversity of peptide arrangement within the sample through a <sup>3</sup>C-<sup>15</sup>N dipolar recoupling <sup>13</sup>C{<sup>15</sup>N} Rotational-Echo Double-Resonance (<sup>13</sup>C{<sup>15</sup>N} REDOR) NMR experiment (Terry Gullion, 1998; T. Gullion & J. Schaefer, 1989). Indeed, several of the REDOR data points fit prediction curves, based on the peptide enrichment scheme, with a range of peptide-peptide arrangements. Each of the structures identified fit an antiparallel in-register peptide arrangement (**Figure 3.18A**), antiparallel out-of-register by one amino-acid peptide arrangement (**Figure 3.18B**), and an antiparallel out-of-

register by two amino-acids peptide arrangement (**Figure 3.18C**). Distances of the  $^{15}\text{N}$  from the adjacent carbonyls for the antiparallel, in-register system were fit to 7.9 Å ( $r_1$ ) and 8.9 Å ( $r_2$ ) with an angle between the two  $^{13}\text{C}$ - $^{15}\text{N}$  internuclear vectors of 68.0°. Distances of the  $^{15}\text{N}$  from the adjacent carbonyls for the antiparallel, out-of-register by one amino-acid system were fit to 5.7 Å ( $r_1$ ) and 6.1 Å ( $r_2$ ) with an angle between the two  $^{13}\text{C}$ - $^{15}\text{N}$  internuclear vectors of 105.6°. Distances of the  $^{15}\text{N}$  from the adjacent carbonyls for the antiparallel, out-of-register by two amino-acid system were fit to 4.1 Å ( $r_1$ ) and 5.3 Å ( $r_2$ ) with an angle between the two  $^{13}\text{C}$ - $^{15}\text{N}$  internuclear vectors of 160.0°. Of the four major populations, three distinct dephasing rates were observed, therefore three prediction REDOR curves were needed to fit the data. Thus, two of these populations shared the same peptide arrangement. **Figure 3.17B** displays the  $^{13}\text{C}\{^{15}\text{N}\}$  REDOR data and fits to antiparallel, out-of-register by one amino-acid and out-of-register by two amino-acids. The third population, antiparallel and in-register, did not fit the ideal model for an antiparallel and in-register system. At longer times, deviations from the ideal  $^{13}\text{C}\{^{15}\text{N}\}$  REDOR dephasing calculation emerged. We considered the possibility that this deviation could be attributed to the  $^{13}\text{C}$ - $^{13}\text{C}$  dipolar coupling contributions. When the peptides are antiparallel and in-register, the  $[1-^{13}\text{C}]\text{Ala}16$ 's reach a distance from one another that is not negligible, <9 Å. However, attempts to correct the fit by introducing  $^{13}\text{C}$ - $^{13}\text{C}$  contributions did not improve the fit within a reasonable range of distances (**Figure 3.19**). Therefore, we attribute the deviation of the  $^{13}\text{C}\{^{15}\text{N}\}$  REDOR data from the ideal fit to the presence of mutations within the antiparallel in-register structure. Optimizations of this fit, accounting for possible mutations, are currently underway. Taken together, these data highlight the morphological and structural diversity accessible

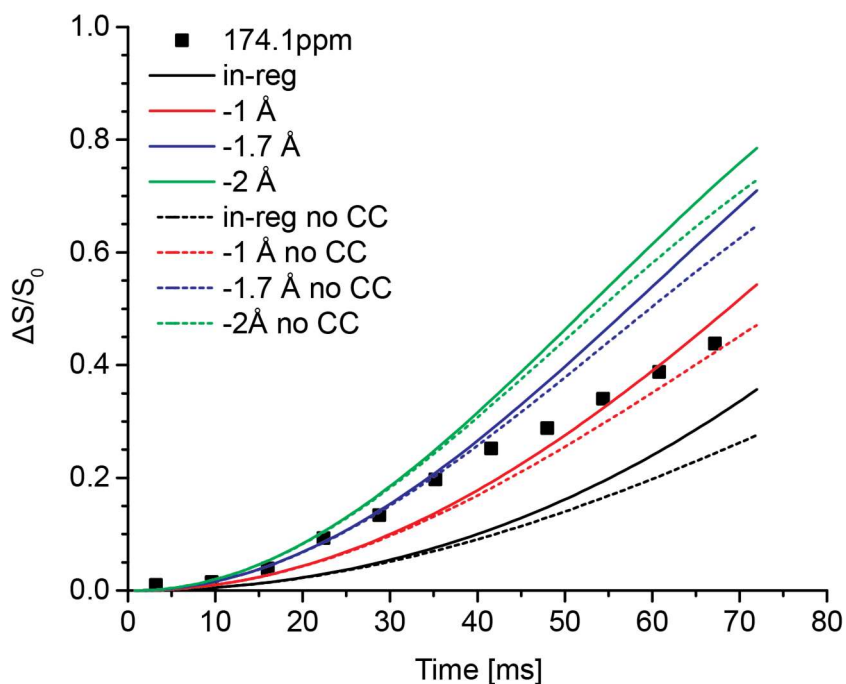
to a single peptide. Such structural information had not yet been demonstrated for the K16A-Zn<sup>2+</sup> assemblies.



**Figure 3.17– Solid-state NMR analysis of K16A-Zn<sup>2+</sup> nanostructures.** (A) CP-MAS NMR spectrum for K16A-Zn<sup>2+</sup> assemblies (black). Deconvolution needed to fit the experimental spectrum: population at 174.1 ppm (blue) makes up 15% of the sample, population at 172.3 ppm (green) makes up 30% of sample, population at 170.4 ppm (red) makes up 25% of the sample, population at 169.3 ppm (magenta) makes up 13% of sample. Dashed red line represents the sum of all contributions and the best fit. (B) Dashed lines show predicted <sup>13</sup>C{<sup>15</sup>N} REDOR dephasing line shapes, given the isotope enrichment model for each of the different peptide arrangements described (antiparallel in-register and antiparallel with registry shifts of one or two amino-acids). Data populations fit all conditions, with strong deviations from the ideal for the antiparallel in-register case which is attributed to mutations within this morphology.



**Figure 3.18 – Diversity of peptide arrangements identified by solid-state NMR in the  $[1-^{13}\text{C}]\text{Ala}16$ ,  $[^{15}\text{N}]\text{Phe}19$  K16A- $\text{Zn}^{2+}$  assemblies. (A) Antiparallel, in-register peptide arrangement. (B) Antiparallel, out-of-register by one amino-acid. (C) Antiparallel, out-of-register by two amino-acids.**



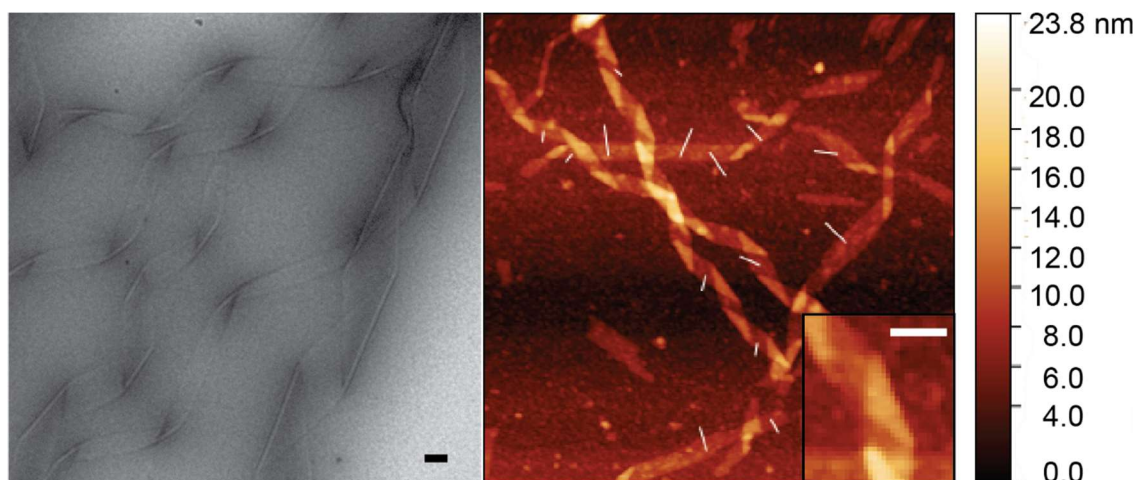
**Figure 3.19 – Fits to  $^{13}\text{C}\{^{15}\text{N}\}$  REDOR data for K16A-Zn $^{2+}$  antiparallel in-register population.** Data fits attempted by shifting  $^{13}\text{C}$ - $^{15}\text{N}$  distance from the ideal for antiparallel in-register peptide arrangement (solid lines). Data fits attempted by shifting  $^{13}\text{C}$ - $^{15}\text{N}$  distance from the ideal for antiparallel in-register peptide arrangement with the addition of  $^{13}\text{C}$ - $^{13}\text{C}$  dipolar coupling contributions, effects are strongest at longer times.

Given the preceding results and others (Dong, 2006; Dong, Shokes, et al., 2006), predictions can be made regarding the different structural assignments to the identified morphologies. Through X-ray absorption spectroscopy (XAS) experiments, specifically Extended X-ray absorption spectroscopy (EXAFS), Dong and co-workers demonstrated that a K16A-Zn $^{2+}$  mixture of fibers, ribbons, and nanotubes have either 3N(Im)/1O or 2N(Im)/2O coordination to Zn $^{2+}$ , where N(Im) refers to histidine imidazole coordination. While it was proposed that these species could exist without the presence of the other, we now propose that a mixture of these coordination environments is more likely given the

diversity of peptide arrangements – where the bis-His (2N(Im)/2O) and tris-His (3N(Im)/1O)  $Zn^{2+}$  coordination densities influence the degree of assembly accessible to the peptides. Such a mixture is likely assigned to the antiparallel out-of-register by one amino acid peptide arrangement or the antiparallel out-of-register by two amino acid peptide arrangement (attributed to ribbons and nanotubes), where at least one histidine side-chain is fully exposed and both His13 and His14 are accessible to participate in  $Zn^{2+}$  binding. The degree of incorporation may be ratio dependent. Dong and co-workers conducted a study in which they found that in the presence of substoichiometric  $Zn^{2+}$ , fibers and twisted ribbons emerged. With increasing  $[Zn^{2+}]$ , however, helical ribbons and nanotubes were evident. EXAFS of these assemblies revealed that at increasing concentrations of  $Zn^{2+}$  a distortion in the  $Zn^{2+}$  coordination environment became prevalent, suggesting the development of a new arrangement of peptides. Given these results, the observed morphological transitions and the structural data herein presented, it is likely that with increasing  $[Zn^{2+}]$  higher concentrations of tris-His develop facilitating intersheet interactions that promote the tris-His coordination driving a shift in peptide registry. Furthermore, atomic force microscopy (AFM) data shows the presence of monolayer and bilayer structures between ribbons of different sizes in a grid with heights measuring  $3.29 \pm 0.23$  nm and  $6.29 \pm 0.73$  nm (**Figure 3.20**). If intersheet interactions expand to interleaflet interactions with increasing concentrations of  $Zn^{2+}$ , this could explain the formation of larger structures with a new coordination environment around  $Zn^{2+}$  and the evolution of a higher density of tris-His in the sample mixture. Indeed,  $Zn^{2+}$  incorporation is more constrained for the antiparallel, in-register, peptide arrangement. We propose that in this arrangement, His13 and His14 may only bind across laminates

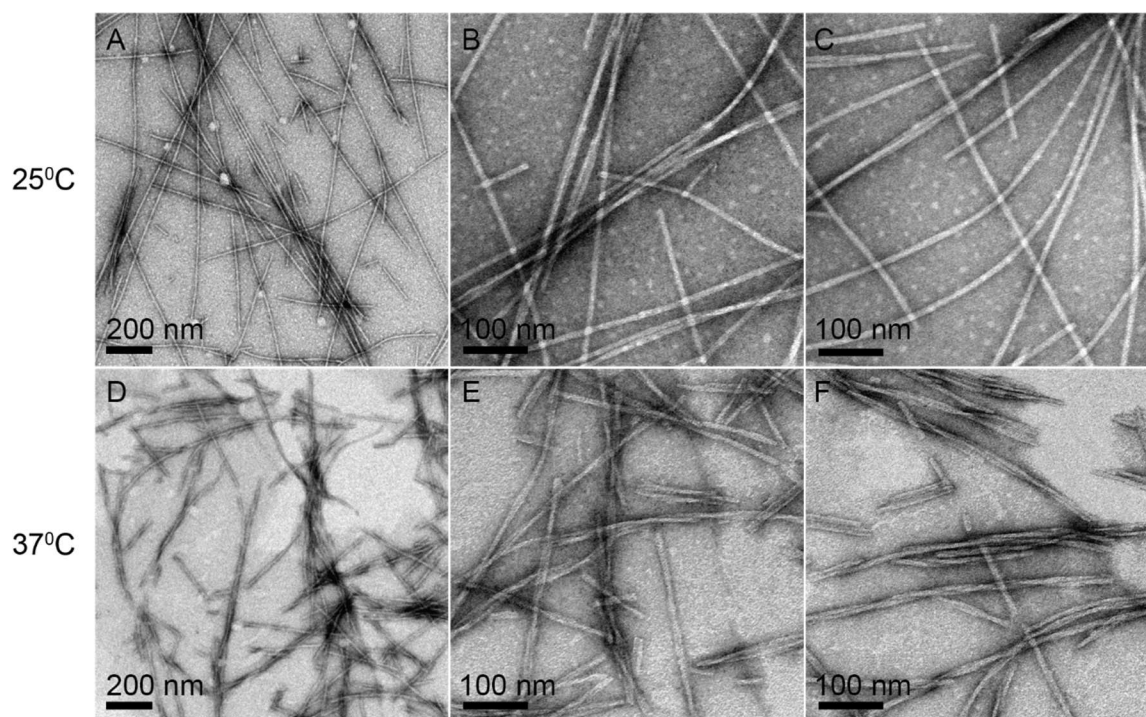
giving a lone population of 2N(Im)/2O that stabilizes this antiparallel peptide arrangement. Of note, the formation of the anti-parallel, in-register peptide arrangement with K16A was first identified in **Chapter 2** (pg.28) for oligomeric particles. We now propose that  $Zn^{2+}$  serves as a stabilizing ion at the assembly nucleus interacting with the peptides between laminates.

Taken together, these results shed light on our understanding of the assembly landscape accessible to K16A. When  $Zn^{2+}$  is co-assembled with the K16A peptide, multiple peptide arrangements emerge, some that were undetectable before our structural analysis of the oligomeric particles described in **Chapter 2**. Within the peptide arrangements characterized in this section, one can be immediately correlated to the peptide arrangement assigned to the oligomeric particles. In these supramolecular assemblies, a kinetically formed nucleus was successfully propagated in the presence of  $Zn^{2+}$ , positioning the  $Zn^{2+}$  interactions in the oligomeric nucleus. While it is possible that the registry shift that exists in the other two peptide arrangements (out-of-register by one and out-of-register by two amino-acids) was driven by  $Zn^{2+}$  alone, it is just as likely that the two other arrangements identified could be other accessible conformations to K16A in its assembly landscape that were kinetically trapped due to the accessibility of  $Zn^{2+}$  in the peptide assembly timeline. Indeed, we have shown that  $Zn^{2+}$  is unable to drive a registry shift on preassembled K16A fibers, suggesting that initial interactions with the histidine side-chains at the assembly on-set are critical to drive a registry shift that facilitates the insulation of the metal from the external environment (**Figure 3.21**). To explore this further, we turn to the supramolecular assemblies formed with Ac-K16A and K16A in the presence of  $Cu^{2+}$ .



**Figure 3.20 – TEM and AFM images of K16A-Zn<sup>2+</sup> assemblies.** Morphologies captured have a diversity of size and helicity, measurements of these structures gave two distinct distributions at  $3.29 \pm 0.23$  nm and  $6.29 \pm 0.73$  nm, where a single peptide extends  $\sim 3.2$  nm, demonstrating the existence of monolayer and bilayer environments. Measurements were done only on single layer sections of the ribbons and are highlighted on the AFM image. Scale bar = 100 nm.





**Figure 3.21 – Morphological effects of Zn<sup>2+</sup> addition to preassembled K16A fibers.**

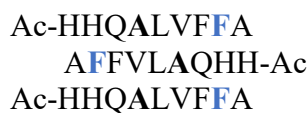
Transmission electron micrographs of K16A fibers assembled at room temperature (A) and 37°C (D). Fibers were incubated with ZnCl<sub>2</sub>, post-assembly, for a period of 2 weeks at room temperature (B and C) as well as 37°C (E and F) – no morphological transition is observed.

### Structure and stability of Ac-K16A-Cu<sup>2+</sup> and K16A-Cu<sup>2+</sup> MANs

Motivated by the homogeneity of the assemblies that form in the presence of Cu<sup>2+</sup>, with both Ac-K16A and K16A (**Figure 3.23**), we sought to learn more about their structure and stability. Indeed, given their morphological similarities we reasoned that their underlying peptide arrangement would be comparable. We also hypothesized that given the results seen for co-assemblies with Zn<sup>2+</sup> regarding apparent stage of incorporation of the metal ion in the K16A co-assemblies, it is likely that Cu<sup>2+</sup> will also be incorporated at the oligomeric stage, the stage where the nucleus to be propagated is selected.

First, we looked to FT-IR to assign constraints on possible peptide arrangements, as this would help in the design of peptides to be prepared for structural analysis. FT-IR in **Figure 3.23** has the  $\beta$ -sheet diagnostic Amide I band at 1626 cm<sup>-1</sup> for both Ac-K16A and K16A co-assemblies with Cu<sup>2+</sup> but, while the Ac-K16A-Cu<sup>2+</sup> assemblies appear to have a second Amide I band at 1694 cm<sup>-1</sup> – diagnostic of an antiparallel peptide arrangement – K16A-Cu<sup>2+</sup> assemblies do not display this peak. The absence of this band for K16A-Cu<sup>2+</sup> ribbons could be due to the large content of free monomer in solution represented by the broad band with a peak at 1674 cm<sup>-1</sup>, or to a parallel arrangement of the peptides. To assess both possibilities, Ac-K16A and K16A were enriched at Ala16/Phe20 and Ala16/Phe19, respectively, to give Ac-HHQ[1-<sup>13</sup>C]ALVF[<sup>15</sup>N]FA-NH<sub>2</sub> and H-HHQ[1-<sup>13</sup>C]ALV[<sup>15</sup>N]FFA-NH<sub>2</sub> for solid-state NMR experiments. The thoughtful design behind this enrichment schemes allowed us to distinguish between a parallel and anti-parallel peptide arrangement as well as an in-register and out-of- register arrangement (with either one, two or three residue shifts).

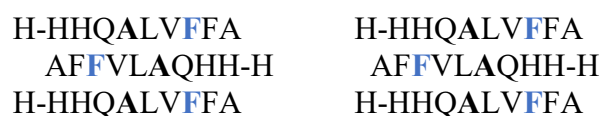
The CP-MAS NMR spectra for Ac-K16A-Cu<sup>2+</sup> and K16A-Cu<sup>2+</sup> show a single peptide arrangement population (**Figure 3.24A and B**) for both peptide assemblies. Insight into the specific peptide arrangement for the Ac-K16A-Cu<sup>2+</sup> ribbons was gained by a <sup>13</sup>C-<sup>15</sup>N dipolar recoupling <sup>13</sup>C{<sup>15</sup>N} Rotational-Echo Double-Resonance (<sup>13</sup>C{<sup>15</sup>N} REDOR) NMR experiment (Terry Gullion, 1998; T. Gullion & J. Schaefer, 1989). The distance of the H-bonded <sup>15</sup>N's from the adjacent carbonyls was fit to 4.4 Å (r<sub>1</sub>) and the distance to the non-H-bonded <sup>15</sup>N's was fit to 5.1 Å (r<sub>2</sub>) with an angle between the two <sup>13</sup>C-<sup>15</sup>N internuclear vectors of 153.0°. Fits to the <sup>13</sup>C{<sup>15</sup>N} REDOR data show strong agreement with an organization to a single population of antiparallel β-strands, out-of-register by two amino-acids:



In this organization, the histidine side-chains are maximally exposed for Cu<sup>2+</sup> binding. Compared the Ac-K16A-Zn<sup>2+</sup> assemblies which forms fibers that are antiparallel, in-register, the antiparallel, out-of-register by two amino-acid rearrangement of the ribbons suggests a Cu<sup>2+</sup> driven registry shift. This can be explained by the higher binding affinity of Cu<sup>2+</sup> toward biological ligands when compared to Zn<sup>2+</sup>, which follows the Irving-Williams series (Foster et al., 2014; Masuoka & Saltman, 1994), as described in an earlier section of this chapter. Thus, once a template for growth is formed in the presence of Cu<sup>2+</sup>, it becomes difficult for a mutation to propagate outside the defined framework.

Given the results obtained for Ac-K16A-Cu<sup>2+</sup> ribbons, we considered that a similar peptide arrangement was likely for K16A + Cu<sup>2+</sup> co-assemblies. Insight into the specific peptide arrangement for the K16A-Cu<sup>2+</sup> ribbons was gained by a <sup>13</sup>C{<sup>15</sup>N}

REDOR NMR experiment (Terry Gullion, 1998; T. Gullion & J. Schaefer, 1989). The distance of the H-bonded  $^{15}\text{N}$ 's from the adjacent carbonyls was fit to 4.4 Å ( $r_1$ ) and the distance to the non-H-bonded  $^{15}\text{N}$ 's was fit to 5.1 Å ( $r_2$ ) with an angle between the two  $^{13}\text{C}$ - $^{15}\text{N}$  internuclear vectors of 153.0°. Fits to the  $^{13}\text{C}\{^{15}\text{N}\}$  REDOR data show strong agreement with an organization of antiparallel  $\beta$ -strands, though the registry of the peptide arrangement is not as readily defined:

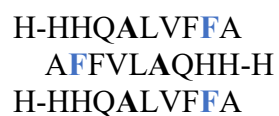


In both arrangements, the distance between  $[1-^{13}\text{C}]\text{Ala}16$  and  $[^{15}\text{N}]\text{Phe}19$  is the same, giving identical results in a  $^{13}\text{C}\{^{15}\text{N}\}$  REDOR experiment. The peptide enrichment sites were designed to help distinguish between these two arrangements by running a  $^{13}\text{C}$  Double-quantum Filtered DRAWS (DQF-DRAWS) experiment, which is used to measure the dipolar coupling between  $^{13}\text{C}$  isotopes. This same experiment helped in the determination of the peptide arrangement for the K16A particles (pg. 28). Because dipolar coupling between nuclei is proportional to the distance between the isotopes as  $1/r^3$ , as the distance between  $[1-^{13}\text{C}]\text{Ala}16$  isotopes increases the dipolar coupling will decrease – reaching a limit at  $\sim 9$  Å distance. Thus, we expected to be able to observe the double quantum buildup for the antiparallel, in-register assemblies, as the  $[1-^{13}\text{C}]\text{Ala}16$ 's are positioned within measurable distances from each other. However, the DQF-DRAWS experiment of the isotope enriched K16A- $\text{Cu}^{2+}$  twisted ribbons yielded no signal, not even background signal. Because data is dependent on the magnetization and magnetization transfer between nuclei in the sample, it is possible that the proximal position to the paramagnetic  $\text{Cu}^{2+}$  reduced the  $T_2$  lifetime (spin-spin relaxation) of the

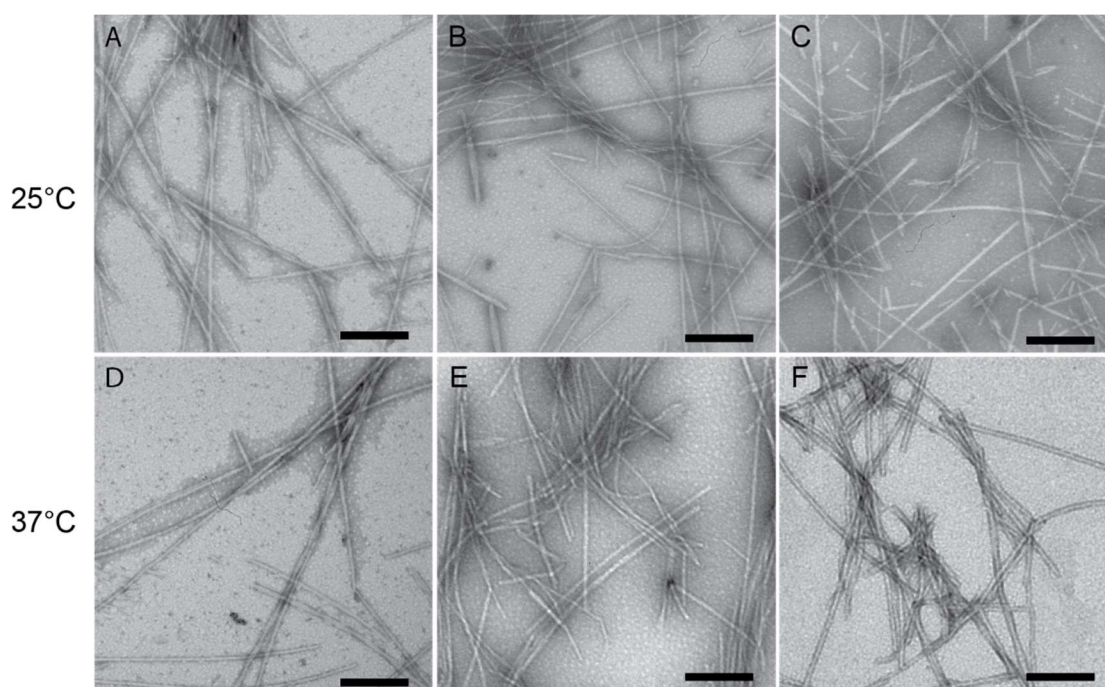
sample and no signal was readily observed. The presence of the paramagnetic  $\text{Cu}^{2+}$  could explain the absence of any background signal as well. In sum, data suggests that the twisted ribbons certainly incorporate a high density of copper and the peptides are organized in an antiparallel arrangement, distinct from the metal-free fibers which come together in a parallel fashion.

Given the high density of  $\text{Cu}^{2+}$  incorporated we hypothesize that a maximal number of ligand contacts should be available. We have already presented that in the antiparallel in-register organization of peptides, His14 is buried within the assembly, inaccessible to coordination, and His13's are separated by 1 nm, a distance too large to facilitate  $\text{Mn}^{2+}$  chelation along a  $\beta$ -sheet. Furthermore, if intersheet interactions stabilize the  $\text{Cu}^{2+}$  within the morphology in question, this would be done following a bis-His coordination environment. **Figure 3.10** shows the blue shift of  $\text{Cu}^{2+}$  when coordinated with K16A. Such a blue shift can be assigned to a coordination environment of  $3\text{N}(\text{Im})/1\text{O}$  (Sigel & Martin, 1982), suggesting intersheet and interleaflet contributions as discussed for K16A- $\text{Zn}^{2+}$  helical ribbons and nanotubes. To define whether these structures form a monolayer, bilayer, or a multilamellar structure we turn to AFM. AFM can map the height of precipitated material on a silicon wafer by measuring the vertical deflections of a cantilever tip using an optical lever which operates based on a reflected laser beam whose position change as the cantilever tip moves across a surface. Thus, information about the angular deflection reports directly on the distance of cantilever motion. Using this technique, the height of the Ac-K16A- $\text{Cu}^{2+}$  ribbons was determined to be  $6.36 \pm 0.48$  nm (**Figure 3.26**), and the height of the K16A- $\text{Cu}^{2+}$  ribbons was determined to be  $5.07 \pm 0.77$  nm (**Figure 3.27**). Given this data, and knowing that a

single peptide extends approximately 3.2 nm in length, we propose that the ribbons form bilayers which fits our current understanding of ribbon forming amyloids. Such interactions favor the antiparallel, out-of-register by two peptide arrangement. Thus, we are confident the peptide arrangement is antiparallel, out-of-register by two amino-acids:

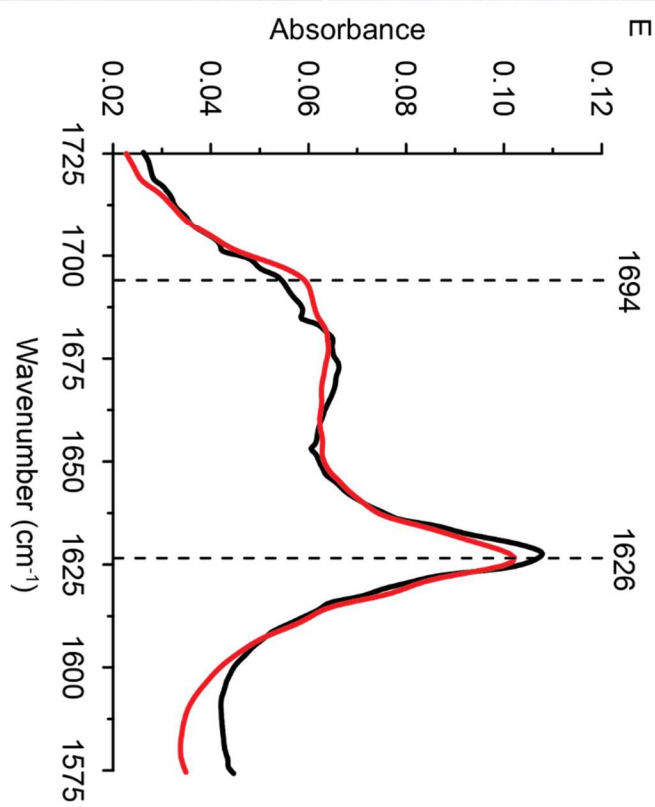
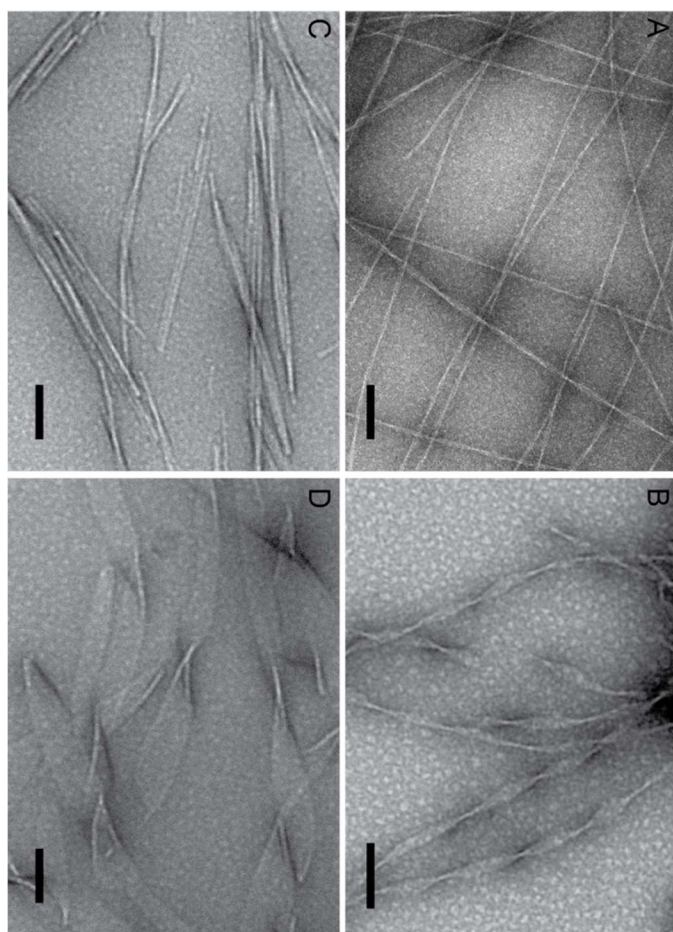


More evidence to demonstrate this assignment is given in **Chapter 4**.



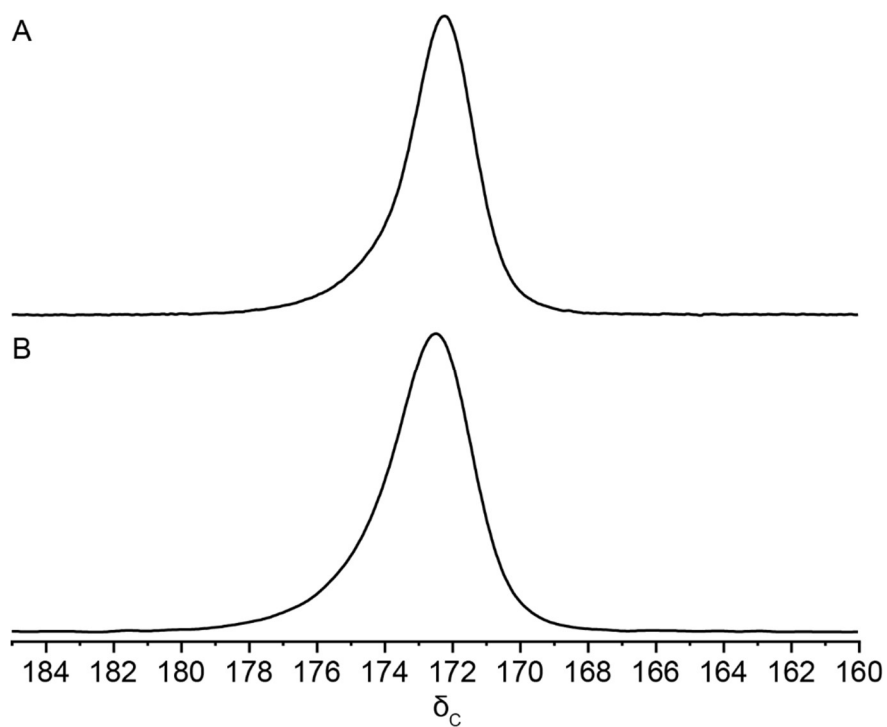
**Figure 3.22 – Morphological effects of  $\text{Cu}^{2+}$  addition to preassembled K16A fibers.**

Transmission electron micrographs of K16A fibers assembled at room temperature (A) and 37°C (D). Fibers were incubated with  $\text{CuCl}_2$ , post-assembly, for a period of 2 weeks at room temperature (B and C) as well as 37°C (E and F) – no morphological transition is observed.



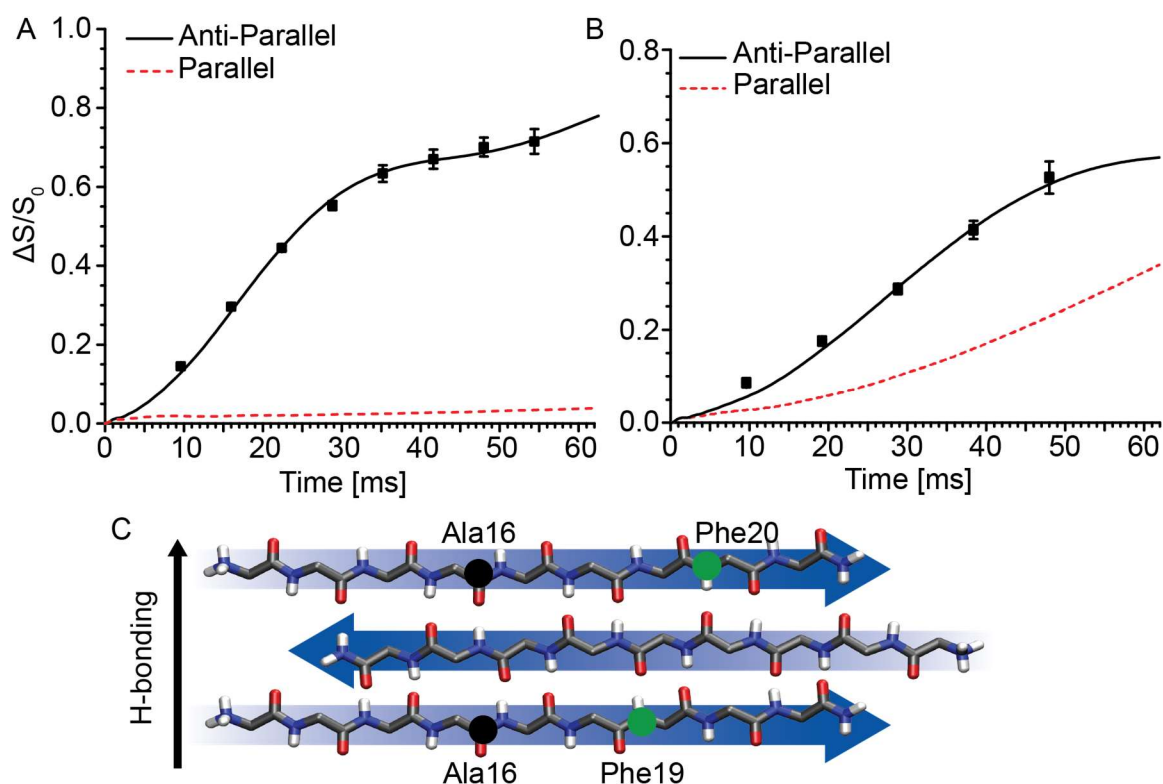
**Figure 3.23 – TEM micrographs and FT-IR of K16A and Ac-K16A in the absence and presence of Cu<sup>2+</sup>.** TEM micrographs of 1 mM K16A fibers (A), K16A + CuCl<sub>2</sub> ribbons (B), Ac-K16A fibers (C), and Ac-K16A + CuCl<sub>2</sub> ribbons (D). FT-IR of K16A (black) and Ac-K16A (red) ribbons. Peptide and CuCl<sub>2</sub> concentrations are 1 mM for all assembly conditions. Amide I band at 1626 cm<sup>-1</sup> is consistent with β-sheet rich assembly and the small band at 1694 cm<sup>-1</sup> for Ac-K16A ribbons suggests peptide organization could be anti-parallel. This band is not readily observed for K16A ribbons, but the possibility of an antiparallel peptide arrangement is not discounted.



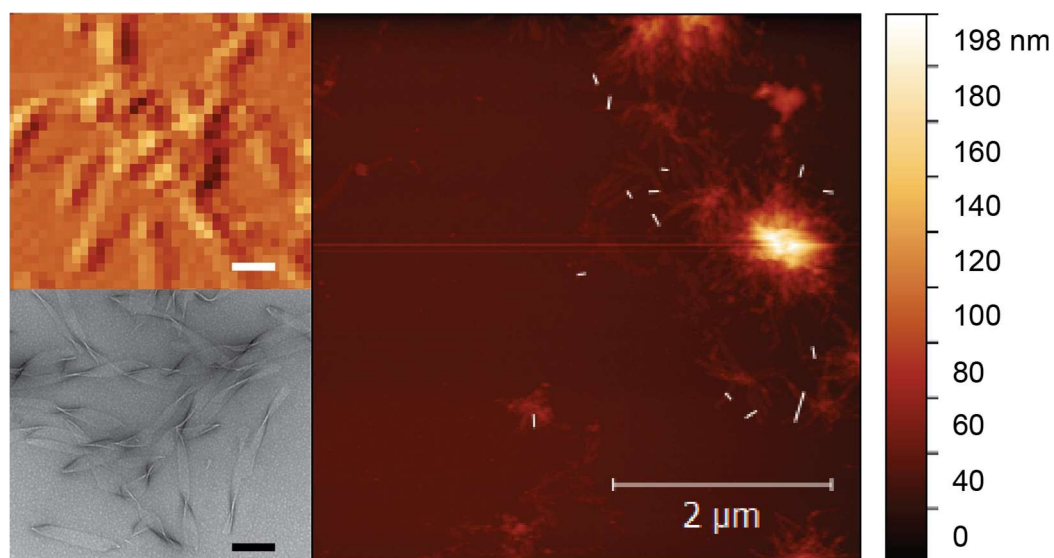


**Figure 3.24 – CP-MAS NMR spectra of Ac-K16A and K16A in the presence of  $\text{Cu}^{2+}$ .**

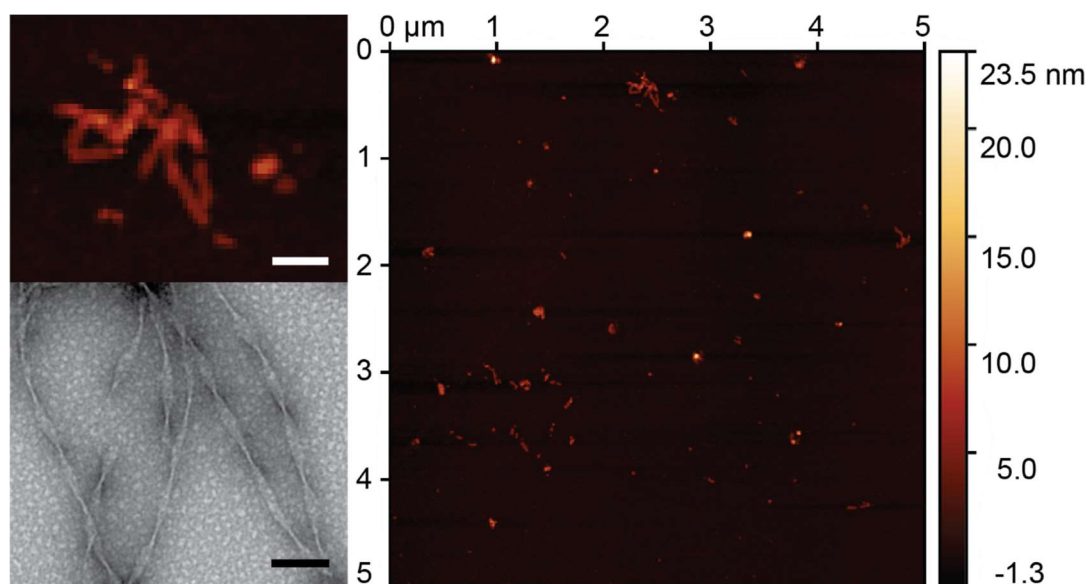
(A) Ac-HHQ[1- $^{13}\text{C}$ ]ALVF[ $^{15}\text{N}$ ]FA-NH $_2$  (Ac-K16A) +  $\text{Cu}^{2+}$ , fit to a single population,  $\delta_c = 172.2$  ppm. (B) H-HHQ[1- $^{13}\text{C}$ ]ALV[ $^{15}\text{N}$ ]FFA-NH $_2$  (K16A) +  $\text{Cu}^{2+}$ , fit to a single population,  $\delta_c = 172.6$  ppm.



**Figure 3.25** –  $^{13}\text{C}\{^{15}\text{N}\}$  REDOR dephasing curves for Ac-K16A-Cu $^{2+}$  and K16A-Cu $^{2+}$  ribbons. (A) The  $^{13}\text{C}\{^{15}\text{N}\}$  REDOR data for Ac-HHQ[1- $^{13}\text{C}$ ]ALVF[ $^{15}\text{N}$ ]F $^{20}$ A-NH $_2$  + Cu $^{2+}$  (Ac-K16A-Cu $^{2+}$ ) ribbons is fit by an ideal REDOR dephasing curve for an anti-parallel out-of-register by two amino-acids model, where the Ala16's and Phe20's are directly above the other along a H-bonded  $\beta$ -sheet. (B) The  $^{13}\text{C}\{^{15}\text{N}\}$  REDOR data for H-HHQ[1- $^{13}\text{C}$ ]ALV[ $^{15}\text{N}$ ]F $^{19}$ FA-NH $_2$  + Cu $^{2+}$  (K16A-Cu $^{2+}$ ) ribbons is fit by an ideal REDOR dephasing curve that could represent an antiparallel out-of-register by two amino-acids model as well as an antiparallel in-register model. An out-of-register by two arrangement maximizes access to the histidine side-chains. (C) Cartoon representation of the out-of-register by two amino-acid  $\beta$ -sheet. Top  $\beta$ -strand enrichment assignment is assigned to panel (A). Bottom  $\beta$ -strand enrichment assignment is assigned to panel (B).



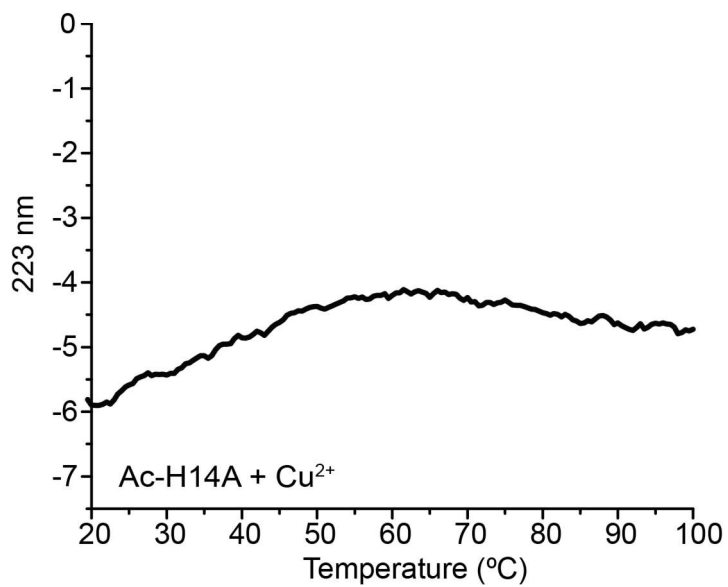
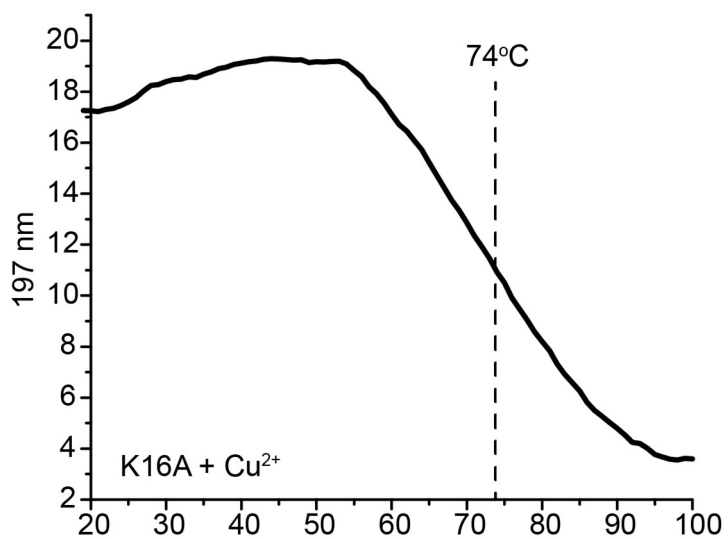
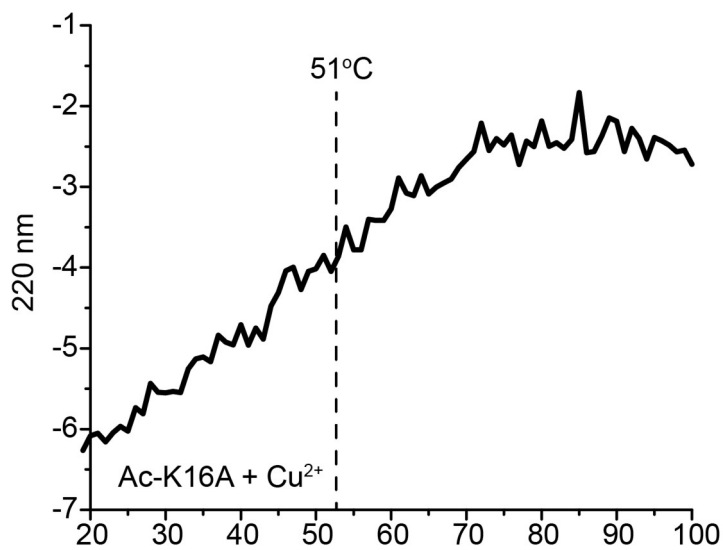
**Figure 3.26 – AFM of Ac-K16A-Cu<sup>2+</sup> ribbons.** Atomic force microscopy (AFM) measurements of the Ac-K16A ribbons  $6.36 \pm 0.48$  demonstrate that these ribbons form bilayer assemblies. Scale bar of rescaled AFM and TEM images = 100 nm.



**Figure 3.27– AFM of K16A-Cu<sup>2+</sup> ribbons.:** Atomic force microscopy (AFM) measurements of the K16A ribbons  $5.07 \pm 0.77$  nm demonstrate that these ribbons form bilayer assemblies. Scale bar of rescaled AFM and TEM images = 100 nm.

Next, we assessed the stability of the Ac-K16A-Cu<sup>2+</sup> ribbons and the K16A-Cu<sup>2+</sup> ribbons by following the change in CD absorbance intensity for diagnostic  $\beta$ -sheet ellipticities. **Figure 3.28** shows the results; relative to Ac-H14A-Cu<sup>2+</sup> fibers which do not lose their  $\beta$ -sheet character up to 100°C, the relative stability follows: Ac-H14A-Cu<sup>2+</sup> ( $T_{1/2} = >100^\circ\text{C}$ ) > K16A + Cu<sup>2+</sup> ( $T_{1/2} = 74^\circ\text{C}$ ) > Ac-K16A + Cu<sup>2+</sup> ( $T_{1/2} = 51^\circ\text{C}$ ). Taken together, this data suggests that K16A + Cu<sup>2+</sup> may yield the most flexibility in terms of material survivability with environment modulation as it relates to temperature. The free N-terminus may play a critical role in this flexibility and may facilitate structural rearrangement in reactivity studies.

Following, we explore the electrochemistry of both Ac-K16A-Cu<sup>2+</sup> and K16A-Cu<sup>2+</sup>. Results are compelling, and they have helped us select for a single structure to fully characterize as a potential MAN with accessible function. We explore the material's reduction/oxidation reversibility, reduction potential and results show that our material shares characteristics with blue copper proteins.



**Figure 3.28 – Melting curves for Ac-K16A-Cu<sup>2+</sup>, K16A-Cu<sup>2+</sup> and Ac-H14A-Cu<sup>2+</sup>.**

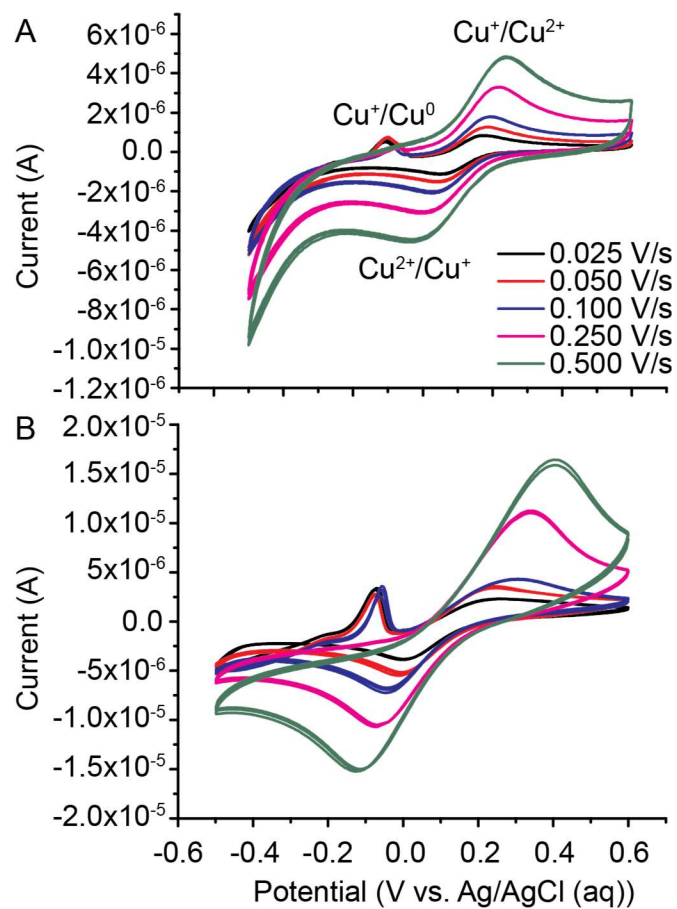
Melting curves monitoring different structural ellipticities for Ac-K16A-Cu<sup>2+</sup> ribbons (top), K16A-Cu<sup>2+</sup> ribbons (middle) and Ac-H14A-Cu<sup>2+</sup> fibers (bottom). Plotted data is displayed in order of stability, lowest to highest, from top to bottom respectively. Ac-K16A-Cu<sup>2+</sup> ribbons have a  $T_{1/2}$  of 51°C, K16A-Cu<sup>2+</sup> ribbons have a  $T_{1/2}$  of 74°C and H14A-Cu<sup>2+</sup> fibers do not melt within the plotted temperature, up to 100°C.

### Reversibility of $\text{Cu}^{2+}/\text{Cu}^+$ cycle in Ac-K16A- $\text{Cu}^{2+}$ and K16A- $\text{Cu}^{2+}$ MANs

To assess the reactivity of these materials, we measured their reversibility and reduction potential by cyclic voltammetry (CV). **Figure 3.29** shows the cyclic voltammograms collected for K16A- $\text{Cu}^{2+}$  ribbons (A) and Ac-K16A- $\text{Cu}^{2+}$  ribbons (B). All experiments were done following a descending potential, where the initial step was the reduction of  $\text{Cu}^{2+}$  to  $\text{Cu}^+$ , represented by the cathodic wave. This initial reduction was followed by an irreversible disproportionation reduction for  $\text{Cu}^+$  to  $\text{Cu}^0$  (seen around -0.107 V vs. Ag/AgCl for K16A and -0.077 V vs. Ag/AgCl for Ac-K16A). The disproportionation step was followed by the anodic wave corresponding to the oxidation of  $\text{Cu}^+$  to  $\text{Cu}^{2+}$ . Both voltammograms share these features, though the disproportionation wave is less obvious for K16A- $\text{Cu}^{2+}$  ribbons. From these voltammograms we can make an initial assessment on the reversibility of the reduction cycle. In the case of our nanostructures, the change in  $\Delta E_p$  with scan rate is diagnostic of quasi-reversibility (M. Mital et al., 2016; Wiloch et al., 2016), these values are summarized in **Table 3.2**. Of note, K16A ribbons have a much lower  $\Delta E_p$  across the different scan rates than Ac-K16A ribbons. This suggests that K16A ribbons display improved reversibility and potential to serve as an electron conductor, because the electron transfer kinetics are faster, resulting in lower deviations with increasing scan rate. It is possible that Ac-K16A, once reduced, has slower oxidation kinetics because the  $\text{Cu}^+$  complex is more stable within the Ac-K16A architecture. It is also possible that upon reduction the material falls apart, due to low stability of the material. The electrochemical characteristics associated with K16A- $\text{Cu}^{2+}$  will be explored in more detail in **Chapter 4**.

Reversibility can also be studied by plotting  $i_p$  vs.  $(v)^{1/2}$ , where  $v$  = scan rate. This plot is known as the Randles-Sevcik plot. A fully linear fit would represent a fully reversible system. **Figure 3.30** shows the Randles-Sevcik plots for the anodic and cathodic waves seen at different scan rates for K16A-Cu<sup>2+</sup> ribbons (A) and Ac-K16A-Cu<sup>2+</sup> ribbons (B). The data deviates from linearity. K16A-Cu<sup>2+</sup> has  $r^2$  values of 0.87 and 0.89 and Ac-K16A-Cu<sup>2+</sup> has  $r^2$  values of 0.95 and 0.93. Indeed, we can also look at the current ratios to assess the reversibility of the system. In the fully reversible system,  $i_{pa}/i_{pc} = 1$ . However, while values approach 1 for the K16A-Cu<sup>2+</sup> material the deviations are much larger for Ac-K16A-Cu<sup>2+</sup> assemblies, values are summarized in **Table 3.2**. This data reaffirms that K16A-Cu<sup>2+</sup> ribbons might serve as the best candidate for making a functional MAN.



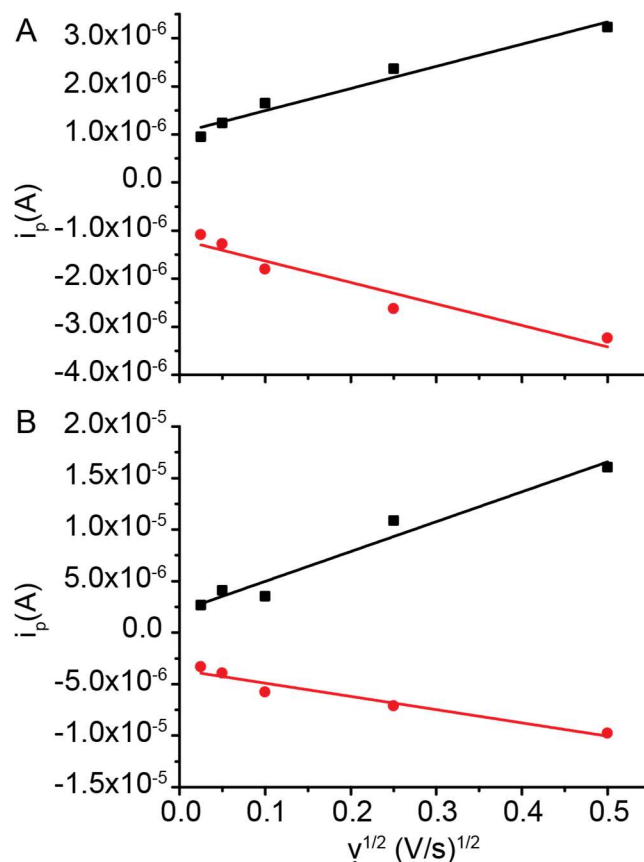


**Figure 3.29 – Cyclic voltammograms of K16A-Cu<sup>2+</sup> and Ac-K16A-Cu<sup>2+</sup> over different scan rates.** Cyclic voltammograms of 1 mM K16A + 1 mM CuCl<sub>2</sub> (A) as well as 1 mM Ac-K16A + 1 mM CuCl<sub>2</sub> (B). (A) Ribbons assembled in the presence of the supporting electrolyte, 100 mM NaCl. (B) Ribbons assembled in the presence of the supporting electrolyte 100 mM NaCl.

**Table 3.2 – Electrochemical properties of K16A-Cu<sup>2+</sup> and Ac-K16A+Cu<sup>2+</sup> MANs.**

Summary of values determined from cyclic voltammetry experiments with K16A + Cu<sup>2+</sup> and Ac-K16A + Cu<sup>2+</sup> MANs:

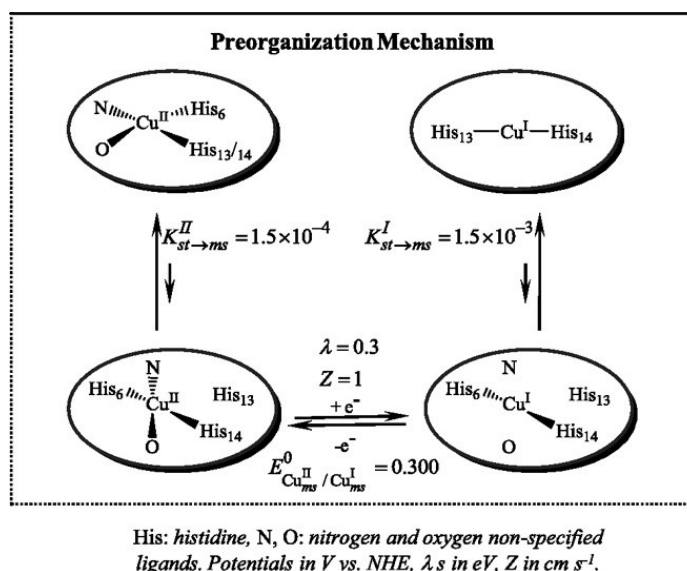
<b>Assembly Conditions</b>	<b>Scan Rate (V/s)</b>	<b><math>i_{pa}/i_{pc}</math></b>	<b><math>\Delta E_p</math> (mV)</b>	<b><math>E_{1/2}</math> vs. RHE (mV)</b>
K16A				
	0.025	1.15	122.86	+ 680.52
	0.050	1.03	143.12	+ 680.56
	0.100	1.10	167.97	+ 678.06
	0.250	1.11	213.54	+ 675.44
	0.500	1.00	269.19	+ 667.86
Ac-K16A				
	0.025	1.25	253.71	+ 695.77
	0.050	0.97	253.79	+ 690.65
	0.100	1.63	349.22	+ 698.26
	0.250	0.66	404.71	+ 700.68
	0.500	0.61	516.18	+ 710.69



**Figure 3.30 – Randles-Sevcik plots for K16A-Cu<sup>2+</sup> and Ac-K16A-Cu<sup>2+</sup> ribbons.**

Randles-Sevcik plots for the anodic (black) and cathodic (red) currents measured for 1 mM K16A + 1 mM CuCl<sub>2</sub> (A) and 1 mM Ac-K16A + 1 mM CuCl<sub>2</sub> (B) across different scan rates (0.025, 0.050, 0.100, 0.250 and 0.500 V/s). (B) K16A ribbons assembled in the presence of the supporting electrolyte, 100 mM NaCl, fit with a Pearson's  $r$  value of 0.95 and -0.96 and an  $r^2$  value of 0.87 and 0.89, respective to the anodic and cathodic fits. (B) Ac-K16A ribbons assembled in the presence of the supporting electrolyte 100 mM NaCl, fit with a Pearson's  $r$  value of 0.98 and -0.97 and an  $r^2$  value of 0.95 and 0.93, respective to the anodic and cathodic fits.

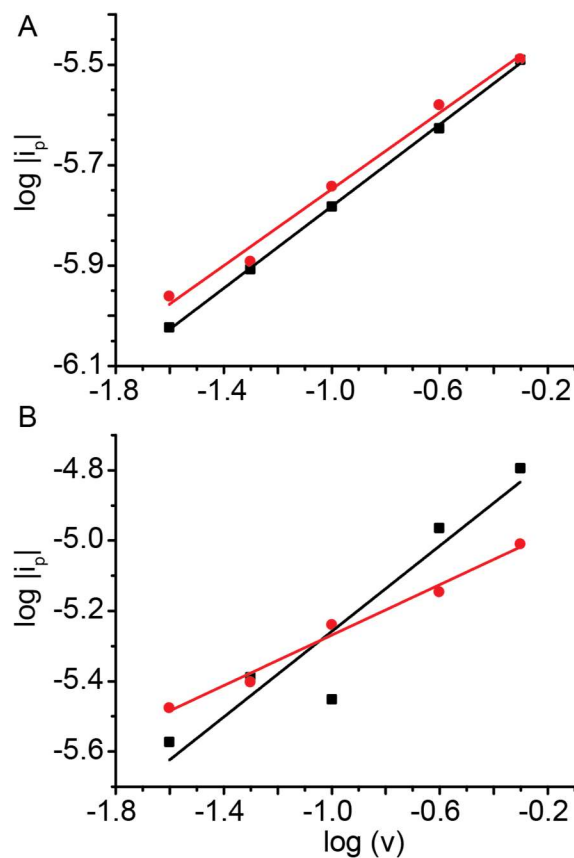
More studies need to be carried out to dissect the mechanism of reduction occurring with this material. Previous research on AD and amyloid- $\beta$  copper complexes have attempted to do just that (Balland, Hureau, & Saveant, 2010). For these complexes, a preorganization electron transfer (POET) mechanism has been proposed (**Figure 3.31**). In the POET mechanism, small fractions of  $\text{Cu}^{2+}(\text{A}\beta)$  and  $\text{Cu}^+(\text{A}\beta)$  complexes are said to adopt similar structures which results in a small electron transfer reorganization energy. Researchers further proposed that these  $\text{Cu}^{2+}$  and  $\text{Cu}^+$  preorganized metastable states are in continuous and rapidly established equilibrium with the corresponding  $\text{Cu}^{2+}$  and  $\text{Cu}^+$  predominant (stable) forms – this allows for the minimal reorganization energy by these structures. The work done by Balland and co-workers provides compelling evidence to support their model. Given the similarities between their peptide sequence and ours, it may be a good point of collaboration as we seek to understand the mechanism of electron transfer for our MAN. This mechanism is further considered in **Chapter 4**.



**Figure 3.31 – Preorganization electron transfer mechanism (POET).** (Reprinted from (Balland et al., 2010) with permission of PNAS publication)

**Figure 3.1** plots  $\log |i_p|$  vs.  $\log (v)$ , where  $v$  = scan rate. It has been demonstrated that in theory, a slope of 0.5 is assigned to a pure diffusion controlled processes whereas a slope of 1 can be assigned to a pure adsorption controlled process and, between that range, an adsorption-diffusion mixture can be observed. In practice, the range for pure diffusion, pure adsorption and the adsorption-diffusion mixed processes are given as 0.20 – 0.60, 0.75 – 1.10 and 0.60 – 0.75, respectively (Gupta, Guin, & Aggarwal, 2012).

While the plots of  $\log |i_p|$  vs.  $\log (v)$  shown in **Figure 3.32A** over the different concentrations, demonstrate that the electrochemical reactions of  $\text{Cu}^{2+}/\text{Cu}^+$  and  $\text{Cu}^+/\text{Cu}^{2+}$  coupled onto the glassy carbon electrode in 25 mM MES + 100 mM NaCl solution are diffusion controlled with slope values ranging from 0.41 ( $r^2 = 0.99$ ) to 0.38 ( $r^2 = 0.99$ ). In contrast, the plots of  $\log |i_p|$  vs.  $\log (v)$  shown in **Figure 3.32B** are not diffusion controlled with slope values ranging from 0.61 ( $r^2 = 0.86$ ) to 0.36 ( $r^2 = 0.98$ ). This data, again, confirms that the material to assess for functional applications is the K16A- $\text{Cu}^{2+}$  ribbons. Studies aimed at understanding the degree of  $\text{Cu}^{2+}$  incorporation within the material as well as its arrangement in the material follow. A ratiometric study of varying  $[\text{Cu}^{2+}]$  vs. [peptide] are presented in **Chapter 4** as well as the development of a more homogeneous nanotube that emerged from the study, characterization, and development of this MAN.



**Figure 3.32 – Plots of  $\log |i_p|$  vs  $\log (v)$  to assess dependence of K16A-Cu<sup>2+</sup> and Ac-K16A-Cu<sup>2+</sup> assemblies on diffusion or adsorption to the glassy carbon electrode.**

Slope values between 0.2 and 0.6 define a pure diffusion control system, 0.6 – 0.75 define a mixture of adsorption-diffusion control, and 0.75 – 1.10 define a pure adsorption control system. (A)  $r^2 = 0.99$  and  $0.99$ , slope =  $0.41 \pm 0.01$  and  $0.38 \pm 0.02$  (B)  $r^2 = 0.86$  and  $0.98$ , slope =  $0.61 \pm 0.12$  and  $0.36 \pm 0.03$ . Results demonstrate the complexity of reactivity within the Ac-K16A nanoribbons which are adsorption-diffusion controlled.

## Conclusion

In this chapter, we set out to challenge our understanding of the self-assembly code of peptides by making nanostructures with tailored function. We began by outlining the design and selection criteria of the peptide structure followed by a full characterization of the peptide architecture. We identified a model peptide that has been shown to coordinate to metal ions ( $H^{13}HQKLVFFA^{21}$ ), and synthesized congeners that form robust homogeneous assemblies (K16A and Ac-K16A) motivated by the intriguing characteristics achieved with a different congener of this model peptide, Ac-H14A. (Dong et al., 2007; Hernández-Guzmán et al., 2013) By reintroducing His14 and increasing the hydrophobic character of the peptide core, we: 1) doubled available metal coordinating sites and 2) increased the self-assembly propensity of the peptide. By surveying a wide range of metal ions – from alkaline earth metals to lanthanoids – we found conditions under which robust metal-incorporating nanostructures could form. Indeed, metal incorporation was initially diagnosed by a morphological transformation. We found that the most robust assemblies, within the conditions tested, formed in the presence of biologically relevant and abundant transition earth metals,  $Cu^{2+}$  and  $Zn^{2+}$ .

While structurally heterogeneous, structural insights gained from  $Zn^{2+}$  coordinating MANs will continue to guide our understanding of the self-assembly code, mainly, the assembly energy landscape involved in the maturation mechanism by which particles mature to a thermodynamically preferred peptide arrangement (refer to **Chapter 2** and pg. 87 for an in-depth structural analysis of this phenomenon). We propose that structural mutations, representing multiple paths in the assembly landscape, are surveyed by the self-assembling peptide as it matures. In the presence of  $Zn^{2+}$ , some of the

surveyed pathways are maintained and propagated. These kinetic traps provide a population distribution that provides insights into the accessible structural landscape of this nine-residue peptide. Knowing what the accessible landscape is could help us in the design of nanoscale materials that select for a specific mutation to highlight a desirable characteristic.

Having gained such unprecedented structural insight, we continued to explore the assembly of Ac-K16A and K16A, now in the presence of the redox active  $\text{Cu}^{2+}$ . Having passed selection constraints thus far presented, we looked to their stability and electrochemical properties as the final selection criteria. The effect that acetylation had on the overall K16A assembly is clear. We found that the  $T_{1/2}$  of Ac-K16A- $\text{Cu}^{2+}$  is less than that of K16A- $\text{Cu}^{2+}$  ribbons by about 20°C (**Figure 3.28**). This change was attributed to the decreased malleability of this bilayer material, a characteristic attributed to the ribbons by AFM experiments where Ac-K16A- $\text{Cu}^{2+}$  MAN have fully extended peptide leaflets while the K16A- $\text{Cu}^{2+}$  MAN have a more flexible bilayer. Furthermore, through a series of CV experiments, we found that the K16A- $\text{Cu}^{2+}$  ribbons are the most electrochemically reversible. While the separation between the two peak potentials ( $\Delta E_p$ ) for both structures deviated from the fully reversible  $59/n$  mV, where 'n' is the number of electrons in a given reaction, the K16A nanostructure's  $\Delta E_p$  ranged from 123 to 269 mV compared to 254 to 516 mV for the Ac-K16A nanostructure (**Table 3.2**). Thus, the electrochemical properties of Ac-K16A- $\text{Cu}^{2+}$  ribbons approach irreversibility. Given these results, K16A- $\text{Cu}^{2+}$  was selected as the most suitable MAN for further characterization and functional application.



In summary, we aimed to design MANs with functional potential. We were motivated by the desire to build a cell-compatible nanomachine with applications as a cellular battery, electron conductor or as a reaction center that can function in electron transfer as an oxidase and a reductase. We found that  $\text{Cu}^{2+}$  incorporating MANs are the most robust, furthermore, the aforementioned functions are accessible to naturally occurring copper proteins. We succeeded in the development of a self-assembling MANs with a blue-copper like appearance and an  $E_{1/2}$  of +675 mV vs. RHE, within the blue copper protein range. In **Chapter 4** we describe the important similarities, and differences, between our K16A- $\text{Cu}^{2+}$  ribbons and blue copper proteins. We go beyond the UV-Vis diagnostic shown here for  $\text{Cu}^{2+}$  coordination and turn to paramagnetic resonance to fully define the  $\text{Cu}^{2+}$  coordination environment of the MAN. Finally, we present a structural model that has been used in simulations giving exciting results and share a first pass experiment to assess the stability of this MAN when reduced in the presence of ascorbate.

## Materials and Methods

### Synthesis and purification of H-HHQALVFFA-NH<sub>2</sub>, H-HHQ[1-<sup>13</sup>C]ALVF[<sup>15</sup>N]FA-NH<sub>2</sub>, H-HHQ[1-<sup>13</sup>C]ALV[<sup>15</sup>N]FFA-NH<sub>2</sub>, Ac-HHQALVFFA-NH<sub>2</sub>, and Ac-HHQ[1-<sup>13</sup>C]ALVF[<sup>15</sup>N]FA-NH<sub>2</sub>

Peptides were synthesized and purified as previously described (**Chapter 2**, pg. 39). H-HHQALVFFA-NH<sub>2</sub> was synthesized with a free N-terminus, while the C-terminus is carboxyamided, while acetyl group caps the N-terminus of Ac-HHQALVFFA-NH<sub>2</sub>. For purification, the elution gradient was optimized for each peptide to elute within ten minutes of the initial starting point, followed by a ten minute wash and a seven minute equilibration step. Once CH<sub>3</sub>CN was removed using a rotary evaporator and left over water/peptide mixture is lyophilized, peptides were stored at room temperature inside a vacuum desiccator until needed.

Fraction purity was confirmed by MALDI-TOF mass spectral analysis using a Applied Biosystem 4700 Proteomics analyzer with a 355 nm ND:Yag laser operating at 200Hz (Foster City, CA, USA). A  $\alpha$ -cyano-4-hydroxycinnamic acid (CHCA) matrix was used for MALDI-TOF experiments (H-HHQALVFFA-NH<sub>2</sub>, 1068.23 (M+H<sup>+</sup>), H-HHQ[1-<sup>13</sup>C]ALV[<sup>15</sup>N]FFA-NH<sub>2</sub> and H-HHQ[1-<sup>13</sup>C]ALVF[<sup>15</sup>N]FA-NH<sub>2</sub>; 1070.39 (M+H<sup>+</sup>), Ac-HHQALVFFA-NH<sub>2</sub>; 1110.27 (M+H<sup>+</sup>), Ac-HHQ[1-<sup>13</sup>C]ALVF[<sup>15</sup>N]FA-NH<sub>2</sub>; 1112.43 (M+H<sup>+</sup>)).

### FMOc protection of isotope enriched amino-acids

FMOc protection of isotope enriched amino-acids (purchased from Cambridge Isotope Laboratories, Inc., Andover, MA, USA) for peptide synthesis was done following

standard methods.(Gawande & Branco, 2011; Samuel-Landtiser et al., 2001). Protocol is described in **Chapter 2** pg. 39.

### **Circular dichroism Spectroscopy (CD)**

CD spectra were recorded using the Jasco-810 CD spectropolarimeter. All measurements were done at room temperature. Spectra between 260 nm and 180 nm were collected with a 0.1mm path length cell, with a step size of 0.2 mm and a speed of 50 nm/s. Three spectra were recorded for each sample and averaged automatically. The ellipticity ( $\theta$ ) with unit mdeg was converted to mean residue molar ellipticity (MRME,  $[\theta]$ ,  $\text{deg}\cdot\text{cm}^2\cdot\text{dmol}^{-1}$ ) by  $[\theta] = \theta/(10\cdot n\cdot C\cdot l)$ , where 'n' is the number of amide bonds per peptide, 'C' is the molar concentration (mol/L) and 'l' is the cell path in cm. Data was plotted and fit using Origin 9.0 to a Boltzmann fit algorithm. Samples incubated in 25 mM MES, pH 5.6 at 25°C for the specified time points.

### **Fourier Transform Infrared Spectroscopy (FT-IR)**

FT-IR spectra were recorded using a Jasco FT-IR 4100 (Easton, MD, USA). Sample aliquots (15  $\mu\text{L}$ ) were dried as thin films on an ATR diamond cell. All IR spectra were acquired at room temperature and averaging 1068 scans with  $2\text{ cm}^{-1}$  resolution. Background spectra were acquired immediately before each sample and were subtracted from each sample spectrum using Jasco software. Data were imported into OriginPro 9.0 for graphing and analysis.

### **UV-Vis Spectroscopy**

UV-Vis spectra were measured with a Cary 100 UV-Vis Spectrophotometer by Agilent Technologies (Santa Clara, CA, USA). For the data collection, a small volume quartz cuvette was used, 50  $\mu\text{L}$  minimum volume, with a 1 cm path length and a

transparency between 170 and 2700 nm (Sterna Cells Inc., Atascadero, CA, USA).

Spectra were collected from 900 to 200 nm, with a 1 nm data interval and 600 nm/min scan rate. Three spectra were recorded for each sample and averaged.

### **Transmission Electron Microscopy (TEM)**

Peptide assemblies were diluted ten times their original volume to a final concentration of 0.05mM, 0.1mM or 0.2mM respectively. About 10 $\mu$ L of the diluted solution was placed on a CF200-Cu Carbon Film 200 Mesh Copper grid purchased from Fisher Scientific (Electron Microscopy Sciences is the provider, Hatfield, PA) held on a set of forceps above the surface. Peptide assemblies were allowed to settle on the grid surface for at least one minute. Excess solution was wicked away using filter paper. Immediately following, 10 $\mu$ L of a 1.5% methylamine tungstate or 1.2% uranyl acetate staining solution was placed on the same grid for about three minutes. Excess staining solution was wicked away. All grids were stored under vacuum in a desiccator before TEM analysis to remove any excess liquid on the grid surface. Electron micrographs were obtained using a Hitachi HT-7700 Transmission Electron Microscope (TEM) operating at 80 kV at the Robert P. Apkarian Integrated Electron Microscopy Core, part of the Emory Integrated Core Facilities.

### **Atomic Force Microscopy (AFM)**

Samples were diluted 100 and 200 times to ensure good dispersion of sample. After sample was diluted to the desired concentration, 45 $\mu$ L of solution was placed on a clean silicon chip for 2 minutes (Ted Pella Inc., Redding, CA), excess solution was wicked away with filter paper. Silicon chips were cleaned with methanol and dried with N<sub>2</sub> gas.

Tapping mode analysis on a Veeco Dimension 5000 atomic force microscope with a full acoustic enclosure was employed using ultra-sharp non-contact silicon cantilevers with typical frequencies ranging from 150 kHz for the largest tip to 315 kHz for the smallest tip (NSC35/AIBS, MikroMasch, Watsonville, CA). The images were flattened and analyzed using Gwyddion AFM data analysis software.

### **Solid-state NMR**

To prepare H-HHQ[1-<sup>13</sup>C]ALV[<sup>15</sup>N]FFA-NH<sub>2</sub>, HHQ[1-<sup>13</sup>C]ALVF[<sup>15</sup>N]FA-NH<sub>2</sub>, and Ac-HHQ[1-<sup>13</sup>C]ALVF[<sup>15</sup>N]FA-NH<sub>2</sub> for solid-state NMR, the samples were first pelleted by centrifugation at 4°C for 60 – 90 min at 9000 rpm (6792 x g calculated with a Horizontal Drum rotor (T-60-11)) using a Eppendorf centrifuge 5804 R (Mississauga, Ontario, CAN) to remove any unassembled peptide. Supernatant was removed and pellets were frozen and lyophilized to yield dry powders. TEM confirmed the presence of fibers and ribbons after lyophilization. The NMR sample (ideally ~40 mg, but can use as little as 10 mg, affecting signal to noise and collection time) is packed into a 4 mm solid-state NMR rotor and centered using boron nitride spacers.

<sup>13</sup>C DQF-DRAWS Solid-state NMR: Method is described in **Chapter 2** pg. 39.

Data fits were done using a Mathematica nonlinear routine assuming a H-bonding distance of 4.7 Å.

REDOR Solid-state NMR: Experimental set-up as described in **Chapter 2** pg. 39.

For each of the samples listed below, data fits were done following parameters in the literature (Goetz & Schaefer, 1997) and used in a Mathematica routine.

1. H-HHQ[1-<sup>13</sup>C]ALV[<sup>15</sup>N]FFA-NH<sub>2</sub> (K16A) fibers: In dephasing the carbonyl carbon of H-HHQ[1-<sup>13</sup>C]ALV[<sup>15</sup>N]FFA-NH<sub>2</sub> fibers, the distance of the H-bonded

$^{15}\text{N}$  from the adjacent carbonyl was fit to 4.8 Å ( $r_1$ ) and the distances to the two non-H-bonded  $^{15}\text{N}$ 's were fit to 6.9 Å ( $r_2$ ) and 8.7 Å ( $r_3$ ). The angle between the three  $^{13}\text{C}$ - $^{15}\text{N}$  internuclear vectors was fit to 108.5°, consistent with dephasing of H-HHQ[1- $^{13}\text{C}$ ]ALV[ $^{15}\text{N}$ ]FFA-NH<sub>2</sub> self-assemblies. The experimental data was fit to a 4-spin system (one  $^{13}\text{C}$  and three  $^{15}\text{N}$ 's) with the  $^{15}\text{N}$ - $^{15}\text{N}$  distance constrained to 9.4 Å.

2. Ac-HHQ[1- $^{13}\text{C}$ ]ALVF[ $^{15}\text{N}$ ]FA-NH<sub>2</sub> (K16A) fibers: In dephasing the carbonyl carbon of Ac-HHQ[1- $^{13}\text{C}$ ]ALV[ $^{15}\text{N}$ ]FFA-NH<sub>2</sub> fibers, the distance of the H-bonded  $^{15}\text{N}$  from the adjacent carbonyl was fit to 7.9 Å ( $r_1$ ) and 8.9 Å ( $r_2$ ). The angle between the two  $^{13}\text{C}$ - $^{15}\text{N}$  internuclear vectors was fit to 68.0°. The experimental data was fit to a 3-spin system (one  $^{13}\text{C}$  and two  $^{15}\text{N}$ 's).
3. H-HHQ[1- $^{13}\text{C}$ ]ALVF[ $^{15}\text{N}$ ]FA-NH<sub>2</sub> + Zn<sup>2+</sup> (K16A-Zn<sup>2+</sup>) fibers, ribbons and tubes: In dephasing the carbonyl carbon of H-HHQ[1- $^{13}\text{C}$ ]ALV[ $^{15}\text{N}$ ]FFA-NH<sub>2</sub> + Zn<sup>2+</sup> four distinct populations were identified: fibers, twisted ribbons, helical ribbons and nanotubes. Thus, the distance of the  $^{15}\text{N}$  from the adjacent carbonyls had to be calculated for each population giving 3 peptide arrangements for the four populations:
  - a. Anti-parallel in-register: Does not fit to ideal distances, 7.9 Å ( $r_1$ ) and 8.9 Å ( $r_2$ ). The angle between the two  $^{13}\text{C}$ - $^{15}\text{N}$  internuclear vectors for the ideal is 68.0°. Experimental data only fits to a system that accounts for collections of multiple structures, suggesting presence of structural mutations.

- b. Anti-parallel out-of-register by one amino-acid: Fit to 5.7 Å ( $r_1$ ) and 6.1 Å ( $r_2$ ). The angle between the two  $^{13}\text{C}$ - $^{15}\text{N}$  internuclear vectors was fit to 105.6°. The experimental data was fit to a 3-spin system (one  $^{13}\text{C}$  and two  $^{15}\text{N}$ 's).
- c. Anti-parallel out-of-register by two amino-acids: Fit to 4.1 Å ( $r_1$ ) and 5.3 Å ( $r_2$ ). The angle between the two  $^{13}\text{C}$ - $^{15}\text{N}$  internuclear vectors was fit to 160.0°. The experimental data was fit to a 3-spin system (one  $^{13}\text{C}$  and two  $^{15}\text{N}$ 's) with the  $^{15}\text{N}$ - $^{15}\text{N}$  distance constrained to 9.4 Å.
4. Ac-HHQ[1- $^{13}\text{C}$ ]ALVF[ $^{15}\text{N}$ ]FA-NH<sub>2</sub> + Zn<sup>2+</sup> (Ac-K16A + Zn<sup>2+</sup>) fibers: In dephasing the carbonyl carbon of Ac-HHQ[1- $^{13}\text{C}$ ]ALV[ $^{15}\text{N}$ ]FFA-NH<sub>2</sub> + Zn<sup>2+</sup> fibers, the distance of the  $^{15}\text{N}$  from the adjacent carbonyl was fit to 7.9 Å ( $r_1$ ) and 8.9 Å ( $r_2$ ). The angle between the two  $^{13}\text{C}$ - $^{15}\text{N}$  internuclear vectors was fit to 68.0°. The experimental data was fit to a 3-spin system (one  $^{13}\text{C}$  and two  $^{15}\text{N}$ 's).
5. H-HHQ[1- $^{13}\text{C}$ ]ALV[ $^{15}\text{N}$ ]FFA-NH<sub>2</sub> + Cu<sup>2+</sup> (K16A-Cu<sup>2+</sup>) ribbons: In dephasing the carbonyl carbon of H-HHQ[1- $^{13}\text{C}$ ]ALV[ $^{15}\text{N}$ ]FFA-NH<sub>2</sub> + Cu<sup>2+</sup> ribbons, the distance of the two non H-bonded  $^{15}\text{N}$ s from the adjacent carbonyls were fit to 4.9 Å ( $r_1$ ) and 6.0 Å ( $r_2$ ). The angle between the two  $^{13}\text{C}$ - $^{15}\text{N}$  internuclear vectors was fit to 114.7°. The experimental data was fit to a 3-spin system (one  $^{13}\text{C}$  and two  $^{15}\text{N}$ 's).
6. Ac-HHQ[1- $^{13}\text{C}$ ]ALVF[ $^{15}\text{N}$ ]FA-NH<sub>2</sub> + Cu<sup>2+</sup> (Ac-K16A-Cu<sup>2+</sup>) ribbons: In dephasing the carbonyl carbon of Ac-HHQ[1- $^{13}\text{C}$ ]ALV[ $^{15}\text{N}$ ]FFA-NH<sub>2</sub> + Cu<sup>2+</sup> ribbons, the distance of the H-bonded  $^{15}\text{N}$  from the adjacent carbonyl was fit to 4.4 Å ( $r_1$ ) and the distance to the non-H-bonded  $^{15}\text{N}$ 's were fit to 5.1 Å ( $r_2$ ). The

angle between the two  $^{13}\text{C}$ - $^{15}\text{N}$  internuclear vectors was fit to  $153.0^\circ$ . The experimental data was fit to a 3-spin system (one  $^{13}\text{C}$  and two  $^{15}\text{N}$ 's).

### **Cyclic Voltammetry (CV)**

Cyclic voltammetry experiments were performed using a WaveDriver potentiostat (Pine Research Instrumentation, Durham, NC, USA). The experiment set-up used a standard three-electrode arrangement and a microvolume cell which could work with sample volume not exceeding 150  $\mu\text{L}$ . All experiments were carried out at room temperature. Electrodes used were a Ag/AgCl reference electrode, a Pt wire counter electrode, and a glassy carbon working electrode (CH Instruments Inc. Electrochemical Instrumentation, Austin, TX, USA). 25 mM MES buffer, pH 5.6 was the sample solvent and 100 mM NaCl was added as the supporting electrolyte. Cyclic voltammetry was carried out in the potential range of -0.500 to 0.600 V vs. Ag/AgCl at a scan rate of 0.025, 0.050, 0.100, 0.250 and 0.500 (V/s) for eight segments at each scan rate with a sensitivity of  $10^{-6}$ . Before each measurement, the solutions were degassed by bubbling  $\text{N}_2$  through the reference buffer for at least 1 minute. The working electrode was polished before use and in-between runs to ensure a clean surface. A background measurement of the buffer was taken in between each run at a scan rate of 0.100 V/s as the background control to ensure experiments were done with a clean working electrode each time. A background measurement of peptide alone was also taken as a secondary control. Data was processed using AfterMath software and plotted in Origin 9.0, standard equations were used (Balland et al., 2010; Gupta et al., 2012; Wiloch et al., 2016).

### **Peptide Assembly**



Assemblies with peptide alone: H-HHQALVFFA-NH<sub>2</sub> and Ac-HHQALVFFA-NH<sub>2</sub> (K16A and Ac-K16A, respectively) were dissolved and allowed to mature in 25mM MES buffer, pH 5.6. Fibers were prepared by first adding half the desired volume of water. Following water addition and a 2-5 sec. vortex period, 50 mM MES buffer at pH 5.6 was added to the desired final volume, this was followed by a brief 1-2 sec. vortex period. Peptide concentration ranged from 0.5 mM, 1 mM and 2 mM. At all concentrations, homogeneous fibril formation was evident after 1 to 3 weeks depending on the peptide concentration. Time needed to reach full maturation was shortened with increasing temperature, 4°C, 25°C and 37°C.

Assemblies with the addition of M<sup>n+</sup>: H-HHQALVFFA-NH<sub>2</sub> and Ac-HHQALVFFA-NH<sub>2</sub> (K16A and Ac-K16A, respectively) were dissolved in water and vortexed for a period of 2-5 sec. Amount of water was half the total volume minus the desired amount of M<sup>n+</sup> to be added from the stock solution prepared at 100 mM for each M<sup>n+</sup>. Immediately following water addition, half the total volume of 50 mM MES buffer at pH 5.6 was added, quickly followed by sample inversion and a vortex period of no more than 2 seconds with the immediate addition of the M<sup>n+</sup> solution to reach the desired final volume. Sample concentrations ranged from 0.5 mM, 1 mM and 2 mM. Time period for maturation of each sample was different. Increasing temperature, 4°C, 25°C and 37°C, decreased the lag-time of assembly for the samples that formed an ordered supramolecular nanostructure.

### **Width Measurements**

All measurements were done using Image J software. For each image measurements were defined based on embedded scale bar.

## **Peptide Representations**

All high-resolution peptide models were built using free Maestro academic version from Schrödinger Computational Software. Images were initially rendered using Visual Molecular Dynamics (VMD) Molecular Graphics Viewer and rendered at high resolution using the Persistence of Vision Raytracer (POV-Ray) software.

## **Chapter 4 : Metalloamyloid Nanostructure (MAN) as a Blue Copper Protein Mimic**

### **Authors**

### **Introduction**

The design and selection of a metalloamyloid nanostructure (MAN) presented in **Chapter 3**, was aimed at creating a material that can function as an electron transporter or an electron storage unit. In **Chapter 3**, we demonstrated that the K16A-Cu<sup>2+</sup> MAN has properties that present it as a good functional candidate (it displays a degree of reduction/oxidation reversibility) with features that resemble those of blue copper proteins.

Blue copper proteins belong to a family of electron transfer proteins characterized by two key features, 1) they have an intense absorption near 600 nm (giving them an intense blue color) and 2) they are paramagnetic in the oxidized form (Adman, 1985). Their ability to transfer electrons is reflected in their oxidizing electron potential, which can range between 180 and 1000 mV (Olsson & Ryde, 1999). Because their functional role in biology requires that this family of proteins readily cycle between Cu<sup>2+</sup> and Cu<sup>+</sup>, the mechanism by which such control is achieved by these proteins has been carefully investigated (Adman, 1985; Gray, Malmstrom, & Williams, 2000; Gross, 1993; Olsson & Ryde, 1999). In short, the low reorganization energy contributing to the ease of electron transfer for these proteins is explained due to the nontypical coordination geometry of the Cu<sup>2+</sup> coordination site(s), favoring both the reduced and oxidized form of copper, as well as the soft and flexible bonds from histidine and the axial ligand.

When these characteristics are compared with those of the K16A-Cu<sup>2+</sup> MAN, parallels are immediately apparent – the nanostructure has an intense absorbance at ~600 nm and Cu<sup>2+</sup>, which is incorporated in its oxidized form, is paramagnetic (spin ½). Furthermore, the reduction potential of 670 mV measured for K16A-Cu<sup>2+</sup> nanostructures in **Chapter 3** falls within the observed range of blue copper proteins: 180 – 1000 mV (Olsson & Ryde, 1999). Given these features, we propose the K16A-Cu<sup>2+</sup> MAN is a blue copper protein mimic and as such, should share in its functional arsenal. To fully understand the functional applications that can be attributed to this new material, we aimed to fully characterize the Cu<sup>2+</sup> coordination environment inside this homogeneous nanostructure. We reason that the coordination environment is histidine controlled, which may be an important factor contributing to the reversibility of reduction/oxidation seen for this MAN. Experiments outlined in this chapter helped define the organization of the histidine ligands around the coordinated Cu<sup>2+</sup>.

In this chapter, we demonstrate the insulation of Cu<sup>2+</sup> ions, organized in an array within the peptide bilayer at high density. We further demonstrate that the insulated Cu<sup>2+</sup> ions are coordinated by histidine side-chains in two distinct arrangements that saturate with increasing Cu<sup>2+</sup> concentrations and the resulting structure is redox active and stable through several cycles of oxidation and reduction and in the presence of a reducing agent. This is the first example, to our knowledge, of a bionanomaterial designed *de novo* that insulates a Cu<sup>2+</sup> ion array in a bilayer with controlled growth in multiple dimensions and displaying reactivity that mimics that of blue copper proteins. We envision that this material could serve as a functional electron conductor or a nanoscale capacitor.

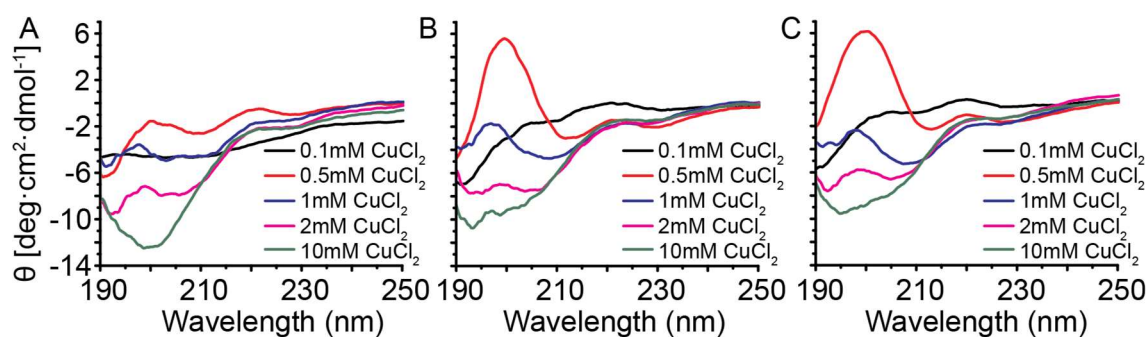
## Results and Discussion

### A ratiometric study of Cu<sup>2+</sup> incorporation by optical spectroscopy and ITC

To interrogate the degree of Cu<sup>2+</sup> saturation of the available binding sites in the K16A-Cu<sup>2+</sup> nanoribbons, we introduced a range of concentrations of Cu<sup>2+</sup> to a constant 1 mM concentration of K16A peptide. We reasoned that an optimum window would be revealed where the K16A-Cu<sup>2+</sup> MAN formed the most robust  $\beta$ -sheet rich assemblies (followed by CD) and where an aquo-Cu<sup>2+</sup> species became the most intense contributor to bulk sample absorbance (followed by UV-Vis). Thus, we looked to these experiments to reveal a range of Cu<sup>2+</sup> concentrations with which the peptide assembled most readily.

CD reports on the secondary structure of chiral molecules and, given the innate chirality of peptide forming molecules, we turned to CD to optimize conditions for  $\beta$ -sheet formation. In CD spectroscopy, absorption in the UV region below 250 nm is due principally to the peptide bond, though aromatic side-chains may also contribute in some cases (Kelly, Jess, & Price, 2005; Micsonai et al., 2015). In general, however, two transitions can be assigned to the peptide backbone centered around 190 nm and 220 nm which correspond to  $n \rightarrow \pi^*$  and  $\pi \rightarrow \pi^*$  transitions, respectively. We first followed the Cu<sup>2+</sup> effects on peptide assembly by looking at a wide range of Cu<sup>2+</sup> concentrations, from 0.1 mM to 10 mM. Followed over a period of 20 days, we noticed the emergence of a clear trend (**Figure 4.1**). At 0.1 mM Cu<sup>2+</sup>, the strongest ellipticity after 20 days is negative at 190 nm, reflective of the  $n \rightarrow \pi^*$  transition associated with random coil. At 2 and 10 mM, the strongest ellipticity values exist between 190 and 200 nm, attributed to random coil or amorphous peptide collections. In the sample vial, peptides begin to form precipitates at these concentrations of Cu<sup>2+</sup>. However, at 0.5 mM Cu<sup>2+</sup> a band with a

positive ellipticity at 200 nm and negative ellipticity at 214 nm emerges after only 5 days. Such a signal describes a  $\beta$ -sheet secondary structure, in agreement with what has been presented by FT-IR in the previous chapter for this nanostructure. While at 1 mM  $\text{Cu}^{2+}$  the positive ellipticity is not as pronounced after 20 days, a clear  $\beta$ -sheet structure can be assigned to the negative ellipticity seen at 212 nm. Thus, there seems to be an optimal  $\beta$ -sheet forming range within the 0.5 – 1 mM  $\text{Cu}^{2+}$  concentration window. To look at this analysis a different way, we turned to UV-Vis spectroscopy.



**Figure 4.1 – CD of K16A- $\text{Cu}^{2+}$  over 20 days at different  $\text{Cu}^{2+}$  ratios.** (A) CD data collected after two days of assembly. (B) CD data collected after 5 days of assembly. (C) CD data collected after 20 days of assembly. CD data shows that the ratio of 1:0.5 peptide: $\text{Cu}^{2+}$  (red throughout time course experiment) displays the strongest  $\beta$ -sheet character. At a 1:1 ratio (blue throughout time course experiment),  $\beta$ -sheet character develops more slowly but is clearly emerging by day 20. All other conditions display a strong random coil signature around 198 nm.

To more clearly pinpoint an optimal range of assembly, we decreased the change between  $\text{Cu}^{2+}$  concentration increments from sample to sample. Keeping the variation between concentration of  $\text{Cu}^{2+}$  across samples small helped highlight a transition range

that matched well with the estimate that we obtained by CD. Data also clarifies other important aspects of the assembly including coordination environment around the Cu<sup>2+</sup> that is incorporated in the K16A-Cu<sup>2+</sup> nanostructure.

As introduced in **Chapter 3** (pg. 73), the d-d transition of Cu<sup>2+</sup> gives rise to visible absorption, with a typical  $\lambda_{\max}$  of ~800 nm for water dissolved CuCl<sub>2</sub> and ~780 nm for MES dissolved CuCl<sub>2</sub>. Indeed, replacement of water ligands with oxygen or nitrogen donor coordinating ligands shifts the  $\lambda_{\max}$  to lower wavelengths, according to the equation:

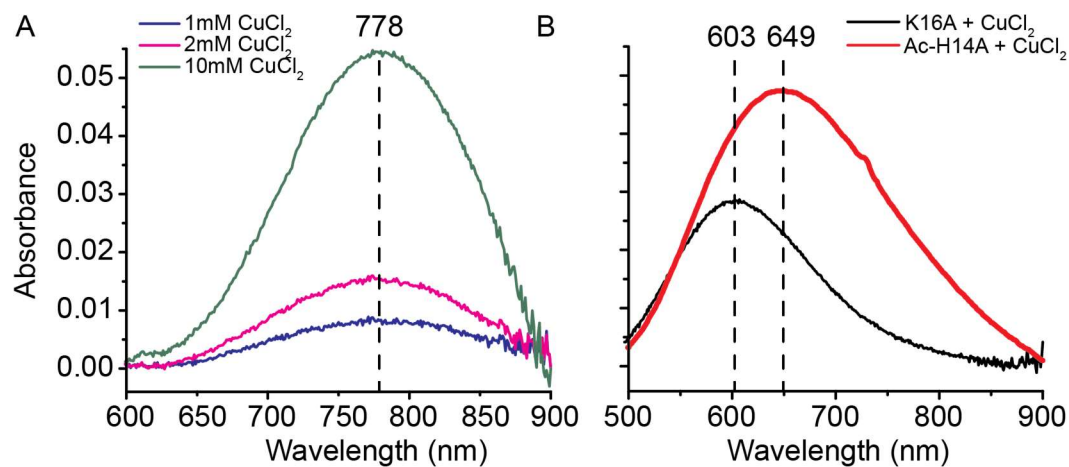
$$\lambda_{\max} = 10^3 / [0.294n(\text{C}\square\text{O}/\text{HO}) + 0.346n(\text{COO}^-) + 0.434n(\text{N}_{\text{Im}}) + 0.460n(\text{NH}_2) + 0.494n(\text{N}^-)]$$

where ‘N<sup>-</sup>’ is deprotonated amide nitrogen, ‘NH<sub>2</sub>’ is amino group, ‘N<sub>Im</sub>’ is the imidazolic nitrogen, ‘COO<sup>-</sup>’ is the carboxylate, ‘C□O’ is the carbonyl, and ‘HO’ is a water donor (Sigel & Martin, 1982). UV-Vis data for the K16A- Cu<sup>2+</sup> nanostructure shows a  $\lambda_{\max}$  at ~600 nm. Given the accessible coordinating ligands, results are most consistent with tris-His coordination (3N<sub>Im</sub>/1O) around the Cu<sup>2+</sup> ions, though contributions from an amino group may explain the 20 nm deviation of the calculated  $\lambda_{\max}$  (626 nm) from the observed. Coordinating ligands are interrogated directly in the next section by EPR and ESEEM experiments.

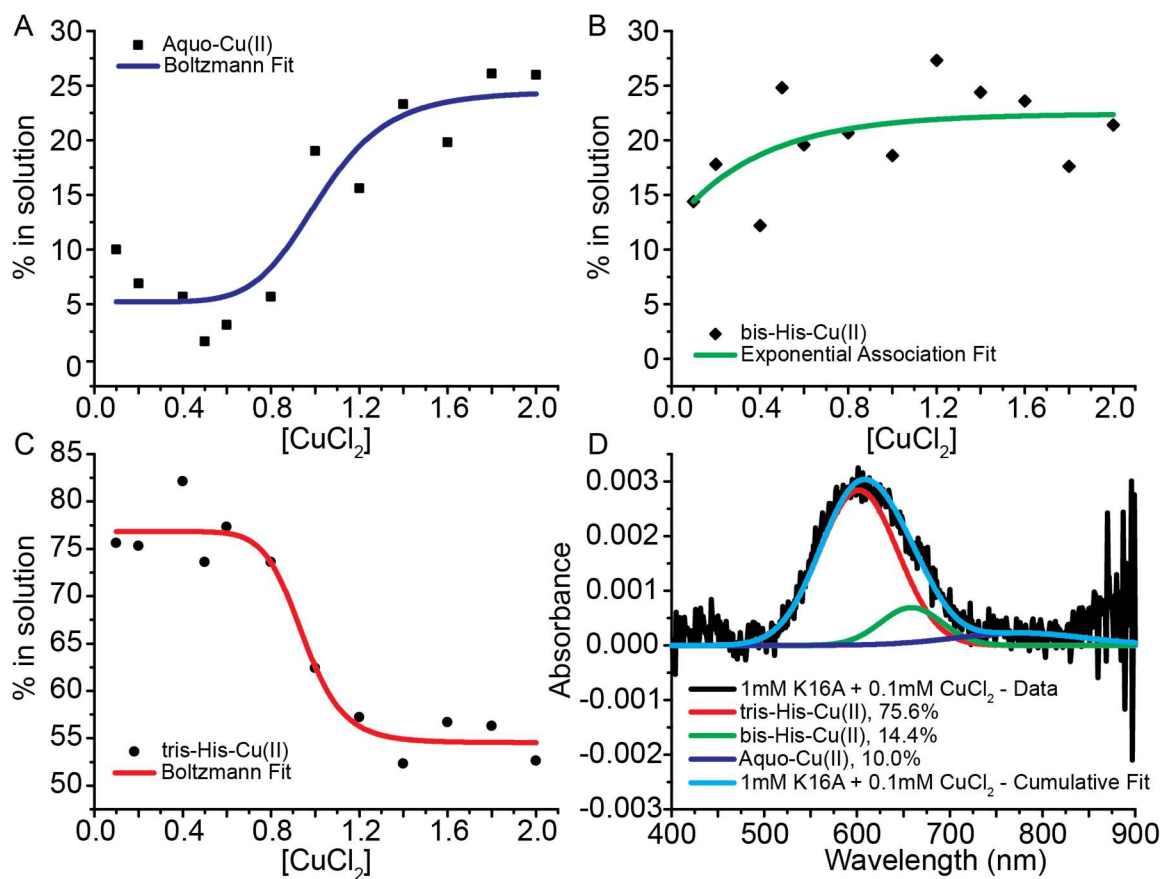
To fit the UV-Vis data across the different Cu<sup>2+</sup> concentrations we developed a basis set for the line fit comprised of the aquo-Cu<sup>2+</sup> absorption, in MES buffer, at 778 nm, bis-His Cu<sup>2+</sup> absorption at ~650 nm seen for Cu<sup>2+</sup>-H14A fibers and characterized previously (Hernández-Guzmán et al., 2013) as well as Cu<sup>2+</sup>-K16A fibers, and the tris-His band characteristic of the Cu<sup>2+</sup>-K16A ribbons at ~600 nm (**Figure 4.2**). At Cu<sup>2+</sup> concentrations below 1 mM (0.1, 0.2, 0.4, 0.5, 0.6 and 0.8 mM) the dominant species was

the tris-His  $\text{Cu}^{2+}$  comprising 73 – 82% of the bulk sample (**Figure 4.3A**). Aquo- $\text{Cu}^{2+}$  range spread from 2 – 10% of the sample (**Figure 4.3C**) and, interestingly, a second population of coordinated  $\text{Cu}^{2+}$  was needed to fit the data; bis-His  $\text{Cu}^{2+}$  made up 15 – 25% of the sample with higher variability across samples (**Figure 4.3B**), fits are summarized in **Figure 4.3D** for 0.1 mM  $\text{CuCl}_2$ . Above the 0.8 mM  $\text{Cu}^{2+}$  concentration there was a non-negligible rise in the presence of aquo- $\text{Cu}^{2+}$  needed to fit the UV-Vis data and a decline in the presence of the tris-His- $\text{Cu}^{2+}$  species present in the sample. These data are in agreement with the CD data previously described that suggests an ideal range of copper incorporation to exist between 0.5 and 1 mM in the presence of 1 mM K16A. Furthermore, the evolution of amorphous aggregates at concentrations above 1.4 mM  $\text{CuCl}_2$  is in agreement with CD data where concentrations of 5 and 10 mM  $\text{CuCl}_2$  appeared to inhibit the assembly of K16A over 20 days. Indeed, TEM images collected for the samples analyzed by UV-Vis show that the nanoribbons are not homogeneously formed above the 1.4 mM concentration (**Figure 4.4A – P**). These amorphous aggregates precipitate at high  $\text{CuCl}_2$  concentrations, which could explain the weak CD signal described above as well as the unobservable optical signal by UV-Vis for peptide bound  $\text{Cu}^{2+}$  at high  $\text{CuCl}_2$  concentrations.

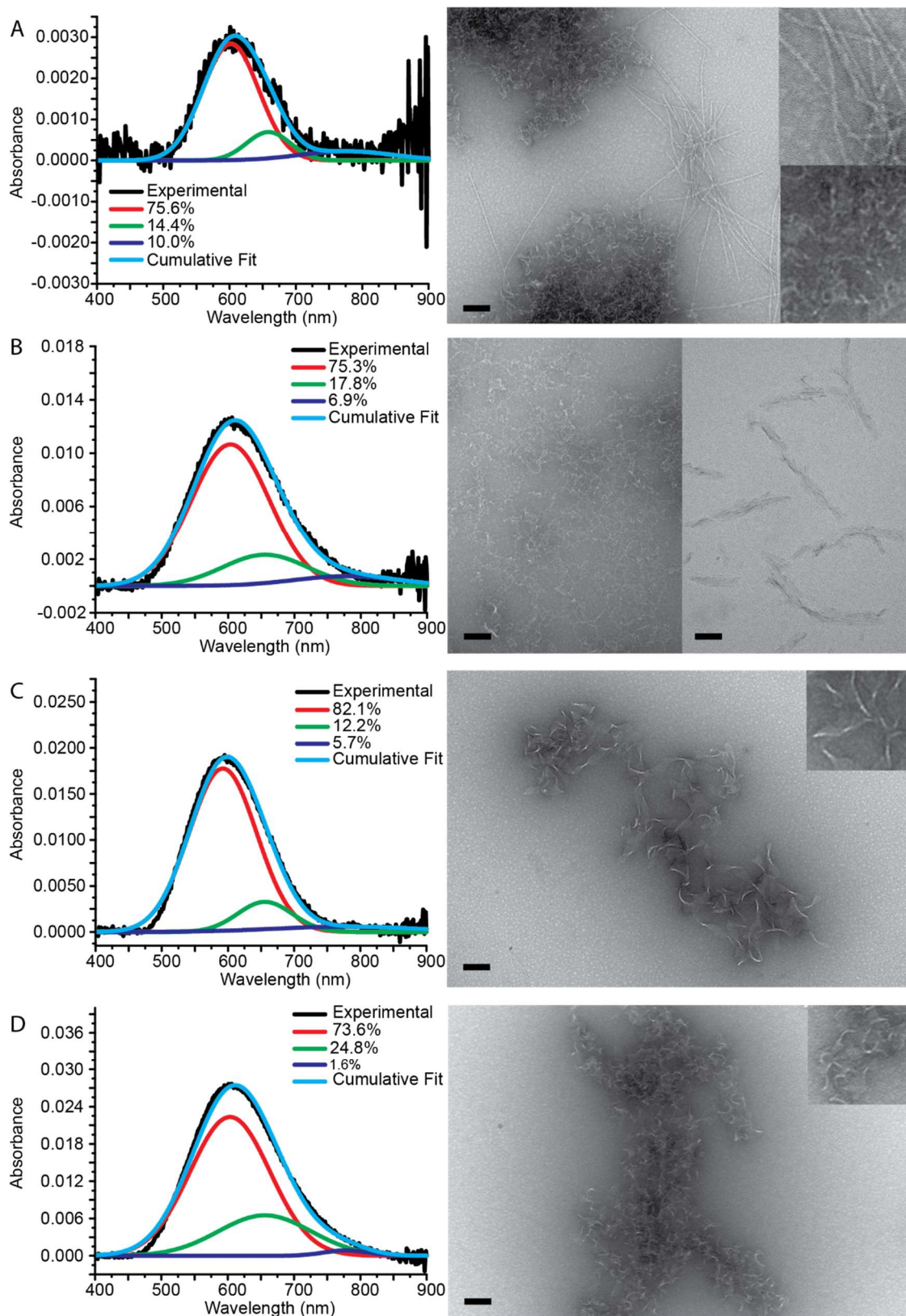


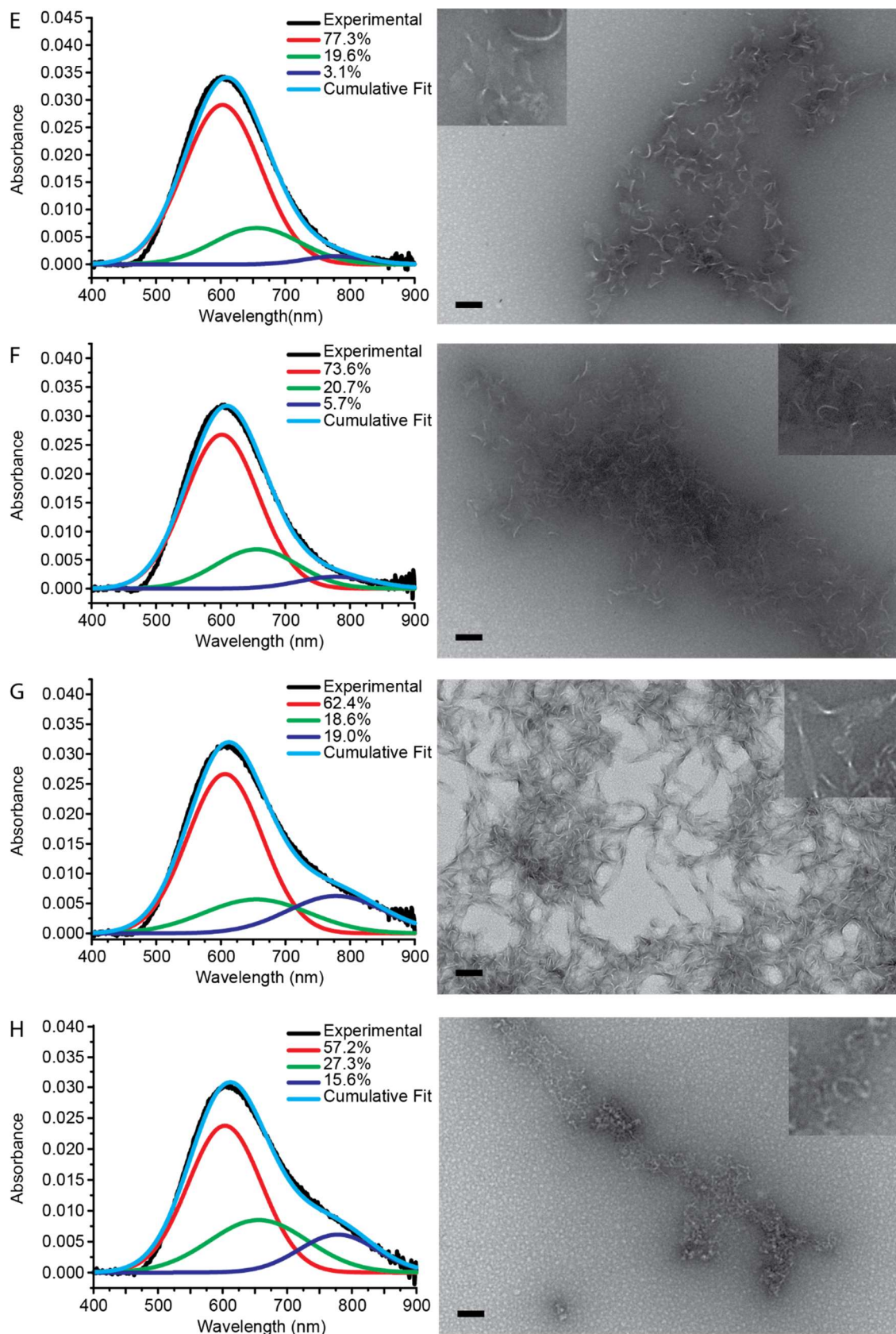


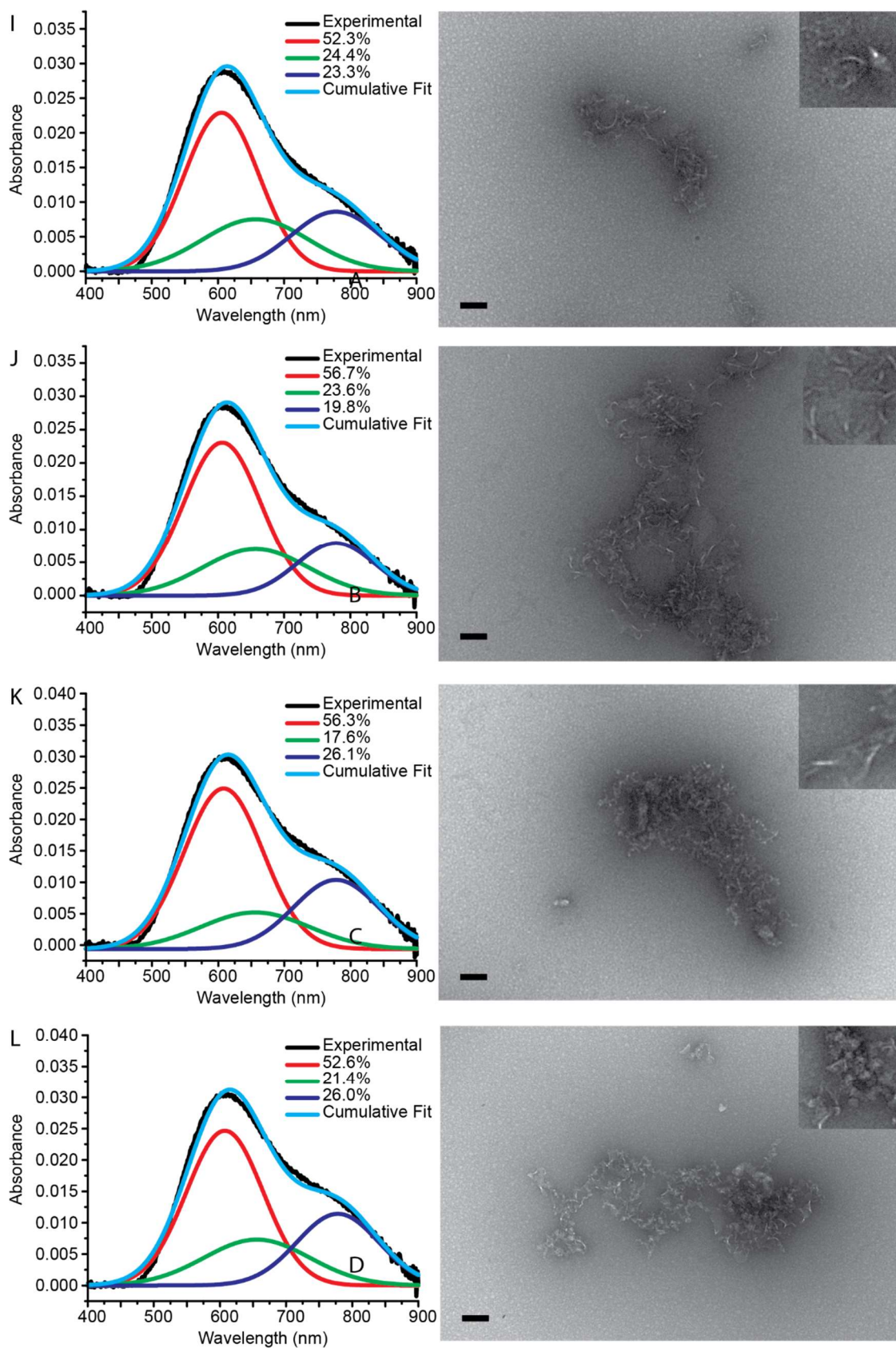
**Figure 4.2 – Absorbance values for basis-set used in UV-Vis fits.** Aquo- $\text{Cu}^{2+}$   $\lambda_{\text{max}} = 778$  nm, K16A- $\text{Cu}^{2+}$   $\lambda_{\text{max}} = 603$  nm, Ac-K16A +  $\text{Cu}^{2+}$   $\lambda_{\text{max}} = 649$  nm.

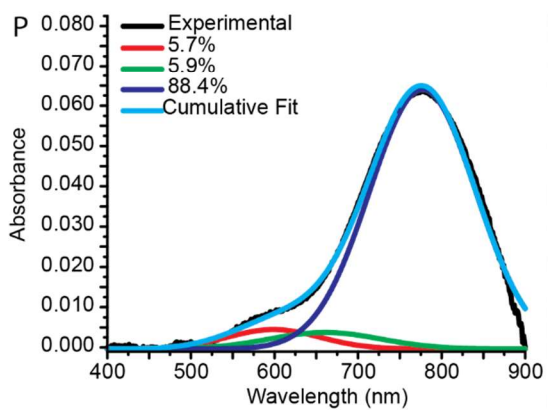
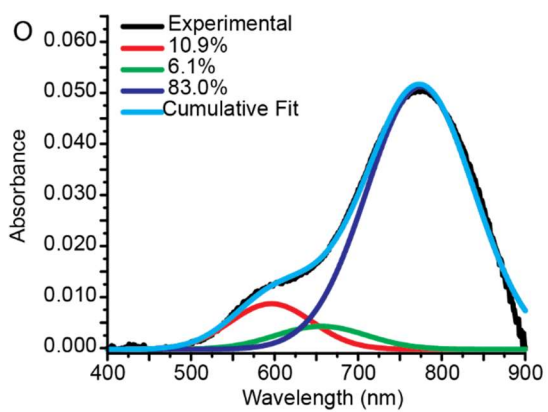
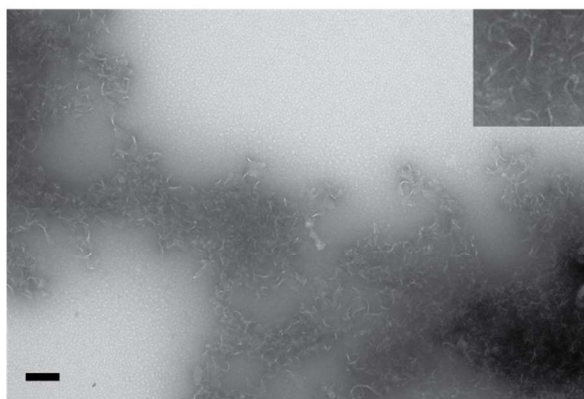
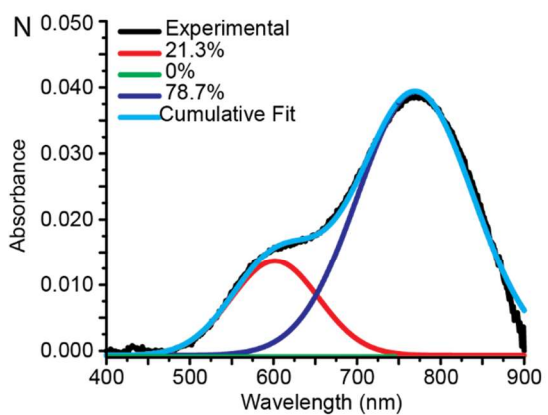
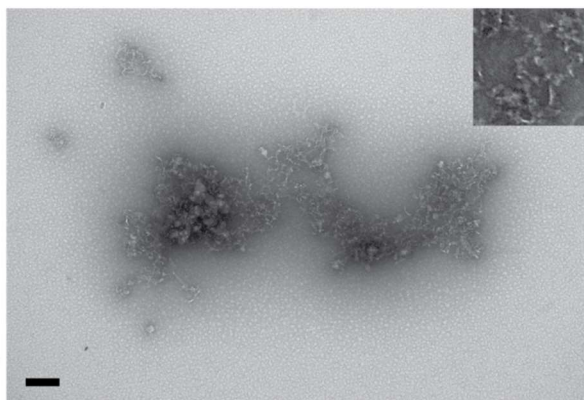
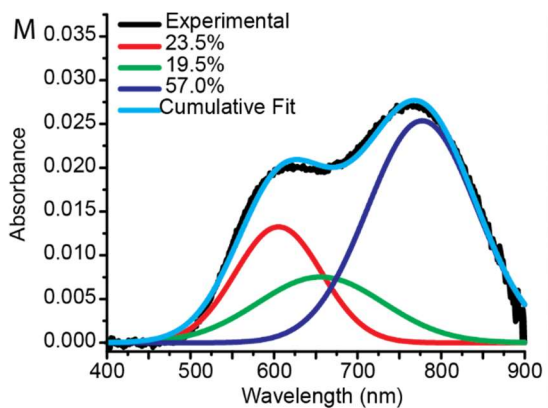


**Figure 4.3 – Summary of basis-set fitting results comparing  $\text{Cu}^{2+}$  coordinate species over a range of  $\text{CuCl}_2$  concentrations at a constant peptide ratio.**  $[\text{CuCl}_2]$  range from 0.2 – 2 mM while  $[\text{K16A}]$  was maintained at 1 mM. (A) Evolution of  $\text{Aquo-Cu}^{2+}$  species as the accessible  $\text{Cu}^{2+}$ -K16A coordination sites become saturated. (B) Evolution of  $\text{bis-His-Cu}^{2+}$  species. While present at a relatively low percent throughout the concentration range this species account for a quarter portion of the available sites that make up the nanoribbon assembly. (C)  $\text{tris-His-Cu}^{2+}$  is the dominant metal-coordination arrangement within the supramolecular ribbon. Beyond a 0.8 ratio (1 mM K16A to 0.8 mM  $\text{CuCl}_2$ ) there is a shift in favor of  $\text{aquo-Cu}^{2+}$  and  $\text{bis-His-Cu}^{2+}$ . (D) UV-Vis spectra of K16A-Cu(II) ribbons at a 1 mM peptide to 0.1 mM  $\text{CuCl}_2$  ratio. Basis set percentages used to build scatter plots are shown in red, green and navy blue respectively.









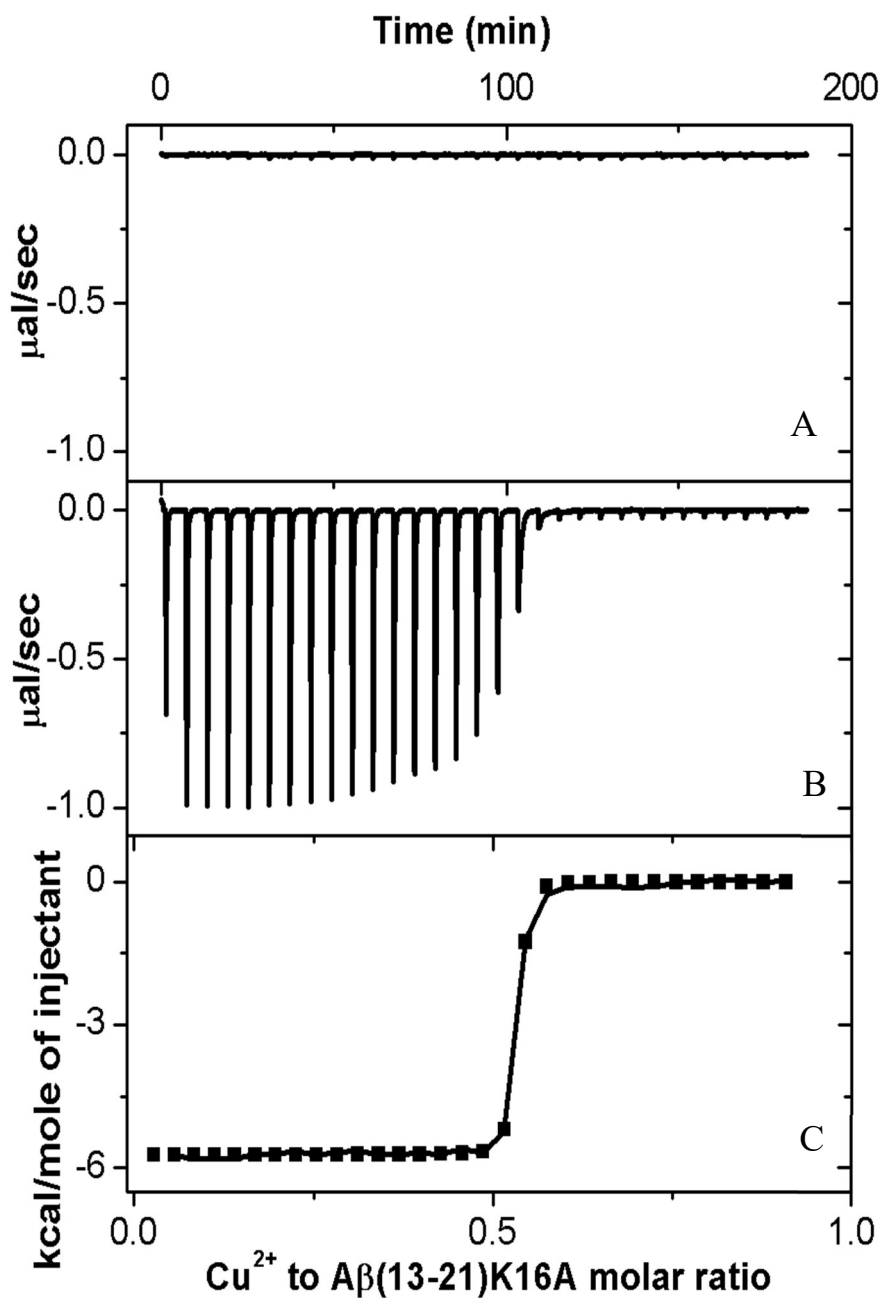
**Figure 4.4 – UV-Vis fits using basis-set absorbance values.** All experiments were done with 1 mM K16A. (A) + 0.1 mM CuCl<sub>2</sub> (aquo-Cu<sup>2+</sup> = 10.0%, bis(His)-Cu<sup>2+</sup> = 14.4%, tris(His)-Cu<sup>2+</sup> = 75.6%). (B) + 0.2 mM CuCl<sub>2</sub> (aquo-Cu<sup>2+</sup> = 6.9%, bis(His)-Cu<sup>2+</sup> = 17.8%, tris(His)-Cu<sup>2+</sup> = 75.3%). (C) + 0.4 mM CuCl<sub>2</sub> (aquo-Cu<sup>2+</sup> = 5.7%, bis(His)-Cu<sup>2+</sup> = 12.2%, tris(His)-Cu<sup>2+</sup> = 82.1%). (D) + 0.5 mM CuCl<sub>2</sub> (aquo-Cu<sup>2+</sup> = 1.6%, bis(His)-Cu<sup>2+</sup> = 24.8%, tris(His)-Cu<sup>2+</sup> = 73.6%). (E) + 0.6 mM CuCl<sub>2</sub> (aquo-Cu<sup>2+</sup> = 3.1%, bis(His)-Cu<sup>2+</sup> = 19.6%, tris(His)-Cu<sup>2+</sup> = 77.3%). (F) + 0.8 mM CuCl<sub>2</sub> (aquo-Cu<sup>2+</sup> = 5.7%, bis(His)-Cu<sup>2+</sup> = 20.7%, tris(His)-Cu<sup>2+</sup> = 73.6%). (G) + 1.0 mM CuCl<sub>2</sub> (aquo-Cu<sup>2+</sup> = 19.0%, bis(His)-Cu<sup>2+</sup> = 18.6%, tris(His)-Cu<sup>2+</sup> = 62.4%). (H) + 1.2 mM CuCl<sub>2</sub> (aquo-Cu<sup>2+</sup> = 15.6%, bis(His)-Cu<sup>2+</sup> = 27.3%, tris(His)-Cu<sup>2+</sup> = 57.2%). (I) + 1.4 mM CuCl<sub>2</sub> (aquo-Cu<sup>2+</sup> = 23.3%, bis(His)-Cu<sup>2+</sup> = 24.4%, tris(His)-Cu<sup>2+</sup> = 52.3%). (J) + 1.6 mM CuCl<sub>2</sub> (aquo-Cu<sup>2+</sup> = 19.8%, bis(His)-Cu<sup>2+</sup> = 23.6%, tris(His)-Cu<sup>2+</sup> = 56.7%). (K) + 1.8 mM CuCl<sub>2</sub> (aquo-Cu<sup>2+</sup> = 26.1%, bis(His)-Cu<sup>2+</sup> = 17.6%, tris(His)-Cu<sup>2+</sup> = 56.3%). (L) + 2.0 mM CuCl<sub>2</sub> (aquo-Cu<sup>2+</sup> = 26.0%, bis(His)-Cu<sup>2+</sup> = 21.4%, tris(His)-Cu<sup>2+</sup> = 52.6%). (M) + 4 mM CuCl<sub>2</sub> (aquo-Cu<sup>2+</sup> = 57.5%, bis(His)-Cu<sup>2+</sup> = 19.5%, tris(His)-Cu<sup>2+</sup> = 23.5%). (N) + 6 mM CuCl<sub>2</sub> (aquo-Cu<sup>2+</sup> = 78.8%, bis(His)-Cu<sup>2+</sup> = 0.0%, tris(His)-Cu<sup>2+</sup> = 21.3%). (O) + 8 mM CuCl<sub>2</sub> (aquo-Cu<sup>2+</sup> = 83.0%, bis(His)-Cu<sup>2+</sup> = 6.1%, tris(His)-Cu<sup>2+</sup> = 10.9%). (P) + 10 mM CuCl<sub>2</sub> (aquo-Cu<sup>2+</sup> = 88.4%, bis(His)-Cu<sup>2+</sup> = 5.9%, tris(His)-Cu<sup>2+</sup> = 5.7%). Scale bar = 100 nm.

Isothermal titration calorimetry (ITC) is a powerful tool that reports on the heat changes during a titration experiment that are produced due to analyte binding. It is most often used to study the binding of small molecules to macromolecules. This technique can provide useful information on the stoichiometry of binding between a small molecule and the macromolecule. A few years ago, a past member of the Lynn lab observed, in a short timeframe, that  $\text{Cu}^{2+}$  produced no supramolecular structures with K16A. Interested in learning more about what appeared to be an inhibitory interaction of  $\text{Cu}^{2+}$  with K16A, Jijun Dong sought to define the binding interactions between these two molecules using ITC. Her data is included in this dissertation because of the nice parallel to our optical data thus far described.

We have thus far shown that optically, it is apparent the optimal range of binding for  $\text{Cu}^{2+}$  to K16A falls between the molar ratios of 0.5:1 and 1:1 ( $\text{Cu}^{2+}$ :K16A). In the ITC experiment it is first demonstrated that  $\text{Cu}^{2+}$  does not interact with the buffer, **Figure 4.5A**. By injecting 1 mM  $\text{Cu}^{2+}$  solution into a 0.05 mM K16A solution at 5  $\mu\text{L}$  increments, the exothermic reaction can be followed over time (**Figure 4.5B**). Upon each injection, the heat released is corrected by heat of dilution measured for  $\text{Cu}^{2+}$  added to 25 mM MES buffer and normalized per mole of  $\text{Cu}^{2+}$  injected. The result is plotted against the molar ratio of  $\text{Cu}^{2+}$  to K16A monomer. Saturation of all sites appears at a molar ratio of  $\sim 0.6$  (**Figure 4.5C**). While there are concerns in regard to the discrepancies heat of assembly could contribute to the data, we are confident that at such low concentrations of peptide (50  $\mu\text{M}$ ) self-assembly is not taking place (see **Chapter 2**). While low concentration of peptide controls for such potential issues, we must also consider the possibility that within the self-assembled nanostructure, binding coordination could be



different, yielding a different degree of saturation. To address these questions more directly, we turn to electron paramagnetic resonance techniques, EPR, in the next section. In sum, data herein presented is in good agreement, and incorporation of  $\text{Cu}^{2+}$  within the peptide assembly appears to be occurring at high density.

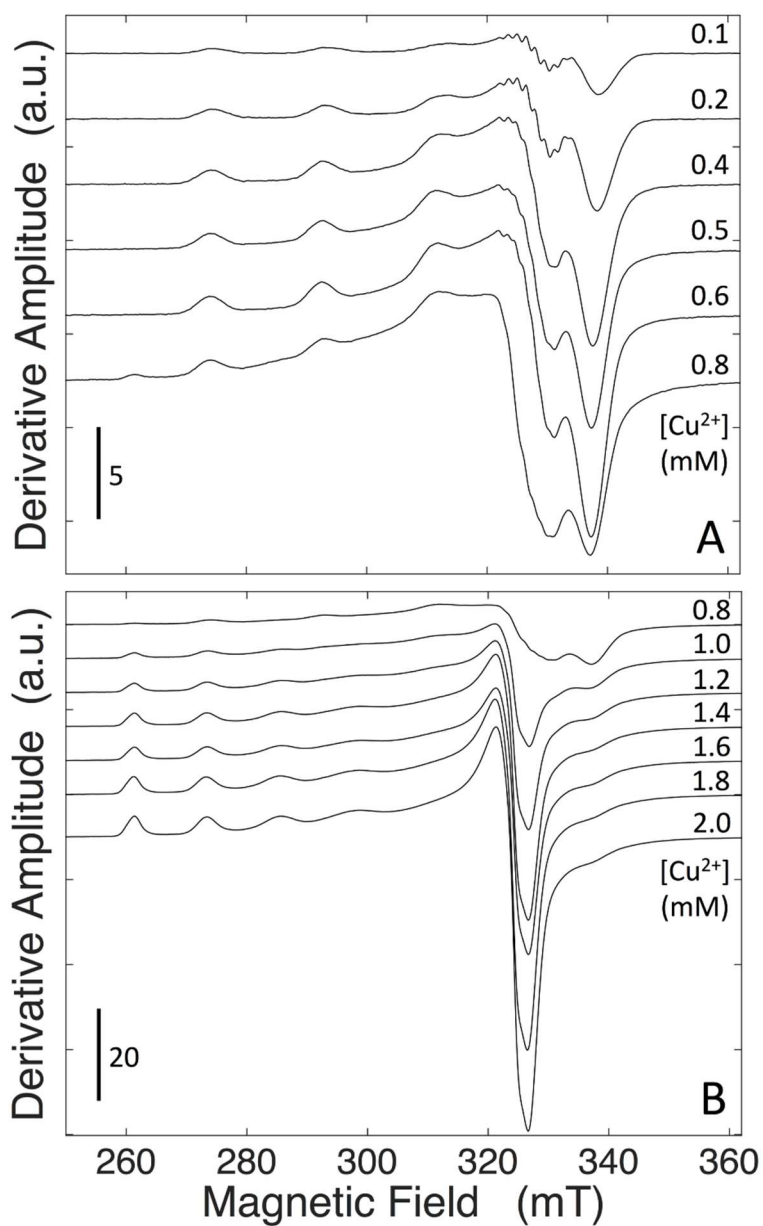


(Dong, 2006)

**Figure 4.5 – ITC of Cu<sup>2+</sup> titration of A $\beta$ (13-21)K16A in MES buffer.** (A) ITC curve of Cu<sup>2+</sup> titration into free-of-peptide buffer solution, 25mM MES pH5.6 with 10mM NaCl in de-ionized distilled water. (B) Typical isothermal titration calorimetry curve of Cu<sup>2+</sup> titration into A $\beta$ (13-21)K16A in MES buffer. 1mM Cu<sup>2+</sup> was injected into 0.05mM A $\beta$ (13-21)K16A while monitoring the heat changes over time with 5  $\mu$ L injections. Both Cu<sup>2+</sup> and A $\beta$ (13-21)K16A solution were prepared with identical buffer solution, 25mM MES pH5.6 with 10mM NaCl in de-ionized distilled water. Titration parameters were identical to A. (C) The heat released per injection is corrected by heat of dilution measured in A, normalized per mole of Cu<sup>2+</sup> injected, and then plotted against the molar ratio of Cu<sup>2+</sup> to A $\beta$ (13-21)K16A monomer. Data was fitted with on-site binding model with all the parameter floating, giving  $N=0.521\pm 9.5E-4$ ,  $K=2.03E8 \pm 6.48E7$  and  $\Delta H=-5817 \pm 26.70$ . (see Materials and Methods for details).

### EPR analysis of K16A-Cu<sup>2+</sup> nanostructures

To corroborate and extend these data, we turned to electron paramagnetic resonance (EPR) spectroscopy to address the degree of Cu<sup>2+</sup> incorporation in the sample across the same concentration range, and to interrogate the presence of a bis-His and a tris-His Cu<sup>2+</sup> species more quantitatively. EPR spectra of Cu<sup>2+</sup> ( $S = 1/2$ ) in the presence of K16A display a distinctive dependence on the metal ion-peptide stoichiometry at a constant peptide concentration (1.0 mM; Fig. 8). At [Cu<sup>2+</sup>] = 0.1 – 0.6, the spectra are typical of a type II Cu<sup>2+</sup> center, in displaying the four Cu ( $I = 3/2$ ) hyperfine features centered around  $g_{\parallel}$ , and the single, broad derivative feature in the higher-field,  $g_{\perp}$  region, which indicates axial symmetry of the complex. The smaller, superhyperfine splitting at  $g_{\perp}$  arises from coupling to multiple, near-equivalent <sup>14</sup>N ( $I=1$ ) ligands, consistent with tris-His coordination. From 0.4 – 0.6 mM Cu<sup>2+</sup>, the <sup>14</sup>N superhyperfine feature diminishes as it broadens and shifts, while the Cu lineshape is maintained. This indicates two populations of Cu<sup>2+</sup> sites, that are distinguished by a difference in magnetic relaxation. Loading of the K16A binding sites saturates between [Cu<sup>2+</sup>] = 0.6 and 0.8 mM, as shown by the appearance of the free-solution, Cu<sup>2+</sup> signal, [Cu(H<sub>2</sub>O)<sub>6</sub>]<sup>2+</sup>, at 0.8 mM (Figure 4.6A), and linear increase in the free Cu<sup>2+</sup> signal at higher concentrations (Figure 4.6B).



**Figure 4.6 – CW-EPR spectra of the K16A-  $\text{Cu}^{2+}$  complex for different  $\text{Cu}^{2+}$ :peptide ratios.** Each spectrum corresponds to the indicated  $\text{Cu}^{2+}$  concentration and 1.0 mM peptide. (A)  $\text{Cu}^{2+}$  concentration range, 0.1 – 0.8 mM. (B)  $\text{Cu}^{2+}$  concentration range, 0.8 – 2.0 mM. The absolute (unnormalized) amplitudes of the spectra in panels A and B are referenced to a common scale (arbitrary units, a. u.), given by the vertical bar. CW-EPR acquisition parameters are provided in Materials and Methods.

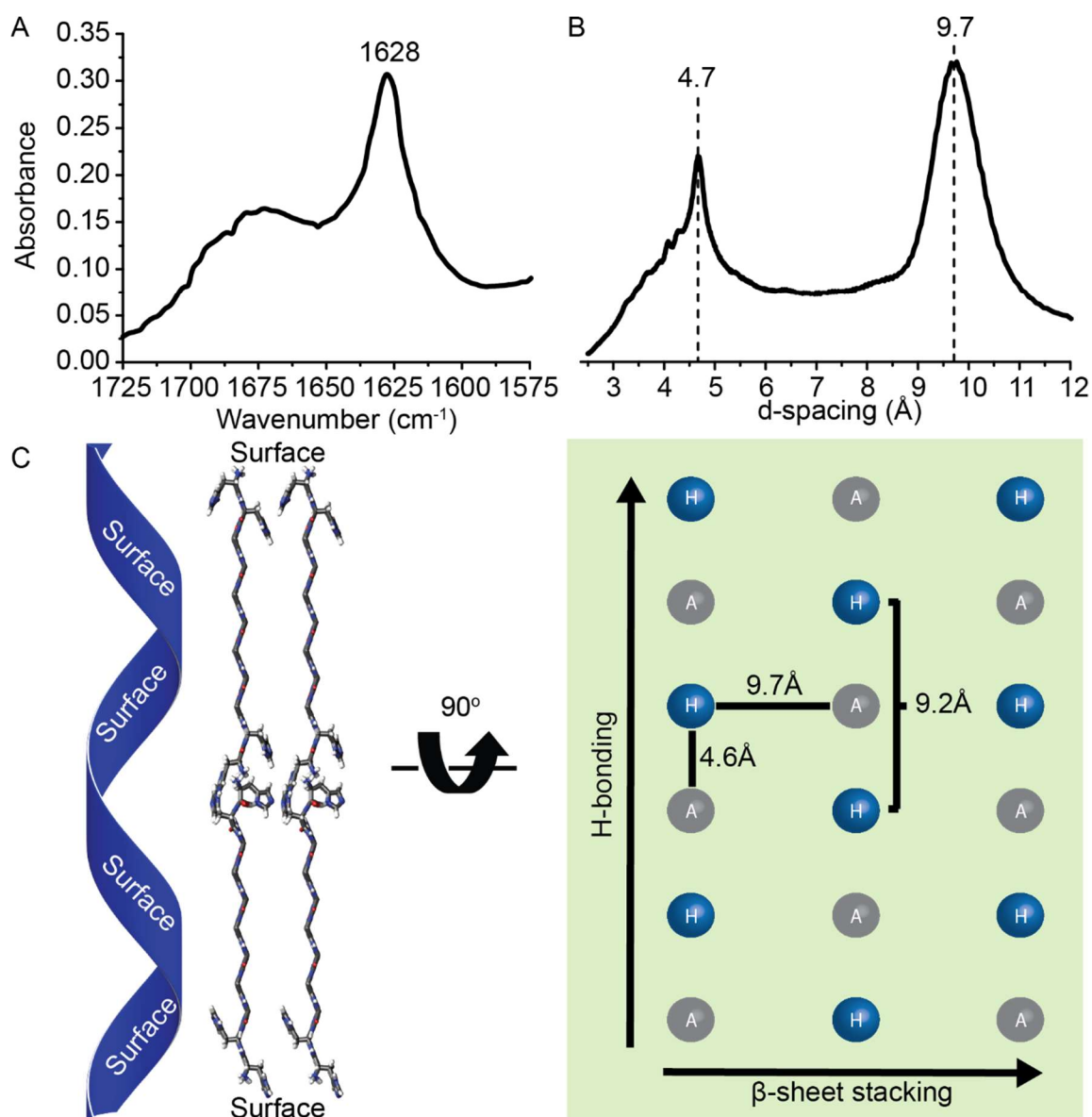
### **Cu<sup>2+</sup> is isolated in the K16A peptide bilayer, not at the nanoribbon surface**

In **Chapter 3**, we demonstrated the peptide arrangement defining K16A-Cu<sup>2+</sup> nanostructures. Furthermore, we determined that the designed MAN is composed of a peptide bilayer. To build a complete model of this MAN, we had to define where the Cu<sup>2+</sup> is incorporated: 1) within the leaflet interface of the bilayer, 2) at the surface of the nanostructure, or 3) at both the surface and the leaflet interface. We reasoned that, given the antiparallel peptide arrangement, and the registry shift by two amino-acids assigned to this K16A-Cu<sup>2+</sup> nanostructure, we needed to design a similar surface to serve as a mimic of the ribbons surface and, in this way, indirectly interrogate the interactions of Cu<sup>2+</sup> at the surface of the MAN. To accomplish this, we first needed to more accurately define the peptide arrangement of the nanostructure by experimentally determining the distances between peptides along a H-bonded  $\beta$ -sheet and in between  $\beta$ -sheet laminates. To do this we looked to X-ray powder diffraction (XRD).

Methodology for preparing samples for XRD can be found in the Materials and Methods section of this chapter. Briefly, all organic solvents are first removed from the sample mixture. Once in water, the sample is frozen and lyophilized until a powder, representing your structure, remains. In some cases, samples must be bundled before lyophilization (Lu et al., 2007). Powder is tightly packed in a capillary tube and placed in the X-ray machine to run experiments. Diffraction data for K16A-Cu<sup>2+</sup> showed two distinct distances characteristic of a cross- $\beta$  rich assembly (**Figure 4.7B**). The first, at 4.7 Å is characteristic of H-bonded peptides in a  $\beta$ -sheet. The second, at 9.7 Å reports on the laminating distance between  $\beta$ -sheets. The  $\beta$ -sheet character is further corroborated by FT-IR data showing an amide I band at 1628 cm<sup>-1</sup> (**Figure 4.7A**). Together with the AFM

data presented in **Figure 3.27**, a 3D model of the ribbon assemblies and a map of the ribbon surface can be organized (**Figure 4.7C**). This representation will aid in the construction and visualization of the supramolecular surface mimic.

While it is clear that a higher density of histidine residues exists at the bilayer interface of the nanoribbon, it is impossible to state with any certainty from this data alone, which portion of the MAN  $\text{Cu}^{2+}$  most densely populates. We predict that given the existence of a bilayer,  $\text{Cu}^{2+}$  will be biased to the region with the largest density of histidine ligands. Nevertheless, our investigation of the nanoribbon surface brought about some interesting results explored in the following subsection.



**Figure 4.7 – Surface characterization of K16A-Cu<sup>2+</sup> nanoribbons.** (A) FT-IR spectrum displays an Amide I band at 1628 cm<sup>-1</sup>, characteristic of a β-sheet peptide assembly. (B) X-Ray powder diffraction data displays the 4.7 Å d-spacing expected for H-bonded peptides extending along a β-sheet. Laminating β-sheets show a d-spacing separation of 9.7 Å. (C) Cartoon representation of the K16A-Cu<sup>2+</sup> ribbon, defined by a peptide bilayer. Rotated 90 degrees, representations of the ribbon surface illustrating the powder diffraction separation between H-bonded peptides and laminating sheets.

### Indirectly isolating the surface of K16A-Cu<sup>2+</sup> ribbons

To define the location of Cu<sup>2+</sup> incorporation in the K16A-Cu<sup>2+</sup> nanostructure, we designed an analogous surface using a well-characterized model peptide (W. Seth Childers et al., 2010; A. K. Mehta et al., 2008). Ac-K<sup>16</sup>LVFFAL<sup>22</sup>-NH<sub>2</sub> (E22L) is an amphiphilic peptide and a congener of the A $\beta$  nucleating core that self-assembles into antiparallel, out-of-register by one amino-acid nanotubes characterized by a peptide bilayer (**Figure 4.8A**). This peptide and the well-defined nanotubes it readily forms (**Figure 4.8B**) have been characterized and shown to assemble independent of pH. Furthermore, the E22L nanotubes were recently shown to function as enantioselective catalysts for retro-aldol chemistry (Omosun et al., 2017). Importantly, because of the peptide arrangement they possess, the surface of these nanotubes is nearly identical to that of the K16A-Cu<sup>2+</sup> ribbons, with small differences in the d-spacing between  $\beta$ -sheets. Regardless, the similarities make this peptide nanotubes excellent candidates for their application in the study of Cu<sup>2+</sup> binding at the ribbon surface. We reasoned that, by changing the lysine residue (Lys16) to histidine (His) we could replicate the ribbon surface on a preassembled peptide nanotube of Ac-H<sup>16</sup>LVFFAL<sup>22</sup>-NH<sub>2</sub> (K16H,E22L), a structure that mimics the surface of K16A-Cu<sup>2+</sup> ribbons more closely.

We initially assembled K16H,E22L in standard conditions for the K16A-Cu<sup>2+</sup> nanoribbons, 25 mM MES, pH: 5.6, to mimic conditions for Cu<sup>2+</sup> addition. However, because of the high dielectric of the solvent, and the rich hydrophobic character of the peptide, the sample reached maturity after only four days of assembly, forming a heterogeneous mixture of twisted ribbons, fibers and belts, not the desired nanotubular assemblies (**Figure 4.9A and B**). Given these results, we followed the assembly



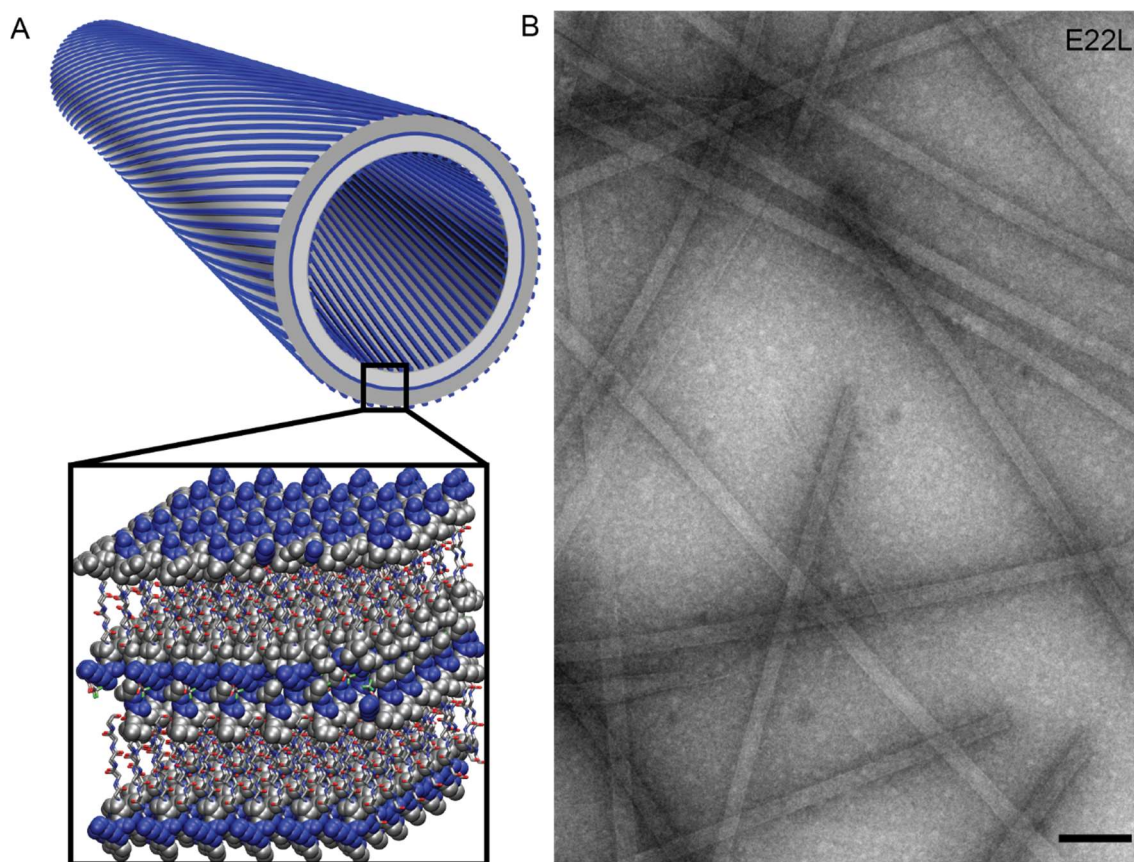
procedure of E22L, 40% CH<sub>3</sub>CN and 60% DI water at pH: 2. Results demonstrate that, after a period of 6 days, the presence of nanotubes is evident among peptide particles and, after 14 days the population of particles has matured and only nanotubes of a homogeneous size remain (**Figure 4.9C and D**). Before moving any further, we looked to characterize these nanotubes to convince ourselves that the surfaces are identical to that of E22L nanotubes.

Comparing the two nanostructures by CD, both are  $\beta$ -sheet rich nanotubes (**Figure 4.10**). FT-IR confirms this structural assignment by the strong Amid I band at 1624 cm<sup>-1</sup> (**Figure 4.12A**). Furthermore, the K16H,E22L nanotubes also have a strong Amide I band at 1694 cm<sup>-1</sup> suggesting peptides in this nanotube are organized in an antiparallel orientation, similar to the E22L nanotubes. Solid-state NMR analysis of the K16H,E22L nanotubes corroborates the antiparallel assignment and defines the peptide registry to be identical to that of the E22L nanotubes, out-of-register by one amino acid (**Figure 4.11**). Finally, XRD data shows a difference in the  $\beta$ -sheet lamination distance of only 0.1 Å (**Figure 4.12B**), further corroborating the similarities between the two nanotubes. Thus, like the surface of the E22L nanotube, the K16H,E22L nanotube is nearly identical to that of the K16A-Cu<sup>2+</sup> nanoribbon and can be used to corroborate whether or not Cu<sup>2+</sup> binds to the surface of the ribbon assembly (**Figure 4.12C and D**).

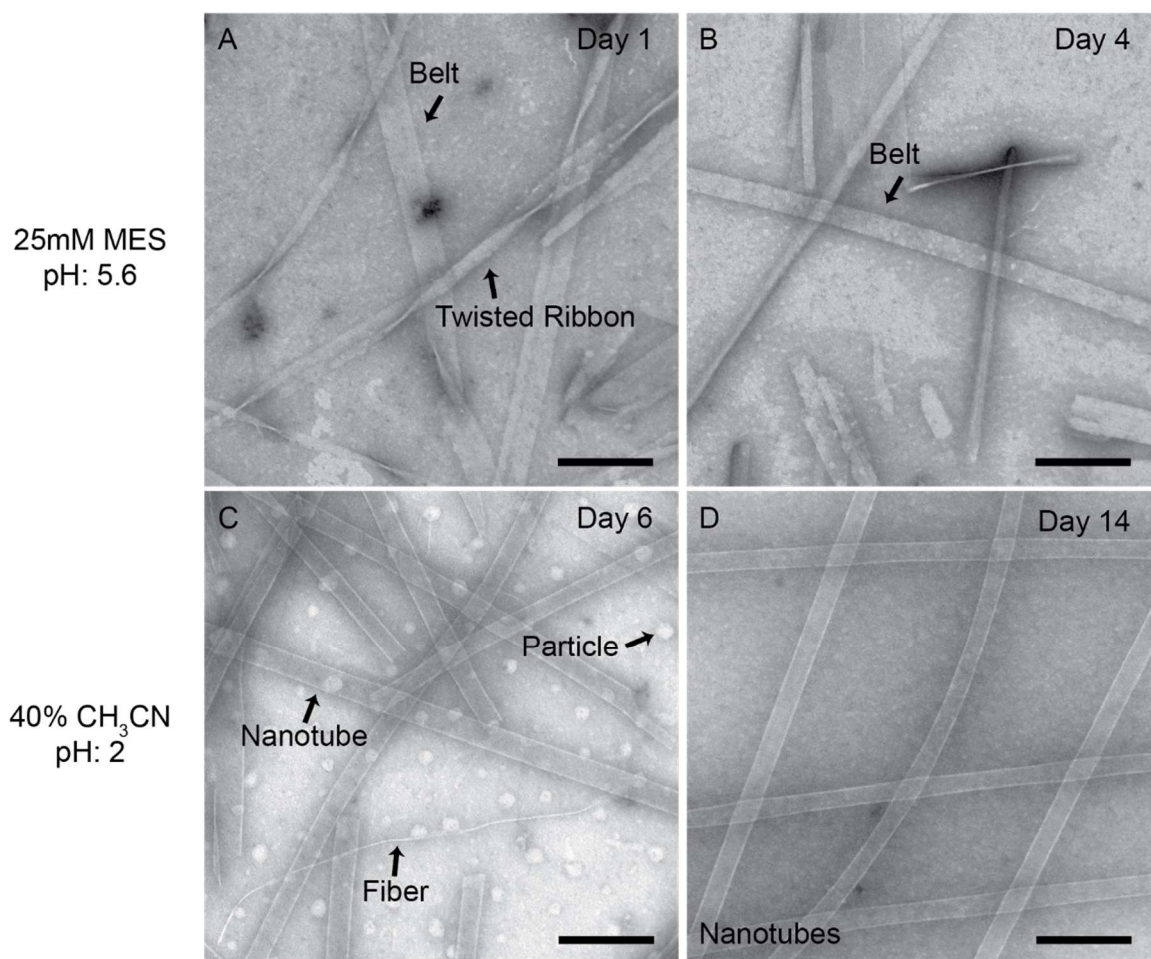
Importantly, E22L assembly conditions are not conducive to metal binding studies as Cu<sup>2+</sup> can readily interact with CH<sub>3</sub>CN (Vitale, Valina, Huang, Amunugama, & Rodgers, 2001). Furthermore, at pH: 2, all histidine side-chains would be protonated and unable to interact with any accessible Cu<sup>2+</sup> in solution. Thus, once formed, the K16H,E22L ribbons had to be isolated by centrifugation and resuspended in water,

followed by a titration of 50 mM MES buffer to reach a final concentration of 25 mM MES buffer, at pH: 5.6. After 24 hrs. these nanotubes remained intact in 25 mM MES buffer (**Figure 4.13A**). Following addition of  $\text{CuCl}_2$  and a 24 hr. long incubation period, another TEM image revealed that the nanotubes remained intact in 25 mM MES buffer (**Figure 4.13B**). Strikingly, no change in the  $\lambda_{\text{max}}$  of the aquo- $\text{Cu}^{2+}$  was evident by UV-Vis (**Figure 4.14**). This result shows that the nanotube surface of K16H,E22L is unable to bind  $\text{Cu}^{2+}$ . While this provides the first bit of evidence that  $\text{Cu}^{2+}$  cannot bind at the K16A- $\text{Cu}^{2+}$  MAN surface, we decided to explore the possibility that our working model may not be ideal, as K16H,E22L nanotubes only have one accessible His side-chain.

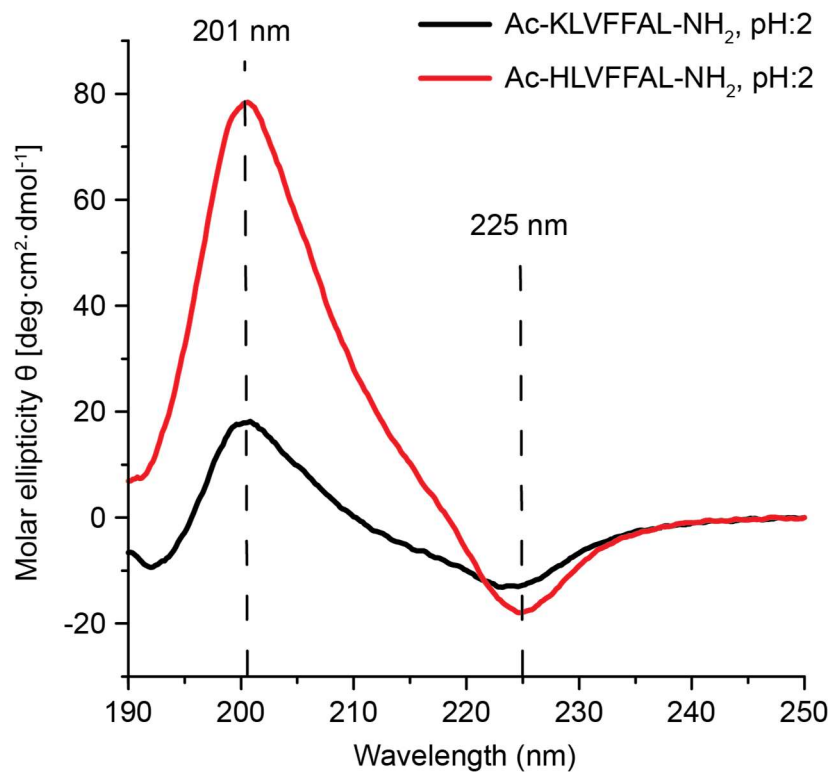
In an effort to improve our model, we extended K16H,E22L nanotubes to include another His side-chain, recreating the HH-dyad accessible in K16A peptides. Ac-HHLVFFAL-NH<sub>2</sub> (K16HH,E22L) also has the richly hydrophobic nucleating core, which should drive its assembly. We reasoned that, given the tunability of E22L – demonstrated by C12 functionalization (Ni et al., 2012) and mutations at Lys16 (S. Li et al., 2014) – at the surface as well as the peptide bilayer leaflet interphase, K16HH,E22L should form nanotubes that would still assemble in a way that maximizes hydrophobic interactions, thereby leaving histidine side-chains exposed for  $\text{Cu}^{2+}$  binding. We were further motivated by histidine's ability to self-stabilize, through  $\pi$ - $\pi$  interactions, cation- $\pi$  interactions, and hydrogen- $\pi$  interactions (Liao, Du, Meng, Pang, & Huang, 2013) as these could be important assembly driving elements in the formation of a peptide bilayer.



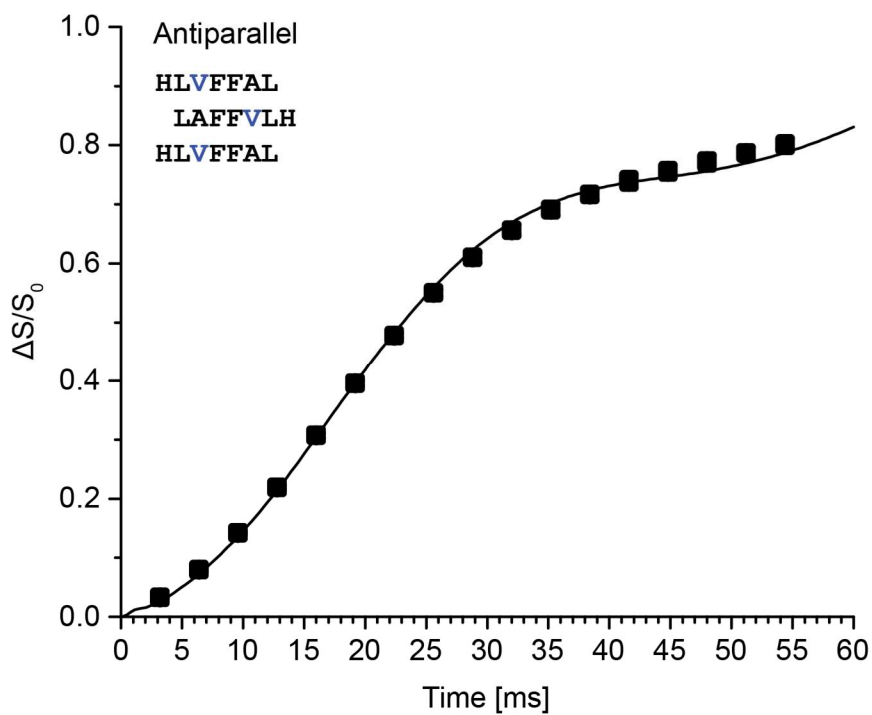
**Figure 4.8 – Cartoon representation and TEM micrograph of nanotubes formed by E22L.** (A) Representation of the nanotubes formed by KLVFFAL (E22L), highlighting the peptide bilayer which defines the nanotube wall. (B) TEM micrograph of E22L nanotubes display a homogeneous distribution throughout the grid. Scale bar = 200 nm.



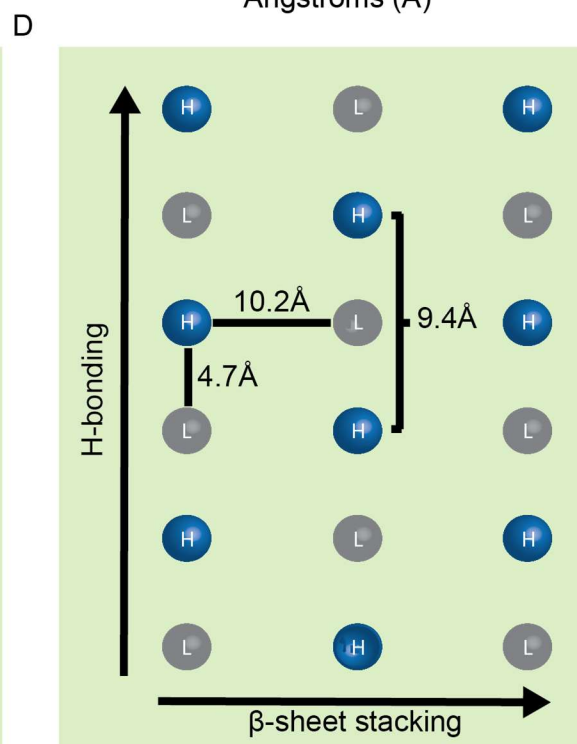
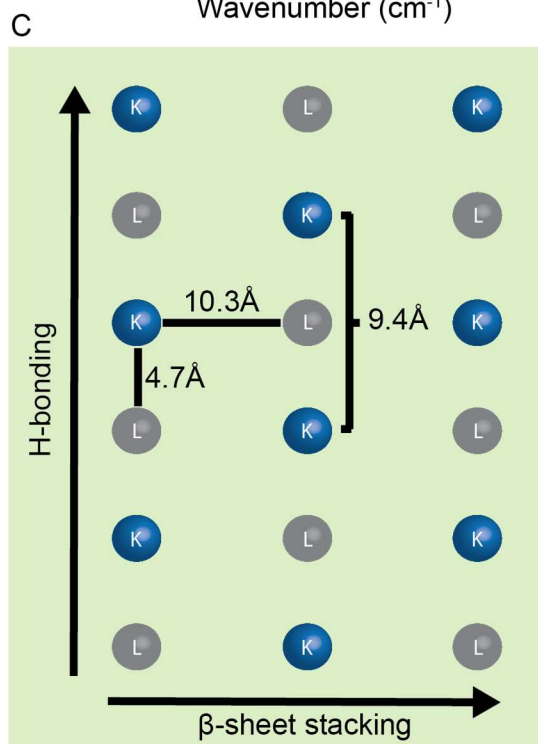
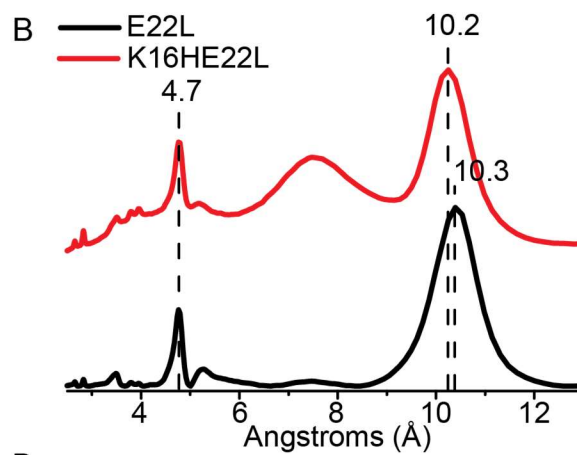
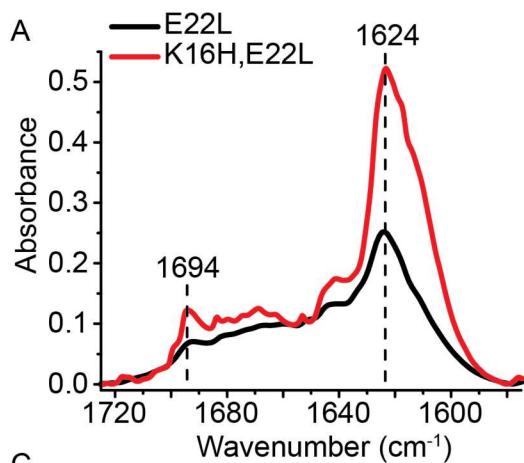
**Figure 4.9 – TEM micrographs of K16H,E22L assembly in different solvents.** (A and B) TEM micrographs taken after 1 day and 6 days for K16H,E22L in 25 mM MES buffer, pH: 5.6. Assemblies were composed of a heterogeneous mixture of twisted ribbons, sheets, belts and fibers. Sample matured within 24 hrs. (C and D) TEM micrographs taken after 6 days and 14 days for K16H,E22L assembled in 40% CH<sub>3</sub>CN. Assemblies were composed of a heterogeneous mixture of particles, fibers and nanotubes after 6 days but the sample matured to a collection of homogeneous nanotubes after 14 days.



**Figure 4.10** – CD spectra of E22L and K16H,E22L nanotubes. E22L (black) and K16H,E22L (red) nanotubes, assembled in 40% CH<sub>3</sub>CN, show identical CD spectra with positive ellipticities at 201 nm and a negative ellipticity of 225 nm, in agreement with a  $\beta$ -sheet rich assembly.

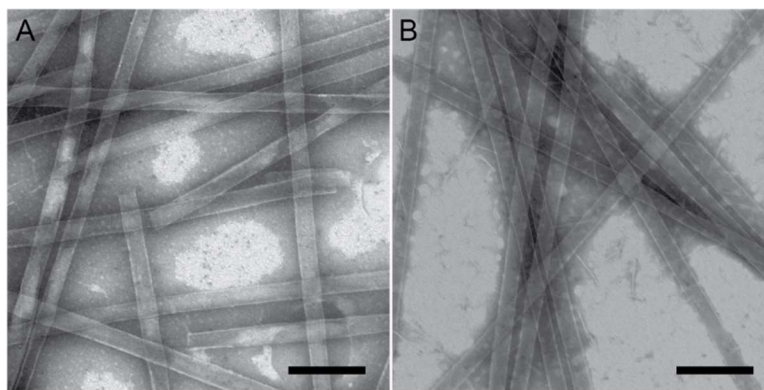


**Figure 4.11 –  $^{13}\text{C}\{^{15}\text{N}\}$  REDOR fit of K16H,E22L nanotubes.** In dephasing the carbonyl carbon of Ac-HL[ $^{15}\text{N}$ ]VFF[ $1\text{-}^{13}\text{C}$ ]AL-NH<sub>2</sub> nanotubes, the distance of the H-bonded  $^{15}\text{N}$  from the adjacent peptide was fit to 4.53 Å ( $r_1$ ) and the distance to the non-H-bonded  $^{15}\text{N}$  was fit to 5.11 Å ( $r_2$ ). The angle between the two  $^{13}\text{C}$ - $^{15}\text{N}$  internuclear vectors was fit to 154°. Results fit an antiparallel, out-of-register by one-amino acid arrangement of peptides.



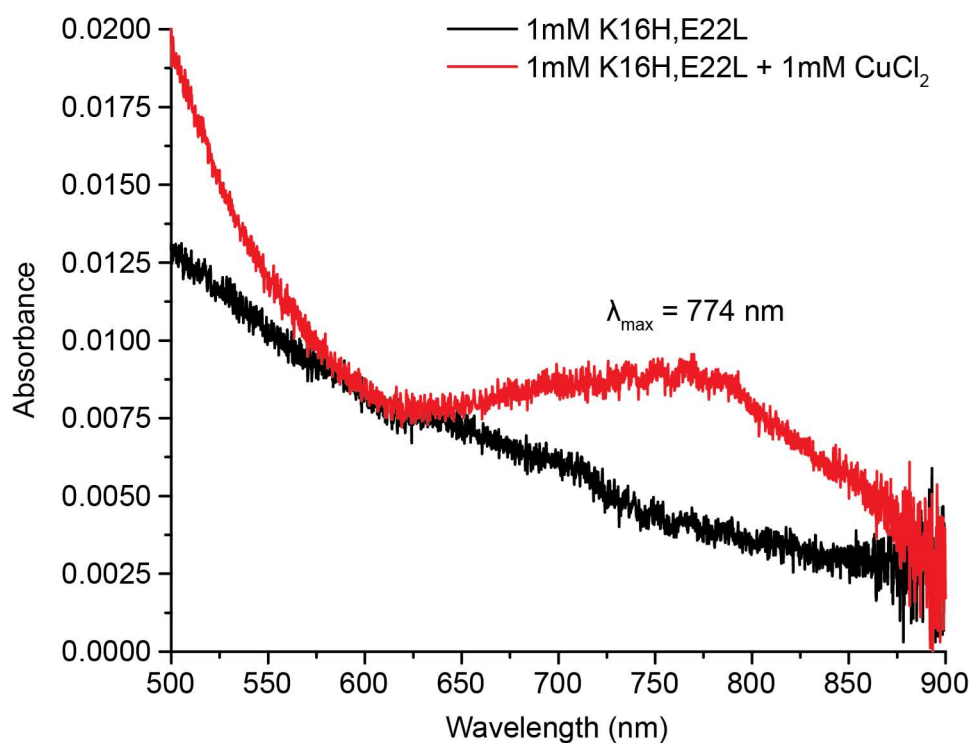
**Figure 4.12 – Surface characterization of E22L and K16H,E22L nanotubes.**

Structural comparison between KLVFFAL (E22L) or HLVFFAL (K16H,E22L) nanotubes. (A) FT-IR data displays an expected Amide I band at  $1624\text{ cm}^{-1}$  characteristic of a  $\beta$ -sheet peptide assembly for both nanotube forming peptides. A band at  $1694\text{ cm}^{-1}$ , diagnostic of an antiparallel  $\beta$ -strand arrangement is also observed. (B) Powder diffraction data displays the  $4.7\text{ \AA}$  d-spacing expected for H-bonded peptides extending along a  $\beta$ -sheet.  $\beta$ -sheet stacking repeats show a d-spacing separation of  $10.3$  and  $10.2\text{ \AA}$  respectively. Cartoon representations of E22L (C) and K16H,E22L (D) nanotube surfaces illustrating the powder diffraction separation between H-bonded peptides and laminating sheets.

**Figure 4.13 – TEM micrographs of K16H,E22L nanotubes in the presence and**

**absence of  $\text{CuCl}_2$ .** (A) TEM micrographs of K16H,E22L nanotubes resuspended in 25 mM MES, pH: 5.6 after 24 hrs. (B) TEM micrographs of K16H,E22L nanotubes in 25 mM MES buffer + stoichiometric amounts of  $\text{CuCl}_2$  – 24hr. incubation period. Scale bar = 200 nm.





**Figure 4.14 – UV-Vis spectrum for K16H,E22L nanotubes in the presence of CuCl<sub>2</sub>.**

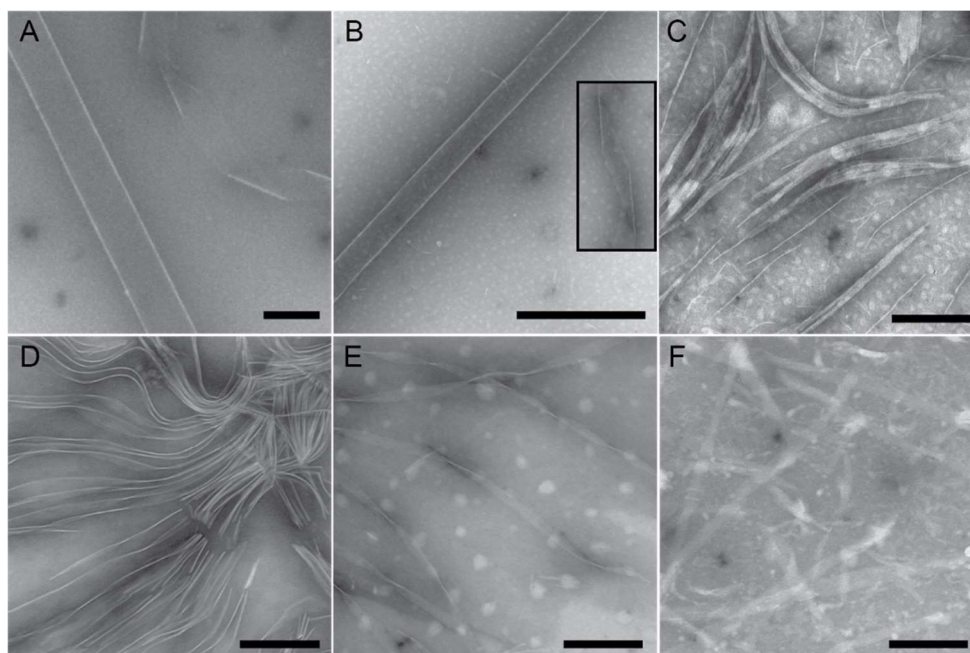
Peptide alone (black) shows the peptide scattering effect on the signal between 500 and 900 nm. In the presence of CuCl<sub>2</sub> (red), the absorbance of Cu<sup>2+</sup> does not change when compared to the MES dissolved CuCl<sub>2</sub> which has an absorbance with a  $\lambda_{\max} = 778 \text{ nm}$ .

Aware that the hydrophobic character of K16HH,E22L had changed in a non-negligible way, as a first pass we assembled K16HH,E22L in six solvent systems, composed of 50%, 40%, 30%, 20%, and 10% CH<sub>3</sub>CN with the corresponding percentages of ASTM Type II H<sub>2</sub>O and one in 100% ASTM Type II H<sub>2</sub>O (**Figure 4.15A-F**). We reasoned that increasing the solvent dielectric would force the hydrophobic collapse of the K16HH,E22L peptide amphiphile. In so doing, the hydrophobic drive of assembly would lead to an initial organization of the hydrophobic side-chains (LVFFAL) which have been shown to most readily organize to form antiparallel, out-of-register  $\beta$ -sheets. In this way, we hoped to assemble peptide nanotubes with exposed histidine side-

chains to compare  $\text{Cu}^{2+}$  binding at the surface of the nanotube with our K16A- $\text{Cu}^{2+}$  MAN.

After a one week incubation under different solvent conditions, assemblies were prepared for TEM. TEM micrographs show a heterogeneous range of morphologies from 20% to 50%  $\text{CH}_3\text{CN}$  (**Figure 4.15C-F**), forming fibers, sheets, and ribbons. In 10%  $\text{CH}_3\text{CN}$  and 100% ASTM Type II  $\text{H}_2\text{O}$ , however, nanotubes and helical ribbons were the dominant species (**Figure 4.15A and B**). Results are in agreement with our hypothesis that, for a more hydrophilic amphiphile like K16HH,E22L, a higher solvent dielectric is needed to facilitate the association of the hydrophobic core of the peptide (LVFFAL) leading to the formation of nanotubes. Indeed, we were encouraged by the fact that nanotubes formed under all conditions considered for assemblies in 100% ASTM Type II  $\text{H}_2\text{O}$  and 10%  $\text{CH}_3\text{CN}$ . **Table 4.1** summarizes assembly results across different temperatures and pH for all solvent conditions considered.

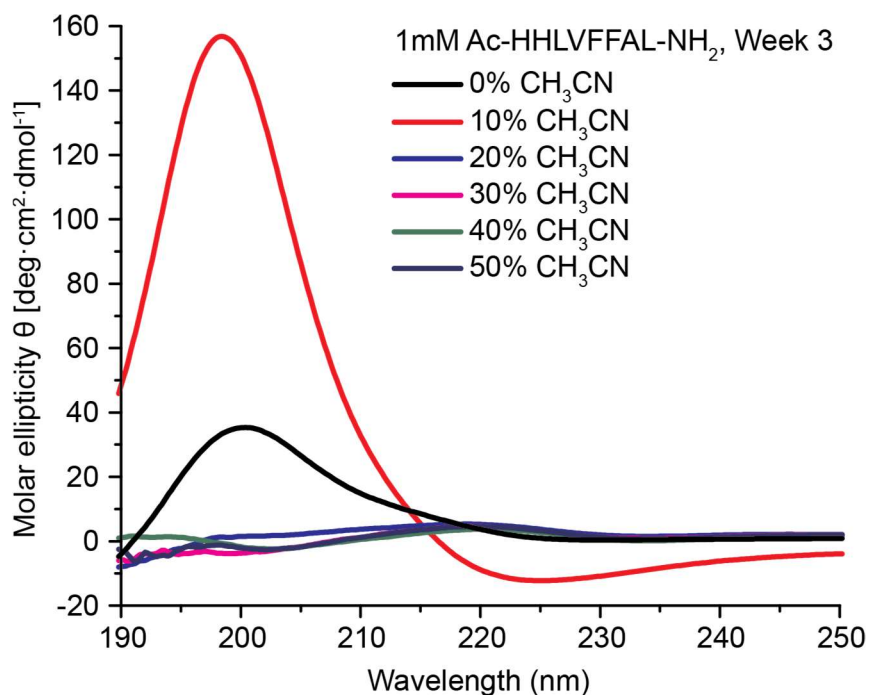
Once the sample was allowed to mature for a period of three weeks, a more homogeneous collection of nanotubes had developed for K16HH,E22L assemblies in 10%  $\text{CH}_3\text{CN}$  and 100% ASTM Type II  $\text{H}_2\text{O}$ . We monitored the degree of assembly by CD and identified the best candidate for  $\text{Cu}^{2+}$  addition studies. **Figure 4.16** shows the CD spectra collected for all solvent conditions after three weeks of assembly. It is evident that the assemblies that matured in 10%  $\text{CH}_3\text{CN}$  form most robustly, followed by assemblies in 100%  $\text{H}_2\text{O}$ . Given these results, we continued experiments using nanotubes assembled in 10%  $\text{CH}_3\text{CN}$  and considered co-assembly effects of K16HH,E22L in the presence of  $\text{Cu}^{2+}$  in aqueous solvents.



**Figure 4.15 – Assembly of K16HH,E22L in different solvent systems.** TEM micrographs of Ac-HHLVFFAL-NH<sub>2</sub> (K16HH,E22L) assembled in different solvent systems for one week. (A) Incubation conditions: ASTM Type II H<sub>2</sub>O. Assembles into helical ribbons and nanotubes. (B) Incubation conditions: 10% CH<sub>3</sub>CN and 90% ASTM Type II H<sub>2</sub>O. Assembles into helical ribbons and nanotubes. (C) Incubation conditions: 20% CH<sub>3</sub>CN and 80% ASTM Type II H<sub>2</sub>O. Assembles into bundled fibers. (D) Incubation conditions: 30% CH<sub>3</sub>CN and 70% ASTM Type II H<sub>2</sub>O. Assembles into bundled fibers. (E) Incubation conditions: 40% CH<sub>3</sub>CN and 60% ASTM Type II H<sub>2</sub>O. Assembles into twisted ribbons. (F) Incubation conditions: 50% CH<sub>3</sub>CN and 50% ASTM Type II H<sub>2</sub>O. Assembles into a mixture of fragmented fibers and sheets. Scale bar = 200 nm.

**Table 4.1 – Summary of morphologies formed in different solvent conditions with varying temperatures and pH for K16HH,E22L.**

Solvent	4°C pH: 2	25°C pH: 2	37°C pH: 2	25°C pH: 7
Water	Tubes/Ribbons	Tubes/Ribbons	Tubes/Sheets	Tubes/Ribbons
10% CH <sub>3</sub> CN	Tubes/Ribbons	Tubes/Ribbons	Tubes/Ribbons	Tubes/Ribbons
20% CH <sub>3</sub> CN	Sheets/Fibers	Ribbons/Fibers	Sheets/Ribbons	No Data
30% CH <sub>3</sub> CN	No Assembly	Fibers	No Data	No Data
40% CH <sub>3</sub> CN	No Assembly	Fibers/Particles	No Data	No Data
50% CH <sub>3</sub> CN	No Assembly	Fibers/Particles	No Data	No Data

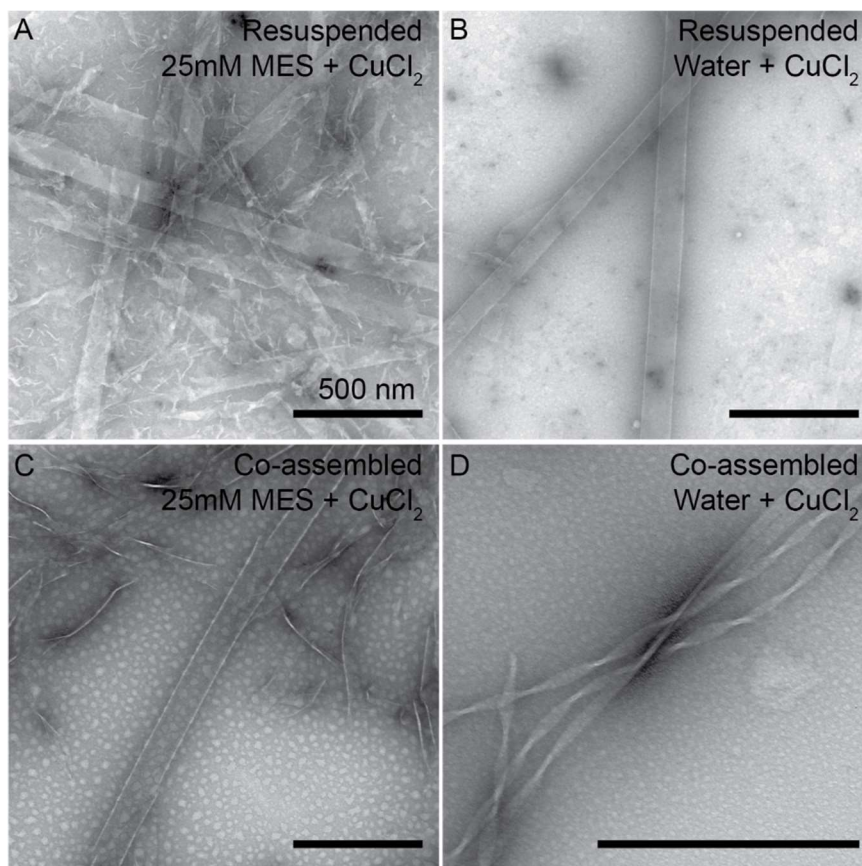


**Figure 4.16 – CD spectra of K16HH,E22L assemblies in different solvent systems.**

After an incubation period of 3 weeks, CD spectra of each of the K16HH,E22L assemblies was collected. It is evident that the conditions leading to the formation of peptide nanotubes (0% and 10% CH<sub>3</sub>CN) also yield the most robust CD spectra. Interestingly, 10% acetonitrile appears to be the ideal solvent system for generation of robust assemblies.

K16HH,E22L nanotubes formed in 10% CH<sub>3</sub>CN were isolated by centrifugation (see Materials and Methods for further details on isolation) and resuspended in aqueous solvent for CuCl<sub>2</sub> addition. After a period of 24 hr. incubation in aqueous solvent, CuCl<sub>2</sub> was added in stoichiometric amounts. TEM micrographs show that the overall morphology of the K16HH,E22L nanotube is maintained in 25 mM MES buffer (standard solvent conditions for K16A-Cu<sup>2+</sup> MAN assembly), though some helical unwinding of the ribbon is observed, and in 100% ASTM Type H<sub>2</sub>O, where no nanotube unwinding is apparent after 24 hrs. (**Figure 4.17 A and B**). Indeed, co-assembly of K16HH,E22L in the presence of CuCl<sub>2</sub> led to the formation of a mixture of twisted ribbons, fibers and nanotubes in 25 mM MES buffer, pH: 5.6, while only a homogeneous mixture of twisted ribbons were observed when peptide and Cu<sup>2+</sup> were co-assembled in 100% H<sub>2</sub>O (**Figure 4.17C and D**). Indeed, when monitored by UV-Vis (**Figure 4.18B**) results show no Cu<sup>2+</sup> binding to the nanotubes formed by the K16HH,E22L peptide, displaying a  $\lambda_{\text{max}}$  of 750 nm.

Even though no solid-state NMR data was collected for the K16HH,E22L nanotubes, FT-IR data highlights important features that gives us confidence in the data herein presented. **Figure 4.18A** shows an overlaid FT-IR spectra of K16H,E22L nanotubes and K16HH,E22L nanotubes. Both spectra share identical features with and Amid I band at 1624 cm<sup>-1</sup>, MES peak at 1640 cm<sup>-1</sup> and the secondary Amide I band at 1694 cm<sup>-1</sup>, diagnostic of an antiparallel peptide arrangement. Thus, we are confident that the surfaces of these structures are organized in much the same way as seen for K16H,E22L nanotubes (**Figure 4.12D**).

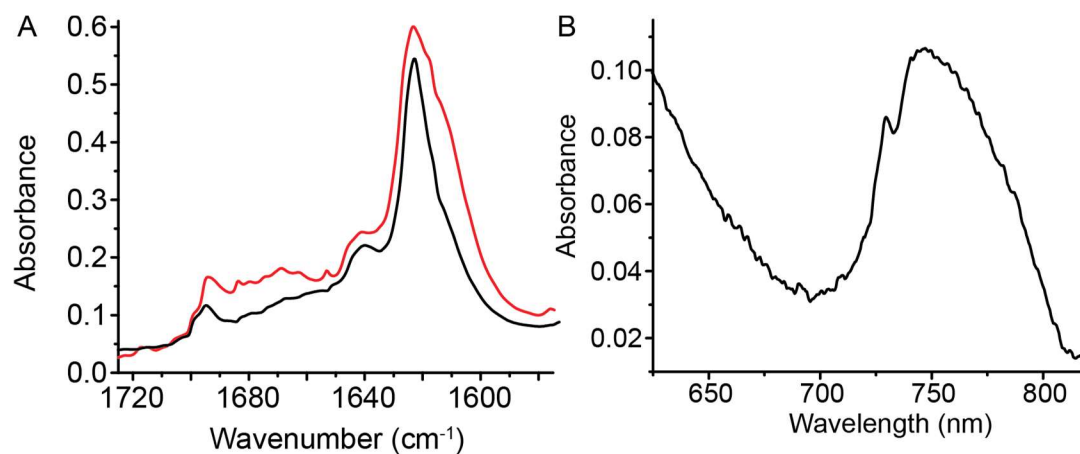


**Figure 4.17 – TEM micrographs of K16HH,E22L in the presence of  $\text{CuCl}_2$ .** (A)

K16HH,E22L nanotubes assembled in 10%  $\text{CH}_3\text{CN}$ , resuspended in 25 mM MES buffer, pH: 5.6 + stoichiometric amounts of  $\text{CuCl}_2$ . Results show a mixture of unwinding helical nanotubes and nanotubes. (B) K16HH,E22L nanotubes assembled in 10%  $\text{CH}_3\text{CN}$ ,

resuspended in ASTM Type II  $\text{H}_2\text{O}$  + stoichiometric amounts of  $\text{CuCl}_2$ . Results show a homogeneous collection of nanotubes. (C) K16HH,E22L nanotubes assembled in 25 mM MES buffer, pH: 5.6, in the presence of stoichiometric amounts of  $\text{CuCl}_2$ . Results show a

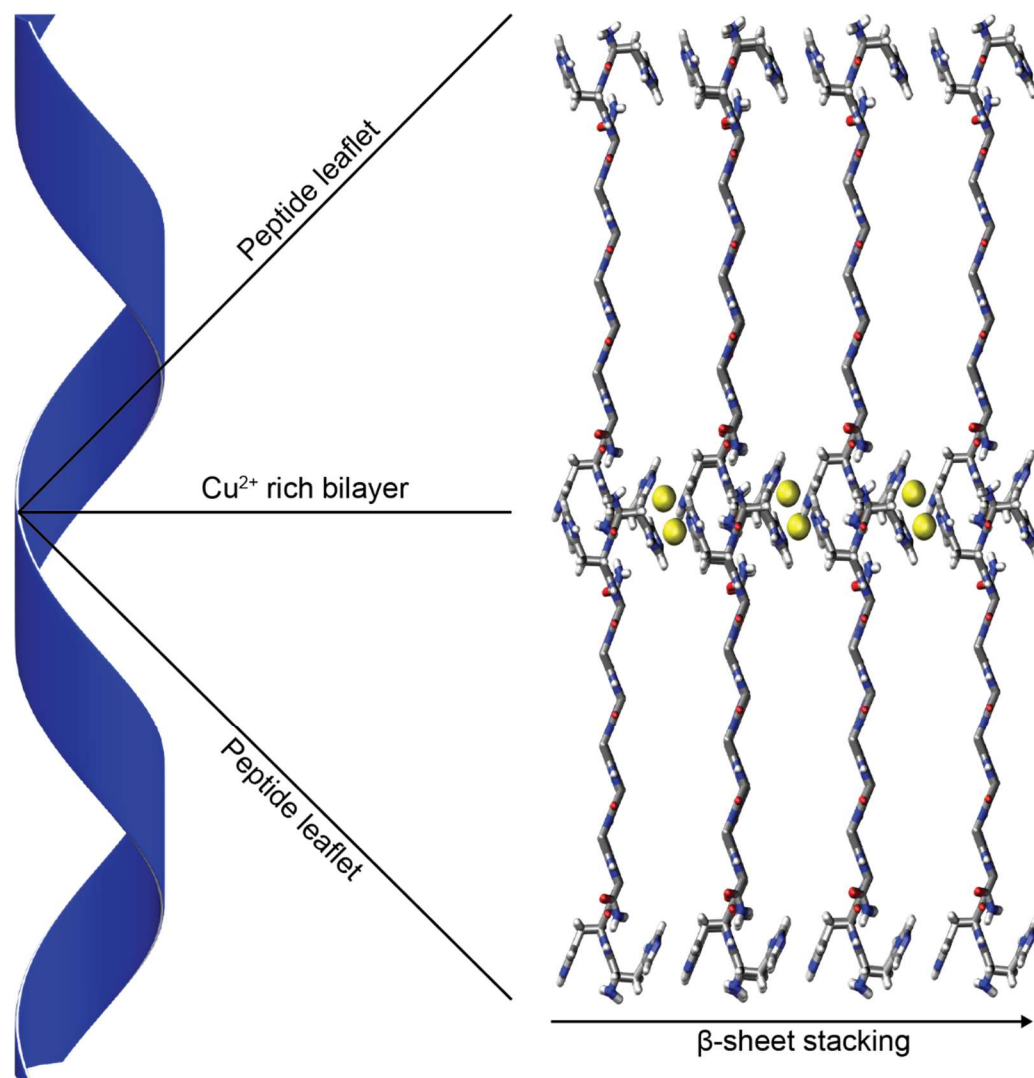
heterogeneous mixture of twisted ribbons and sparse amounts of nanotubes. (D) K16HH,E22L nanotubes assembled in ASTM Type II  $\text{H}_2\text{O}$  in the presence of stoichiometric amounts of  $\text{CuCl}_2$ . Results show twisted ribbons across the TEM grid.



**Figure 4.18 – FTIR and UV-Vis of K16HH,E22L nanotubes.** (A) FT-IR overlay of K16HH,E22L (black) and K16H,E22L (red) nanotubes. Both share identical Amide I band features at 1624 cm<sup>-1</sup> and 1694 cm<sup>-1</sup>, peak at 1640 cm<sup>-1</sup> is attributed to MES buffer. (B) UV-Vis absorbance seen for K16HH,E22L nanotubes after 24 hr. incubation in 25 mM MES with stoichiometric amounts of CuCl<sub>2</sub>,  $\lambda_{\max} = 750$  nm. No significant Cu<sup>2+</sup> interactions occur at the K16HH,E22L nanotube surface.



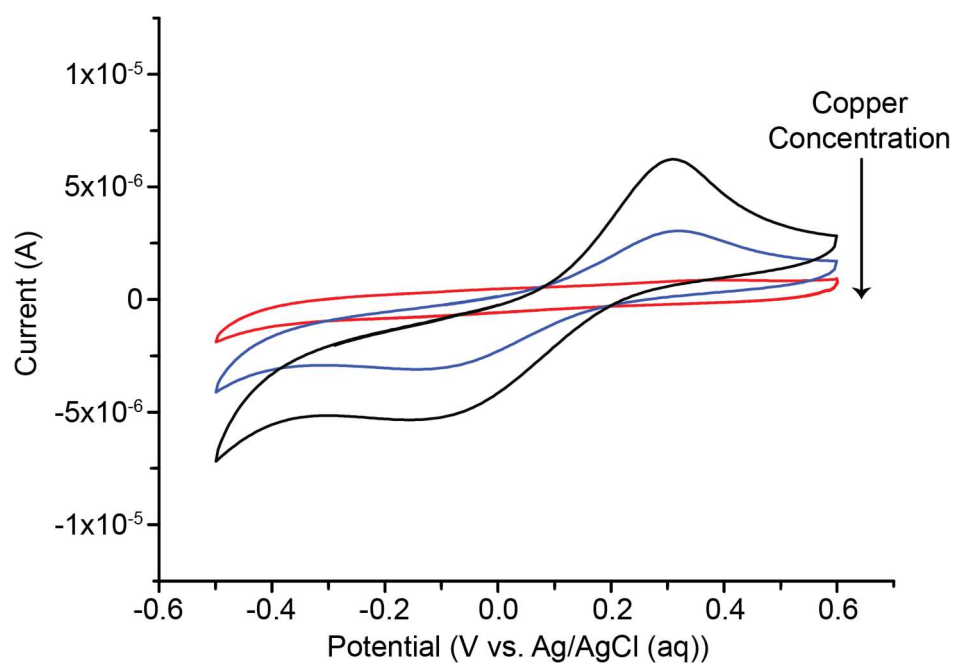
Together, these results demonstrate that the K16A-Cu<sup>2+</sup> MAN surface is unable to bind Cu<sup>2+</sup> and, thus, Cu<sup>2+</sup> must be incorporated at the peptide bilayer of this nanostructure. The compelling evidence positions the metal array inside the peptide bilayer, isolated from aqueous solvent (**Figure 4.19**).



**Figure 4.19 – Cartoon representation of the K16A peptide bilayer and the insulated copper, away from the ribbon surface. All copper bound to the ribbon is isolated from the aqueous media except at the ribbon edges.**

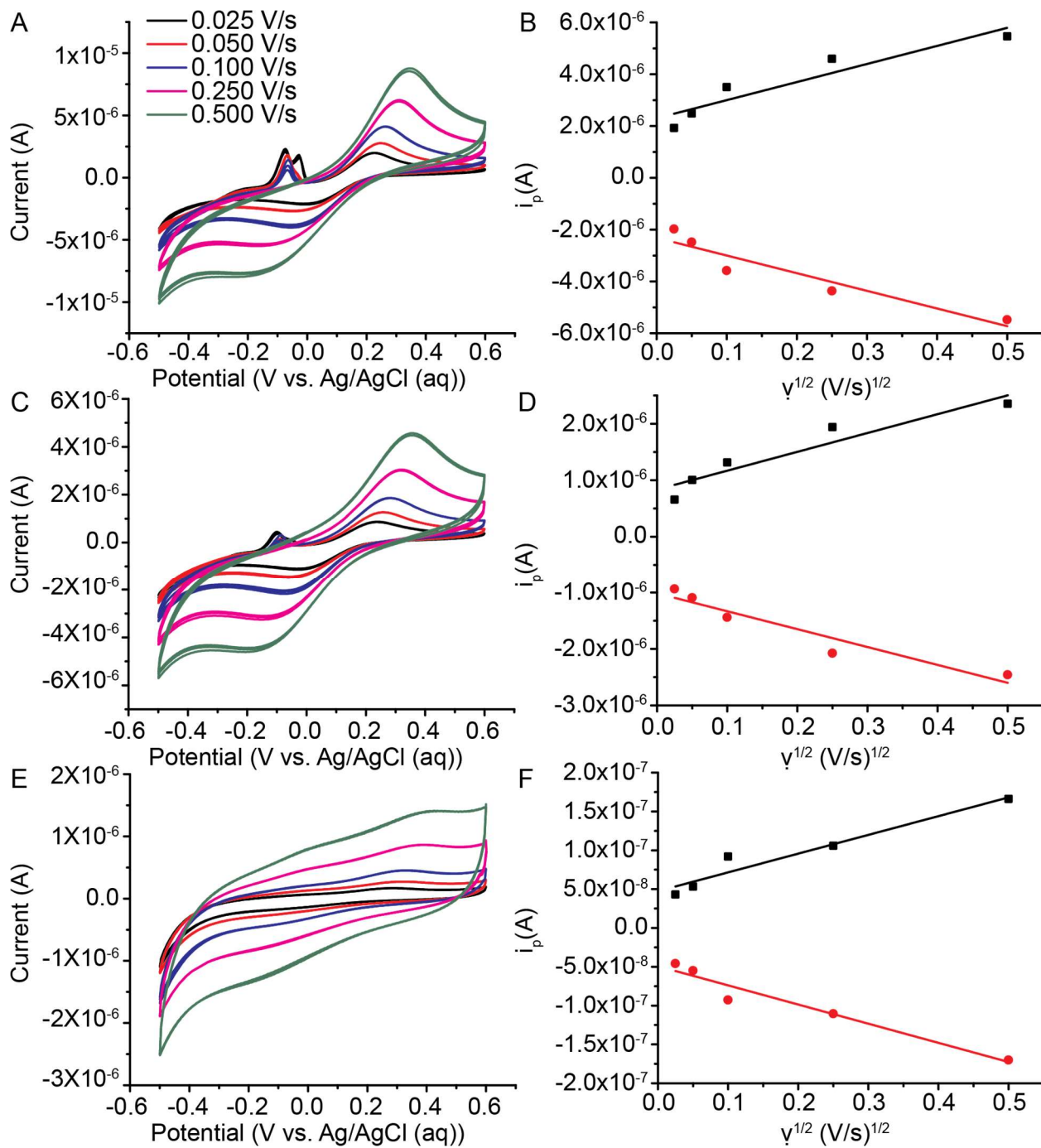
### Assessing K16A-Cu<sup>2+</sup> reactivity

To interrogate the reduction potential and gain insight into the reactivity of the metalloamyloid array we turned to electrochemistry. Cyclic voltammetry (CV) is a powerful technique that can be used to assess the electrochemical properties of an analyte in solution. We hypothesized that CV could also inform us on the different potentials associated with having two distinct metal center environments within the K16A-Cu<sup>2+</sup> ribbon architecture. If at low concentrations a scattered population of Cu<sup>2+</sup> was incorporated within the ribbon architecture with one preferential coordination environment (tris-His), as more Cu<sup>2+</sup> became accessible and saturated the secondary metal coordination sites (bis-His) there would be a change in the electrochemical properties of the metalloamyloid array. Effects on the reduction potential across different concentrations would be observed as the density and proximity of Cu<sup>2+</sup> increased with concentration. Cyclic voltammetry experiments were therefore run at three different concentrations of Cu<sup>2+</sup>, 0.25 mM, 0.4 mM and 0.5 mM while maintaining the peptide concentration at 0.5 mM. These three concentrations were chosen to assess electrochemical effects in the presence of large Cu<sup>2+</sup> excess, minimal Cu<sup>2+</sup> excess and no free Cu<sup>2+</sup> in solution. **Figure 4.20** highlights the concentration effects on current for voltammograms of K16A-Cu<sup>2+</sup> ribbons collected at a 0.25 V/s scan rate. At 0.25 mM [Cu<sup>2+</sup>] we approach the instrumentation limit as the voltammogram looks similar to the solvent background, however, the anodic and cathodic waves are still distinguishable and current values are listed in **Table 4.2**.



**Figure 4.20 – Concentration effects on electrochemical signal for K16A-Cu<sup>2+</sup>**

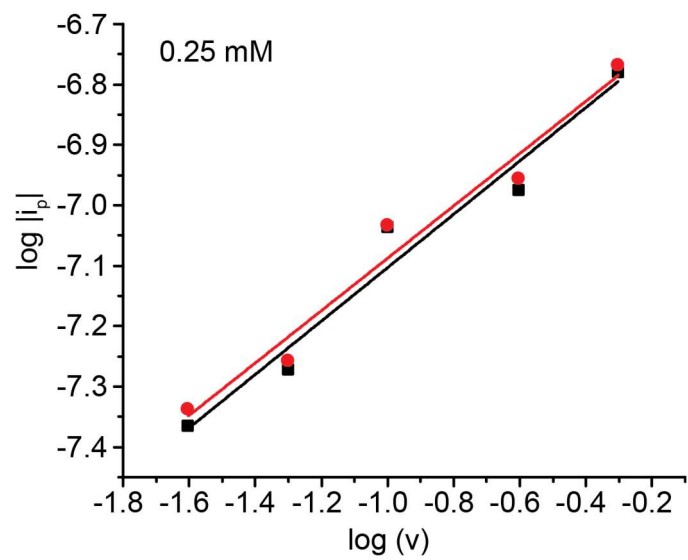
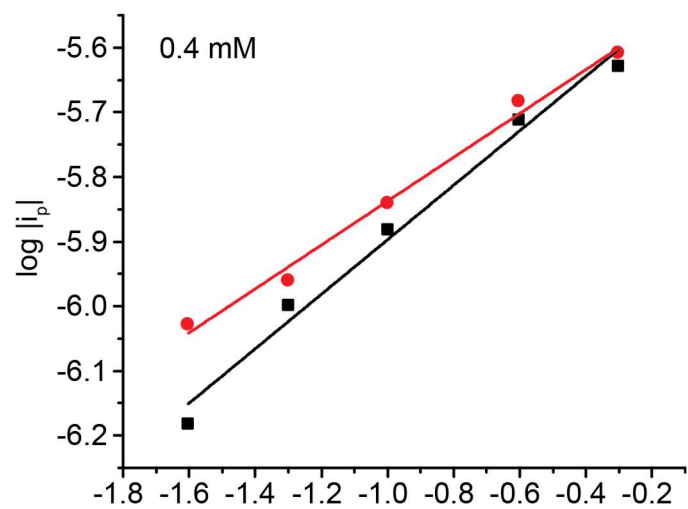
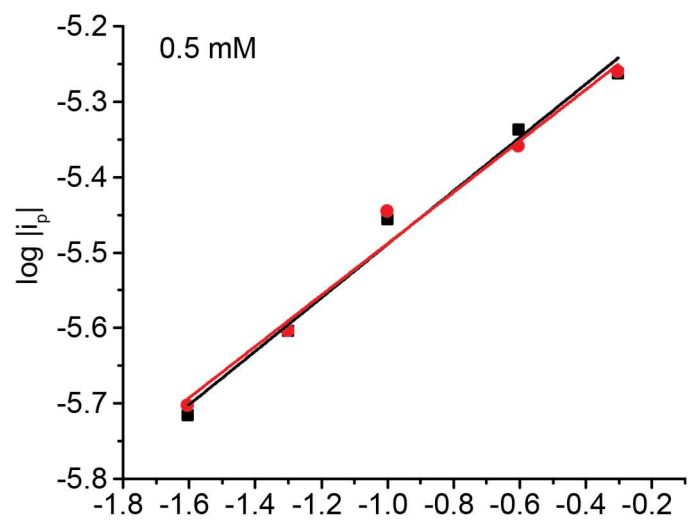
**nanostructures.** Voltammograms collected at a scan rate of 0.25 V/s for K16A-Cu<sup>2+</sup> assemblies with 0.5 mM (black), 0.4 mM (blue) and 0.25 mM (red) Cu<sup>2+</sup> concentrations demonstrate the concentration effects on the intensities for the anodic and cathodic waves. To a first approximation peak position does not change.



**Figure 4.21 – Voltammograms and Randles-Sevcik plots of K16A-Cu<sup>2+</sup> ribbons at different scan rates.** CV experiments were conducted across different Cu<sup>2+</sup> concentrations with the peptide concentration maintained at 0.5 mM throughout each experiment. (A and B) 0.5 mM Cu<sup>2+</sup> concentration. The Randles-Sevcik plot (B) represent the anodic (black squares) and cathodic (red circles) current at the given Cu<sup>2+</sup> concentration with Pearson's r values of 0.94 and -0.95 respectively and r<sup>2</sup> values of 0.85 and 0.87 respectively. C and D represent a 0.4 mM Cu<sup>2+</sup> concentration. The Randles-Sevcik plot (D) represent the anodic (black squares) and cathodic (red circles) current at the given Cu<sup>2+</sup> concentration with Pearson's r values of 0.95 and -0.96 respectively and r<sup>2</sup> values of 0.87 and 0.89 respectively. E and F represent a 0.25 mM Cu<sup>2+</sup> concentration. The Randles-Sevcik plots represent the anodic (black squares) and cathodic (red circles) current at the given Cu<sup>2+</sup> concentration with Pearson's r values of 0.97 and -0.98 respectively and r<sup>2</sup> values of 0.92 and 0.93, respectively.

**Figure 4.21A, C and E** show the voltammograms collected at the three different concentrations (0.5, 0.4 and 0.25 mM respectively) across five different scan rates. The anodic and cathodic waves are assigned to the  $\text{Cu}^+/\text{Cu}^{2+}$  and  $\text{Cu}^{2+}/\text{Cu}^+$  transitions. In the presence of large copper excess (**Figure 4.21A**), a wave is observed around -0.1 V which is assigned to  $\text{Cu}^+/\text{Cu}^0$  transition for copper that remains in solution;  $\text{Cu}^+$  in aqueous solution is unstable and subject to reduction and oxidation disproportionation. At minimal copper excess (**Figure 4.21C**) this wave ( $\text{Cu}^+/\text{Cu}^0$ ) is nearly absent, this gives us confidence in our assignment of this species to copper that remains in solution. With no free copper in solution, the  $\text{Cu}^+/\text{Cu}^0$  disproportionation wave is not observed, however, this could be due to the Helmholtz layer effects of the solvent which may drown out the metalloamyloid signal as it is very weak at the 0.25 mM analyte concentration, thus, emphasis for the assignment of this wave to copper in solution is placed on the effects seen from 0.5 mM to 0.4 mM  $\text{Cu}^{2+}$ . The Randles-Sevcik plots of **Figure 4.21** display the relationship between current and scan rate. Deviations from linearity demonstrate deviation from reversibility. It is observed that K16A- $\text{Cu}^{2+}$  ribbons display the best linear relationship with no free copper (**Figure 4.21F**), while with increasing copper concentrations in solution increasing deviation is observed for both anodic and cathodic currents (**Figure 4.21B and D**). From the slope of these lines the diffusion coefficient (D) can be obtained for the samples at each of the different concentrations, these are summarized in **Table 4.2**. The values of the measured diffusion coefficients match nicely with that of plastocyanin,  $8.9\text{E}10^{-7}$  ( $\text{cm}^2/\text{s}$ ) (Sanderson, Anderson, & Gross, 1986). Given these values, it became important to interrogate the form of interaction between the redox species and electrode surface. The interactions could take place by pure diffusion control,

pure adsorption control or a mixture of adsorption-diffusion controlled processes. Indeed, the dominating process can be diagnosed from the slope of the straight line of  $\log |i_p|$  vs.  $\log (v)$  as discussed in **Chapter 3**. The plots of  $\log |i_p|$  vs.  $\log (v)$  shown in **Figure 4.22** over the different concentrations demonstrate that the electrochemical reactions of  $\text{Cu}^{2+}/\text{Cu}^+$  and  $\text{Cu}^+/\text{Cu}^{2+}$  coupled onto the glassy carbon electrode in 25 mM MES + 100 mM NaCl solution are diffusion controlled with slope values ranging from 0.34 ( $r^2 = 0.99$ ) to 0.44 ( $r^2 = 0.95$ ). The diffusion coefficients can thus be used to confirm whether we are looking at peptide bound  $\text{Cu}^{2+}$  or free  $\text{Cu}^{2+}$  in solution. To do this, we compare the diffusion coefficient value of  $\text{CuCl}_2$  in aqueous media at  $298.15^\circ\text{C}$  measured to be  $1.3\text{E}10^{-5}$  ( $\text{cm}^2/\text{s}$ ) (Ribeiro et al., 2005). The difference suggests that the diffusion coefficient value we are measuring for the K16A- $\text{Cu}^{2+}$  ribbons can be attributed to peptide bound  $\text{Cu}^{2+}$  as the diffusion is slower and consistent with plastocyanin (Sanderson et al., 1986).





**Figure 4.22 – Plots of  $\log |i_p|$  vs.  $\log (v)$ .** Plot results help assess dependence of K16A-Cu<sup>2+</sup> nanostructures on diffusion or adsorption to the glassy carbon electrode. (Top)  $r^2 = 0.98$  and  $0.98$ , slope =  $0.35 \pm 0.03$  and  $0.34 \pm 0.03$  (Middle)  $r^2 = 0.98$  and  $0.99$ , slope =  $0.42 \pm 0.03$  and  $0.34 \pm 0.02$  (Bottom)  $r^2 = 0.95$  and  $0.96$ , slope =  $0.44 \pm 0.05$  and  $0.43 \pm 0.05$ . Results are consistent with pure diffusion control electrochemical reactions of Cu<sup>2+</sup>/Cu<sup>+</sup> and Cu<sup>+</sup>/Cu<sup>2+</sup> coupled onto the glassy carbon electrode.

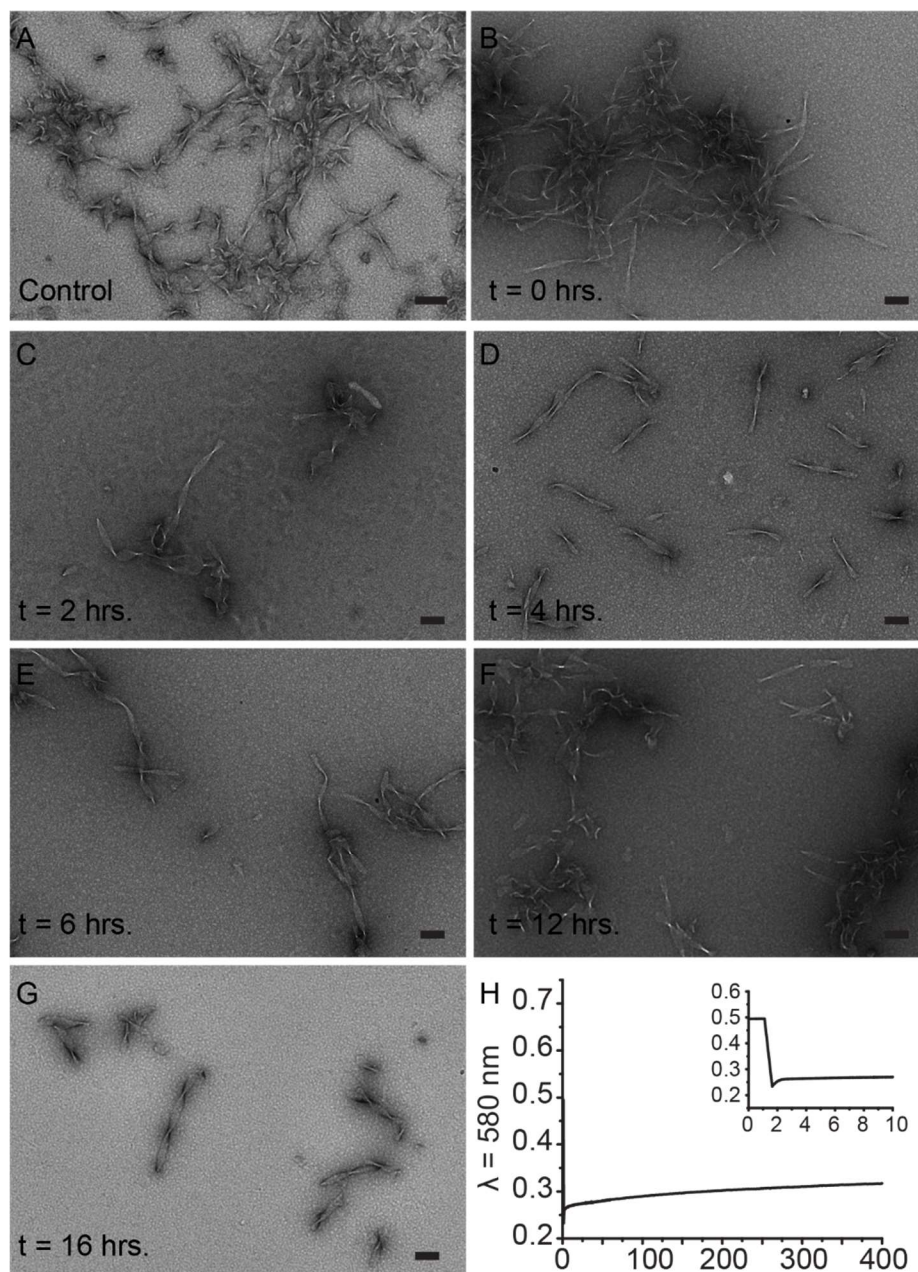
Across the three different concentrations, K16A-Cu<sup>2+</sup> ribbons display electrochemical quasi-reversibility. For a fully reversible system three parameters must be met: 1) peak-to-peak potential separation  $\Delta E_p (= E_{pc} - E_{pa}) = \leq 59.2/n$  mV at all scan rates at 25°C, 2) the peak current ratio ( $i_{pa}/i_{pc}$ ) = 1 at all scan rates and 3) a Randles-Sevcik plot must yield a linear relationship demonstrating peak current independence from scan rate. While the K16A-Cu<sup>2+</sup> ribbons abide by the second and third parameters, the designed metallamyloid has peak-to-peak values  $\Delta E_p > 59.2/n$  mV at all scan rates (summarized in **Table 4.2**). This is certainly influenced by the aqueous environment but also likely due to slow electron transfer kinetics as the  $\Delta E_p$  value increases with increasing scan rate, an archetypal effect seen for quasi-reversible materials. The quasi-reversibility of our designed metalloamyloid array could be an effect of larger reorganization energies. However, given the larger deviation at the anodic potential (Cu<sup>+</sup>/Cu<sup>2+</sup>) it is possible that the Cu<sup>+</sup> is preferentially stabilized, once reduced, over Cu<sup>2+</sup>. Indeed, given the diverse coordination sites and environments for Cu<sup>2+</sup> that exists within this MAN, and given the cupredoxin-like behavior displayed by K16A-Cu<sup>2+</sup>, we suggest that the coordination environment in this MAN may be preorganized to facilitate the coordination of both Cu<sup>2+</sup> and Cu<sup>+</sup>. Thus, it is unlikely that the reorganization energies

for K16A-Cu<sup>2+</sup> are much larger than those previously reported for other amyloid-Cu<sup>2+</sup> complexes (Balland et al., 2010). This is an interesting observation that has some precedent in the blue copper protein literature as well (Olsson & Ryde, 1999). This is encouraging for applications of this MAN in electron storage.

The similarities to blue copper proteins should be summarized. The ribbons absorb at a  $\lambda_{\text{max}}$  of 600 nm, also typical of blue copper proteins. The diffusion coefficient of the metalloamyloid array matches within the order of magnitude as that seen for pastocyanin. Finally, the  $E_{1/2}$  of the developed material, summarized in **Table 4.2**, also falls within that observed for blue copper proteins which range from +300 – +1000 mV. Most strikingly, the survivability of the material to the introduction of a reducing agent was visually followed by TEM for 16hrs. Ribbons were exposed stoichiometric amounts of ascorbate and the Cu<sup>2+</sup> to Cu<sup>+</sup> reduction was followed by UV-Vis. Over the course of 16hrs., the Cu<sup>+</sup> species formed become re-oxidized to Cu<sup>2+</sup> without a morphological effect (**Figure 4.23**). Taken together, this data demonstrates that we have designed and characterized a material with feasible applications in cell-compatible environments as oxidases or energy storage centers.

**Table 4.2 – Summary table of K16A-Cu<sup>2+</sup> electrochemical parameters.** Cathodic and Anodic peak currents for K16A-Cu<sup>2+</sup> assemblies in 25 mM MES buffered at pH: 5.6 across various scan rates with a summary of the peak potential separation, calculated analyte diffusion coefficients and half-reduction potential values at the various Cu(II) concentrations assessed. Supporting electrolyte: 100 mM NaCl.

[Cu <sup>2+</sup> ] (mM)	$\Delta E_p$ (mV)	Scan Rate (V/s)	$i_{pa}$ (A)	$i_{pc}$ (A)	D (cm <sup>2</sup> /s)	E <sub>1/2</sub> vs. RHE (mV)
0.5					6.98 x 10 <sup>-6</sup>	
	232.5	0.025	1.93 x 10 <sup>-6</sup>	-1.98 x 10 <sup>-6</sup>		+630.2
	293.3	0.050	2.48 x 10 <sup>-6</sup>	-2.49 x 10 <sup>-6</sup>		+640.3
	218.4	0.100	3.50 x 10 <sup>-6</sup>	-3.58 x 10 <sup>-6</sup>		+672.8
	473.9	0.250	4.60 x 10 <sup>-6</sup>	-4.37 x 10 <sup>-6</sup>		+670.4
555.0	0.500	5.46 x 10 <sup>-6</sup>	-5.48 x 10 <sup>-6</sup>	+675.4		
0.4					3.33 x 10 <sup>-6</sup>	
	262.7	0.025	6.57 x 10 <sup>-7</sup>	-9.38 x 10 <sup>-7</sup>		+645.1
	313.4	0.050	1.00 x 10 <sup>-6</sup>	-1.09 x 10 <sup>-6</sup>		+650.3
	353.8	0.100	1.31 x 10 <sup>-6</sup>	-1.44 x 10 <sup>-6</sup>		+670.4
	463.8	0.250	1.94 x 10 <sup>-6</sup>	-2.08 x 10 <sup>-6</sup>		+670.4
555.2	0.500	2.35 x 10 <sup>-6</sup>	-2.46 x 10 <sup>-6</sup>	+670.3		
0.25					2.41 x 10 <sup>-7</sup>	
	368.5	0.025	4.31 x 10 <sup>-8</sup>	-4.60 x 10 <sup>-8</sup>		+675.4
	388.9	0.050	5.33 x 10 <sup>-8</sup>	-5.52 x 10 <sup>-8</sup>		+677.9
	419.3	0.100	9.19 x 10 <sup>-8</sup>	-9.27 x 10 <sup>-8</sup>		+672.9
	519.6	0.250	1.06 x 10 <sup>-7</sup>	-1.11 x 10 <sup>-7</sup>		+672.9
576.0	0.500	1.66 x 10 <sup>-7</sup>	-1.70 x 10 <sup>-7</sup>	+667.9		



**Figure 4.23 – Ascorbate reduced K16A-Cu<sup>2+</sup> MAN.** K16A-Cu<sup>2+</sup> metalloamyloid array exposed to a reducing agent, ascorbate, at a 1:1 ratio. (A) Control demonstrating the ribbon morphology before the addition of the ascorbate, peptide concentration started at 2 mM. (B) Ribbon morphology persists upon initial addition of ascorbate; peptide concentration was reduced to 1 mM to reach 1 mM ascorbate concentration. Following, timepoint representations of the ribbon morphology were collected (C – G). (H) UV-Vis collected at  $\lambda = 580$ , the  $\lambda_{\text{max}}$  of K16A-Cu<sup>2+</sup> assemblies. Over the course of time, re-oxidation continues without reaching a true plateau.

## Conclusion

The K16A-Cu<sup>2+</sup> MAN is a unique nanostructure with functional potential. Unlike the Ac-H14A-Cu<sup>2+</sup> fibers, which isolate a single histidine from adjacent peptides for metal ion coordination, the K16A peptide reintroduces the HH-dyad to increase accessible Cu<sup>2+</sup> coordination sites while the Lys16 → Ala mutation increased peptide amphiphilicity and hydrophobicity. In **Chapter 3**, we described the design, development and selection of the K16A-Cu<sup>2+</sup> MAN. We showed that, when Cu<sup>2+</sup> is introduced at the onset of assembly and allowed to co-assemble with the K16A peptide, there is a striking morphological transition from fibers to twisted ribbons (this transition is not seen when Cu<sup>2+</sup> is added to preformed ribbons **Figure 3.22**). These ribbons are structurally homogeneous by TEM, and their incorporation of Cu<sup>2+</sup> is evident optically.

In this chapter, we carefully interrogate the degree of Cu<sup>2+</sup> incorporation by the K16A-Cu<sup>2+</sup> nanoribbons using CD, UV-Vis, ITC and EPR. The CD ratiometric studies demonstrated the evolution of structural density across different Cu<sup>2+</sup> ratios added to a constant concentration of peptide. Through these studies, we identified that the ideal peptide:Cu<sup>2+</sup> ratio would likely fall between 1:0.5 and 1:1. To identify a tighter window, we conducted ratiometric studies by UV-Vis, where we followed the evolution of the blue shifted Cu<sup>2+</sup> absorbance ( $\lambda_{\text{max}} \sim 600$  nm) in relation to aquo-Cu<sup>2+</sup> with increasing [Cu<sup>2+</sup>]. Through these experiments, we were able to identify the ideal peptide:Cu<sup>2+</sup> ratio to lie between 1:0.6 to 1:0.9. ITC confirmed that the optimal ratio is at least 1:0.6 (peptide:Cu<sup>2+</sup>), however, we cannot ignore the possibility that higher concentrations of Cu<sup>2+</sup> can be incorporated when peptide concentrations reach the self-assembly ratio (avoided for ITC experiments), as the peptide bilayer may facilitate binding sites that are

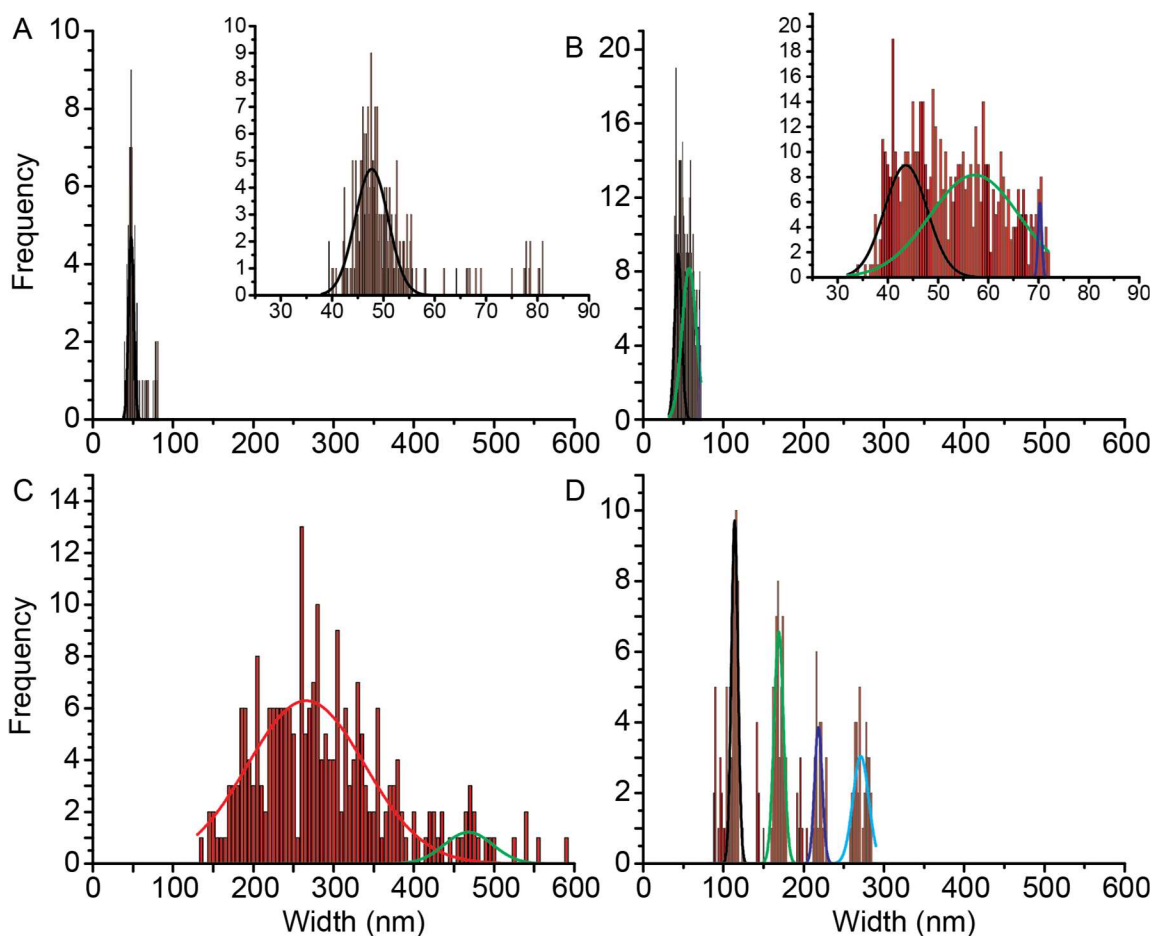
not accessible to the soluble peptide. Indeed, EPR studies demonstrate that the optimal ratio of incorporation for  $\text{Cu}^{2+}$  falls between 1:0.6 and 1:0.8 (peptide: $\text{Cu}^{2+}$ ). This ratio was determined by looking at the evolution of aquo- $\text{Cu}^{2+}$  signal with increasing concentrations of  $\text{Cu}^{2+}$  relative to the available peptide. Furthermore, we identified the unique histidine side-chain coordination around the  $\text{Cu}^{2+}$  centers through ESEEM experiments. Thus, through the study of the structural density of K16A- $\text{Cu}^{2+}$ , the optical absorbance of  $\text{Cu}^{2+}$ , the energy of binding over controlled titrations of  $\text{Cu}^{2+}$ , and the vibronic behavior of  $\text{Cu}^{2+}$  we determined that the ideal density of incorporation for  $\text{Cu}^{2+}$  within this K16A MAN lies between 60 and 80% of the stoichiometrically accessible peptide and the coordination geometries which it likely assumes once incorporated.

Having characterized the peptide arrangement through solid-state NMR in **Chapter 3**, demonstrating that the peptide  $\beta$ -strand arrangement is antiparallel, and having demonstrated that these structures form a bilayer by AFM (pg. 87), we sought to define the precise sites of incorporation along the K16A- $\text{Cu}^{2+}$  nanostructure. To this end, we designed peptide nanotubes that mimicked the surface of an antiparallel nanostructure, incorporating the K16A metal binding side-chain, histidine. We demonstrated a true understanding of the self-assembly code of E22L by designing two congener peptides that assembled into nanotubes with a surface analogous to that of the K16A- $\text{Cu}^{2+}$  MAN. Furthermore, we demonstrated that, upon addition of  $\text{Cu}^{2+}$  to a collection of these nanotubes, resuspended in 25 mM MES buffer at pH: 5.6, no  $\text{Cu}^{2+}$  binding was observed. These results helped define the surface of K16A- $\text{Cu}^{2+}$  nanostructures  $\text{Cu}^{2+}$  free, identifying the only available site for  $\text{Cu}^{2+}$  incorporation as the nanoribbon bilayer.

While these results were exciting, experiments that led to this conclusion gave us some new, and interesting, nanomaterials that could help advance our understanding of side-chain packing within the supramolecular assemblies, as well extend the range of functionalities accessible to catalytically active nanotubes (Omosun et al., 2017). One of the biggest challenges in the structural study and design of peptide formed supramolecular assemblies is our inability to map the way amino-acid side-chains pack within a supramolecular construct. Cryo-TEM provides a methodology that could help circumvent such limitations. However, to successfully reconstruct a structure by cryo-TEM helical reconstruction methodology, we must have a supramolecular structure which is regular in size and dimensions, giving a translatable base unit across the majority of the nanotubes captured in a single grid. To date, our most regular assembly for such a purpose was the E22L nanotube. However, attempts to reconstruct the structure of these nanostructures were not successful due to the imperfections along the length of single nanotubes. In the studies presented in this chapter, we synthesized a nanotube that is highly regular, robust, and as of now, fully characterized. The K16H,E22L nanotubes form structures that, when compared with E22L nanotubes, prove to serve as the next great candidates for cryo-TEM reconstruction attempts. With the added effect of a proposed histidine stabilization at the peptide bilayer leaflet interface (Liao et al., 2013), these nanotubes form a normal distribution with a center at  $47.7 \pm 0.2$  nm and a distribution of  $6.4 \pm 0.4$  nm, compared to E22L nanotubes which spread along two normal distributions centered at  $43.6 \pm 0.8$  nm and  $57.3 \pm 3.1$  nm with distributions of  $8.5 \pm 2.1$  nm and  $17.7 \pm 6.1$  nm, respectively (



**Figure 4.24A and B).** Given these results, we propose that the K16H,E22L nanotubes should be used as the next best candidates for cryo-TEM studies to advance our understanding of the peptide assembly code, as side-chain packing has important effects in the morphology accessible to nanoscale assemblies.



**Figure 4.24 – Width measurements of E22L, K16H,E22L, and K16HH,E22L**

**nanotubes.** (A) K16H,E22L nanotubes with a Gaussian fit centered at , and a distribution of . (B) E22L nanotubes with two Gaussian fits centered at  $43.6 \pm 0.8$  nm and  $57.3 \pm 3.1$  nm, and distributions of  $8.5 \pm 2.1$  nm and  $17.7 \pm 6.1$  nm, respectively. (C) K16HH,E22L nanotubes assembled in 10% CH<sub>3</sub>CN with two Gaussian fits centered at  $265.8 \pm 5.5$  nm and  $468.1 \pm 18.2$  nm, and distributions of  $146.0 \pm 12.4$  nm and  $60.1 \pm 36.8$  nm, respectively. (D) K16HH, E22L in ASTM Type II H<sub>2</sub>O with four Gaussian fits centered at  $114.0 \pm 0.5$  nm,  $169.0 \pm 0.9$  nm,  $218.3 \pm 1.3$  nm and  $271.2 \pm 2.4$  nm, and distributions of  $8.1 \pm 1.0$  nm,  $11.8 \pm 1.7$  nm,  $9.6 \pm 2.6$  nm and  $19.8 \pm 5.0$  nm, respectively.

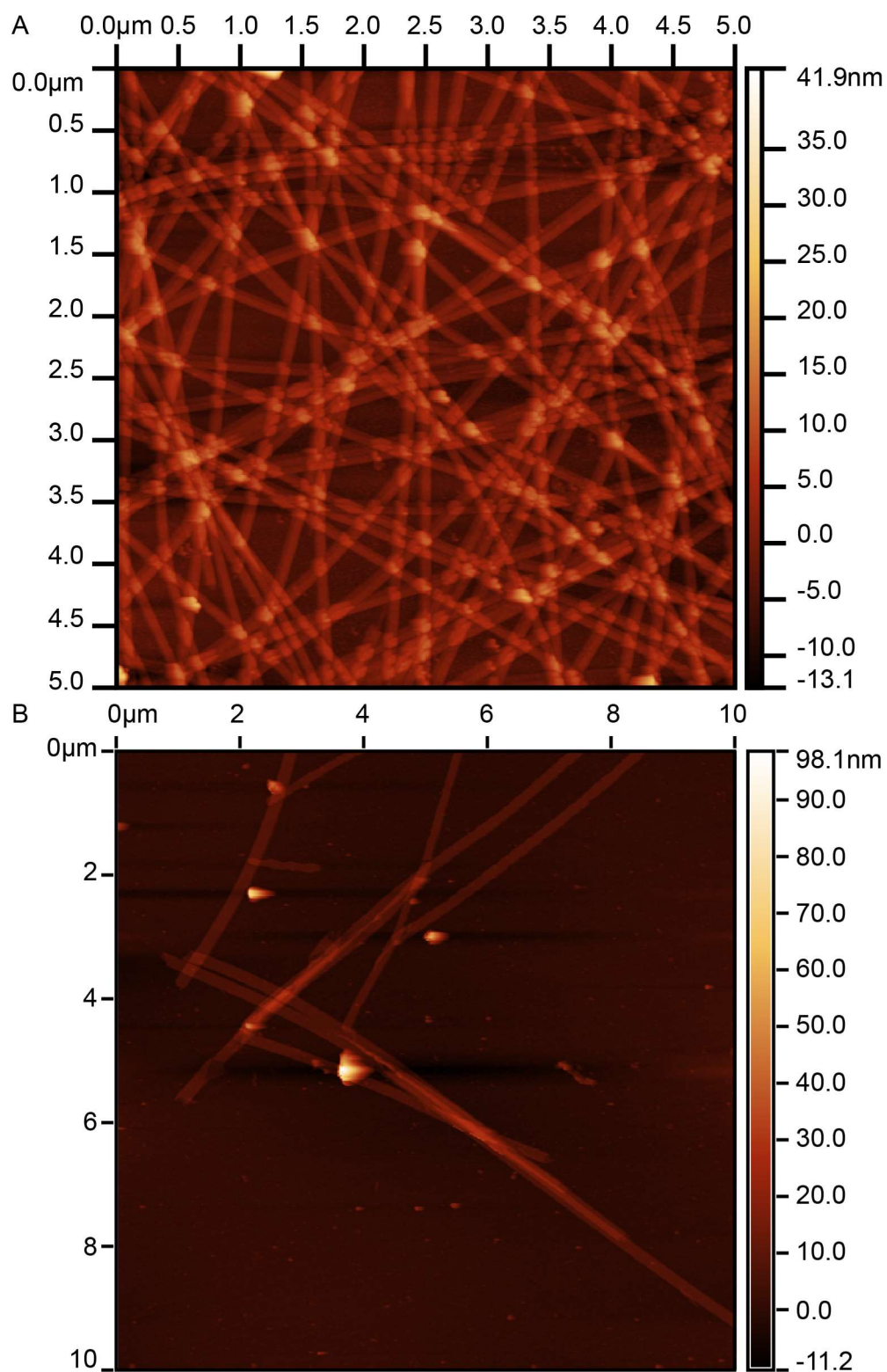
Indeed, the size distribution of K16HH,E22L nanotubes is extensive, and surprisingly, most diverse for the assemblies formed in 10% CH<sub>3</sub>CN (**Figure 4.24**), these nanotubes may provide a different dimension of functional applications. While solid-state NMR data for this sample is not currently available and thus, we do not have a defined registry for this peptide assembly, we know from the data herein presented, that these nanotubes form antiparallel  $\beta$ -sheets. We reasoned that, in a solvent with a high dielectric, the hydrophobic core would dictate the self-assembly driving the formation of nanotubes. Because of this, we propose that these assemblies have a two amino-acid registry shift, which is one of the reasons why the nanotube diameter is so large, to accommodate for the dangling peptide ends. All in all, having two accessible side chains for metal binding, in this case, may not have been enough to drive metal chelation, however, these nanotubes could function as phosphocarrier proteins (van Nuland et al., 1994), or serve as sites for deposition of functionalized nanoparticles to extend the applications beyond biology. Such modifications are discussed in more detail in **Chapter 5**.

In the final section of this chapter, we looked at the reactivity of the K16A-Cu<sup>2+</sup> MAN in more detail. UV-Vis and EPR data taught us that two Cu<sup>2+</sup> centers exist in the K16A-Cu<sup>2+</sup> nanostructure bilayer (**Figure 4.26B and C**). We therefore reasoned that each of these Cu<sup>2+</sup> sites would have a distinct reduction potential. Knowing that the tris-His site is saturated first, at low Cu<sup>2+</sup> concentrations, with the evolution of bis-His Cu<sup>2+</sup> at higher concentrations of Cu<sup>2+</sup> we designed CV experiments aimed at distinguishing between the different reduction potentials that must exist within this MAN. However, in the conditions we investigated (ratios of 0.5, 0.8 and 1 Cu<sup>2+</sup>/peptide) we only identified a

single reduction potential (+670 mV vs. RHE), comparable to the reduction potential of blue copper proteins (Gray et al., 2000; Olsson & Ryde, 1999). It could be that multiple potentials exist, but the anodic and cathodic waves are so broad the individual potentials are hidden within. Regardless, in this section we confirmed that the K16A-Cu<sup>2+</sup> MAN is indeed quasi-reversible, as first suggested in **Chapter 3**. We further found another the system is a diffusion controlled system (**Figure 4.22**) and that the diffusion coefficient of our material ( $10^{-7}$ ) is comparable to the diffusion coefficient of Plastocyanin (Sanderson et al., 1986), a small blue copper protein that serves as an electron shuttle between cytochrome f of photosystem II and P700+ of photosystem I (Gross, 1993). In terms of durability, we have demonstrated that this material is stable under a variety of conditions (), however, the most exciting piece of data that highlights potential functional applications from this material came upon introduction of a reducing agent, ascorbic acid (vitamin C). Once the material was reduced, it took some time to completely re-oxidize the material, and the material was stable within the experimental timeframe. Upon further improvements, we are confident that we may be able to expand the functional applications of this material to efficient energy storage and transport.

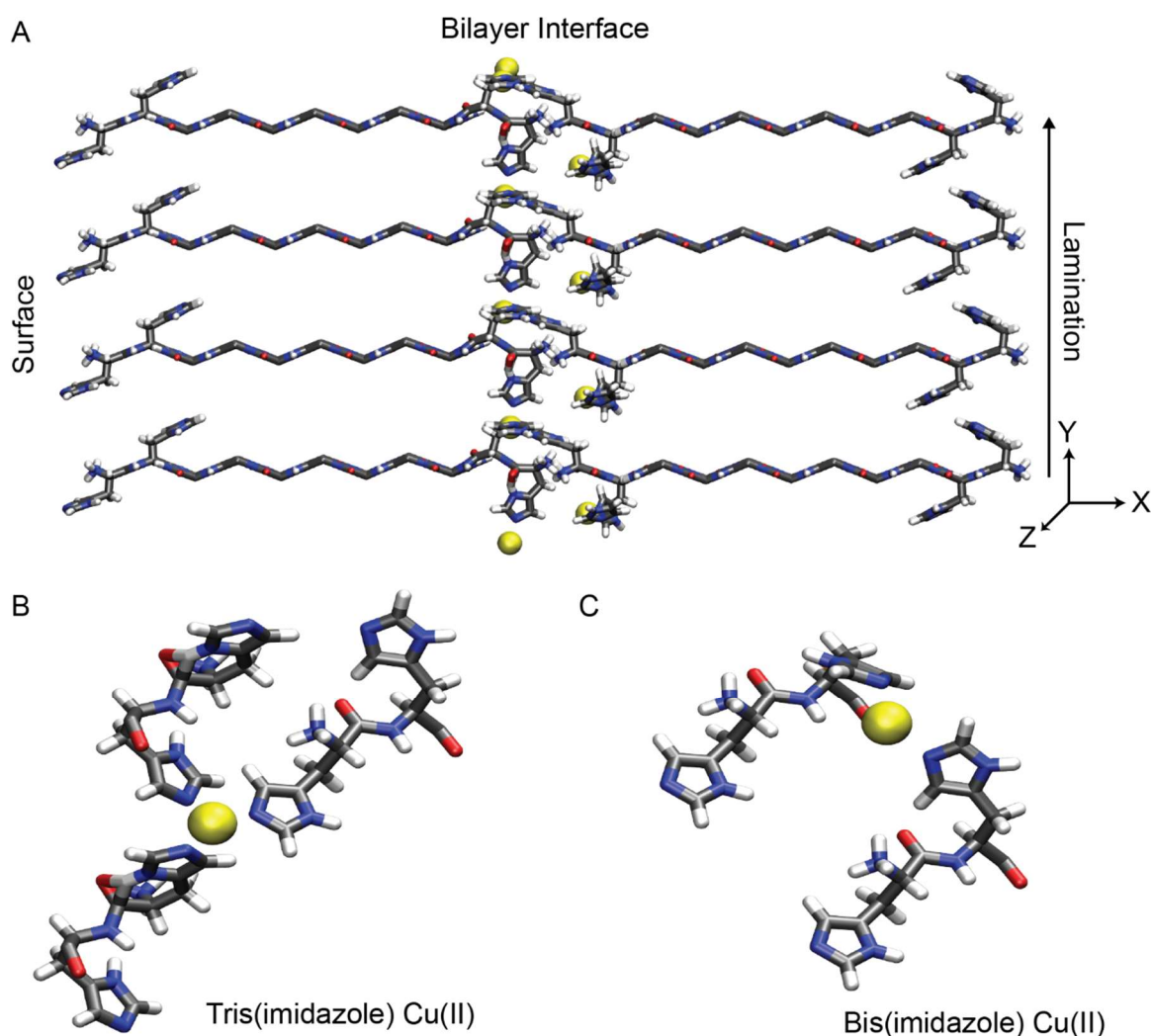
Given what we learned from the design of K16H,E22L and K16HH,E22L nanotubes (**Figure 4.25**) about the K16A-Cu<sup>2+</sup> MAN surface, together with the spectroscopic data that reported on the density of Cu<sup>2+</sup> incorporation, we developed a model where Cu<sup>2+</sup> is insulated in the peptide bilayer and isolated from the solvent space. This organization is unlike the Ac-H14A-Cu<sup>2+</sup> MAN, which binds Cu<sup>2+</sup> on the fiber surface at a peptide:Cu<sup>2+</sup> ratio of 1:0.5 or less, and remain solvent exposed. In this model, we were able to put constraints given by XRD on peptide H-bonding and laminate

distance, solid-state NMR on peptide arrangement and registry, and EPR/ESEEM, on the coordination geometry of the histidine side-chains around the  $\text{Cu}^{2+}$  centers. We incorporated Euler angles given by these analysis for the tri-His species, and estimated bis-His organization around  $\text{Cu}^{2+}$  ions based on the 2 Å distance recorded in the literature for  $\text{Cu}^{2+}$ -His coordination (Camerman, Fawcett, Kruck, Sarkar, & Camerman, 1978). The model fits the experimental results quite nicely. In fact, the ratio of peptide: $\text{Cu}^{2+}$  approaches a ratio of 1:0.67. This ratio matches well with the limits identified in the ratiometric studies described in the first section of this chapter (pg. 134), between 1:0.6 and 1:0.8. Indeed, the design, selection and characterization of the K16A- $\text{Cu}^{2+}$  MAN came together nicely in the development of this final model, presented in **Figure 4.26**, which captures every aspect of the data first presented in **Chapter 3** and fully developed in **Chapter 4**.



**Figure 4.25 – AFM micrographs of K16H,E22L and K16HH,E22L nanotubes.** AFM micrographs highlight the degree of assembly achieved by (A) K16H,E22L and (B) K16HH,E22L in the formation of peptide nanotubes. Height measurement of the assemblies are  $6.22 \pm 0.84$  nm for K16H,E22L and  $7.00 \pm 0.76$  for K16HH,E22L.

As was first alluded to in **Chapter 3** and elaborated on in the introduction to this chapter, the K16A-Cu<sup>2+</sup> MAN is a cupredoxin-like material, rich blue in color, absorbing at ~600 nm, and sharing electrochemical properties with these beautifully colored enzymes. There are several important distinctions, but the most relevant for applications as a functional material is that, unlike most cupredoxins, the MAN herein described has active sites along the length of the twisted ribbons. Importantly, while metalloproteins accommodate a handful of binding sites per quaternary structure, this K16A MAN boasts tens of thousands per structure, if not more. With so many active sites, these materials have possible applications as long-range electron transporters. We envision this material to have improved conductivity, analogous to the improved signal conduction of myelinated axons vs. unmyelinated axons. Combined with the relative stability of the material, the possibilities are becoming more and more tangible. In sum, our data demonstrates that this K16A MAN has potential applications in the development of nanowires, nanobatteries or nanocapacitors.



**Figure 4.26 – Complete structural model of the K16A-Cu<sup>2+</sup> MAN.** (A) Model with applied experimental constraints highlighting the bilayer interface and the ribbons surface. Axis displayed to define the assembly architecture, where ‘x’ lies in the direction of the peptide length, ‘y’ defines the lamination direction, and ‘z’ defines the H-bonding direction. (B) Close-up to the Tris(imidazole) Cu<sup>2+</sup> center, dominant species making up 67% of all bound copper at the saturation concentration (0.6 mM CuCl<sub>2</sub>). (C) Close-up to the Bis(imidazole) Cu<sup>2+</sup> center, making up 33% of bound copper at the saturation concentration (0.6 mM CuCl<sub>2</sub>).



## Materials and Methods

### Synthesis and purification of H-HHQALVFFA-NH<sub>2</sub> (K16A), Ac-KLVFFAL-NH<sub>2</sub> (E22L), Ac-HLVFFAL-NH<sub>2</sub> (K16H,E22L), Ac-HL<sup>[15N]</sup>VFF[1-<sup>13</sup>C]AL-NH<sub>2</sub> (enriched K16H,E22L), and Ac-HHLVFFAL-NH<sub>2</sub> (K16HH,E22L)

Peptides were synthesized and purified as previously described (**Chapter 2**, pg. 39). H-HHQALVFFA-NH<sub>2</sub> was synthesized with a free N-terminus, while the C-terminus is carboxyamided. Acetyl group caps the N-terminus of all other peptides. For purification, the elution gradient was optimized for each peptide to elute within ten minutes of the initial starting point, followed by a ten minute wash and a seven minute equilibration step. Elution fractions were manually collected and Once CH<sub>3</sub>CN was removed using a rotary evaporator and left-over water/peptide mixture is lyophilized, peptides were stored at room temperature inside a vacuum desiccator until needed.

Fraction purity was confirmed by MALDI-TOF mass spectral analysis using a Applied Biosystem 4700 Proteomics analyzer with a 355 nm ND:Yag laser operating at 200Hz (Foster City, CA, USA). A  $\alpha$ -cyano-4-hydroxycinnamic acid (CHCA) matrix was used for MALDI-TOF experiments (H-HHQALVFFA-NH<sub>2</sub>, 1068.23 (M+H<sup>+</sup>), Ac-KLVFFAL-NH<sub>2</sub>, 878.11 (M+H<sup>+</sup>), Ac-HLVFFAL-NH<sub>2</sub>, 887.07 (M+H<sup>+</sup>), Ac-HL<sup>[15N]</sup>VFF[1-<sup>13</sup>C]AL-NH<sub>2</sub>, 889.23 (M+H<sup>+</sup>), and Ac-HHLVFFAL-NH<sub>2</sub>, 1024.22 (M+H<sup>+</sup>)).

### FMOC protection of isotope enriched amino-acids

FMOC protection of isotope enriched amino-acids (purchased from Cambridge Isotope Laboratories, Inc., Andover, MA, USA) for peptide synthesis was done following

standard methods.(Gawande & Branco, 2011; Samuel-Landtiser et al., 2001). Protocol is described in **Chapter 2** pg. 39.

### **UV-Vis Spectroscopy**

Experimental set-up has been previously described, see **Chapter 3**, pg. 123.

Data Analysis: OriginPro 9.0 software was used for all fits and baseline corrections. Basis set was defined according to known values for Aquo-Cu<sup>2+</sup> in MES buffer (778 nm), H14A-Cu<sup>2+</sup> in HEPES buffer, pH: 7.4 (650 nm), and K16A-Cu<sup>2+</sup> in 25mM MES, pH 5.6 (600 nm). A multiple peak function was selected to assign the basis set values – x-axis values were fixed in the nonlinear fit to a standard Gaussian function. Percent populations of each species was estimated from the area under the curve needed to fit the experimental data. Before each fit, a baseline correction was conducted for each data-set from 900 to 400 nm to remove the peptide scattering effect. The peak analyzer function was set to subtract the baseline from the selected data. Adjacent-averaging smoothing method was selected for the determination of anchor points; user defined anchor points were added as appropriate to generate a baseline at  $y = 0$  beyond the region of interest.

### **Circular Dichroism Spectroscopy (CD)**

CD spectra collection and conversion was done following previously defined methods, see **Chapter 3**, pg. 123.

### **Fourier Transform Infrared Spectroscopy (FT-IR)**

All FT-IR spectra collection and conversion was done following previously defined methods, see **Chapter 3**, pg. 123.

### **X-Ray Powder Diffraction (XRD)**

Assembled H-HHQALVFFA-NH<sub>2</sub> (K16A), Ac-KLVFFAL-NH<sub>2</sub> (E22L), Ac-HLVFFAL-NH<sub>2</sub> (K16H,E22L), and Ac-HHLVFFAL-NH<sub>2</sub> (K16HH,E22L) ribbons and nanotubes were collected by centrifugation using an Eppendorf centrifuge 5810 R (Mississauga, Ontario, CAN) at 4000 rpm held at 4°C to prevent heating and melting the sample and to remove any small heterogeneities from the assembly mixture. Nanotubes formed with E22L, K16H,E22L and K16HH,E22L peptides were first bundled with sodium sulfate (Na<sub>2</sub>SO<sub>4</sub>) added to final concentration of  $\leq 9$  mM. Upon sulfate addition, a white precipitate forms (Lu et al., 2007). Bundled tubes were centrifuged under the conditions described above. The pellet formed for each sample was frozen and lyophilized to yield a dry powder for XRD. The powder spectra were obtained using a Bruker D8 Discover diffractometer, equipped with a multi-position X, Y, Z stage, a cobalt X-ray tube with a Goebel mirror and a Vantec1 solid state detector. The sample was placed in a zero-background holder on the stage and the spectrum obtained using Bragg-Brentano geometry. The scan step was repeated several times to improve signal to noise.

### **Transmission Electron Microscopy (TEM)**

Sample preparation and staining methods are described previously, see **Chapter 3**, pg. 123.

### **Atomic Force Microscopy (AFM)**

Experimental set-up and data collection was done as previously described (**Chapter 3**, pg. 123)

## Cyclic Voltammetry (CV)

Cyclic voltammetry experimental set-up is described in **Chapter 3**, pg. 123.

## Solid-state NMR

In dephasing the carbonyl carbon of Ac-HL[<sup>15</sup>N]VFF[1-<sup>13</sup>C]AL-NH<sub>2</sub> nanotubes, the distance of the H-bonded <sup>15</sup>N from the adjacent peptide was fit to 4.53 Å (*r*<sub>1</sub>) and the distance to the non-H-bonded <sup>15</sup>N was fit to 5.11 Å (*r*<sub>2</sub>). The angle between the two <sup>13</sup>C-<sup>15</sup>N internuclear vectors was fit to 154°. The experimental data were fit to a linear combination of 3-spin (one <sup>13</sup>C and two <sup>15</sup>N's) and <sup>13</sup>C{<sup>15</sup>N}REDOR curve corresponding to the <sup>13</sup>C-<sup>15</sup>N distances sufficient to fit the experimental data points using the Non-Linear Fit routine in Mathematica.

## Isothermal Titration Calorimetry (ITC)

The binding of Cu<sup>2+</sup> to H-HHQUALVFFA-NH<sub>2</sub> (K16A) was analyzed by measuring heat changes during the titration of CuCl<sub>2</sub> in the peptide solution using a VP-ITC titration microcalorimeter (Micro-Cal, Inc., Northhampton, MA). All solutions were degassed under vacuum and equilibrated at 25°C prior to titration. The sample cell (1.4 mL) contained 25mM MES buffer pH5.6, 10mM NaCl with or without 0.05 mM K16A, while the reference cell contained the same buffer solution, 25mM MES buffer pH5.6 and 10mM NaCl. After equilibration, an 8 mM titration solution, prepared in the same buffer as used in the sample cell, was titrated into the sample cell through the titration syringe. The injection sequence consisted of an initial injection of 1 μL to prevent artefacts arising from the filling of the syringe (not used in data fitting), followed by injections of 5 μL aliquots using the default injection rate with a 360 sec. interval between each injection to

allow the sample to return to baseline. The solution in the cell was stirred by the syringe at 270 rpm, which ensured rapid mixing but did not cause foaming of the peptide solution. To correct for heats of dilution and mixing, blank titrations of  $\text{Cu}^{2+}$  into buffer were subtracted from the K16A- $\text{Cu}^{2+}$  titration. The resulting titration curves were analyzed using Origin for ITC software supplied by MicroCal (Northampton, MA). Care was taken to properly clean the ITC sample cell and syringe prior to each titration by flushing the cell and the syringe with 100mL of 2% Contrad detergent solution (Decon Laboratories, Inc., Bryn Mawr, PA) followed by 100 mL of metal-free deionized  $\text{H}_2\text{O}$  before loading the next sample.

### **Peptide Assembly**

H-HHQALVFFA- $\text{NH}_2$  (K16A) assemblies and buffers were prepared using ASTM Type II Water, Produced by RO/DI (EMD Chemicals Inc., Gibbstown, NJ, USA).

Fiber Formation: K16A peptide was dissolved and assembly matured in 25mM MES buffer, pH 5.6. The sample was dissolved by first adding half the desired volume of water. Following water addition and a 2-5sec vortex period, 50 mM MES buffer, pH 5.6 was added to the desired final volume, this was followed by a brief 1-2 sec vortex period. For any further dilutions of peptide sample to a new overall concentration, a stock solution of 25 mM MES buffer at pH 5.6 was used. Peptide concentration ranged from 0.5 mM, 1 mM and 2 mM. At all concentrations, fibril formation was evident.

Ribbon Formation: K16A peptide was dissolved and assembly matured in 25mM MES buffer, pH 5.6. Sample was dissolved by first adding half the desired volume of water minus the calculated volume of  $\text{CuCl}_2$  for the desired stoichiometry of peptide to  $\text{Cu}^{2+}$ . 100 mM  $\text{CuCl}_2$  stock solution was also dissolved in ASTM Type II Water.

Following water addition to K16A peptide powder and a 2-3sec vortex period, half the total desired volume of 50 mM MES buffer, pH 5.6 was added. Buffer addition was followed by a brief 1-2 sec vortex period. Addition of  $\text{Cu}^{2+}$  happened immediately after the final vortex period to reach the desired final volume and buffer concentration. Sample was inverted three times, not vortexed, following addition of  $\text{Cu}^{2+}$ . Dilutions of peptide sample to a new overall concentration were done using a stock solution of 25 mM MES buffer at pH 5.6. Peptide concentration ranged from 0.5 mM, 1 mM and 2 mM. At all concentrations, ribbon formation was evident.

Nanotube Formation: E22L and K16H,E22L peptides were dissolved and assembly matured in a 40%  $\text{CH}_3\text{CN}$  solution using HPLC grade solvents purchased from Sigma-Aldrich (St. Louis, MO, USA) with 0.1% TFA. Initial dilution occurred in half the total volume of 80%  $\text{CH}_3\text{CN}$  to which  $\text{H}_2\text{O}$  was slowly added to reach the desired 40%  $\text{CH}_3\text{CN}$  incubation conditions. Prior to  $\text{CuCl}_2$  addition to K16H,E22L nanotubes, these were pelleted from the 40%  $\text{CH}_3\text{CN}$  solvent using a Eppendorf centrifuge 5810 R (Mississauga, Ontario, CAN) at 4000 rpm held at  $4^\circ\text{C}$  to remove any unassembled peptide monomers. Pellet was resuspended in water to half the desired volume and 50 mM MES was slowly titrated in to reach the desired total volume with a final buffer concentration of 25 mM MES, pH 5.6. Once resuspended,  $\text{CuCl}_2$  was added at desired concentrations to mimic K16A- $\text{Cu}^{2+}$  assembly conditions.

### **Width Measurements**

All measurements were done using Image J software. For each image measurements were defined based on embedded scale bar.

## **Peptide Representations**

All high-resolution peptide models were built using free Maestro academic version from Schrödinger Computational Software. Images were initially rendered using Visual Molecular Dynamics (VMD) Molecular Graphics Viewer and rendered at high resolution using the Persistence of Vision Raytracer (POV-Ray) software.

## Chapter 5 What next?

In this dissertation, I outlined experiments that demonstrated, for the first time, the defined structure of one type of oligomeric particle. I proposed a model for the structural rearrangement that takes place from oligomeric particle to a mature supramolecular structure, and we have identified conditions under which mutations that lead to the structural rearrangement can be prevented. I have also outlined the design of a metalloamyloid nanostructure (MAN) that is stable, can be reduced and oxidized quasi-reversibly, and has cupredoxin-like characteristics. This is, to the best of my knowledge, the first example of a nanoscale self-assembling material that insulates  $\text{Cu}^{2+}$  within a peptide bilayer, is morphologically homogeneous, and has controlled growth in multiple dimensions.

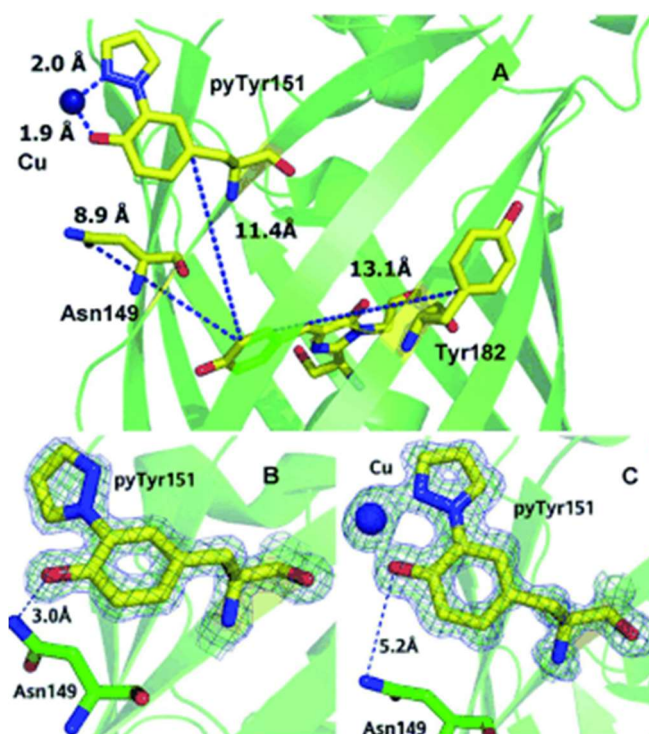
In this chapter I outline project ideas that have arisen organically, through conversations with my research advisor, faculty members, and research colleagues whom I met during my graduate career. I hope that the research presented herein will highlight the impact that developing a clear and fundamental understanding of self-assembly can have in the development of new functional materials. Indeed, although the A $\beta$  peptide is primarily researched in the context of disease, understanding the intricate mesoscale assemblies of this beautifully constructed peptide can help advance our understanding of its significance in biology and promote the discovery of applications in technology.



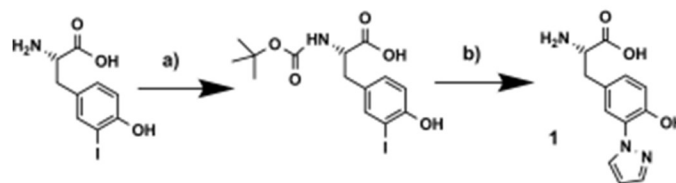
### **Non-canonical amino-acids serve as $e^-$ acceptors in the presence of $\text{Cu}^{2+}$ .**

In previous sections of this dissertation, we discussed the importance of electron transfer in electrochemical processes, particularly in the context of photosynthesis. Electron transfer has also been important to the development of our increasing understanding of macromolecular conformational dynamics. However, due to the limited number of naturally occurring amino acids that can serve as electron donors, the use of fluorescence quenching techniques to understand the conformational dynamics of large proteins has been complicated by limitations of their presence in biological systems. To remove such limitations, one research group developed a noncanonical metal-chelating amino-acid, that can be incorporated at desired sites of a protein sequence by genetic manipulation of the amber stop codon, TAG, for site specific incorporation of an efficient electron acceptor (**Figure 5.1**) (X. Liu et al., 2012). The description of the metal-chelating amino acid (S)-2-amino-3-[4-hydroxy-3-(1H-pyrazol-1-yl)phenyl]propanoic acid (abbreviated pyTyr), motivated me to propose its incorporation to make a new iteration to the MAN.

Benchtop synthesis of pyTyr has been described (**Figure 5.2**) (X. Liu et al., 2012). The resulting noncanonical amino acid can then be Fmoc protected and incorporated within the sequence of a self-assembling peptide. Careful selection of a model peptide, whose final structure is well defined, is advised. By incorporating this efficient electron acceptor, we may be able to overcome the limitations thus far observed, and previously described, for the K16A- $\text{Cu}^{2+}$  MAN. With improved electrochemical properties, the new cell compatible system will boast  $e^-$  transfer efficiency and conditions for long-term  $\text{Cu}^{2+}$  reduction, a missing piece in the creation of a metalloamyloid battery.



**Figure 5.1 – Structural representation of genetically engineered pyTyr amino-acid in GFP.** (A) Overall structure of GFP-151pyTyrCu complex. Cu<sup>II</sup> ion is blue sphere; GFP chromophore, and residues 151, 149, and 182 are sticks; C yellow, N blue, O red. (B) pyTyr151 *F<sub>o</sub>-F<sub>c</sub>* omit electron density map (contoured at 4.5σ) in the absence of Cu<sup>II</sup> ions. (C) Electron density map of the pyTyr151Cu complex. (Reprinted from (X. Liu et al., 2012) with permission of John Wiley and Sons)



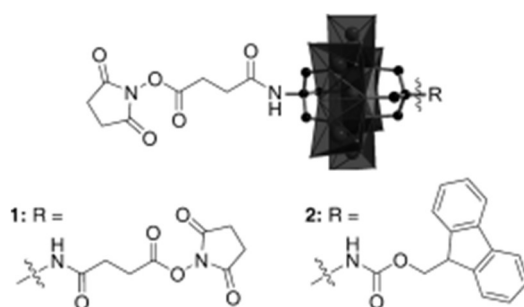
**Figure 5.2 – Synthesis of pyTyr.** (a) Di-*tert*-butyl dicarbonate, tetrahydrofuran, 1 n NaOH, RT, 4 h. (b) pyrazole, Cs<sub>2</sub>CO<sub>3</sub>, CuI, DMF, heated to reflux, 16 h. (Reprinted from (X. Liu et al., 2012) with permission of John Wiley and Sons)

### Peptide driven polyoxometalate (POM) self-assembly.

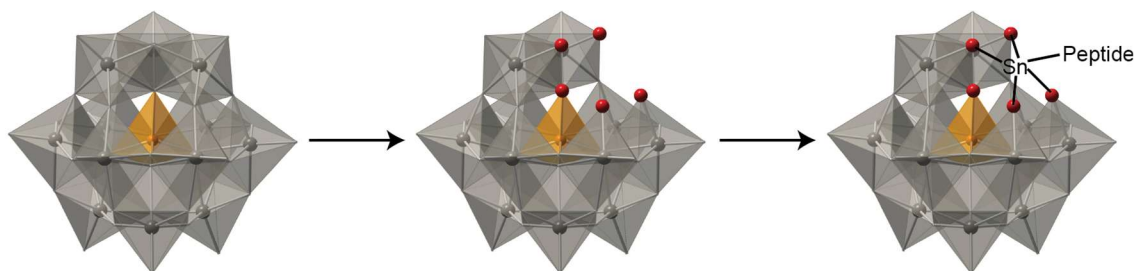
One of the most promising family of functional materials, polyoxometalates (POMs), has been proposed as templates for the design of nanoscale materials (D.-L. Long, Tsunashima, & Cronin, 2010). However, the organization of POMs across the desired size scales remains a challenge. To our benefit, it has been demonstrated that POMs can be tethered to a peptide sequence by functionalization of a Mn-Anderson type POM (**Figure 5.3**) (Yvon et al., 2014). The significance of this lies in the peptide's ability to self-organize into highly order, homogeneous assemblies. In this dissertation alone, we describe a handful of structures that self-organize to form highly regular, highly ordered structures. I propose that, by tethering a POM to a self-assembling peptide whose structure has been well defined, and has been fully characterized, we may be able to circumvent the current challenge in the design of functional micro- and even nano-scale structures.

Even though Anderson type POMs may not be the most reactive of the POM structures, recent publications may allow us to expand beyond this POM type (Debela, Ortiz, ÓSullivan, Thorimbirt, & Hasenknopf, 2014). The  $\alpha$ -Keggin type POM provides a rich framework that can be functionalized by tin chemistry. **Figure 5.4** shows a general representation of an  $\alpha$ -Keggin type POM and how it could be tethered to any given peptide sequence following procedures previously outlined (Debela et al., 2014). Keggin's can expand a diameter of about 1 nm, which, given the self-assembling dimensions on an antiparallel surface surrounding a single peptide (1 nm x 1 nm), a POM of this size would fit perfectly. I suspect that different ratios of POM tethered peptide and non-functionalized peptide may have to be added. Regardless, if a single POM can store

up to  $26 e^-$ , we need not worry about the density of incorporation just yet, instead we should focus on fraction incorporation and maximizing the electron charging efficiency for the available POM. Given the heavy charge capacity, we must be cautious about the effects increased density of incorporation may have on the peptide surface once these are charged to full capacity.



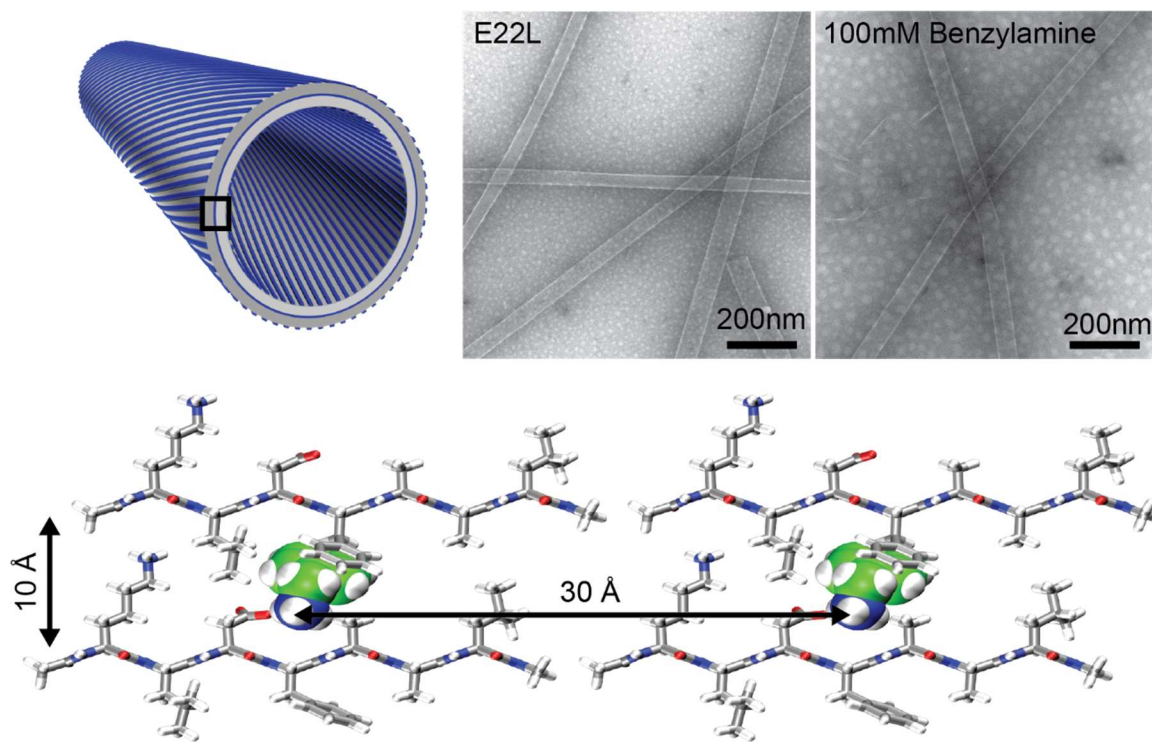
**Figure 5.3 – Mn-Anderson type POM functionalized for peptide synthesis.** Mn-Anderson precursors **1–2** activated as NHS esters. Polyhedral/ball and stick representation of the Mn-Anderson  $[MnMo_6O_{18}(O(CH_2)_3C)_2]^{3-}$  core;  $MnO_6$  and  $MoO_6$  are shown as light grey and black octahedra, respectively, and carbon atoms are depicted as black spheres; counterions were omitted for clarity. (Reprinted from (Yvon et al., 2014) with permission of John Wiley and Sons)



**Figure 5.4 – Representation of Sn functionalization of a POM for peptide incorporation.** From left to right: POM, Keggin, peptide functionalized Keggin.  $\alpha$ -Keggin has the form  $\text{XM}_{12}\text{O}_{40}$ , where ‘X’ is a tetrahedral template and ‘M’ represented either tungstate (W) or molybdenum (Mo).

#### **Expanding the complexity of self-assembling nanostructures by rational design.**

Early in my research, I proposed that redox active small molecules can be incorporated within the peptide architecture by design. I was fascinated by the fact that such high organization of small chromophores could be achieved on the surface of self-forming nanotubes (**Chapter 1**). To this end, I redesigned the nanotube forming model peptide Ac-KLVFFAL-NH<sub>2</sub> (E22L), reasoning that by creating a binding ‘pocket’ within the peptide architecture, and introducing a small molecule that mimicked the elements I had removed to create that pocket, I could recover E22L’s native morphology.

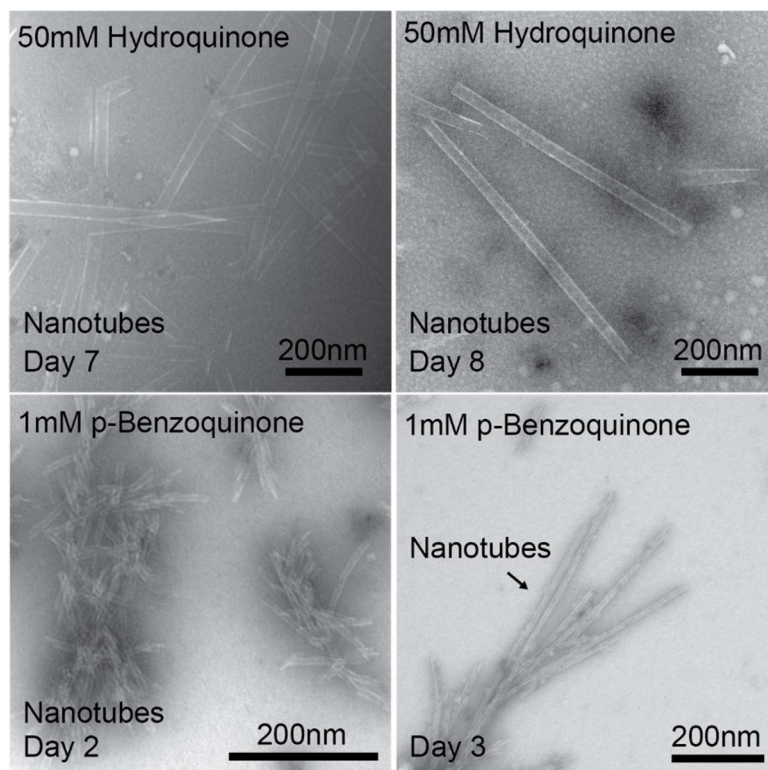


**Figure 5.5 – Benzylamine driven assembly of nanotubes.** TEM micrographs highlight the morphological similarities between the E22L nanotubes and the benzylamine assembled nanotubes. Cartoon representation shows the predicted arrangement of the small-molecules inside the peptide architecture.

Ac-KLDFAAL-NH<sub>2</sub> (V18D,F20A,E22L), incorporates the elements we thought were important for small molecule incorporation within the supramolecular nanostructure. First, aspartic acid (D) provides the docking site for a small molecule at neutral pH. Second, the removal of a phenylamine (F) amino acid, created a pocket within the supramolecular assembly that needed to be filled in order to optimize side-chain packing. Finally, **Figure 5.5** shows that we were able to recover the native morphology by rational design of the peptide. By introducing large amounts of benzylamine, we were able to drive the formation of nanotubes, though these were not

stable enough for full characterization. Most striking about this research was that we demonstrated that our understanding of the assembly code for E22L was at a point where we could rationally design the assembly of complex supramolecular structures by carefully selecting and replacing elements critical to the assembly propensity of a native sequence. If these structures are stabilized by covalently attaching a benzylamine molecule to the V18D position of the peptide, this project could expand to designing molecular carriers that are responsive to pH for encapsulation and release of their contents. Given that the small molecules are incorporated inside the supramolecular assembly, the surfaces could be functionalized. This motivated the incorporation of redox active small molecules within redesigned peptide architecture.

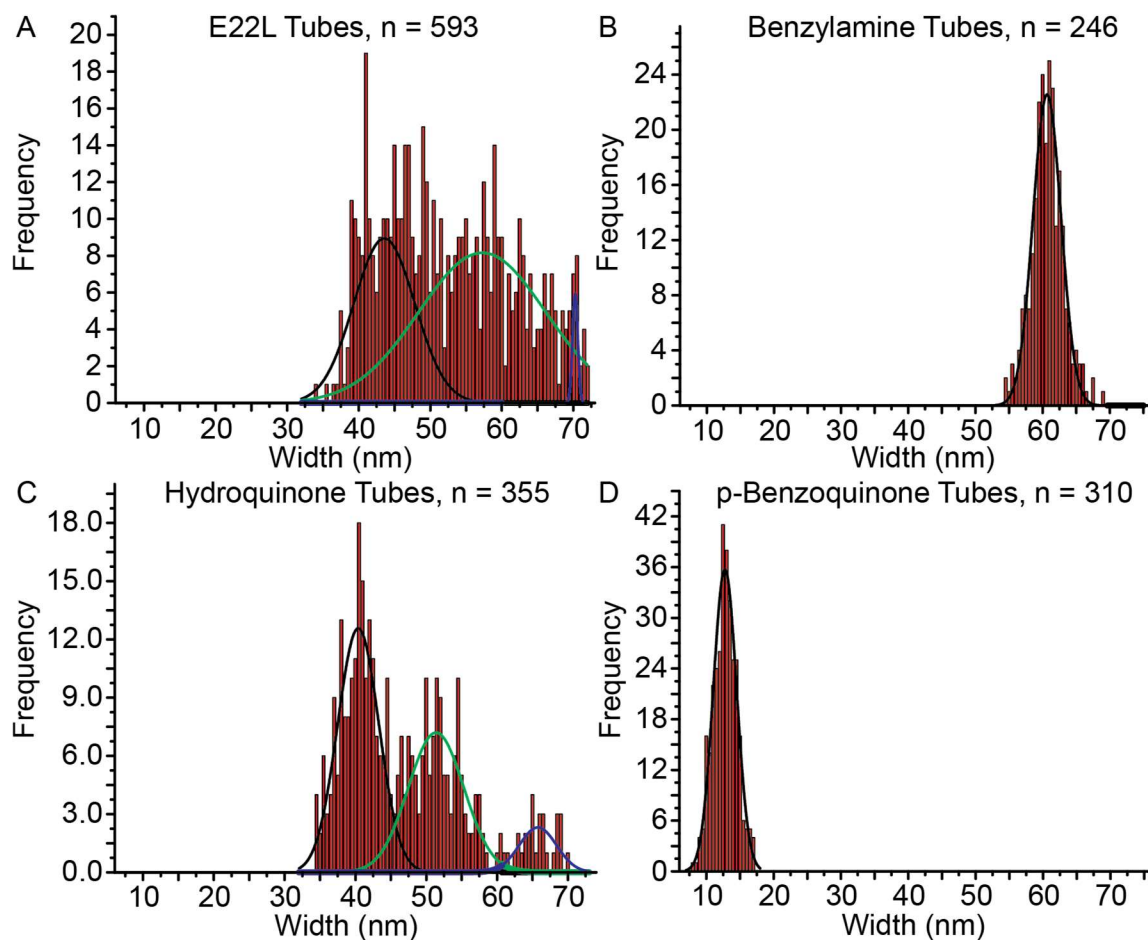
Hydroquinone and benzoquinone are important redox couples in biology (Nawar, Huskinson, & Aziz, 2013). We reasoned that given their conjugated ring structures, Phe19 could potentially stabilize their incorporation by face-face or edge-face  $\pi$ - $\pi$  interactions. Using the same peptide, V18D,F20A,E22L, we were able to recover the native morphology of E22L at high concentrations of hydroquinone and low concentrations of benzoquinone (**Figure 5.6**). These results again highlight the strides we have made by characterizing model systems in past years. Without such knowledge of the native structures, rational design of small-molecule encapsulating systems would never be possible.



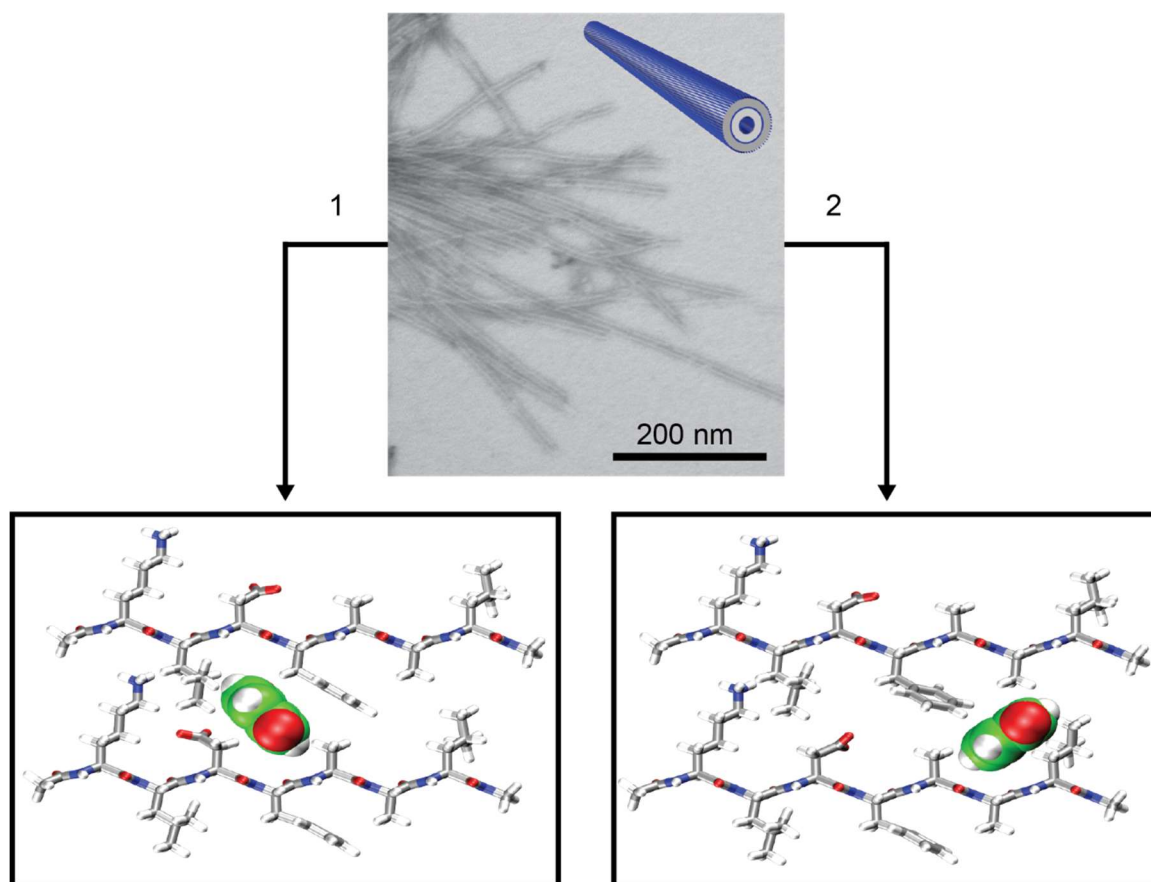
**Figure 5.6 – TEM micrographs of hydroquinone and quinone driven assembly of peptide nanotubes.**

Even though the structures formed in these experiments were homogenous and highly robust (**Figure 5.7**), they were not stable. All attempts to characterize their structure were frugal. I propose a model of incorporation of the quinone couple (**Figure 5.8**), supported by molecular dynamics simulations which maintain the small-molecule within the pocket, however, experimental confirmation is still needed.





**Figure 5.7 – Width distribution of rationally designed nanotubes.** All nanotubes assembled in water, pH: 7, adjusted with NaOH. (A) E22L nanotubes assembled in 40%  $\text{CH}_3\text{CN}$  with two Gaussian fits centered at  $43.6 \pm 0.8$  nm and  $57.3 \pm 3.1$  nm, and distributions of  $8.5 \pm 2.1$  nm and  $17.7 \pm 6.1$  nm, respectively. (B) Ac-KLDFAAL- $\text{NH}_2$  + Benzylamine nanotubes with one Gaussian fit centered at  $60.5 \pm 0.1$  nm, and a distribution of  $4.2 \pm 0.2$  nm. (C) Ac-KLDFAAL- $\text{NH}_2$  + p-Hydroquinone nanotubes with three Gaussian fits centered at  $40.4 \pm 0.3$  nm,  $51.4 \pm 0.5$  nm, and  $65.8 \pm 1.0$  nm and distributions of  $5.8 \pm 0.5$  nm,  $7.8 \pm 1.2$  and  $5.3 \pm 2.1$  nm, respectively. (D) Ac-KLDFAAL- $\text{NH}_2$  + p-Benzoquinone nanotubes with one Gaussian fit centered at  $12.6 \pm 0.1$  nm, and a distribution of  $3.4 \pm 0.2$  nm.



**Figure 5.8 - Quinone arrangement in peptide nanotubes.** TEM micrographs highlight the morphology of quinone assembled nanotubes. Cartoon representations show two possible arrangements for quinone incorporation within the peptide architecture. Quinone is shown to be stabilized by face-face interactions with Phe19 or face-edge interactions with Phe19.

The summary of results herein presented are meant to highlight the rational design of a complex, small-molecule encapsulating, self-assembling amyloid. The degree of control we have achieved in the design of complex self-assembling systems demonstrates that we are ready to move from characterization to functionalization of amyloids using the rules of peptide self-assembly we have thus far defined.

## **Conclusion**

MANs are likely to have a significant impact on the field of nanobiotechnology. Our group has developed a thorough understanding of self-assembling, prion-like amyloids. In cultivating this deeper understanding of self-assembly rules for these model peptides, we have developed functional catalysts and enzyme-like materials. These self-assembling systems are capable of templating the growth of homogeneous metalloamyloid nanostructures with demonstrated reactivity. The findings reported in this dissertation have the potential to shift the focus of research from structural design to rational functional design of self-assembling amyloids.

## References

- Adlard, P. A., & Bush, A. I. (2006). Metals and Alzheimer's disease. *Journal of Alzheimer's Disease*, *10*(2), 145-163.
- Adman, E. T. (1985). Structure and Function of Small Blue Copper Proteins. In P. Harrison (Ed.), *Metalloproteins Part 1: Metal proteins with redox roles* (pp. 1-42).
- Ahmed, M., Davis, J., Aucoin, D., Sato, T., Ahuja, S., Aimoto, S., . . . Smith, S. O. (2010). Structural conversion of neurotoxic amyloid-b(1-42) oligomers to fibrils. *Nature Structural & Molecular Biology*, *17*(5), 561-U556.  
doi:10.1038/Nsmb.1799
- Allsop, D., Mayes, J., Moore, S., Masad, A., & Tabner, B. J. (2008). Metal-dependent generation of reactive oxygen species from amyloid proteins implicated in neurodegenerative disease. *Biochemical Society Transactions*, *36*, 1293-1298.  
doi:10.1042/Bst0361293
- Ansari-Oghol-Beig, D., Rostami, M., Chernobrovkina, E., Saikin, S. K., Valleau, S., Mosallaei, H., & Aspuru-Guzik, A. (2013). Parametric hierarchical matrix approach for the wideband optical response of large-scale molecular aggregates. *Journal of Applied Physics*, *114*(16), 164315. doi:10.1063/1.4826189
- Anthony, N. R., Berland, K. M., Mehta, A. K., Lynn, D. G., & Seth Childers, W. (2014a). Chapter 3 - Imaging Nucleation, Growth and Heterogeneity in Self-Assembled

Amyloid Phases. In V. N. Uversky & Y. L. Lyubchenko (Eds.), *Bio-nanoimaging* (pp. 27-36). Boston: Academic Press.

Anthony, N. R., Berland, K. M., Mehta, A. K., Lynn, D. G., & Seth Childers, W. (2014b). Imaging Nucleation, Growth and Heterogeneity in Self-Assembled Amyloid Phases. In V. N. Uversky & Y. L. Lyubchenko (Eds.), *Bio-nanoimaging* (pp. 27-36). Boston: Academic Press.

Anthony, N. R., Mehta, A. K., Lynn, D. G., & Berland, K. M. (2014). Mapping amyloid-b(16-22) nucleation pathways using fluorescence lifetime imaging microscopy. *Soft Matter*, *10*(23), 4162 - 4172. doi:10.1039/C4SM00361F

Antzutkin, O. N., Leapman, R. D., Balbach, J. J., & Tycko, R. (2002). Supramolecular structural constraints on Alzheimer's b-amyloid fibrils from electron microscopy and solid-state nuclear magnetic resonance. *Biochemistry*, *41*(51), 15436-15450.

Arvanitis, D. A., Vafiadaki, E., Sanoudou, D., & Kranias, E. G. (2011). Histidine-rich calcium binding protein: The new regulator of sarcoplasmic reticulum calcium cycling. *Journal of Molecular and Cellular Cardiology*, *50*(1), 43-49. doi:10.1016/j.yjmcc.2010.08.021

Auer, S., Ricchiuto, P., & Kashchiev, D. (2012). Two-Step Nucleation of Amyloid Fibrils: Omnipresent or Not? *Journal of Molecular Biology*, *422*(5), 723-730. doi:10.1016/j.jmb.2012.06.022

Axelrod, D. (1979). Carbocyanine dye orientation in red cell membrane studied by microscopic fluorescence polarization. *Biophys J*, *26*(3), 557-573. doi:10.1016/S0006-3495(79)85271-6

- Bagriantsev, S. N., Kushnirov, V. V., & Liebman, S. W. (2006). Analysis of amyloid aggregates using agarose gel electrophoresis. *Methods in Enzymology*, *412*, 33-48. doi:10.1016/S0076-6879(06)12003-0
- Bak, M., Rasmussen, J. T., & Nielsen, N. C. (2000). SIMPSON: A general simulation program for solid-state NMR spectroscopy. *Journal of Magnetic Resonance*, *147*(2), 296-330. doi:10.1006/jmre.2000.2179
- Balbach, J. J., Ishii, Y., Antzutkin, O. N., Leapman, R. D., Rizzo, N. W., Dyda, F., . . . Tycko, R. (2000). Amyloid fibril formation by Ab16-22, a seven-residue fragment of the Alzheimer's b-amyloid peptide, and structural characterization by solid state NMR. *Biochemistry*, *39*(45), 13748-13759.
- Baldwin, R. L., & Rose, G. D. (2013). Molten globules, entropy-driven conformational change and protein folding. *Current Opinion in Structural Biology*, *23*(1), 4-10. doi:10.1016/j.sbi.2012.11.004
- Balland, V., Hureau, C., & Saveant, J. M. (2010). Electrochemical and homogeneous electron transfers to the Alzheimer amyloid-beta copper complex follow a preorganization mechanism. *Proceedings of the National Academy of Sciences of the United States of America*, *107*(40), 17113-17118. doi:DOI 10.1073/pnas.1011315107
- Barnham, K. J., McKinstry, W. J., Multhaup, G., Galatis, D., Morton, C. J., Curtain, C. C., . . . Cappai, R. (2003). Structure of the Alzheimer's disease amyloid precursor protein copper binding domain - A regulator of neuronal copper homeostasis. *Journal of Biological Chemistry*, *278*(19), 17401-17407. doi:DOI 10.1074/jbc.M300629200

- Baumkötter, F., Schmidt, N., Vargas, C., Schilling, S., Weber, R., Wagner, K., . . . Kins, S. (2014). Amyloid Precursor Protein Dimerization and Synaptogenic Function Depend on Copper Binding to the Growth Factor-Like Domain. *Journal of Neuroscience*, *34*(33), 11159-11172. doi:10.1523/Jneurosci.0180-14.2014
- Benzinger, T. L. S., Gregory, D. M., Burkoth, T. S., Miller-Auer, H., Lynn, D. G., Botto, R. E., & Meredith, S. C. (2000). Two-Dimensional Structure of  $\beta$ -Amyloid(10–35) Fibrils†. *Biochemistry*, *39*(12), 3491-3499. doi:10.1021/bi991527v
- Bonnefoy, J., Legrand, A., Quadrelli, E. A., Canivet, J., & Farrusseng, D. (2015). Enantiopure Peptide-Functionalized Metal-Organic Frameworks. *Journal of the American Chemical Society*, *137*(29), 9409-9416. doi:10.1021/jacs.5b05327
- Bower, P. V., Oyler, N., Mehta, M. A., Long, J. R., Stayton, P. S., & Drobny, G. P. (1999). Determination of torsion angles in proteins and peptides using solid state NMR. *Journal of the American Chemical Society*, *121*(36), 8373-8375. doi:10.1021/Ja991330q
- Brauner, J. W., Dugan, C., & Mendelsohn, R. (2000).  $^{13}\text{C}$  Isotope Labeling of Hydrophobic Peptides. Origin of the Anomalous Intensity Distribution in the Infrared Amide I Spectral Region of  $\beta$ -Sheet Structures. *Journal of the American Chemical Society*, *122*(4), 677-683. doi:10.1021/ja992522o
- Brovchenko, I., Burri, R. R., Krukau, A., & Oleinikova, A. (2009). Thermal expansivity of amyloid b(16-22) peptides and their aggregates in water. *Physical Chemistry Chemical Physics*, *11*(25), 5035-5040. doi:10.1039/b820340g

- Burkoth, T. S., Benzinger, T. L. S., Urban, V., Morgan, D. M., Gregory, D. M., Thiagarajan, P., . . . Lynn, D. G. (2000). Structure of the b-amyloid<sub>(10-35)</sub> fibril. *Journal of the American Chemical Society*, *122*(33), 7883-7889.
- Camerman, N., Fawcett, J. K., Kruck, T. P. A., Sarkar, B., & Camerman, A. (1978). Copper(II)-Histidine Stereochemistry - Structure of L-Histidinato-D-Histidinatodiaquocopper(II) Tetrahydrate. *Journal of the American Chemical Society*, *100*(9), 2690-2693. doi:DOI 10.1021/ja00477a020
- Castelletto, V., Hamley, I. W., Hule, R. A., & Pochan, D. (2009). Helical-Ribbon Formation by a b-Amino Acid Modified Amyloid b-Peptide Fragment. *Angewandte Chemie International Edition*, *48*(13), 2317-2320. doi:10.1002/anie.200805500
- Catalano, S. M., Dodson, E. C., Henze, D. A., Joyce, J. G., Krafft, G. A., & Kinney, G. G. (2006). The role of amyloid-b derived diffusible ligands (ADDLs) in Alzheimer's disease. *Current Topics in Medicinal Chemistry*, *6*(6), 597-608.
- Chen, C., Tan, J., Hsieh, M.-C., Pan, T., Goodwin, J. T., Mehta, A. K., . . . Lynn, D. G. (2017). Design of multi-phase dynamic chemical networks. *Nature Chemistry*, advance online publication. doi:10.1038/nchem.2737
- Cheon, M., Chang, I., & Hall, C. K. (2011). Spontaneous formation of twisted Ab(16-22) fibrils in large-scale molecular-dynamics simulations. *Biophysical Journal*, *101*(10), 2493-2501. doi:10.1016/j.bpj.2011.08.042
- Childers, W. S., Anthony, N. R., Mehta, A. K., Berland, K. M., & Lynn, D. G. (2012). Phase Networks of Cross- $\beta$  Peptide Assemblies. *Langmuir*, *28*(15), 6386-6395. doi:10.1021/la300143j



- Childers, W. S., Mehta, A. K., Lu, K., & Lynn, D. G. (2009). Templating Molecular Arrays in Amyloid's Cross- $\beta$  Grooves. *Journal of the American Chemical Society*, *131*(29), 10165-10172. doi:10.1021/ja902332s
- Childers, W. S., Mehta, A. K., Ni, R., Taylor, J. V., & Lynn, D. G. (2010). Peptides Organized as Bilayer Membranes. *Angewandte Chemie International Edition*, *49*(24), 4104-4107. doi:10.1002/anie.201000212
- Childers, W. S., Ni, R., Mehta, A. K., & Lynn, D. G. (2009). Peptide membranes in chemical evolution. *Current Opinion in Chemical Biology*, *13*(5-6), 652-659. doi:10.1016/j.cbpa.2009.09.027
- Christensen, A. M., & Schaefer, J. (1993). Solid-state NMR determination of intra- and intermolecular  $^{31}\text{P}$ - $^{13}\text{C}$  distances for shikimate 3-phosphate and [ $1\text{-}^{13}\text{C}$ ]glyphosate bound to enolpyruvylshikimate-3-phosphate synthase. *Biochemistry*, *32*(11), 2868-2873. doi:10.1021/bi00062a018
- Cummings, J. L. (2004). Alzheimer's disease. *New England Journal of Medicine*, *351*(1), 56-67. doi:10.1056/NEJMra040223
- Dai, B., Li, D., Xi, W., Luo, F., Zhang, X., Zou, M., . . . Liu, C. (2015). Tunable assembly of amyloid-forming peptides into nanosheets as a retrovirus carrier. *Proceedings of the National Academy of Sciences, USA*, *112*(10), 2996-3001. doi:10.1073/pnas.1416690112
- Debela, A. M., Ortiz, M., ÓSullivan, C. K., Thorimbert, S., & Hasenknopf, B. (2014). Postfunctionalization of Keggin silicotungstates by general coupling procedures. *Polyhedron*, *68*, 131-137. doi:<http://dx.doi.org/10.1016/j.poly.2013.10.020>

- Debeljuh, N., Barrow, C. J., & Byrne, N. (2011). The impact of ionic liquids on amyloid fibrilization of Ab16-22: tuning the rate of fibrilization using a reverse Hofmeister strategy. *Physical Chemistry Chemical Physics*, *13*(37), 16534-16536. doi:10.1039/C1cp22256b
- DeMay, B. S., Noda, N., Gladfelter, A. S., & Oldenbourg, R. (2011). Rapid and quantitative imaging of excitation polarized fluorescence reveals ordered septin dynamics in live yeast. *Biophys J*, *101*(4), 985-994. doi:10.1016/j.bpj.2011.07.008
- Dias, E. M., & Petit, C. (2016). Towards the use of metal-organic frameworks for water reuse: a review of the recent advances in the field of organic pollutants removal and degradation and the next steps in the field (vol 3, pg 22484, 2015). *Journal of Materials Chemistry A*, *4*(9), 3565-3565. doi:10.1039/c6ta90036d
- Dong, J. (2006). *Metal Ions: a Probe of Amyloid Fibril Formation*. (Ph.D.), Emory university, Atlanta.
- Dong, J., Apkarian, R. P., & Lynn, D. G. (2005). Imaging amyloid  $\beta$  peptide oligomeric particles in solution. *Bioorganic & Medicinal Chemistry*, *13*(17), 5213-5217. doi:<http://dx.doi.org/10.1016/j.bmc.2005.05.052>
- Dong, J., Canfield, J. M., Mehta, A. K., Shokes, J. E., Tian, B., Childers, W. S., . . . Lynn, D. G. (2007). Engineering metal ion coordination to regulate amyloid fibril assembly and toxicity. *Proceedings of the National Academy of Sciences, USA*, *104*(33), 13313-13318. doi:10.1073/pnas.0702669104
- Dong, J., Lu, K., Lakdawala, A., Mehta, A. K., & Lynn, D. G. (2006). Controlling amyloid growth in multiple dimensions. *Amyloid*, *13*(4), 206-215. doi:10.1080/13506120600960809

- Dong, J., Shokes, J. E., Scott, R. A., & Lynn, D. G. (2006). Modulating Amyloid Self-Assembly and Fibril Morphology with Zn(II). *Journal of the American Chemical Society*, 128(11), 3540-3542. doi:10.1021/ja055973j
- Elgersma, R. C., van Dijk, M., Dechesne, A. C., van Nostrum, C. F., Hennink, W. E., Rijkers, D. T., & Liskamp, R. M. (2009). Microwave-assisted click polymerization for the synthesis of Ab(16-22) cyclic oligomers and their self-assembly into polymorphous aggregates. *Organic & Biomolecular Chemistry*, 7(21), 4517-4525. doi:10.1039/b912851d
- Foster, A. W., Osman, D., & Robinson, N. J. (2014). Metal Preferences and Metallation. *The Journal of biological chemistry*, 289(41), 28095-28103. doi:10.1074/jbc.R114.588145
- Fraser, P. E., McLachlan, D. R., Surewicz, W. K., Mizzen, C. A., Snow, A. D., Nguyen, J. T., & Kirschner, D. A. (1994). Conformation and fibrillogenesis of Alzheimer Ab peptides with selected substitution of charged residues. *Journal of Molecular Biology*, 244(1), 64-73. doi:10.1006/jmbi.1994.1704
- Fung, B. M., Khitrin, A. K., & Ermolaev, K. (2000). An improved broadband decoupling sequence for liquid crystals and solids. *Journal of Magnetic Resonance*, 142(1), 97-101. doi:10.1006/jmre.1999.1896
- Gangu, K. K., Maddila, S., Mukkamala, S. B., & Jonnalagadda, S. B. (2016). A review on contemporary Metal-Organic Framework materials. *Inorganica Chimica Acta*, 446, 61-74. doi:10.1016/j.ica.2016.02.062

- Gawande, M. B., & Branco, P. S. (2011). An efficient and expeditious Fmoc protection of amines and amino acids in aqueous media. *Green Chemistry*, *13*(12), 3355-3359. doi:10.1039/C1GC15868F
- Gehman, J. D., Separovic, F., Lu, K., & Mehta, A. K. (2007). Boltzmann statistics rotational-echo double-resonance analysis. *Journal of Physical Chemistry B*, *111*(27), 7802-7811. doi:10.1021/jp072504q
- Gilead, S., & Gazit, E. (2005). Self-organization of short peptide fragments: From amyloid fibrils to nanoscale supramolecular assemblies. *Supramolecular Chemistry*, *17*(1-2), 87-92.
- Goetz, J. M., & Schaefer, J. (1997). REDOR Dephasing by Multiple Spins in the Presence of Molecular Motion. *Journal of Magnetic Resonance*, *127*(2), 147-154. doi:10.1006/jmre.1997.1198
- Gorbitz, C. H. (2013). Theoretical Basis of Biological Self-Assembly. In J. Castillo-Leon, L. Sasso, & W. E. Svendsen (Eds.), *Self-Assembled Peptide Nanostructures: Advances and Applications in Nanobiotechnology* (pp. 1-32). Singapore: Pan Stanford Publishing Pte. Ltd.
- Govindjee, Kern, J. F., Messinger, J., & Whitmarsh, J. (2001). Photosystem II *eLS*: John Wiley & Sons, Ltd.
- Gray, H. B., Malmstrom, B. G., & Williams, R. J. P. (2000). Copper coordination in blue proteins. *Journal of Inorganic Chemistry*, *5*, 551-559. doi:10.1007/s007750000146
- Gregory, D. M., Benzinger, T. L., Burkoth, T. S., Miller-Auer, H., Lynn, D. G., Meredith, S. C., & Botto, R. E. (1998). Dipolar recoupling NMR of biomolecular self-

assemblies: determining inter- and intrastrand distances in fibrilized Alzheimer's b-amyloid peptide. *Solid State Nuclear Magnetic Resonance*, 13(3), 149-166.  
doi:10.1016/S0926-2040(98)00086-1

Gregory, D. M., Mehta, M. A., Shiels, J. C., & Drobny, G. P. (1997). Determination of local structure in solid nucleic acids using double quantum nuclear magnetic resonance spectroscopy. *Journal of Chemical Physics*, 107(1), 28-42.  
doi:10.1063/1.474350

Gross, E. L. (1993). Plastocyanin: Structure and function. *Photosynthesis Research*, 37(2), 103-116. doi:10.1007/BF02187469

Gullion, T. (1998). Introduction to rotational-echo, double-resonance NMR. *Concepts in Magnetic Resonance A.*, 10(5), 277-289. doi:10.1002/(SICI)1099-0534(1998)10:5<277::AID-CMR1>3.0.CO;2-U

Gullion, T., Baker, D. B., & Conradi, M. S. (1990). New, Compensated Carr-Purcell Sequences. *Journal of Magnetic Resonance*, 89(3), 479-484. doi:10.1016/0022-2364(90)90331-3

Gullion, T., & Schaefer, J. (1989). Detection of Weak Heteronuclear Dipolar Coupling by Rotational-Echo Double-Resonance NMR. *Advances in Magnetic and Optical Resonance*, 13, 57-84. doi:10.1016/B978-0-12-025513-9.50009-4

Gullion, T., & Schaefer, J. (1989). Rotational-Echo Double-Resonance NMR. *Journal of Magnetic Resonance*, 81(1), 196-200. doi:10.1016/0022-2364(89)90280-1

Guo, Q., Mehta, A. K., Grover, M. A., Chen, W., Lynn, D. G., & Chen, Z. (2013). Shape-Selection and Multi-stability in Helical Ribbons. *Applied Physics Letters*, in press.

- Gupta, R., Guin, S. K., & Aggarwal, S. K. (2012). A mechanistic study on the electrocatalysis of the Pu(iv)/Pu(iii) redox reaction at a platinum electrode modified with single-walled carbon nanotubes (SWCNTs) and polyaniline (PANI). *RSC Advances*, 2(5), 1810-1819. doi:10.1039/C1RA01010G
- Habenstein, B., Loquet, A., Giller, K., Becker, S., & Lange, A. (2013). Structural characterization of supramolecular assemblies by C-13 spin dilution and 3D solid-state NMR. *Journal of Biomolecular NMR*, 55(1), 1-9. doi:10.1007/s10858-012-9691-9
- Hamley, I. W. (2007). Peptide fibrillization. *Angewandte Chemie-International Edition*, 46(43), 8128-8147. doi:10.1002/anie.200700861
- Hamley, I. W. (2014). Peptide Nanotubes. *Angewandte Chemie International Edition*, 53(27), 6866-6881. doi:10.1002/anie.201310006
- Hatch, G. P. (2012). Dynamics in the Global Market for Rare Earths. *Elements*, 8(5), 341-346. doi:10.2113/gselements.8.5.341
- Hegetschweiler, K., & Saltman, P. (1986). Interaction of copper(II) with N-(2-hydroxyethyl)piperazine-N'-ethanesulfonic acid (HEPES). *Inorganic Chemistry*, 25(1), 107-109. doi:10.1021/ic00221a028
- Hernández-Guzmán, J., Sun, L., Mehta, A. K., Dong, J., Lynn, D. G., & Warncke, K. (2013). Copper(II)-bis-Histidine Coordination Structure in a Fibrillar Amyloid  $\beta$ -Peptide Fragment and Model Complexes Revealed by Electron Spin Echo Envelope Modulation Spectroscopy. *ChemBioChem*, 14(14), 1762-1771. doi:10.1002/cbic.201300236

- Hesse, L., Beher, D., Masters, C. L., & Multhaup, G. (1994). The Beta-A4 Amyloid Precursor Protein-Binding to Copper. *FEBS Letters*, *349*(1), 109-116. doi:10.1016/0014-5793(94)00658-X
- Holtzman, D. M., Morris, J. C., & Goate, A. M. (2011). Alzheimer's disease: the challenge of the second century. *Science Translational Medicine*, *3*(77), 77sr71. doi:10.1126/scitranslmed.3002369
- Hong, Y., Pritzker, M. D., Legge, R. L., & Chen, P. (2005). Effect of NaCl and peptide concentration on the self-assembly of an ionic-complementary peptide EAK16-II. *Colloids and Surfaces B-Biointerfaces*, *46*(3), 152-161. doi:10.1016/j.colsurfb.2005.11.004
- Horcajada, P., Gref, R., Baati, T., Allan, P. K., Maurin, G., Couvreur, P., . . . Serre, C. (2012). Metal-organic frameworks in biomedicine. *Chemical Reviews*, *112*(2), 1232-1268. doi:10.1021/cr200256v
- Hsieh, M.-C., Liang, C., Mehta, A. K., Lynn, D. G., & Grover, M. A. *Previous submission in this series.*
- Hung, Y. H., Robb, E. L., Volitakis, I., Ho, M., Evin, G., Li, Q. X., . . . Bush, A. I. (2009). Paradoxical condensation of copper with elevated beta-amyloid in lipid rafts under cellular copper deficiency conditions: implications for Alzheimer disease. *Journal of Biological Chemistry*, *284*(33), 21899-21907. doi:10.1074/jbc.M109.019521
- Hureau, C., & Faller, P. (2009). A $\beta$ -mediated ROS production by Cu ions: Structural insights, mechanisms and relevance to Alzheimer's disease. *Biochimie*, *91*(10), 1212-1217. doi:10.1016/j.biochi.2009.03.013

- Iqbal, P., Preece, J. A., & Mendes, P. M. (2012). Nanotechnology: The "Top-Down" and "Bottom-up" approaches. In J. W. Steed & P. A. Gale (Eds.), *Supramolecular Chemistry: From Molecules to Nanomaterials* (Vol. 8, pp. 3589-3602): John Wiley & Sons, Ltd. .
- Irback, A., & Mitternacht, S. (2008). Spontaneous b-barrel formation: An all-atom Monte Carlo study of Ab(16-22) oligomerization. *Proteins: Structure, Function & Bioinformatics*, 71(1), 207-214. doi:Doi 10.1002/Prot.21682
- Ivanova, M. I., Sievers, S. A., Sawaya, M. R., Wall, J. S., & Eisenberg, D. (2009). Molecular basis for insulin fibril assembly. *Proceedings of the National Academy of Sciences of the United States of America*, 106(45), 18990-18995. doi:10.1073/pnas.0910080106
- Jarvie, T. P., Went, G. T., & Mueller, K. T. (1996). Simultaneous multiple distance measurements in peptides via solid-state NMR. *Journal of the American Chemical Society*, 118(22), 5330-5331. doi:10.1021/Ja960188f
- Jayawarna, V., & Ulijn, R. V. (2012). Designing Peptide-Based Supramolecular Biomaterials *Supramolecular Chemistry*: John Wiley & Sons, Ltd.
- Jiang, D. L., Zhang, L., Grant, G. P. G., Dudzik, C. G., Chen, S., Patel, S., . . . Zhou, F. M. (2013). The Elevated Copper Binding Strength of Amyloid-beta Aggregates Allows the Sequestration of Copper from Albumin: A Pathway to Accumulation of Copper in Senile Plaques. *Biochemistry*, 52(3), 547-556. doi:10.1021/bi301053h
- Jiang, T., Xu, C., Liu, Y., Liu, Z., Wall, J. S., Zuo, X., . . . Conticello, V. P. (2014). Structurally Defined Nanoscale Sheets from Self-Assembly of Collagen-Mimetic



Peptides. *Journal of the American Chemical Society*, 136(11), 4300-4308.

doi:10.1021/ja412867z

Jomova, K., Vondrakova, D., Lawson, M., & Valko, M. (2010). Metals, oxidative stress and neurodegenerative disorders. *Molecular and Cellular Biochemistry*, 345(1-2), 91-104. doi:10.1007/s11010-010-0563-x

Jucker, M., & Walker, L. C. (2015). Neurodegeneration: Amyloid-[beta] pathology induced in humans. *Nature*, 525(7568), 193-194. doi:10.1038/525193a

Kabir, M. E., & Safar, J. G. (2014). Implications of prion adaptation and evolution paradigm for human neurodegenerative diseases. *Prion*, 8(1), 111-116.

Karran, E., Mercken, M., & Strooper, B. D. (2011). The amyloid cascade hypothesis for Alzheimer's disease: an appraisal for the development of therapeutics. *Nature Reviews: Drug Discovery*, 10(9), 698-712.

Kasotakis, E., Mossou, E., Adler-Abramovich, L., Mitchell, E. P., Forsyth, V. T., Gazit, E., & Mitraki, A. (2009). Design of metal-binding sites onto self-assembled peptide fibrils. *Peptide Science*, 92(3), 164-172. doi:10.1002/bip.21163

Kelly, S. M., Jess, T. J., & Price, N. C. (2005). How to study proteins by circular dichroism. *Biochimica Et Biophysica Acta-Proteins and Proteomics*, 1751(2), 119-139. doi:10.1016/j.bbapap.2005.06.005

Kim, J. H., Lee, M., Lee, J. S., & Park, C. B. (2012). Self-Assembled Light-Harvesting Peptide Nanotubes for Mimicking Natural Photosynthesis. *Angewandte Chemie International Edition*, 51(2), 517-520. doi:10.1002/anie.201103244

- Kitazawa, M., Medeiros, R., & LaFerla, F. M. (2012). Transgenic Mouse Models of Alzheimer Disease: Developing a Better Model as a Tool for Therapeutic Interventions. *Current Pharmaceutical Design*, *18*(8), 1131-1147.
- Klein, W. L., Krafft, G. A., & Finch, C. E. (2001). Targeting small Ab oligomers: the solution to an Alzheimer's disease conundrum? *Trends in Neurosciences*, *24*(4), 219-224. doi:10.1016/S0166-2236(00)01749-5
- Klimov, D. K., Straub, J. E., & Thirumalai, D. (2004). Aqueous urea solution destabilizes Ab(16-22) oligomers. *Proceedings of the National Academy of Sciences of the United States of America*, *101*(41), 14760-14765. doi:10.1073/pnas.0404570101
- Klimov, D. K., & Thirumalai, D. (2003). Dissecting the assembly of Ab(16-22) amyloid peptides into antiparallel  $\beta$  sheets. *Structure*, *11*(3), 295-307.
- Knauer, M. F., Soreghan, B., Burdick, D., Kosmoski, J., & Glabe, C. G. (1992). Intracellular accumulation and resistance to degradation of the Alzheimer amyloid A4/b protein. *Proceedings of the National Academy of Sciences of the United States of America*, *89*(16), 7437-7441.
- Krone, M. G., Hua, L., Soto, P., Zhou, R., Berne, B. J., & Shea, J. E. (2008). Role of water in mediating the assembly of Alzheimer amyloid- $\beta$  Ab16-22 protofilaments. *Journal of the American Chemical Society*, *130*(33), 11066-11072.
- Lee, J., Kwak, J. H., & Choe, W. (2017). Evolution of form in metal-organic frameworks. *Nature Communications*, *8*. doi:ARTN 14070
- 10.1038/ncomms14070

- Li, G., & Pomès, R. (2013). Binding Mechanism of Inositol Stereoisomers to Monomers and Aggregates of A $\beta$ (16-22). *Journal of Physical Chemistry B*, 117(22), 6603-6613. doi:10.1021/jp311350r
- Li, H., Luo, Y., Derreumaux, P., & Wei, G. (2011). Carbon Nanotube Inhibits the Formation of  $\beta$ -Sheet-Rich Oligomers of the Alzheimer's Amyloid- $\beta$ (16-22) Peptide. *Biophysical Journal*, 101(9), 2267-2276. doi:10.1016/j.bpj.2011.09.046
- Li, S., Mehta, A. K., Sidorov, A. N., Orlando, T. M., Jiang, Z., Anthony, N. R., & Lynn, D. G. (2016). Design of Asymmetric Peptide Bilayer Membranes. *Journal of the American Chemical Society*, 138(10), 3579-3586. doi:10.1021/jacs.6b00977
- Li, S., Sidorov, A. N., Mehta, A. K., Bisignano, A. J., Das, D., Childers, W. S., . . . Lynn, D. G. (2014). Neurofibrillar Tangle Surrogates: Histone H1 Binding to Patterned Phosphotyrosine Peptide Nanotubes. *Biochemistry*, 53(26), 4225–4227. doi:10.1021/bi500599a
- Liang, C., Ni, R., Smith, J. E., Childers, W. S., Mehta, A. K., & Lynn, D. G. (2014). Kinetic Intermediates in Amyloid Assembly. *Journal of the American Chemical Society*, 136(43), 15146-15149. doi:10.1021/ja508621b
- Liang, Y., Guo, P., Pingali, S. V., Pabit, S., Thiyagarajan, P., Berland, K. M., & Lynn, D. G. (2008). Light harvesting antenna on an amyloid scaffold. *Chemical Communications*(48), 6522-6524. doi:10.1039/B814262A
- Liang, Y., Lynn, D. G., & Berland, K. M. (2010). Direct Observation of Nucleation and Growth in Amyloid Self-Assembly. *Journal of the American Chemical Society*, 132(18), 6306-6308. doi:10.1021/ja910964c

- Liang, Y., Pingali, S. V., Jogalekar, A. S., Snyder, J. P., Thiyagarajan, P., & Lynn, D. G. (2008). Cross-Strand Pairing and Amyloid Assembly. *Biochemistry*, *47*(38), 10018-10026. doi:10.1021/bi801081c
- Liao, S. M., Du, Q. S., Meng, J. Z., Pang, Z. W., & Huang, R. B. (2013). The multiple roles of histidine in protein interactions. *Chemistry Central Journal*, *7*. doi:Artn 44  
10.1186/1752-153x-7-44
- Lin, D., Luo, Y., Wu, S., Ma, Q., Wei, G., & Yang, X. (2014). Investigation of the Aggregation Process of Amyloid- $\beta$ -(16-22) Peptides and the Dissolution of Intermediate Aggregates. *Langmuir*, *30*(11), 3170-3175. doi:10.1021/la4048165
- Liu, B., Moloney, A., Meehan, S., Morris, K., Thomas, S. E., Serpell, L. C., . . . Crowther, D. C. (2011). Iron promotes the toxicity of amyloid beta peptide by impeding its ordered aggregation. *Journal of Biological Chemistry*, *286*(6), 4248-4256. doi:10.1074/jbc.M110.158980
- Liu, K., Abass, M., Zou, Q., & Yan, X. (2017). Self-assembly of biomimetic light-harvesting complexes capable of hydrogen evolution. *Green Energy & Environment*, *2*(1), 58-63. doi:<https://doi.org/10.1016/j.gee.2016.12.005>
- Liu, K., Kang, Y., Ma, G., Mohwald, H., & Yan, X. (2016). Molecular and mesoscale mechanism for hierarchical self-assembly of dipeptide and porphyrin light-harvesting system. *Physical Chemistry Chemical Physics*, *18*(25), 16738-16747. doi:10.1039/C6CP01358A
- Liu, K., Xing, R., Chen, C., Shen, G., Yan, L., Zou, Q., . . . Yan, X. (2015). Peptide-Induced Hierarchical Long-Range Order and Photocatalytic Activity of Porphyrin

Assemblies. *Angewandte Chemie International Edition*, 54(2), 500-505.

doi:10.1002/anie.201409149

Liu, K., Xing, R., Li, Y., Zou, Q., Möhwald, H., & Yan, X. (2016). Mimicking Primitive Photobacteria: Sustainable Hydrogen Evolution Based on Peptide–Porphyrin Co-Assemblies with a Self-Mineralized Reaction Center. *Angewandte Chemie International Edition*, 55(40), 12503-12507. doi:10.1002/anie.201606795

Liu, P., Ni, R., Mehta, A. K., Childers, W. S., Lakdawala, A., Pingali, S. V., . . . Lynn, D. G. (2008). Nucleobase-Directed Amyloid Nanotube Assembly. *Journal of the American Chemical Society*, 130(50), 16867-16869. doi:10.1021/ja807425h

Liu, X., Li, J., Dong, J., Hu, C., Gong, W., & Wang, J. (2012). Genetic incorporation of a metal-chelating amino acid as a probe for protein electron transfer. *Angewandte Chemie, International Edition in English*, 51(41), 10261-10265. doi:10.1002/anie.201204962

Long, D.-L., Tsunashima, R., & Cronin, L. (2010). Polyoxometalates: Building Blocks for Functional Nanoscale Systems. *Angewandte Chemie International Edition*, 49(10), 1736-1758. doi:10.1002/anie.200902483

Long, J. R., Dindot, J. L., Zebroski, H., Kiihne, S., Clark, R. H., Campbell, A. A., . . . Drobny, G. P. (1998). A peptide that inhibits hydroxyapatite growth is in an extended conformation on the crystal surface. *Proceedings of the National Academy of Sciences of the United States of America*, 95(21), 12083-12087.

Lu, K., Guo, L., Mehta, A. K., Childers, W. S., Dublin, S. N., Skanthakumar, S., . . . Lynn, D. G. (2007). Macroscale assembly of peptide nanotubes. *Chemical Communications*(26), 2729-2731. doi:10.1039/B701029J

- Lu, K., Jacob, J., Thiyagarajan, P., Conticello, V. P., & Lynn, D. G. (2003). Exploiting Amyloid Fibril Lamination for Nanotube Self-Assembly. *Journal of the American Chemical Society*, *125*(21), 6391-6393. doi:10.1021/ja0341642
- M de Groot, H. J. (2010). Photosynthetic Antennae and Reaction Centers *Solid-state NMR studies of biopolymers* (pp. 509 - 517): Wiley.
- Ma, B., & Nussinov, R. (2002). Stabilities and conformations of Alzheimer's b-amyloid peptide oligomers (Ab16-22, Ab16-35, and Ab10-35): Sequence effects. *Proc Natl Acad Sci*, *99*(22), 14126-14131.
- Manske, A. K., Glaeser, J., Kuypers, M. A. M., & Overmann, J. (2005). Physiology and phylogeny of green sulfur bacteria forming a monospecific phototrophic assemblage at a depth of 100 meters in the Black Sea. *Applied and Environmental Microbiology*, *71*(12), 8049-8060. doi:10.1128/Aem.71.12.8049-8060.2005
- Mantion, A., Massuger, L., Rabu, P., Palivan, C., McCusker, L. B., & Taubert, A. (2008). Metal-peptide frameworks (MPFs): "Bioinspired" metal organic frameworks. *Journal of the American Chemical Society*, *130*(8), 2517-2526. doi:10.1021/ja0762588
- Martinez, A. V., Małolepsza, E., Rivera, E., Lu, Q., & Straub, J. E. (2014). Exploring the role of hydration and confinement in the aggregation of amyloidogenic peptides A $\beta$ 16–22 and Sup357–13 in AOT reverse micelles. *Journal of Chemical Physics*, *141*(22), 22D530. doi:10.1063/1.4902550
- Masuoka, J., & Saltman, P. (1994). Zinc(II) and Copper(II) Binding to Serum Albumin. *The Journal of biological chemistry*, *269*(41), 25557-25561.

- McGuire, C. V., & Forgan, R. S. (2015). The surface chemistry of metal-organic frameworks. *Chemical Communications*, 51(25), 5199-5217.  
doi:10.1039/c4cc04458d
- Mehta, A. K., Lu, K., Childers, W. S., Liang, Y., Dublin, S. N., Dong, J., . . . Lynn, D. G. (2008). Facial Symmetry in Protein Self-Assembly. *Journal of the American Chemical Society*, 130(30), 9829-9835. doi:10.1021/ja801511n
- Mehta, A. K., Rosen, R. F., Childers, W. S., Gehman, J. D., Walker, L. C., & Lynn, D. G. (2013). Context dependence of protein misfolding and structural strains in neurodegenerative diseases. *Biopolymers*, 100(6), 722-730.  
doi:10.1002/bip.22283
- Mehta, M. A., Eddy, M. T., McNeill, S. A., Mills, F. D., & Long, J. R. (2008). Determination of peptide backbone torsion angles using double-quantum dipolar recoupling solid-state NMR Spectroscopy. *Journal of the American Chemical Society*, 130(7), 2202-2212. doi:10.1021/Ja074244w
- Micsonai, A., Wien, F., Kernya, L., Lee, Y. H., Goto, Y., Refregiers, M., & Kardos, J. (2015). Accurate secondary structure prediction and fold recognition for circular dichroism spectroscopy. *Proceedings of the National Academy of Sciences of the United States of America*, 112(24), E3095-E3103. doi:10.1073/pnas.1500851112
- Minter, M. R., Taylor, J. M., & Crack, P. J. (2015). The contribution of neuroinflammation to amyloid toxicity in Alzheimer's disease. *Journal of Neurochemistry*, 1-18. doi:10.1111/jnc.13411
- Mital, M., Zawisza, I. A., Wiloch, M. Z., Wawrzyniak, U. E., Kenche, V., Wroblewski, W., . . . Drew, S. C. (2016). Copper Exchange and Redox Activity of a

- Prototypical 8-Hydroxyquinoline: Implications for Therapeutic Chelation.  
*Inorganic Chemistry*, 55(15), 7317-7319. doi:10.1021/acs.inorgchem.6b00832
- Mital, M., Zawisza, I. A., Wiloch, M. Z., Wawrzyniak, U. E., Kenche, V., Wróblewski, W., . . . Drew, S. C. (2016). Copper Exchange and Redox Activity of a Prototypical 8-Hydroxyquinoline: Implications for Therapeutic Chelation.  
*Inorganic Chemistry*, 55(15), 7317-7319. doi:10.1021/acs.inorgchem.6b00832
- Mitraki, A., & Kasotakis, E. (2013). Natural and Designed Self-Assembling Peptides and Their Applications in Bionanotechnology. In J. Castillo-Leon, L. Sasso, & W. E. Svendsen (Eds.), *Self-Assembled Peptide Nanostructures: Advances and Applications in Nanobiotechnology* (pp. 39-58). Singapore: Pan Stanford Publishing Pte. Ltd.
- Morgan, D. M., Dong, J., Jacob, J., Lu, K., Apkarian, R. P., Thiyagarajan, P., & Lynn, D. G. (2002). Metal switch for amyloid formation: insight into the structure of the nucleus. *Journal of the American Chemical Society*, 124(43), 12644-12645.  
doi:10.1021/ja0273086
- Nawar, S., Huskinson, B., & Aziz, M. J. (2013). Benzoquinone-Hydroquinone Couple for Flow Battery. *Mater. Res. Soc. Symp. Proc.*, 1491(mrsf12-1491-c08-09).
- Nelson, P. T., Alafuzoff, I., Bigio, E. H., Bouras, C., Braak, H., Cairns, N. J., . . . Beach, T. G. (2012). Correlation of Alzheimer Disease Neuropathologic Changes With Cognitive Status: A Review of the Literature. *Journal of Neuropathology & Experimental Neurology*, 71(5), 362-381. doi:10.1097/NEN.0b013e31825018f7
- Ni, R., Childers, W. S., Hardcastle, K. I., Mehta, A. K., & Lynn, D. G. (2012). Remodeling Cross- $\beta$  Nanotube Surfaces with Peptide/Lipid Chimeras.



*Angewandte Chemie International Edition*, 51(27), 6635-6638.

doi:10.1002/anie.201201173

O'Brien, R. J., & Wong, P. C. (2011). Amyloid precursor protein processing and Alzheimer's disease. *Annual Review of Neuroscience*, 34, 185-204.

doi:10.1146/annurev-neuro-061010-113613

Ohgushi, M., & Wada, A. (1983). Molten-Globule State - a Compact Form of Globular-Proteins with Mobile Side-Chains. *FEBS Letters*, 164(1), 21-24. doi:Doi

10.1016/0014-5793(83)80010-6

Olsson, M. H. M., & Ryde, U. (1999). The influence of axial ligands on the reduction potential of blue copper proteins. *Journal of Biological Inorganic Chemistry*, 4, 654-663.

Omosun, T. O., Hsieh, M.-C., Childers, W. S., Das, D., Mehta, A. K., Anthony, N. R., . . . Lynn, D. G. (2017). Catalytic diversity in self-propagating peptide assemblies. *Nature Chemistry*, advance online publication. doi:10.1038/nchem.2738

<http://www.nature.com/nchem/journal/vaop/ncurrent/abs/nchem.2738.html#supplementary-information>

Oostergetel, G. T., van Amerongen, H., & Boekema, E. J. (2010). The chlorosome: a prototype for efficient light harvesting in photosynthesis. *Photosynthesis Research*, 104(2-3), 245-255. doi:10.1007/s11120-010-9533-0

Otsuka, T., Maeda, T., & Hotta, A. (2014). Effects of Salt Concentrations of the Aqueous Peptide-Amphiphile Solutions on the Sol-Gel Transitions, the Gelation Speed, and the Gel Characteristics. *Journal of Physical Chemistry B*, 118(39), 11537-11545. doi:10.1021/jp5031569

- Ozbas, B., Kretsinger, J., Rajagopal, K., Schneider, J. P., & Pochan, D. J. (2004). Salt-triggered peptide folding and consequent self-assembly into hydrogels with tunable modulus. *Macromolecules*, 37(19), 7331-7337. doi:10.1021/ma0491762
- Pachahara, S. K., & Nagaraj, R. (2015). Probing the role of aromatic residues in the self-assembly of A $\beta$ (16–22) in fluorinated alcohols and their aqueous mixtures. *Biochemistry and Biophysics Reports*, 2, 1-13. doi:10.1016/j.bbrep.2015.04.005
- Pagano, G., Guida, M., Tommasi, F., & Oral, R. (2015). Health effects and toxicity mechanisms of rare earth elements—Knowledge gaps and research prospects. *Ecotoxicology and Environmental Safety*, 115, 40-48. doi:<http://dx.doi.org/10.1016/j.ecoenv.2015.01.030>
- Pan, Y.-x., Liu, C.-j., Zhang, S., Yu, Y., & Dong, M. (2012). 2D-Oriented Self-Assembly of Peptide Induced by Hydrated Electrons. *Chemistry - A European Journal*, 18(46), 14614-14617. doi:10.1002/chem.201200745
- Paparcone, R., Sanchez, J., & Buehler, M. J. (2010). Comparative Study of Polymorphous Alzheimer's A beta(1-40) Amyloid Nanofibrils and Microfibers. *Journal of Computational and Theoretical Nanoscience*, 7(7), 1279-1286. doi:10.1166/jctn.2010.1481
- Paramonov, S. E., Jun, H. W., & Hartgerink, J. D. (2006). Self-assembly of peptide-amphiphile nanofibers: The roles of hydrogen bonding and amphiphilic packing. *Journal of the American Chemical Society*, 128(22), 7291-7298.
- Peng, Y., Wang, F., Wang, Z. R., Alsayed, A. M., Zhang, Z. X., Yodh, A. G., & Han, Y. L. (2015). Two-step nucleation mechanism in solid-solid phase transitions. *Nature Materials*, 14(1), 101-108. doi:10.1038/Nmat4083

- Petty, S. A., & Decatur, S. M. (2005). Experimental evidence for the reorganization of b-  
strands within aggregates of the Ab(16-22) peptide. *Journal of the American  
Chemical Society*, 127(39), 13488-13489. doi:10.1021/ja054663y
- . Preparation of Nanostructures. (2007). In W. Fritzsche & M. Kohler (Eds.),  
*Nanotechnology: An Introduction to Nanostructuring Techniques* (Vol. 2, pp. 87-  
148). Weinheim: Wiley-VCH Verlag GmbH & Co.
- Rengifo, R. F., Li, N. X. A., Sementilli, A., & Lynn, D. (2017). Amyloid Scaffolds as  
Alternative Chlorosomes. *Organic & Biomolecular Chemistry*.  
doi:10.1039/C7OB01170A
- Ribeiro, A. C. F., Estes, M. A., Lobo, V. M. M., Valente, A. J. M., Simões, S. M. N.,  
Sobral, A. J. F. N., & Burrows, H. D. (2005). Diffusion Coefficients of Copper  
Chloride in Aqueous Solutions at 298.15 K and 310.15 K. *Journal of Chemical  
and Engineering Data*, 50(6), 1986-1990. doi:10.1021/je050220y
- Roberts, B. R., Ryan, T. M., Bush, A. I., Masters, C. L., & Duce, J. A. (2012). The role of  
metallobiology and amyloid-beta peptides in Alzheimer's disease. *Journal of  
Neurochemistry*, 120 Suppl 1, 149-166. doi:10.1111/j.1471-4159.2011.07500.x
- Rojas, S., Devic, T., & Horcajada, P. (2017). Metal organic frameworks based on  
bioactive components. *J. Mater. Chem. B*. doi:10.1039/c6tb03217f
- Sabale, S., Zheng, J., Vemuri, R. S., Yu, X.-Y., McGrail, B. P., & Motkuri, R. K. (2016).  
Recent Advances in Metal-Organic Frameworks for Heterogeneous Catalyzed  
Organic Transformations. *Synthesis and Catalysis*, 1, 1-8.

- Saitô, H., & Ando, I. (1989). High-Resolution Solid-State NMR Studies of Synthetic and Biological Macromolecules. In G. A. Webb (Ed.), *Annual Reports on NMR Spectroscopy* (Vol. Volume 21, pp. 209-290): Academic Press.
- Samuel-Landtiser, M., Zachariah, C., Williams, C. R., Edison, A. S., & Long, J. R. (2001). Incorporation of Isotopically Enriched Amino Acids *Current Protocols in Protein Science*: John Wiley & Sons, Inc.
- Sanderson, D. G., Anderson, L. B., & Gross, E. L. (1986). Determination of the redox potential and diffusion coefficient of the protein plastocyanin using optically transparent filar electrodes. *Biochimica et Biophysica Acta (BBA) - Bioenergetics*, 852, 269-278.
- Santini, S., Mousseau, N., & Derreumaux, P. (2004). In silico assembly of Alzheimer's Ab(16-22) peptide into  $\beta$ -sheets. *Journal of the American Chemical Society*, 126(37), 11509-11516. doi:10.1021/ja047286i
- Scanlon, S., & Aggeli, A. (2008). Self-assembling peptide nanotubes. *Nano Today*, 3(3-4), 22-30. doi:10.1016/S1748-0132(08)70041-0
- Schneider, R., Schumacher, M. C., Mueller, H., Nand, D., Klaukien, V., Heise, H., . . . Baldus, M. (2011). Structural characterization of polyglutamine fibrils by solid-state NMR spectroscopy. *Journal of Molecular Biology*, 412(1), 121-136. doi:10.1016/j.jmb.2011.06.045
- Sengupta, U., Nilson, A. N., & Kaye, R. (2016). The Role of Amyloid-beta Oligomers in Toxicity, Propagation, and Immunotherapy. *Ebiomedicine*, 6, 42-49. doi:10.1016/j.ebiom.2016.03.035

- Sevigny, J., Chiao, P., Bussiere, T., Weinreb, P. H., Williams, L., Maier, M., . . . Sandrock, A. (2016). The antibody aducanumab reduces A beta plaques in Alzheimer's disease. *Nature*, *537*(7618), 50-56. doi:10.1038/nature19323
- Shanmugam, G., & Polavarapu, P. L. (2011). Isotope-assisted vibrational circular dichroism investigations of amyloid b peptide fragment, Ab(16-22). *Journal of Structural Biology*, *176*(2), 212-219. doi:10.1016/j.jsb.2011.08.004
- Sheldon, R. A., & Arends, I. W. C. E. (2006). Catalytic oxidations mediated by metal ions and nitroxyl radicals. *Journal of Molecular Catalysis a-Chemical*, *251*(1-2), 200-214. doi:10.1016/j.molcata.2006.02.016
- Sigel, H., & Martin, R. B. (1982). Coordinating Properties of the Amide Bond. Stability and Structure of Metal Ion Complexes of Peptides and Related Ligands. *Chemical Reviews*, *82*, 385-426.
- Silva, C. G., Corma, A., & Garcia, H. (2010). Metal-organic frameworks as semiconductors. *Journal of Materials Chemistry*, *20*(16), 3141-3156. doi:10.1039/b924937k
- Sinz, A., Jin, A. J., & Zschornig, O. (2003). Evaluation of the metal binding properties of a histidine-rich fusogenic peptide by electrospray ionization Fourier transform ion cyclotron resonance mass spectrometry. *Journal of Mass Spectrometry*, *38*(11), 1150-1159. doi:10.1002/jms.532
- Smith, J. E., Liang, C., Tseng, M., Li, N., Li, S., Mowles, A. K., . . . Lynn, D. G. (2015). Defining the Dynamic Conformational Networks of Cross- $\beta$  Peptide Assembly. *Israel Journal of Chemistry*, *55*(6-7), 763-769. doi:10.1002/ijch.201500012

- Sokolowska, M., Pawlas, K., & Bal, W. (2010). Effect of common buffers and heterocyclic ligands on the binding of Cu(II) at the multimetal binding site in human serum albumin. *Bioinorganic Chemistry and Applications*, 725153. doi:10.1155/2010/725153
- Soltau, S. R., Niklas, J., Dahlberg, P. D., Poluektov, O. G., Tiede, D. M., Mulfort, K. L., & Utschig, L. M. (2015). Aqueous light driven hydrogen production by a Ru-ferredoxin-Co biohybrid. *Chemical Communications*, 51(53), 10628-10631. doi:10.1039/C5CC03006D
- Soto, C. (2011). Prion hypothesis: the end of the controversy? *Trends in Biochemical Sciences*, 36(3), 151-158. doi:10.1016/j.tibs.2010.11.001
- Tichy, M., & MRucki, M. (2013). Lanthanides, Toxicity. In R. H. Kretsinger, V. N. Uversky, & E. A. Permyakov (Eds.), *Encyclopedia of Metalloproteins* (pp. 1149 - 1151). New York: Springer.
- Torok, M., Milton, S., Kaye, R., Wu, P., McIntire, T., Glabe, C. G., & Langen, R. (2002). Structural and dynamic features of Alzheimer's Ab peptide in amyloid fibrils studied by site-directed spin labeling. *Journal of Biological Chemistry*, 277(43), 40810-40815. doi:10.1074/jbc.M205659200
- Valery, C., Artzner, F., & Paternostre, M. (2011). Peptide nanotubes: molecular organisations, self-assembly mechanisms and applications. *Soft Matter*, 7(20), 9583-9594. doi:10.1039/C1SM05698K
- van Nuland, N. A. J., Hangyi, I. W., van Schaik, R. C., Berendsen, H. J. C., van Gunsteren, W. F., Scheek, R. M., & Robillard, G. T. (1994). The High-resolution Structure of the Histidine-containing Phosphocarrier Protein HPr from

- Escherichia coli Determined by Restrained Molecular Dynamics from Nuclear Magnetic Resonance Nuclear Overhauser Effect Data. *Journal of Molecular Biology*, 237(5), 544-559. doi:<http://dx.doi.org/10.1006/jmbi.1994.1254>
- Vitale, G., Valina, A. B., Huang, H., Amunugama, R., & Rodgers, M. T. (2001). Solvation of copper ions by acetonitrile. Structures and sequential binding energies of  $\text{Cu}+(\text{CH}_3\text{CN})(x)$ ,  $x=1-5$ , from collision-induced dissociation and theoretical studies. *Journal of Physical Chemistry A*, 105(50), 11351-11364. doi:10.1021/jp0132432
- Vorontsova, M. A., Maes, D., & Vekilov, P. G. (2015). Recent advances in the understanding of two-step nucleation of protein crystals. *Faraday Discussions*, 179, 27-40. doi:10.1039/c4fd00217b
- Walker, L. C., Rosen, R. F., & Levine, H., 3rd. (2008). Diversity of Ab deposits in the aged brain: a window on molecular heterogeneity? *Romanian journal of morphology and embryology = Revue roumaine de morphologie et embryologie*, 49(1), 5-11.
- Wallace, J. A., & Shen, J. K. (2010). Probing the Strand Orientation and Registry Alignment in the Propagation of Amyloid Fibrils. *Biochemistry*, 49(25), 5290-5298. doi:10.1021/bi100137y
- Walsh, D. M., Hartley, D. M., Kusumoto, Y., Fezoui, Y., Condron, M. M., Lomakin, A., . . . Teplow, D. B. (1999). Amyloid b-protein fibrillogenesis. Structure and biological activity of protofibrillar intermediates. *The Journal of biological chemistry*, 274(36), 25945-25952.

- Walsh, D. M., Lomakin, A., Benedek, G. B., Condron, M. M., & Teplow, D. B. (1997). Amyloid b-protein fibrillogenesis. Detection of a protofibrillar intermediate. *The Journal of biological chemistry*, 272(35), 22364-22372.
- Wang, H., Zhu, Q.-L., Zou, R., & Xu, Q. (2017). Metal-Organic Frameworks for Energy Applications. *Chem*, 2(1), 52-80. doi:10.1016/j.chempr.2016.12.002
- Wang, J. X., Lei, Q., Luo, G. F., Cai, T. T., Li, J. L., Cheng, S. X., . . . Zhang, X. Z. (2013). Controlled Arrays of Self-Assembled Peptide Nanostructures in Solution and at Interface. *Langmuir*, 29(23), 6996-7004. doi:Doi 10.1021/La4010714
- Weitkamp, J. (2000). Zeolites and catalysis. *Solid State Ionics*, 131(1-2), 175-188. doi:Doi 10.1016/S0167-2738(00)00632-9
- Wiloch, M. Z., Wawrzyniak, U. E., Ufnalska, I., Piotrowski, G., Bonna, A., & Wroblewski, W. (2016). Redox Activity of Copper(II) Complexes with NSFRY Pentapeptide and Its Analogues. *PloS One*, 11(8), e0160256. doi:10.1371/journal.pone.0160256
- Wishart, D. S., Sykes, B. D., & Richards, F. M. (1991). Relationship between nuclear magnetic resonance chemical shift and protein secondary structure. *Journal of Molecular Biology*, 222(2), 311-333. doi:10.1016/0022-2836(91)90214-Q
- Xie, L., Luo, Y., & Wei, G. (2013). A $\beta$ (16–22) Peptides Can Assemble into Ordered  $\beta$ -Barrels and Bilayer  $\beta$ -Sheets, while Substitution of Phenylalanine 19 by Tryptophan Increases the Population of Disordered Aggregates. *Journal of Physical Chemistry B*, 117(35), 10149-10160. doi:10.1021/jp405869a
- Yi, C. S., Kwon, K. H., & Lee, D. W. (2009). Aqueous Phase C-H Bond Oxidation Reaction of Arylalkanes Catalyzed by a Water-Soluble Cationic Ru(III) Complex



$[(\text{pymox-Me}_2)_2\text{RuCl}_2]^+\text{BF}_4^-$ . *Organic Letters*, 11(7), 1567-1569.

doi:10.1021/OI900097y

Yvon, C., Surman, A. J., Hutin, M., Alex, J., Smith, B. O., Long, D.-L., & Cronin, L.

(2014). Polyoxometalate Clusters Integrated into Peptide Chains and as Inorganic

Amino Acids: Solution- and Solid-Phase Approaches. *Angewandte Chemie*,

126(13), 3404-3409. doi:10.1002/ange.201311135

Zhou, H. C., Long, J. R., & Yaghi, O. M. (2012). Introduction to Metal-Organic

Frameworks. *Chemical Reviews*, 112(2), 673-674. doi:10.1021/cr300014x

Zou, Q., Liu, K., Abbas, M., & Yan, X. (2016). Peptide-Modulated Self-Assembly of

Chromophores toward Biomimetic Light-Harvesting Nanoarchitectonics.

*Advanced Materials*, 28(6), 1031-1043. doi:10.1002/adma.201502454